Journal of Engineering

February
2013

Number 2
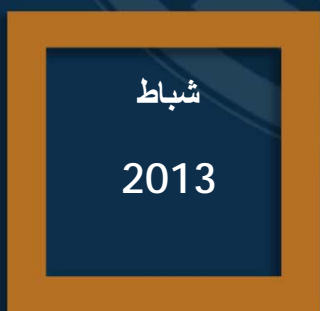
Volume 19

ENGINEERING

College of Engineering   Baghdad University   Baghdad

List of Contents

English Section: Page

Experimental Investigation Utilizing Thermal Image Technique to the Heat Transfer Enhancement Using Oscillated Fins

Prof. Dr. Ihsan Y. Hussain
Asst.Prof. Dr.Karima E.Amori
Asst.Lecturer. Dheya G. Mutasher

. . .   :

يتناول البحث* الدار السكني العراقي في العقد الاول من القرن الواحد والعشرين متخذاً الاعظمية إنموذجاً، ومعتمداً المنهج الوصفي الاستقرائي لدراسة هذا العقد. من خلال اجراء الدراسة الميدانية لثلاث محلات سكنية في منطقة الاعظمية. والتي تناولت المقارنة بين دور المرحلة الاولى من العقد الاول من القرن الواحد والعشرين بالمرحلة الثانية المتمثلة بالعقود الاخيرة من القرن العشرين. وعلى عدة جوانب شملت المساحات والحجوم والتشكيل وتوجيه انفتاح الدار السكني والوظيفة، للوصول الى أبرز التحولات في الدار السكني العراقي في العقد الاول من هذا القرن لإعطاء صورة عن الواقع السكني لهذه الحقبة.

كلمات رئيسة : الدار السكني، تقسيم الدور السكنية، تنطيق الفضاءات، تداخل الانطقة، الفضاء العام، الفضاء الخاص، الفضاء الانتقالي، الدور الشريطية.

ABSTRACT

This research describes Iraqi housing in the first decade of the twenty-first century, taking AL-Adhamiya as a model, depending on descriptive method of inductive approach to the study of this decade. By doing the field study for three neighborhood in Adhamiya district. Which takes in consideration the comparison between housing in the first period of the first decade of the twenty-first century with the second period of this decade: the latest decades of 21th century. And for many aspects involving areas, sizes, forming, direction of opening of housing and the function, to reach the most important transformation of Iraqi housing in the first decade of this century in order to give a picture of the residential fact for this period.

أ.م.د. أريج كريم مجيد السدخان
المهندسة: هالة علاء الدين

1-1– :

:

. **1-1-1** :

:

1

. .

.

2-1-1 :

.

. –

. **1–** :

. **3-1-1** :

( ) ( )

308 310 (312

( ) .) 100 .

(

2003

. **1-2** :

. –

:

:

153 .

.

53

100 .

%25 (.)

.

(2003) 7

1-3

: 	 . 	 (1).

(1)

.

.

.

1-3-1 	 :

	2003	2003
	2 24-12	2 42-12
	2 22-4	2 36,5-8
		2 18,4-0
	2 16-	2 59-18
	2 22-13	2 30-22
+	2 6-4,5	
	2 1,5 -	2 7,8-3,6
	2 1 -	2 4-1,5
		2 8-2
		2 4-0
	2 1 -	2 50-7,5
	2 10 -	2 35-15

:

•

–

800-300- 	 55-65%

(	 – 	 1975

(1137

2 390

.

.

.

2 100 	 2 50

(	) . 	 – 	)

(

•

: (	 - 	 *)

:

– 	 :

2003

. 	 .

.

(Standards)

.

60

360 .

40

———————————

* 	 .

.

أ.م.د. أريج كريم مجيد السدخان
المهندسة: هالة علاء الدين

240 .

.

. .

2003

– .

–.

2003 .

) .

" "

.(**2008**

)

–) . 750–500 .(

((–)

: – .

: –

–

. –

–

2003 .

126

– . 75

.2003 **http://www.dijlh.net/showthread.php/742**

) (**882**

(

) . (43 **2006**) .

) .

(: –

. .

. .

(–)

.

2-3-1   :   :

●

20

(double

.(volume.

(Cantilever)

.(1)

–   –

(2)   (double volume.)

.   : (

- 2010)

100 2

.

100 2

(–

.(3) (2)

(3)   (double volume.)

.   : (

- 201

●

2004

"

(1)   (double volume.)

..   : (

- 2010)

أ.م.د. أريج كريم مجيد السدخان
المهندسة: هالة علاء الدين

9

يكون الدار بثلاث طوابق

ضمن محددات الارتفاع اعلاه " (

http://www.mayoralty-

baghdad.com/PageViewer.aspx?id=35 .

3-3-1

–

–

. –

(Rapoport,1969,p.18).

–

. (54   2002   ) .

Rapoport[*]

(Rapoport,1969,p.49) .

)
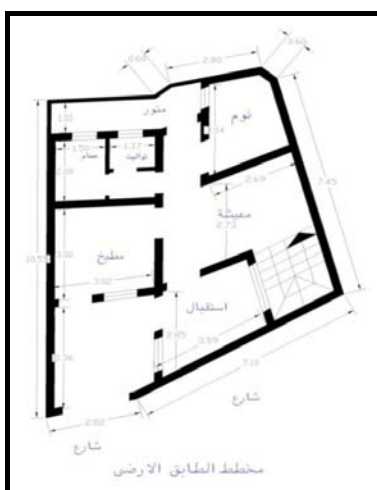
(4)   (

.

.

Rapoport   :

•

•   Rapoport

:

. –

. –

–

. –

_____

[*] Ropoport:

.

(4)   .

. :). – – –

)

•

.

.

6

)

.(

3,5

. 35-30

) . (   )

.(

.

(   )

. (-   )

. (5)

-        .-

.(6)   .

.

)   -

.(2010)

(7)
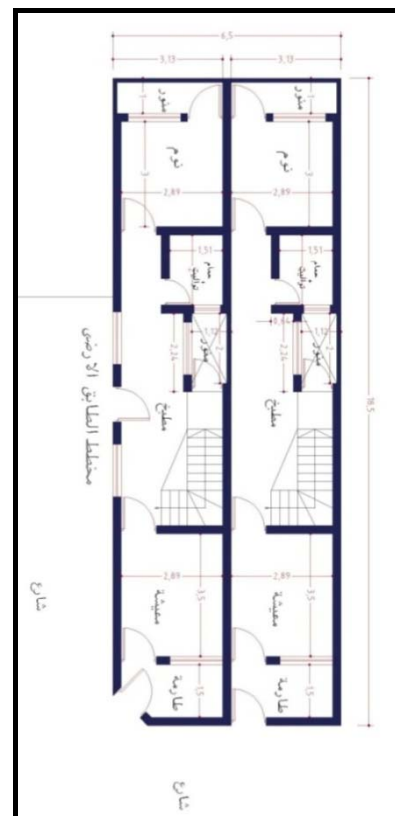
شكل (5) الدور الشريطية. المصدر:
(الباحثتان -الدراسة الميدانية)

●

(2)

. .   : (–

(

%14	
%70	
%16	

1 – 3 – 4

(6)

.

.

2003

. .   : (–   )

.

.

.

.

(7)

.   : (

2010 –

–

–   ).

.(2010 – 2011)

.

–

. –

(   )   . (
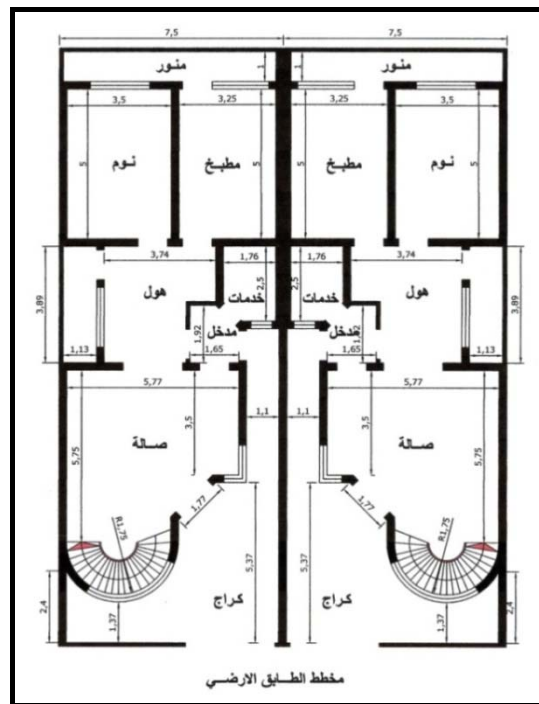
--	%86	%14	
--	%85	%15	
%94	--	%6	
%96	--	%4	
%67	--	%33	

:

•

.

.

%93   21

)

(   )   (
              (   )

         -    ) .

(2011-2010)   (9) .

.   (8)   (-   )

(8)

(.)

(-   ) :   .

4-4-1   :

.

:
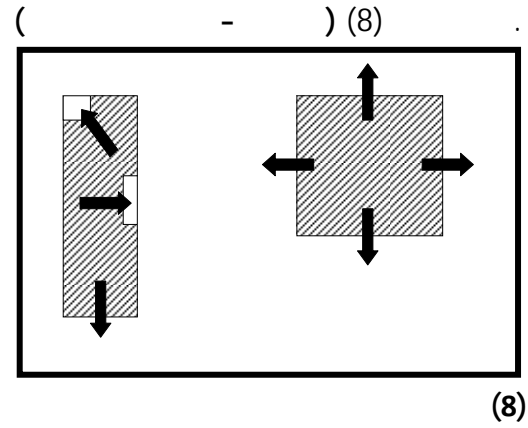
(3)

(-   ) : 2010-
(2011

%93	--	%7	
--	%53	%47	
--	%70	%30	
--	%14	%83	
%29	--	%71	
--	--	%100	

(10)

(9)

(11)

(:) -
( )

.

(:) -

•

2003

2 100

47% –

.-

.

(10).

. -)

(2011-2010).

(11).

(:) ( ) -

( )

2003

مخطط الطابق الارضي

(12)

: (-)

•

6

(-)

.(2011-2010

.(13)

.(156 1992)

(- 2010-

.(14) .(2011

)

.(

•
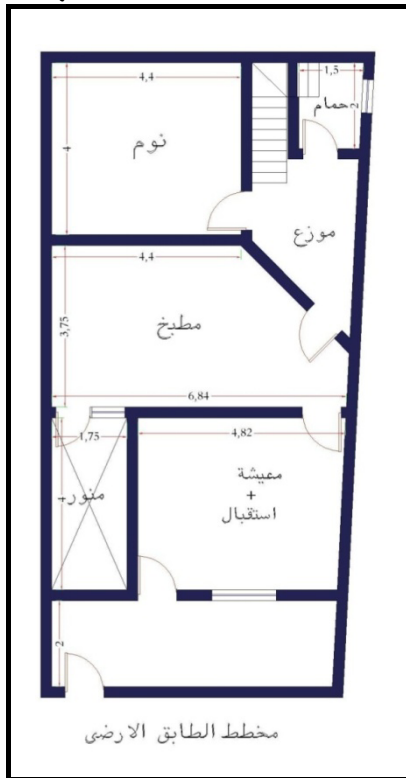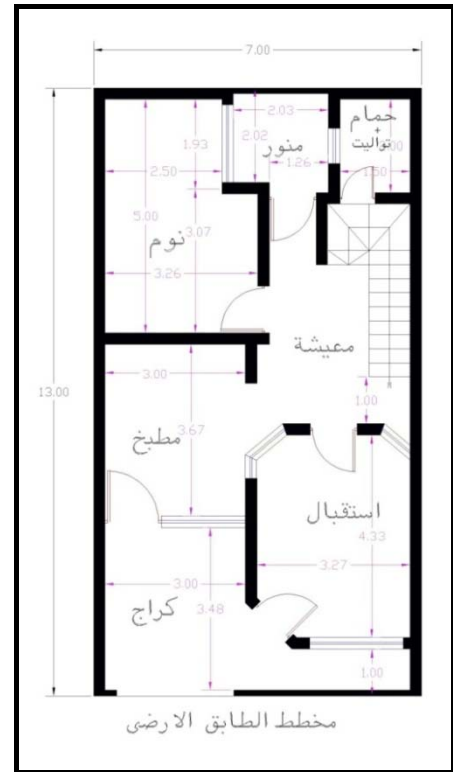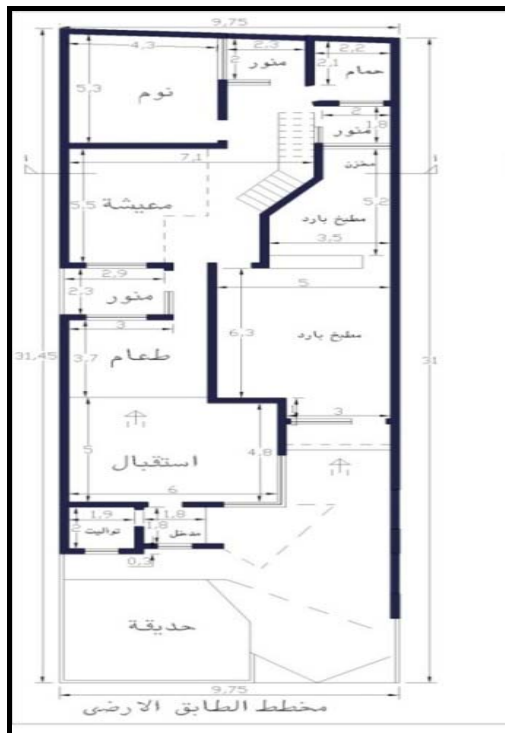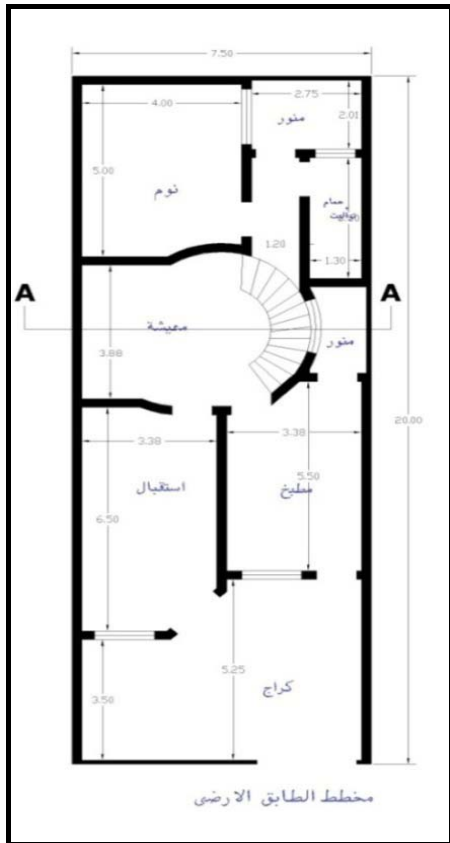
%70

.2003

.

.

( )

) ( )

.(

.

) .

.(

) . -)

.(12).. (2011-2010

)

Court ( )
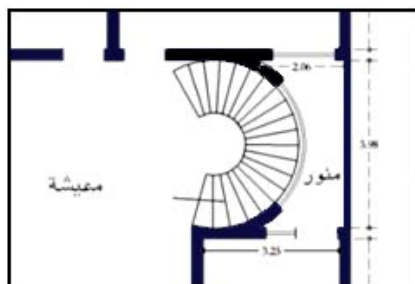
.

.

(13)

(29%)

.

.

.(15)

.

.

2004
.

.

(-) : .

(14)

(-) .

(-) :
•

(2003)
.

(15)

-) : .
)

•

2003

%86
-
-.

(   )

(-   ) .

.(16)

(16)   2003.
: (-   )

.(-   )

U L   )
•   (
.(17)

U

L

(17)   2003.
: (-   )   -   -

.(   )

(   )   .

.(18)   (   )

35%   2003

22%   2008

.

.

(2010)

(18)   2003.

:(–   )

•   :

.

2007

)

.(

.

.

–   94%-

94%

.   •

.   •

.

.   :

.

•

.   .

.   )   –

(

(1992)

•

121-125).(

14

(1992 129).

.2003

– %67-

90 2

( ) .

(2010-2011) .

(19) :

(-)

(19) .

.

.

.

21

أ.م.د. أريج كريم مجيد السدخان
المهندسة: هالة علاء الدين

5-1 :

(4) . :

(-   )

2003	2003	
)	)	
(	(	
.		
.	.	
.		
.	.	
.( )		

(5) . : (-   2010–

(2011

		■				■		■			
		■				■		■			
		■			▦			■			
	▦	■			▦			■			
	▦				▦			■			
		■				■	▦				
		■				■	▦				
		■				■	▦				
		■				■	▦				
☐								■			
☐				☐				■			

Ⅲ   ☐   ▦   ■

5-1   :

-

-

-

-

6-1   :

-

-

●

.

●

.

●

.

●

.

●

.

7-1 :

1- Rapoport, "House Form and Culture" Prentice-Hall, Inc., 1969

2-

.2002

3-

.1992

4- "

" ( )

2006

5-

1975

6-

http://www.dijlh.net/showthread.p
hp/742882- 2010

7- "

"

:
http://www.elaphblog.com/posts.asp
x?u=4708&A=59325 20.

8- :

http://www.mayoralty-
baghdad.com/PageViewer.aspx?id=3
5
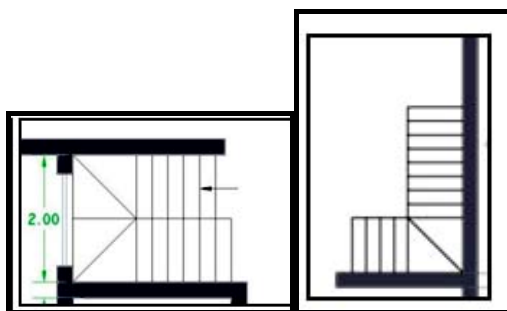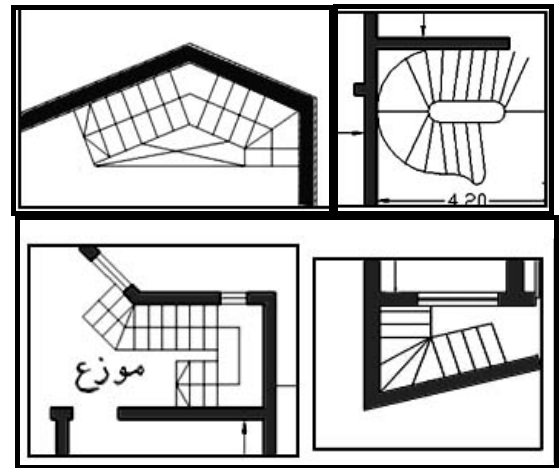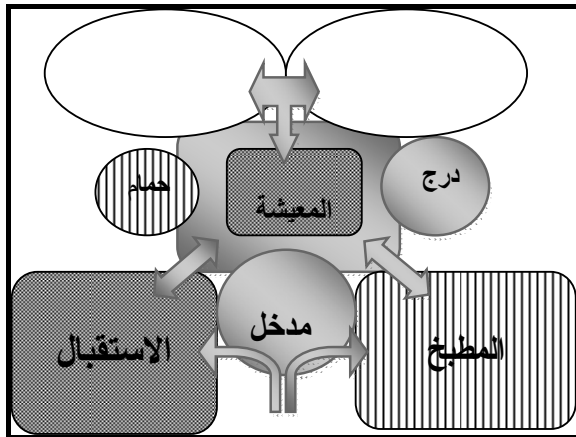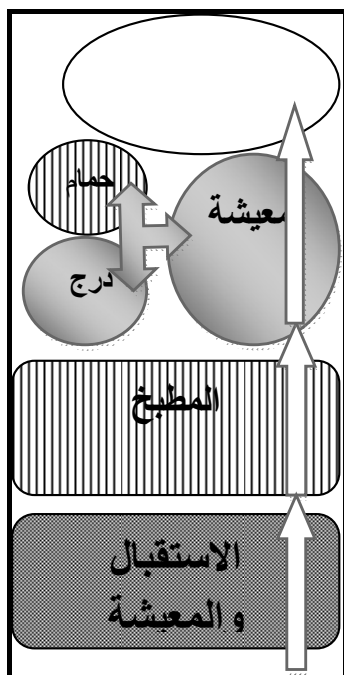
9- "

"

:
http://www.iraqoftomorrow.org/civi
l_studies/60349.html 2008

Investigation of Backfill Compaction Effect on Buried Concrete Pipes

By

Prof. Dr. Mosa Jawad Al-Mosawe, University of Baghdad, prof_mosa_2006@yahoo.com
Ass. Prof. Dr. AbdulMuttalib Issa Said, University of Baghdad, abdmusawi@yahoo.com
Abbas Oda Dawood, University of Maysan, abbasoda03@yahoo.com

ABSTRACT

The present study deals with the experimental investigation of buried concrete pipes. Concrete pipes are buried in loose and dense conditions of gravelly sand soil and subjected to different surface loadings to study the effects of the backfill compaction on the pipe. The experimental investigation was accomplished using full-scale precast unreinforced concrete pipes with 300 mm internal diameter tested in a laboratory soil box test facility set up for this study. Two loading platforms are used namely, uniform loading platform and patch loading platform. The wheel load was simulated through patch loading platform which have dimensions of 254 mm *508 mm, which is used by AASHTO to model the wheel load of a HS20 truck. The pipe-soil systems were loaded up to pipes collapse. Pipes were instrumented with strain gauges to measure circumferential strains, in addition to dial gauges, for measurements of the pipe vertical deflections and settlement of the loading platforms. The test results indicated that flexure governed the buried pipe behavior. Flexural cracks formed slightly before the ultimate load. A comparison of soil backfill, between a loose and dense compaction, showed that the dense backfill improve largely the pipe installation and the strength of pipe-soil system.

KEYWORDS: Buried concrete pipes, Backfill compaction, Bedding factors, Strain gages, Patch loading.

<div dir="rtl">

تحري تاثير حدل تربة الدفن على الانابيب الخرسانية المطمورة

د.موسى جواد الموسوي (استاذ)
د.عبد المطلب عيسى سعيد (استاذ مساعد)
د.عباس عوده داود (مدرس)

الخلاصة

الدراسة الحالية تتعلق بالتحري التجريبي للانابيب الخرسانية المطمورة. في هذه الدراسة تم دفن الانابيب في ظروف تربة مرصوصة و غير مرصوصة من الحصى الخابط و تم تسليط احمال سطحية مختلفة لدراسة تاثير حدل تربة الدفن على سلوك الانبوب. تم اجراء فحص النماذج باستخدام انابيب خرسانية غير مسلحة مسبقة الصب باحجام حقيقية و بقطر داخلي مقداره 300 ملم حيث تم فحصها مختبريا باستخدام صندوق تربة و هيكل فحص تم تصنيعهما خصيصا لهذه الدراسة. تم استخدام نوعين من منصات تسليط الاحمال و هي منصة تسليط الاحمال المنتظمة و منصة تسليط احمال الرقعة (الاحمال المركزه) . حمل اطار المركبة تم تمثيله من خلال تحميل الرقعة و التي ابعادها 254*508 ملم و المعتمدة من قبل AASHTO لتمثيل حمل اطار مركبة HS20. منظومة الانبوب-التربة تم تحميلها لغاية انهيار الانبوب. جُهزت الانابيب بمقاييس الانفعالات لقياس الانفعالات المحيطية بالاضافة الى تم تثبيت مقاييس الهطول لقياس التغييرات العمودية في قطر الانبوب بالاضافة الى مقاييس نزول منصات التحميل. نتائج الفحوص اشارت الى ان سلوك الانحناء هو الذي يحكم تصرف الانبوب و ان شقوق الانحناء تتكون قبل حمل الفشل بقليل. من مقارنة تربة الدفن بين الحدل المفكك و المرصوص تبين بان الدفن المرصوص يُحسن بشكل كبير طريقة تنصيب الانبوب و كذلك قابلية تحمل منظومة الانبوب-التربة.

الكلمات الرئيسية : الانابيب الخرسانية المطمورة ، حدل تربة الدفن ، معاملات الوسادة ، مجسات الانفعالات ، احمال الرقعة.

</div>

Prof. Dr. Mosa Jawad Al-Mosawe
Ass. Prof. Dr. AbdulMuttalib Issa Said
Abbas Oda Dawood

INTRODUCTION

Buried pipes are constructed from various materials in wide range of sizes and shapes and were primarily used for drainage applications prior to 19th century. Today buried pipe infrastructure serve many purposes, including sewer lines, drain lines, water mains, telephone and electrical conduits, highway and railway culverts, gas and liquid-petroleum lines, coal slurry lines, pedestrian and stock passes, subway tunnels, heat distribution lines and numerous other special functions [Bashir 2000].

Buried pipes are classified as either rigid or flexible. A flexible pipe is defined as one that will deflect at least 2 percent of its diameter without structural distress while rigid pipe is generally those that cannot deflect more than 2% of its diameter before failing. In the industrial market, the most common rigid pipes are clay, cast iron, unreinforced concrete and reinforced concrete pipes, etc, while flexible pipes includes PVC, Steel, Ductile iron, etc [Moser and Folkman 2008].

Concrete Pipes plays a significant role in highway construction, sewerage water disposal and canal flow. The economics of manufacturing, durability of pipe, and rigidity under a load make them an attractive choice in many situations [Haque 1998].

Today, it is well known that besides the pipe material, the installation procedures have a great effect on the performance of the pipe-soil system.

The present study is to evaluate the structural behavior of a full scale non-reinforced concrete pipe installed under earth and exposed live loadings. The pipes installed in a laboratory soil box. Gravelly sand was used as the soil. Deep burial was simulated by applying a surcharge load after the soil box had been filled with soil. The loading system is a special load frame facility.
The pipes were instrumented to record data for strain and the change in vertical diameter. The strain gages were wired to data acquisition system. Data was directly read by a computer activated system. The measured data were the applied load, surface strains at crown, invert and springlines, vertical diameter change (deflection) and loading platform settlement.

The main objective of the current work is to investigate the behavior of the concrete pipes subjected to different loading systems and its interaction with surrounding soil at different compaction efforts.

MATERIAL DESCRIPTIONS
CONCRETE PIPE

Full scale non-reinforced concrete pipes of 300 mm internal diameter, 394 mm external diameter and thickness of 47 mm were used in the present work. The length of pipes was 1000mm. The concrete compressive strength of the pipe is determined by using non-destructive tests, namely ultrasonic pulse velocity. The ultrasonic test was performed on two pipes, for each test 10 readings were taken by direct method, and the average compressive strength is about 30 MPa.

The elastic constants of concrete and steel (in case of reinforced pipe) are necessary when calculating wall thrust and bending moment. The elastic modulus values used in concrete design computations are usually estimated from empirical expressions that assume direct dependence of the elastic modulus on the strength and density of concrete [Mehta and Monteiro 2006].

According to ACI Building Code 318 [ACI Code 318M 2008], with a concrete unit weight between 1500 and 2500 kg/m3, the modulus of elasticity were determined from:

$$E_c = \gamma_c^{1.5} * 0.043 \, f_c'^{1/2} \qquad (1)$$

Where
E_c = static modulus of elasticity (MPa)
γ_c = concrete unit weight (kg/m^3)
f_c' = 28-day compressive strength of standard cylinders (MPa).

Thus, based on the density of concrete pipe of 2280 kg/m^3 and the compressive strength of 30 MPa, the value of modulus of elasticity according to Eq.(1) is 25634 MPa. In this study Poisson ratio is assumed equal to 0.129 [Haque 1998].

The cross sectional area A and moment of inertia I of the pipe, per unit length (namely plane pipe) are $A = 1 * t$ and $I = 1 * t^3 / 12$, and they equal to 47 mm^2/mm and 8651.917 mm^4/mm respectively.

BACKFILL SOIL

The soil used in this study was relatively uniform gravelly sand with maximum particle size of 25 mm, it pass through sieve #25.

According to ASTM D422, the backfill soil composed of approximately 13 % Medium Gravel, 74% Sand, and 1.17% fines passing sieve No. 200, by weight. The particle size distribution curve for backfill material is shown in **Fig.1**. The uniformity coefficient, Cu and coefficient of curvature Cc are calculated based on **Fig. 1**.

$$C_u = \frac{D_{60}}{D_{10}} = \frac{1.9}{0.125} = 15.2 \qquad (2)$$

$$C_c = \frac{(D_{30})^2}{D_{10} \times D_{60}} = \frac{(0.31)^2}{0.125 * 1.9} = 0.4046 \quad (3)$$

Where, D10, D30, and D60 are the diameters corresponding to percents finer than 10, 30, and 60 %, respectively [Das 1984]. Based on **Fig. 1** it is found that $D_{10} = 0.125$ mm, $D_{30} = 0.31$ mm and $D_{60} = 1.9$ mm.

Thus based on grain size curve and with the uniformity coefficient, Cu = 15.2 and the coefficient of curvature, Cc = 0.404, the backfill soil is classified as poorly graded sand with gravel (SP) according to unified soil classification system USCS. And it is classified as A-1-b soil class according to AASHTO. According to Iraqi standards this soil is classified as Granular base material Type D. According to ASTM C1479-07a it is meets the gradation requirements of Category I-SIDD (Standard Installation Direct Design) soil. The soil classification according the above data is summarized in **Table 1**.

BEDDING

Bedding is the first layer of embedment material around the tested pipe. It was finished before the installation of pipe. The bottom base of the soil box was directly overlain by the gravelly sand material which served as the bedding layer. Overall thickness of the bedding layer below pipe invert is constant for all tests and equal to 30 cm. Before transporting the complete instrumented pipe to the Lab the trench and bedding is completed. compacted backfill soil (Dense bedding) were used in this study, The dense bedding layer was leveled and compacted sufficiently using hand tamper.

DESCRIPTION OF EXPERIMENTAL APPARATUS

SOIL BOX

A fabricated steel box with dimensions 1.5m by 1.05m in plane and 1.3m in height was used to study the behavior of buried concrete pipe. As mentioned previously the pipes had a length of 1000 mm, so that the ends of the pipe would not touch the sidewalls of the test box in which its width equal to 1050 mm. This means that the ends of the pipe are not restrained, but are free to undergo axial (longitudinal) expansion just as they would if placed with bell and spigot connections in the field [Moore et al., 2004].

The soil box was designed to have two trench widths, a wide trench, 1.5 m wide in which the clear distance between pipe and the trench wall is 1.375 Do , namely 0.55 m , and a narrow trench, 0.8 m wide, in which the clear distance between pipe and the trench wall is 0.5 Do , namely 0.2 m. The natural ground (at bedding foundation and two sides of the trench) was simulated by soil box steel walls.

LOADING SYSTEM

The loading frame system included three essential components:

1-Reaction frame: which is constructed using steel I sections and anchored into concrete footing with clear width of 1.73 m and clear height from the ground of 2.21 m, as shown in **Fig. 2**.

3-Hydraulic jack: A hydraulic jack of 400 kg/cm^2 maximum capacity (which equivalent to 39.3 MPa or 23 tons in force unit) with a piston diameter of 87.8 mm was used to apply the load on the backfill. The piston is connected to hydraulic power supply/control unit which operate manually.

3- Loading Platform: After the tank was filled with soil a grillage consisting of three layers of steel sections was assembled on 6mm steel plates rest on top of the leveled soil surface for loading applications as will be discussed later.

Prof. Dr. Mosa Jawad Al-Mosawe
Ass. Prof. Dr. AbdulMuttalib Issa Said
Abbas Oda Dawood

Investigation of Backfill Compaction
Effect on Buried Concrete Pipes

MODELING OF LOADING

The load was transferred from the bottom face of the hydraulic cylinder to the top of the backfill over the pipe by a loading platform. There are two types of loading platforms depending on the type of loading namely uniformly distributed load and patch loading.

Thus two types of loading platforms were used in the present study, namely uniform load platform and patch platform. Each platform is a simulation of an actual loading type, as summarized in **Table 2**.

UNIFORM LOADING PLATFORM (EARTH FILL)

The bottom of the platform comprised of steel plates of thickness 6 mm and dimensions cover the top of leveled backfill, and then closely arranged IPE 140 steel I-beams of 1m length which approximately cover the top of the backfill and its top plates. At the top of IPE 140 beams structure there was two HP 150 beam sections installed transversely at 1/3 span of the IPE 140 beams from each end so that the load on these HP 150 beams will distributed equally to the IPE 140 beams. The hydraulic cylinder rests on a heavy beam of length 0.85m which in turn rest on the transverse HP 150 beams.

PATCH LOADING PLATFORM

A steel plate of size 508 mm * 254 mm with thickness of 30 mm was used for transferring the load from the hydraulic cylinder to the top of the backfill to represent the AASHTO HS20 truck wheel loading.

The dimensions of the platform plate is based on the AASHTO specifications, due to the HS 20, 32,000 pound and the Alternate Truck 25,000 pound design axle are carried on dual wheels. The contact area of the dual wheels with the ground is assumed to be a rectangle, with dimensions of 10 in * 20 in, [ACPA 2009].

DESCRIPTION OF EXPERIMENTAL INSTRUMENTS

The experimental instruments used in the test series of pipe included mainly two systems: the data acquisition system, the pipe deflection measurement system, and the loading system. The data acquisition system consists of strain indicator unit. The pipe deflection measurement system consists of a dial gauges. The loading system is a special load frame facility.

DATA ACQUISITION SYSTEM

Strains of pipe surface were measured using a mobile data acquisition system. The data acquisition system used in this study includes personal desktop computer, strain indicator has 8 channels and accompanying software. The measured data comprised output voltages, which were then post processed using application programs and spreadsheets to derive design variables.

In the present work the strain gauges were directly wired into the individual quarter-bridge Wheatstone circuit using the active-dummy method, where one strain gage serves as a dummy gage and one strain gage serve as active gage.

TML Strain gauges Type PL-60-11 are used in all tests. It is an electrical resistance unidirectional strain gauges metal foil gages 60mm in length designed for measuring concrete strain on the surface of a concrete structure. All gauges had a nominal resistance of 120 ohms and a nominal gauge factor of 2.22.

There was one primary section for each pipe. Four strain gages were installed in each layer (inner concrete and outer concrete) of the primary section. A total of 8 gages were installed for each pipe, which sums up a total of 16 gages for both active and dummy pipes. Uniaxial strain gauges were used to measure the circumferential strains at four separate locations around the pipe circumference: at the Crown, Invert and both Springlines. The strain gauge locations were at mid-span for patch loading and at 330 mm for uniform loadings.

DEFLECTION DIAL GAUGE

A dial gage of 1 cm reading capacity was used to measure the vertical deflection of pipe. A special stand was manufactured capable of adjusting the vertical position of dial gauge arm in addition to keeping it firmly inside the pipe as shown in **Fig. 3**. Dial gauge is installed at mid span for patch loading and at 250mm for uniform and strip loadings.

SETTLEMENT MEASUREMENT DIAL GAUGE

The settlement of the loading platforms was monitored using dial gauge of 5 cm reading capacity.

COMPACTION CONTROL OF GRANULAR FILL AND COMPACTION EQUIPMENT

In geotechnical engineering practice, it is customary to use the dry density of the compacted fill to control the field compaction operation. Accordingly, a standard Proctor density test, AASHTO T-90 or ASTM D698 (or Modified Proctor Compaction Test AASHTO T-180 or ASTM D1557) is performed on the soil and the maximum dry density of the soil determined. The target dry density to be achieved in the field is then expressed as a percentage of the maximum dry density.

In this study the compaction characteristics of the test soil were determined in accordance with Modified Proctor Test, ASHTTO T-180. Six compaction tests were performed to obtain the moisture-density relationship of the backfill soil. The maximum dry density obtained was 21.5 kN/m^3 with a corresponding optimum moisture content of 7.6% as shown in **Fig.4**.

The field compaction devices that are most commonly used in the compaction of pipe embedment materials are impact rammers and vibratory plates. In this study the mechanical compactor could not be used due to the limited space of soil box, therefore a hand tampers are used as compaction tool, namely manual compaction is used in this study. Two steel hand tampers with height of 1.35 m are used in this study, one with contact area of 200 *200 mm steel plate with thickness of 16 mm, and total weight of 14.7 kg as shown in **Fig. 5**. This tamper was used for all layers except for narrow trench between pipe and wall region. The second is smaller than first tamper; which consist of a steel plate with 200 * 100 mm contact area and thickness of 16 mm, and total weight of 10.9 kg as shown in **Fig. 5**. This tamper was used mainly with narrow trench conditions to compact the soil between pipe and trench.

FIELD DENSITY MEASUREMENT

In-situ density and moisture content of the backfill and bedding layer was monitored according to AASHTO T191-86 sand cone method. Sand passed through sieve No. 20 and retained on sieve No.50 was used in the sand cone apparatus. Density of the standard sand was determined in the laboratory and the average value was 1.53 g/cm^3. Weight and volume of the soil specimen was measured in the lab to compute the test density and then the compaction degree based on the maximum dry density of 21.5 kN/m^3 and optimum moisture content of 7.6%. The backfill compaction results for each test and bedding layer compaction are presented in **Table 3**. In the present study the terms dense soil or dense compaction are used for compaction greater than 92% and loose soil or loose compaction for compaction less than 90%.

TEST VARIABLES

Test variables included trench width, compaction degree, and backfill cover. All these variables are investigated under two types of loadings, uniform, and patch loadings.

The investigation is accomplished to select which combinations could provide the proper information. A total of 4 tests were conducted with the test variables and 2 tests for the sake of failure load analysis (bedding factor analysis) in addition to the three edge bearing test, thus a total of 7 tests were accomplished. The test variables are summarized in **Table 4**.

The descriptions of tests according to their variables are shown in **Fig. 7**.

THREE EDGE BEARING TEST, TEB

A three-edged bearing test is used to determine the strength of a rigid pipe in which this test strength is directly related to the load carrying capacity of the buried pipe. The pipe is supported at two locations along the bottom, and a vertical load is applied at the top until the pipe fails. When concrete pipe is subjected to a load, either by a testing apparatus or a field installation, this load tries to deform the pipe into an elliptical shape. During the loading process, tensile stresses develop on the inside of the pipe at the crown and invert and on the outside of the pipe at the

Prof. Dr. Mosa Jawad Al-Mosawe
Ass. Prof. Dr. AbdulMuttalib Issa Said
Abbas Oda Dawood

**Investigation of Backfill Compaction
Effect on Buried Concrete Pipes**

springline, and compressive stresses develop opposite these tensile stresses. Since concrete is

strong in compression but weak in tension, cracks form in the tensile zones [WRI 2003].

The test pipes failed during the three edge bearing test at the applied vertical pressure of 73.79 bar which equivalent to a line load of 44.68 kN/m. Thus according ASTM C14M, the test pipes were belonging to Class 3.

BEDDING FACTORS ANALYSIS

As described earlier, the test pipe was subjected to loading controlled by a hydraulic jack. The load was applied until one of the following conditions was met:
1. Maximum capacity of the load cell was achieved, or
2. Invert and crown strain gages had failed, or
3. Failure of the pipe

The failure load is good criterion for the sake of comparison between tests and clearly reflects the effect of test variables on the pipe strength. It should be noted that failure load here is the load of total collapse of the pipe. Also due to unreinforced concrete pipe the crack load is slightly less than collapse load.

In this study the failure load analysis was achieved through the bedding factor analysis, in which the Three Edge Bearing TEB test result is considered as a reference quantity for comparison of buried pipe strength or loading capacity. Due to TEB test results was in kN/m units at the pipe crown, therefore the vertical stress at pipe crown level due to the failure loads of different loading platforms are calculated firstly using or approximate method and then converted from stress to equivalent line loads.

The vertical stress at the crown level due to patch loading platform is determined using an approximate method called the 2:1 method for rectangular loads. In this method the surface load on an area B x L is dispersed at a depth z over an area (B + z) x (L + z) as shown in the **Fig. 6**. The vertical stress increment under the center of the load is [USACE (EM 1110-1-1904) 1990]:

$$P_Q = \frac{Q}{(B+z) \cdot (L+z)} \qquad (4)$$

Where Q = is the resultant of a surface rectangular load, kN.
Finally, for uniform loading platform which could be expressed as simulated earth fill; the overburden pressure due to gravity loads is expressed by the following relation:

$$P_g = \gamma_s H \qquad (5)$$

where, γ_s = unit weight of soil.

Thus after determination the vertical stress at the buried pipe crown due to applied surface load, it is converted to equivalent line load at the pipe crown by multiplying the stress by outside diameter of the pipe, namely 397 mm as shown in **Table 5**.

Once the pipe load has been determined, the next step in pipe failure load investigation involves defining the bedding factor. The bedding factor is defined as the ratio between the supporting strength of the buried pipe to the strength of the pipe in a three-edge bearing test [Selig and Packard 1987]. The bedding factor is determined according to the following equation [Wong et al., 2002]:

$$B_f = \frac{W_L + W_E}{TEB} \qquad (6)$$

Where B_f is the bedding factor, W_L is live load such as vehicle load, W_E is earth load (here due to 30cm or 60 cm backfill covers) and TEB is the Three Edge Bearing test strength. According to above equations the bedding factors for each test were calculated and summarized in **Table 5**.

In the present study the bedding factors are indication for quality of pipe-soil system, namely as the bedding factor values are high as the installation quality is good. Thus higher values of bedding factors are not necessary to be accompanied with higher failure loads.

Based on **Table 5**, the highest bedding factor is 2.30 for Test No.5 and lowest bedding factor is 1.26 for Test No.6, these results are expected due to Test No.5 used dense backfill while for Test No.6 uncompacted backfill was used.

For the same backfill cover and the same bedding conditions as for Tests No.1 and 2 the bedding factors are considerably different due to different compaction efforts which indicate that the pipe-soil strength considerably is affected by the

backfill compaction although similar conditions of bedding or cover conditions.

ANALYSIS OF BACKFILL COMPACTION EFFECT

The comparison was accomplished for two loadings types, uniform loading and patch loading as shown in **Table 6**.

STRAIN ANALYSIS

Generally, the experimental data obtained from the tests were not the direct reading of strain, and they were only the readings of voltage change. Therefore, to obtain the readings of the strain, the experimental data needed to be transformed after tests, in this study an Excel Spreadsheets are developed for data transformation.

According to quarter-bridge Wheatstone circuit, if the resistances are R1, R2, R3 and R4 (in Ohm, Ω) and the bridge voltage is E (in Volt, V). Then, the output voltage v_o (Volts) is obtained with the following equation:

$$v_o \approx \frac{1}{4} \cdot \frac{\Delta R}{R} \cdot E = \frac{1}{4} \cdot G_s \cdot \varepsilon \cdot E \qquad (7)$$

Where
R1 = Strain gage resistance
ΔR_1 = Change in strain resistance
ε = strain
G_s = Gage factor

Thus the obtained is an output voltage that is proportional to a change in resistance, i.e. a change in strain. This microscopic output voltage is amplified for analog recording or digital indication of the strain.

Thus the strain is computed from the following equation

$$\varepsilon = \frac{4 * \Delta V}{G_s * E} \qquad (8)$$

Where ΔV = change in voltage (reading of the increment of voltage)

In general the strains for loose compaction were always greater than that of dense compaction which is expected conclusion as shown in **Fig. 8**

to **Fig. 11**. At springlines there are relatively slight different between tests set for both loading conditions as shown in **Fig. 10** and **Fig. 11** which mean that there are small difference between compaction in both tests either loose or dense compaction. The approximately similar compaction effort at springlines of tests sets are due to the compaction by hand tamper faced difficulties at springlines region such as limited space or avoid pipe damage, thus this results are expected.
The tensile strains are relatively closed between tests set in case of uniform load but there are clear gaps in case of patch loading especially at invert and crown as shown in **Fig. 8b** and **Fig. 9b**, in which there are rapid and sharp increasing in tensile strains with increasing loadings in case of loose compaction which reflect the probability of rapid growth of cracking. .
In contrast, the compressive strains are relatively closed between tests set in case of patch loading but there are clear gaps in case of uniform loadings, in which the gap increased with load increasing as shown in **Fig. 8a** and **Fig. 9a**.

BENDING MOMENT ANALYSIS

The bending moment and the thrust force can be obtained from the experimental strain data of the test pipes. If the strains are known through the thickness, then the bending moment and thrust in the pipe wall can be computed from equations of mechanics of materials.
From the principles of strength of materials, circumferential stresses at the inside and the outside walls of the pipe due to beam bending and axial forces are expressed as follows

$$\sigma_i = \frac{P}{A} + \frac{M * c}{I} \qquad (9)$$

$$\sigma_o = \frac{P}{A} - \frac{M * c}{I} \qquad (10)$$

Where ,
σ_i , σ_o = Circumferential stresses at the inside and outside of the pipe respectively N/m^2.
P = Axial thrust per unit length of the pipe, N/m
A = Cross-sectional area per unit length of the pipe, m^2/m).
M = Bending moment per unit length of the pipe , N-m/m.
c = Distance from the neutral axis to the extreme fiber, m.

I = Moment of inertia of unit length of pipe wall (m^4/m).

According to the principles of theory of elasticity, the circumferential stresses can be related to the strain gage readings from the inner and the outside walls of the pipe as

$$\sigma_i = E_c * \varepsilon_i \qquad (11)$$

$$\sigma_o = E_c * \varepsilon_o \qquad (12)$$

where,

ε_i , ε_o = Circumferential strains at the inside and outside of the pipe wall respectively,

E_c = Young's modulus of pipe materials, N/m2.

Further, when subtracting Eq.(9) from Eq.(10), and substituting the value for circumferential stresses from Eq.(11) and Eq.(12) , the equation to calculate the bending moment is obtained as follows:

$$M = \frac{(\sigma_i - \sigma_o)}{2*c} * I = \frac{(\varepsilon_i - \varepsilon_o)}{2*c} * E_c * I \qquad (13)$$

The sign conventions are, the axial thrust is assumed to be positive in tension and the bending moment is positive when producing tension in the exterior fibers of the pipe wall.

In general the bending moments for loose compaction under similar loading were always greater than that of well compacted soil, the results are shown in **Fig. 12** and **Fig. 13**. At both springlines the bending moments coincided, this is because springline compaction (by hand tamper) is less than the rest to avoid pipe damage, thus these results are expected. At crown and invert, the bending moment of pipe with loose backfill were higher that those of well compacted backfill with gap increasing with increasing applied load.

At invert, there is sharp increase in bending moment of loose backfill in comparison with well compacted backfill under both loading conditions as shown in **Fig. 13a** and **Fig. 13b**,

DEFLECTION ANALYSIS

As expected the vertical deflection of pipe in case of loose backfill are greater than that of well compacted backfill as shown in **Fig. 14** (for Tests No.1 and No.2 there are no available data for deflection). The deflection of Test No.4 (dense

compaction) at load increment before failure was 0.14 mm (0.047% as percent from internal diameter of 300mm) while for Test No.3 (loose compaction) the deflection for load increment before failure was 0.185mm. this reflect that the buried strength increased considerably with compaction effort of surround backfill.

SETTLEMENT ANALYSIS

The settlement actually decreased with increasing backfill effort, this concept clearly appears in **Fig. 15**. It clearly indicate that settlement of patch platform was much greater than the settlement of uniform platform due to small contact area of patch platform in comparison with uniform platform. **Fig. 15** indicate that the shape of settlement curve patch loading platform were sharply increased with increasing loading after loading of 19 kN in case of loose backfill while the sharp increase start after loading of 78 kN in case of well compacted backfill.

FAILURE LOAD ANALYSIS

The failure loads of dense compaction tests were higher than that of loose compaction tests, as shown in **Table 7**.

In general a single crack pattern has been observed for all pipes pipe, which appear as longitudinal and approximately straight cracks along the inner faces of invert and crown and outer faces of springlines, namely flexural cracks as shown in **Fig. 16**.

CONCLUSIONS

Based on the analysis results the following conclusions can be drawn:

1. The highest bedding factor obtained is 2.30 for dense backfill and lowest bedding factor is 1.26 for uncompacted backfill.

2.For the same backfill cover and the same bedding conditions as for the bedding factors are considerably different due to different compaction effort which indicate that the pipe-soil strength considerably affected by the backfill compaction although similar conditions of bedding or cover conditions.

3. It is found that the compaction of backfill cover of 30 cm or 60 cm over the pipe crown and also

The backfill below the springline will improve the installation of the concrete pipe and then the strength of pipe-soil system.

4. The collapse loads of pipes under uniform load with 60cm backfill cover; ranged from surface overburden pressures of 131.2 kPa (very loose backfill) to 248.2 kPa (well compacted backfill) overburden pressures which yield that installation quality can increase the strength of pipe-soil system to approximately 50% as an upper limit.

REFERENCES

- ACI Code 318M-05 **"Building Code Requirements for Structural Concrete and Commentary (ACI 318M-08)"**, American Concrete Institute 2005.

- ACPA, Design Data 1" **Highway Live Loads on Concrete Pipe"**, American Concrete pipe Association, 2009.

- Bashir R. **"Analysis and Design of Buried Pipelines"** M.Sc. Thesis, King Fahd University of Petroleum & Minerals Dhahran, Saudi Arabia, 2000.

- Das, B. M., **"Principles of Foundation Engineering"**, Brooks/Cole Engineering Division, 1984.

- Haque M. M. **"Comparison of Behavior of 1520 mrn (60 in.) Concrete Pipe with SIDD Design Under Deep Cover"**, M.Sc. Thesis, Ohio University, 1998.

- Mehta P. K. and Monteiro P. M. " **Concrete: Microstructure, Properties, and Materials"**, Third Edition, McGraw-Hill, 2006.

- Moore I. D., Lapos B., and Mills C., **"Biaxial testing to investigate soil-pipe interaction of Buried fiber reinforced cement pipe"** Transportation Research Record No. 1868, Soil Mechanics, Washington, DC USA, 2004.

- Moser A. P. and Folkman S. **"Buried Pipe Design"** Third edition, McGraw-Hill, 2008.

- Selig E. T. and Packard D. L., **"Buried Concrete Pipe Trench Installation Analysis"** ASCE, Journal of Transportation Engineering, Vol. 113, No. 5, September, 1987, pp.485-501.

- U.S. Army Corps of Engineers, USACE " **Settlement Analysis: Stress Distribution in Soil"** EM 1110-1-1904, 1990.

- Wong L.S., Allouche E.N. and Moore I.D. **"Long-Term Monitoring and Analysis of Full Scale Concrete Pipe Test Beds"** ASCE, Proceedings of Pipeline Division Specialty Conference, 2002.

- WRI, Wire Reinforcement Institute **"TECH FACTS: Metric Welded Wire Reinforcement for Concrete Pipe"**, 2003.

Prof. Dr. Mosa Jawad Al-Mosawe
Ass. Prof. Dr. AbdulMuttalib Issa Said
Abbas Oda Dawood

Investigation of Backfill Compaction
Effect on Buried Concrete Pipes

Table (1): Soil Classifications

Standards	ASTM D2487	AASHTO M145	Iraqi S	ASTM C1479-07a
Soil Classification	SP (Poorly graded sand with gravel)	A-1-b	Class D	Gravelly Sand (Category I)

Table (2): Loading Platforms Types

No.	Loading Platform	Simulation of	Length, m	Width, m	Contact area m2
1	Uniform loading	Earth fill	0.8	1.05	0.840
2	Patch Platform	AASHTO HS20 wheel	0.508	.254	0.129

Table (3): Soil Densities and Compaction Degree for Tests

Test No.	Wet Density	Dry Density	Water Content	Compaction
Dense Bedding	22.15	21.18	4.60	98.51
Test_No.1	19.75	19.07	3.56	88.71
Test_No.2	20.78	19.90	4.45	92.54
Test_No.3	20.81	19.23	8.20	89.45
Test_No.4	21.07	19.92	5.75	92.65
Test_No.5	21.27	20.19	5.37	93.90
Test_No.6	19.09	18.37	3.91	85.43

Table (4): Variables of Tests

Test No.	Trench width	Cover of backfill	Backfill Compaction	Loading	Bedding compaction
1	Narrow	30 cm	Loose Compacted	Uniform loading	Compacted
2	Narrow	30 cm	Dense Compacted	Uniform loading	Compacted
3	Wide	60 cm	Loose Compacted	Patch Platform	Compacted
4	Wide	60 cm	Dense Compacted	Patch Platform	Compacted
5	Narrow	60 cm	Dense Compacted	Uniform loading	Compacted
6	Narrow	60 cm	Not Compacted (Rained Soil)	Uniform loading	Compacted
7	Three Edge Bearing Tests				

Table (5): Bedding Factors for Different Tests

Test No.	Cover above crown	Loading Type	Failure Loading kN	Failure Loading kN/m²	Vertical Stress at crown kN/m²	Vertical Load kN/m	Bedding Factor, B_d
1	30 cm	Uniform	156.4	186.2	192.29	75.76	1.70
2	30 cm	Uniform	178.7	212.8	218.89	86.24	1.93
3	60 cm	Patch	134	1039.0	155.50	61.27	1.37
4	60 cm	Patch	141.5	1096.8	163.52	64.43	1.44
5	60 cm	Uniform	208.5	248.2	260.38	102.59	2.30
6	60 cm	Uniform	110.2	131.2	143.38	56.49	1.26

Table (6): Tests Used in Backfill Compaction Analysis

Set No.	Dense Compaction Tests	Loose Compaction Tests	Loading Type
1	Test No.2	Test No.1	Uniform
2	Test No.4	Test No.3	Patch

Table (7): Effect of Backfill Compaction on Failure Load

Set No.	Dense Compaction Tests Test No.	Dense Compaction Tests Failure Load	Loose Compaction Tests Test No.	Loose Compaction Tests Failure Load	Loading Type
1	Test No.2	212.8 KN/m²	Test No.1	186.2 KN/m²	Uniform
2	Test No.4	141.5 KN	Test No.3	134 KN	Patch
3	Test No.5	248.2 KN/m²	Test No.6	131.2 KN/m²	Uniform
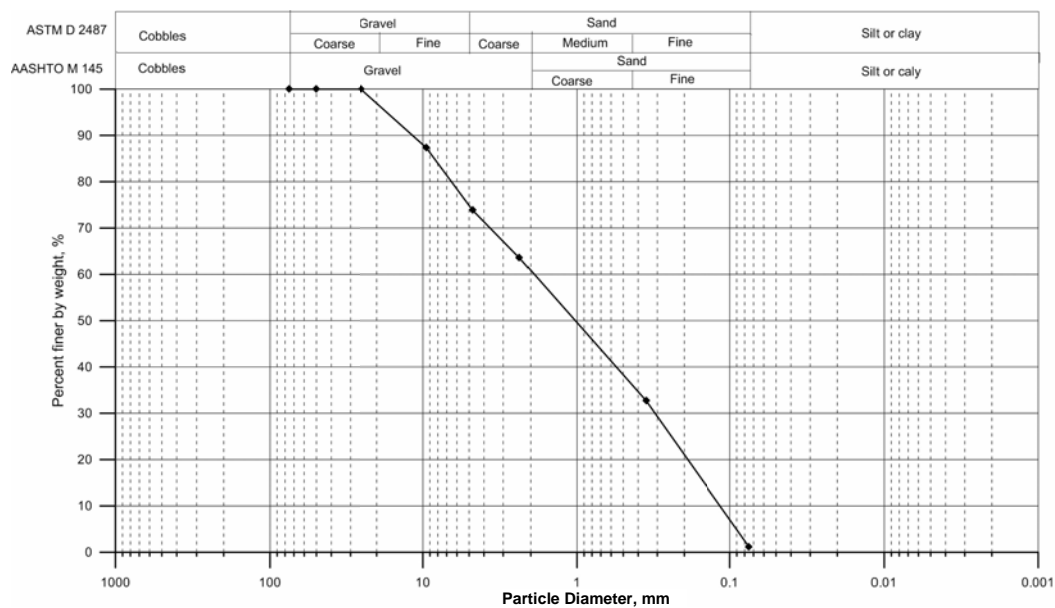
Figure (1): Grain Size Distribution For Backfill Soil

Prof. Dr. Mosa Jawad Al-Mosawe
Ass. Prof. Dr. AbdulMuttalib Issa Said
Abbas Oda Dawood

Investigation of Backfill Compaction
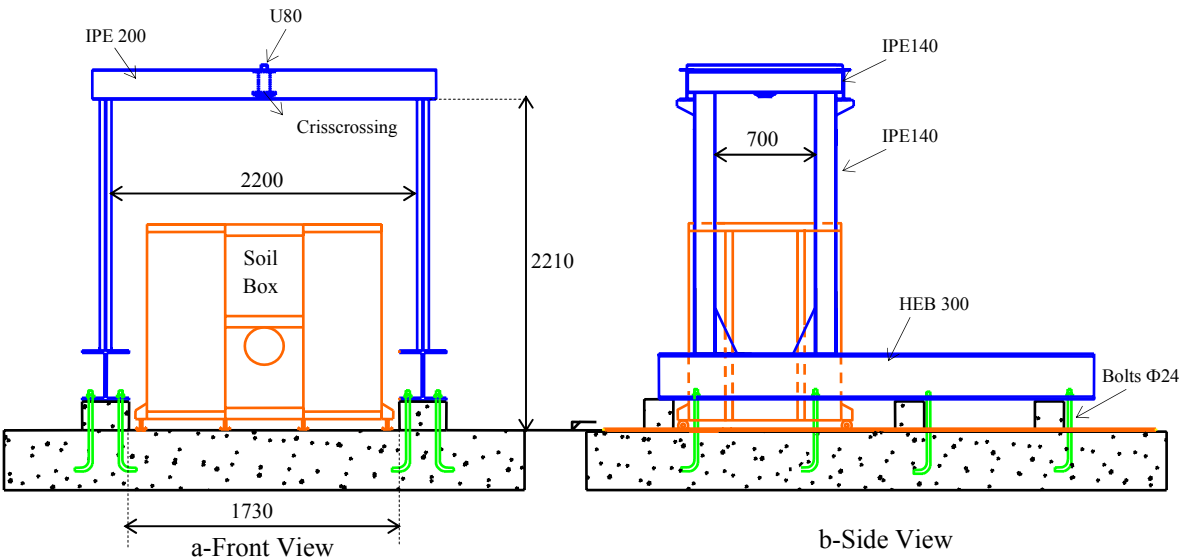**Effect on Buried Concrete Pipes**

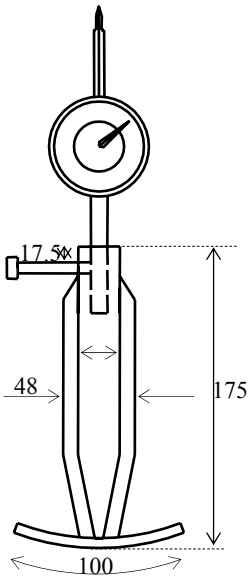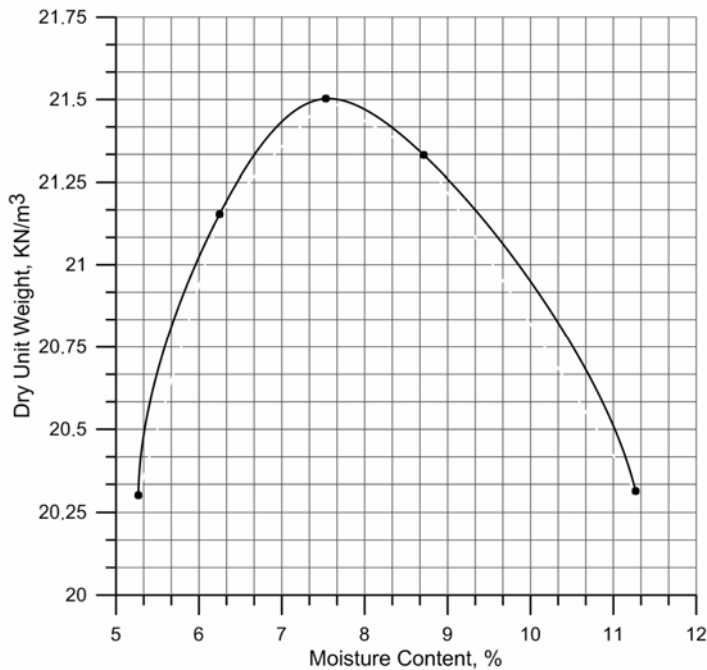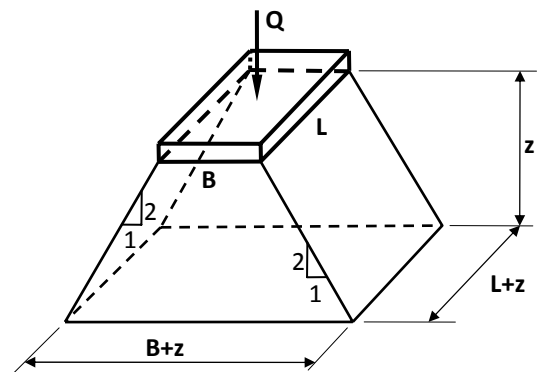**Figure (2): Reaction Frame Dimensions in Millimeters**

Figure (3): Deflection Dial Gauge and Its Adjustable Stand

Figure (4): Typical Compaction Curve (Water Content versus Dry Unit Weight)

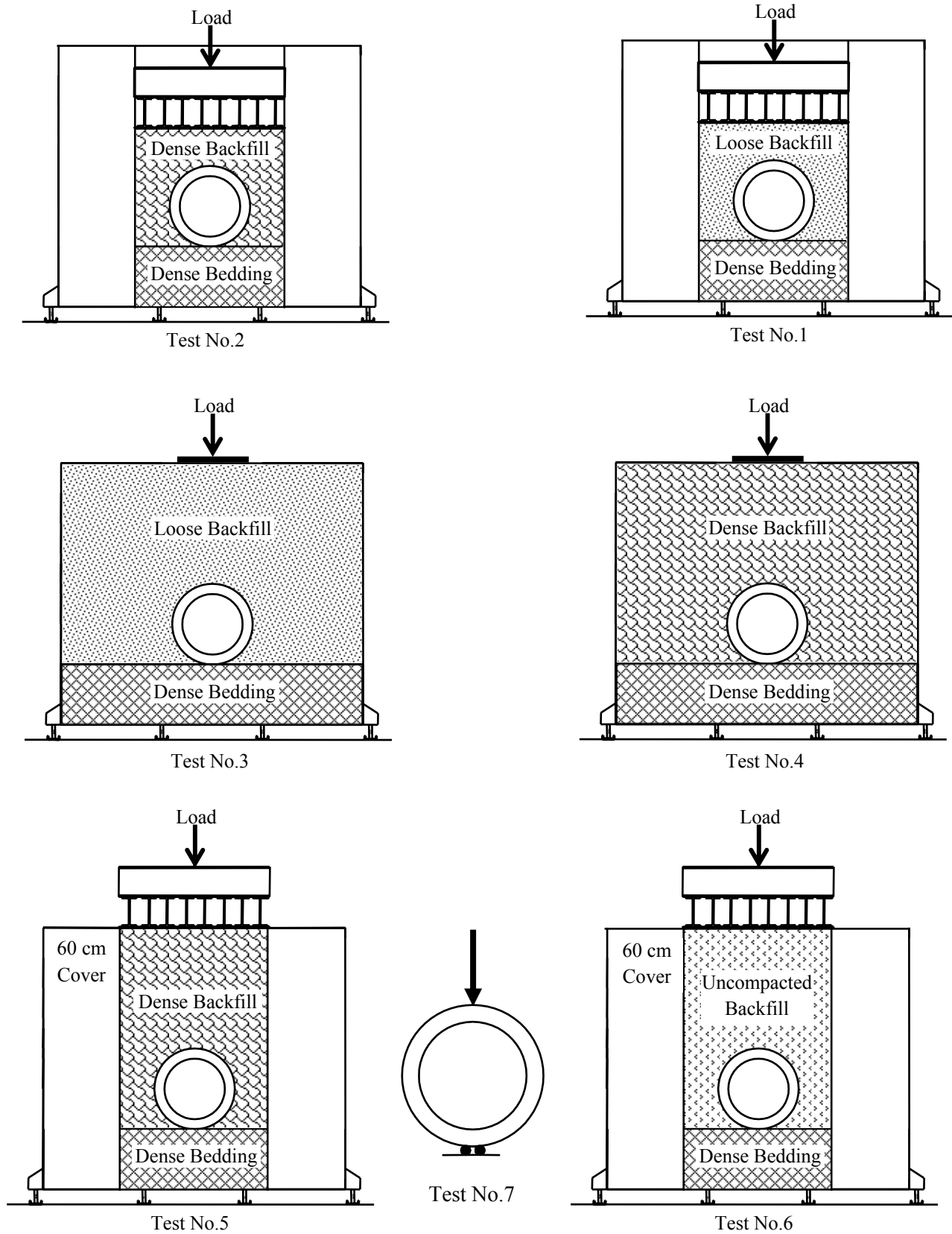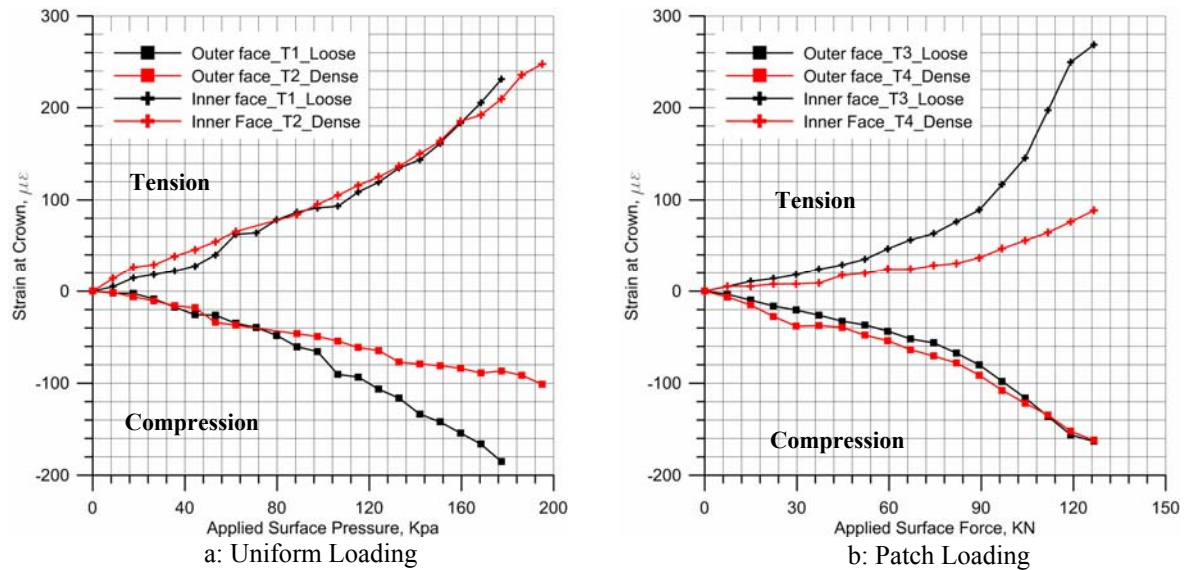**Figure (6) : Approximate Stress Distribution by the 2:1 Method**

Figure (5): Steel Hand Tampers
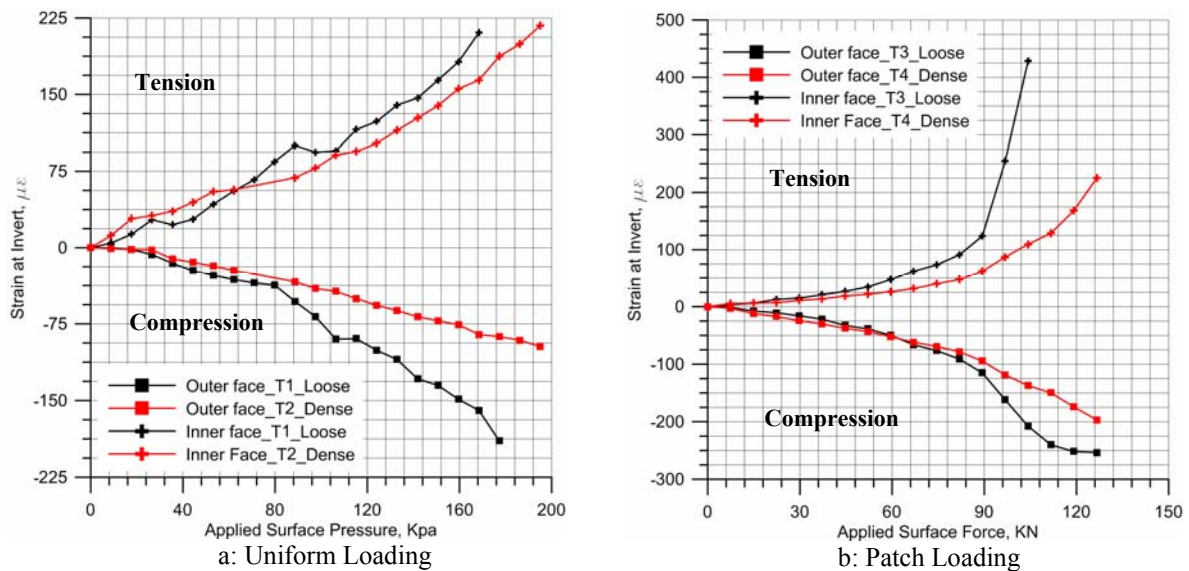
Prof. Dr. Mosa Jawad Al-Mosawe
Ass. Prof. Dr. AbdulMuttalib Issa Said
Abbas Oda Dawood

**Investigation of Backfill Compaction
Effect on Buried Concrete Pipes**

Figure (7): Description of Tests Variables

a: Uniform Loading　　　　　　　　　　b: Patch Loading

Figure (8): Compaction Effect on Pipes Strains at Crown

a: Uniform Loading　　　　　　　　　　b: Patch Loading

Figure (9): Compaction Effect on Pipes Strains at Invert

a: Uniform loading　　　　　　　　　　b: Patch loading
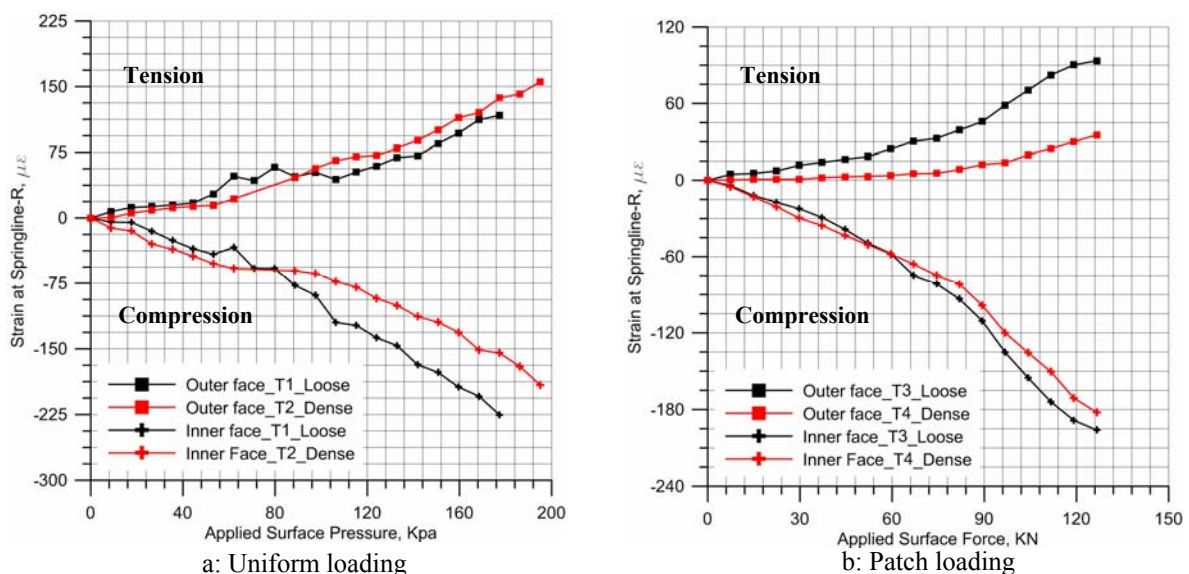
Figure (10): Compaction Effect on Pipes Strains at Right Springline

Prof. Dr. Mosa Jawad Al-Mosawe
Ass. Prof. Dr. AbdulMuttalib Issa Said
Abbas Oda Dawood

Investigation of Backfill Compaction
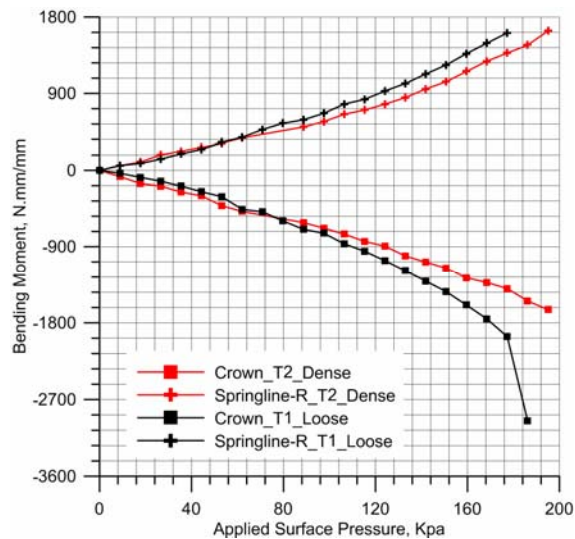**Effect on Buried Concrete Pipes**
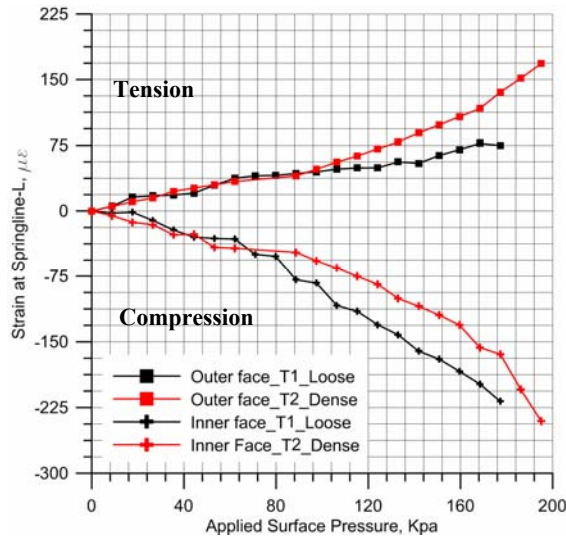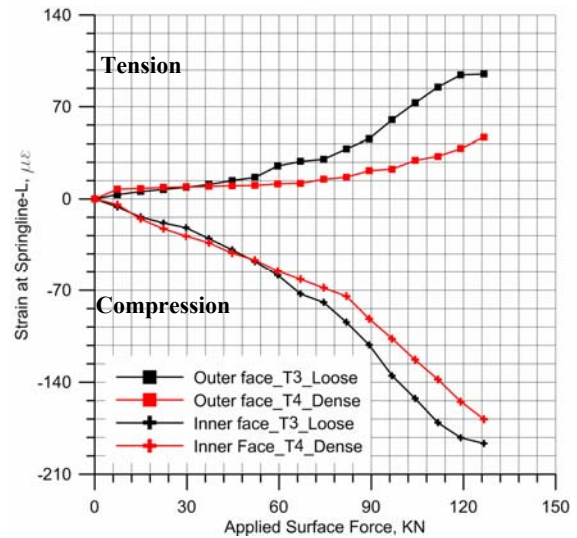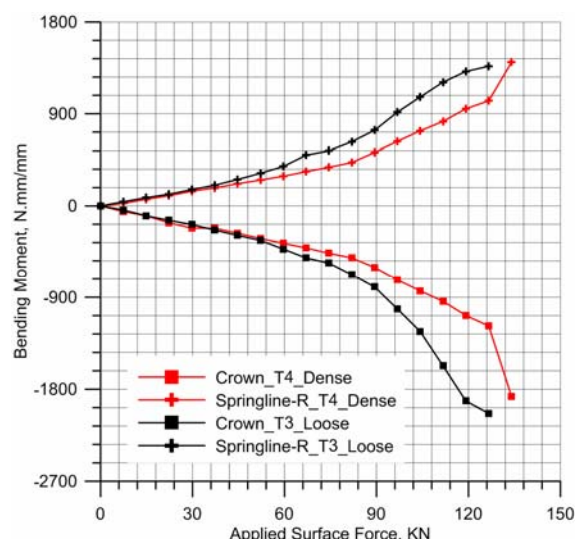
a: Uniform Loading   b: Patch Loading
Figure (11): Compaction Effect on Pipes Strains at Left Springline
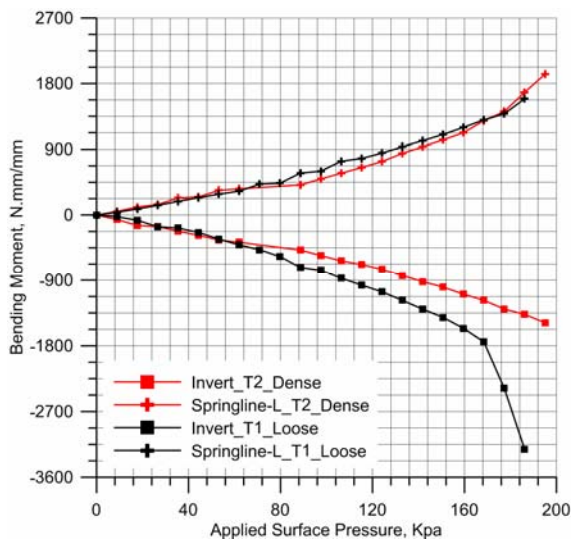
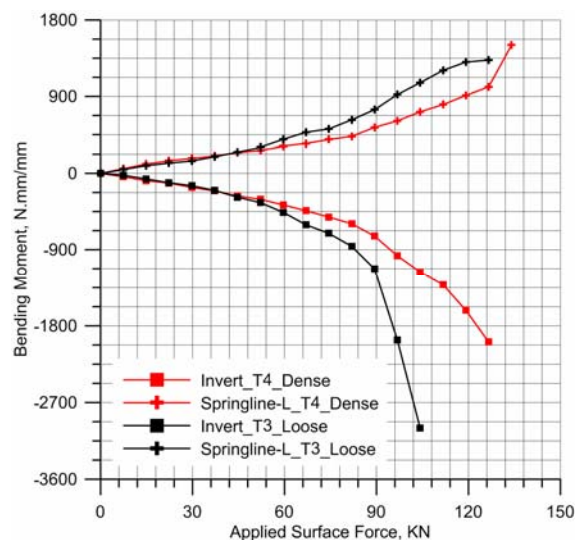

a: Uniform Loading   b: Patch Loading
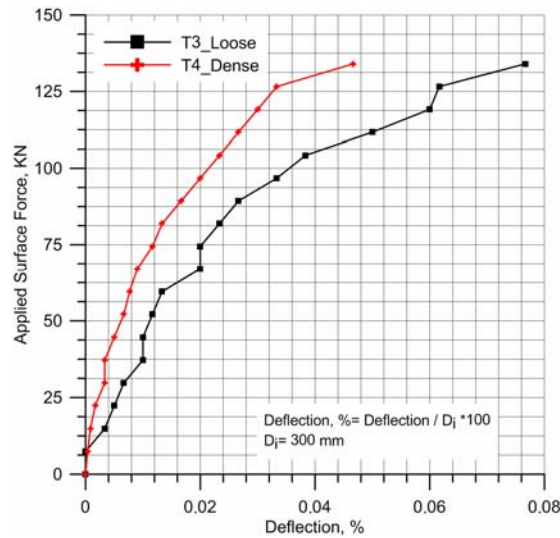**Figure (12): Compaction Effect on Pipes Bending Moments at Crown and Right Springline**
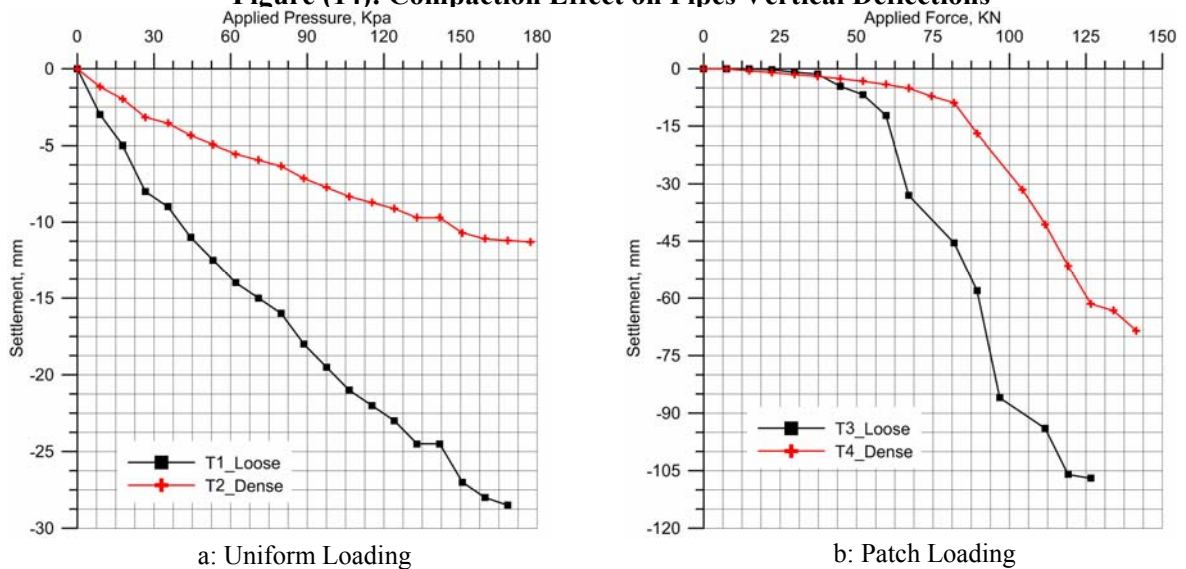

a: Uniform Loading   b: Patch Loading
Figure (13): Compaction Effect on Pipes Bending Moments at Invert and Left Springline

195

Figure (14): Compaction Effect on Pipes Vertical Deflections

a: Uniform Loading   b: Patch Loading

Figure (15): Compaction Effect on Loading Platform Settlement

Figure (16): Cracking Pattern

Estimation of Flexural Strength of Plain Concrete from Ultrasonic Pulse Velocity

Dr. Ala'a Hussein. Alwan Al-Zuhairi
Lecturer, Eng. College-Civil Dept.
Baghdad University
Email: alaalwn@yahoo.com

ABSTRACT
The aim of this study is to propose mathematical expressions for estimation of the flexural strength of plain concrete members from ultrasonic pulse velocity (UPV) measurements. More than two hundred pieces of precast concrete kerb units were subjected to a scheduled test program. The tests were divided into two categories; non-destructive ultrasonic and bending or rupture tests. For each precast unit, direct and indirect (surface) ultrasonic pulses were subjected to the concrete media to measure their travel velocities. The results of the tests were mointered in two graphs so that two mathematical relationships can be drawn. Direct pulse velocity versus the flexural strength was given in the first relationship while the second equation describes the flexural strength as a function of indirect (surface) pulse velocity. The application of these equations may be extended to cover the assessment of flexural strength of constructed concrete kerb units or in-situ concreting kerbstone and any other precast concrete units. Finally, a relation between direct and indirect pulse velocities of the a given concrete was predicted and suggested to be employed in case when one of the velocities is not available can be measured for other ultrasonic pulse test applications

KEY WORDS: Nondestructive tests, ultrasonic, pulse velocity, flexural strength, concrete kerbs.

1. INTRODUCTION

The non Destructive Testing (NDT) of concrete has a great technical and useful importance. This testing technique has been grown during the last decads especially in the case of construction quality assessement (Shariati et al.). The main advantage of (NDT) method is to avoid damaging of concrete or impairing the function of consrtucted structural components. Besides, its use is simple, quick and test results are avialble on the site (Hobbs and Tchoketch). Ultrasonic pulse velocity (UPV) and Shmidt rebound hammer (SRH) are so familiar (NDT) methods. The use of (UPV) to non-destructive assessment of concrete quality has been extensively investigated for decads (Solis-Carcano and Moreno). The test is based on measuring the velocity of an ultrasonic pulse passing through the tested solid material. According to the theory of the sound propagation, the pulse velocity depends on the density and elastic properties of that material and independent of the frequency of the pulse (C.N.S. Electronics).

It can be shown that the pulse velocity of longitudinal ultrasonic vibration travelling through an elastic solid is given by: (Krautkramer and Krautkramer)

$$UPV = \sqrt{\frac{E}{\rho}\frac{(1-\nu)}{(1+\nu)(1-2\nu)}} \qquad (1)$$

Where, E = dynamic elastic modulus

ρ = the density

ν = Poisson's ratio.

When ultrasonic testing is applied to metals to detect internal flaws, the former send the echoes back in the direction of the incident beam of pulse. The measurment of time taken for the pulse to travel from a surface to a flaw and back again enables the position of the flaw to be located. Such a technique can not be applied to hetrogeneous materials like concrete since echoes are generated at numerous boundaries of different phases within these materials resulting in a general scattering of pulse energy in all directions. Based on this fact, it is recommended that the pulse frequency used for testing concrete is much lower than that used in metal testing. The higher the frequency, the narrower the incident beam of pulse propagation but the greater the attenuation (or damping out) of the pulse vibration. The frequencies suitable for these materials (metal and concrete) range from about 20kHz to 250kHz with 50kHz being appropriate for the field testing of concrete (C.N.S. Electronics).

1.1 Historical Backgroud

The historical review of development of ultrasonic pulse test shows that the technique is used first in 1946 and 1947 in Canada by engineers at the Hydro-Electric Power Commission of Ontario to investigate the extent of cracking in dams. The developed device is called *Sonicsop*. It was capable of penetrating up to 15m of concrete and measure the travel time with an accuracy of 3%. In early uses of the soniscope on mass concrete, the emphasis was on measuring the pulse velocity rather than estimating strength of concrete.

As stated by Carino (1994), Parker (1953) reported on early attempts at Ontario Hydro to develop relationships between pulse velocity and compressive strength. At the same time when work on the soniscope was in progress in Canada, R.Jones and co-workers at the Road Research Laboratory (RRL) in England were involved to develop an ultrasonic testing apparatus (Jones (1949) stated by Carino (1994)). The apparatus that was developed and called *Ultrasonic Concrete Tester* operated at a higher frequency than the soniscope to produce pulses of shorter path lengths.

Through his wide experience in UPV test, Jones (Carino) established the inherent problems in using the pulse velocity to estimate concrete strength. Despite these early finding, numerous researchers dealed with prediction of concrete compressive strength by measuring the pulse velocity through their media. Most of these works proposed corellations or imperical equations for application to extended ranges of concrete.

1.2 Literature Review

A brief review of some selected works from the avialable literature is shown in Table1. The review was concenterated on works from which the mathematical correlations were proposed.

Through this fair review of literature it was seen that most of researchers (if not all) dealed with the estimation of concrete compressive strength from UPV test. No work was found interested in estimation of flextural strength. For this reason the present study was conducted. On the other hand, flexural strength estimation from UPV helps to control the quality of some precast units that should resist a certain value of flexural stress.

Table 1: Review of some sellected works from literature

No.	Author	Year	Proposed Correlation	Notes
1	Jones	1962	$f_{cu} = 2.8\,exp^{0.53V}$	f_{cu} = compressive strength in MPa. V = direct pulse velocity in km/sec. V_s = indirect (surface) pulse velocity in km/sec.
2	Elvery and Ibrahim	1976	$f_{cu} = 0.0012\,exp^{2.27V}$	
3	Raouf and Ali	1983	$f_{cu} = 2.016\,exp^{0.61V}$	
4	Abdul-Salam	1992	$f_{cu} = -199 + 123V$	
5	Lopes and Neponmuceno	2001	$f_{cu} = 0.00015\,exp^{2.885V}$	
6	Tumendemberel and Baigalimaa	2001	$f_{cu} = 1.356 \times 10^{-5}V^2 - 0.076V + 111.502$	
7	Malhotra and Carino	2004	$f_{cu} = -109.6 + 0.033V$	
8	Nash't et al.	2005	$f_{cu} = 1.19\,exp^{0.715V}$	
9	Ali	2008	$f_{cu} = 0.26\,exp^{V_s} - 0.83$	
10	Lawson et al.	2011	$f_{cu} = 0.053\,exp^{0.001V}$	
11	Shariati et al.	2011	$f_{cu} = 15.533V - 34.358$	
12	Jassim	2012	$f_{cu} = 0.395\,exp^{0.964V}$	

2. EXPERIMENTAL WORKS

203 precast concrete kerb units were used through out this work. The units have different dimensions. The length is ranged between 500-1000mm and width between 100-200mm while 250-300mm is the range of height. Each unit is submitted to the following testing program:

1. Measuring of dimensions and locating the points at which the ultrasonic transducers will be attached for both direct and indirect tests (Fig.1.a).
2. Grease oil is used at located points to be a suitable coplent between transducer and concrete face of the precast units (Fig.1.b).
3. Five direct UPV tests were taken for each unit using 55kHz transducers. The tests were conducted in a mannar so that the travel path of the ultrasonic pulse is across the width of the unit (Fig.1.c). This is done to simulate the future field UPV test on constructed concrete kerb units in the road.
4. Indirect (surface) UPV tests were performed at a constant pulse travel distance of 200mm (Fig.1.d) using the same transducers that used in direct test.
5. Finally, each precast unit was subjected to flextural stress to the failure via utilizing the

bending machine shown in Fig.2. The flextural strength is computed from eq.1:

$$f_r = \frac{PLy}{4I} \tag{1}$$

Where,
f_r = flexural strength in MPa
P = applied force in Newtons
L = span length in mm
y = distance from the neuteral axis of precast unit section to the extreme fiber in mm
I = moment of inertia of precast unit section in mm⁴.

3. RESULTS AND DISCUSSION

The results of the direct and indirect tests that were conducted on the precast concrete kerb units were tabulated in Table2. Direct and indirect (or surface) velocities were calculated at five different locations for each precast kerb unit. Then the average velocity of these five readings in both direct and surface tests was determined. To investigate the scattering of the velocities in both direct and indirect tests, the standard deviation was calculated.

In all tests, as it was expected, the average direct velocity was greater than the indirect one.

The increase in the length of pulse insident beam from the measured distance between transducers in the indirect test stand behind this fact.

It was noted that the maximum value of standard deviation was 0.055 km/sec for direct tests and 0.057 km/sec for surface tests. The corresponding coefficients of variation were 1.37% and 1.24% respectively.

Table 2: Ultrasonic pulse velocity test results

No.	Av. V km/sec	SDD km/sec	Av. V_s km/sec	SDS km/sec	f_r MPa	No.	Av. V km/sec	SDD km/sec	Av. V_s km/sec	SDS km/sec	f_r MPa
1	4.70	0.021	4.26	0.042	3.11	53	4.65	0.023	3.75	0.035	3.44
2	4.79	0.024	4.28	0.024	3.15	54	4.59	0.022	3.76	0.049	3.56
3	4.83	0.046	4.29	0.027	3.18	55	4.61	0.022	3.78	0.032	3.36
4	3.48	0.019	3.38	0.013	2.09	56	4.25	0.050	4.13	0.028	3.50
5	3.50	0.041	3.44	0.039	2.13	57	4.32	0.030	4.06	0.017	3.73
6	3.50	0.037	3.48	0.034	2.21	58	4.66	0.043	4.40	0.034	3.45
7	4.13	0.044	3.92	0.022	2.22	59	3.76	0.029	3.15	0.021	2.02
8	4.12	0.045	3.95	0.038	2.29	60	4.32	0.031	3.71	0.014	3.06
9	4.08	0.026	3.97	0.038	2.30	61	4.34	0.044	3.98	0.046	2.96
10	4.33	0.031	3.92	0.055	3.33	62	4.45	0.027	4.38	0.038	3.60
11	4.40	0.053	3.94	0.037	3.77	63	4.46	0.044	4.43	0.024	3.76
12	2.89	0.015	2.56	0.007	1.39	64	4.46	0.030	4.41	0.043	3.98
13	2.89	0.017	2.55	0.012	1.40	65	4.43	0.030	4.38	0.053	3.82
14	2.91	0.018	2.55	0.005	1.42	66	4.42	0.053	4.37	0.051	3.92
15	3.33	0.027	3.10	0.017	2.40	67	4.50	0.035	4.48	0.050	3.71
16	3.33	0.014	3.08	0.016	2.33	68	4.80	0.028	3.86	0.018	3.37
17	3.37	0.036	3.06	0.024	2.33	69	4.39	0.040	3.98	0.024	2.73
18	4.78	0.026	4.46	0.040	3.83	70	4.31	0.051	3.94	0.037	2.73
19	4.89	0.021	4.52	0.026	4.11	71	4.26	0.013	3.95	0.029	2.67
20	4.81	0.033	4.49	0.050	3.99	72	4.18	0.054	3.94	0.047	2.72
21	4.91	0.047	4.51	0.048	3.94	73	4.13	0.032	3.92	0.052	2.81
22	4.79	0.021	4.48	0.040	4.16	74	4.16	0.037	3.90	0.028	2.72
23	4.89	0.026	4.46	0.047	3.83	75	4.91	0.029	4.56	0.023	3.75
24	4.59	0.043	4.37	0.031	3.90	76	3.56	0.035	2.30	0.018	1.77
25	4.74	0.048	4.21	0.029	3.59	77	3.55	0.034	2.29	0.016	1.82
26	4.83	0.016	4.33	0.017	3.82	78	3.60	0.020	2.30	0.035	1.77
27	4.72	0.036	4.28	0.054	3.70	79	5.07	0.041	4.90	0.033	4.61
28	4.79	0.026	4.19	0.033	2.87	80	5.17	0.050	4.89	0.040	4.73
29	4.87	0.017	4.24	0.039	2.93	81	5.15	0.031	4.88	0.045	4.67
30	4.16	0.023	3.85	0.049	2.38	82	4.65	0.052	3.92	0.040	3.25
31	4.28	0.036	3.81	0.045	2.42	83	4.74	0.027	4.16	0.054	3.34
32	4.25	0.046	3.86	0.039	2.44	84	4.79	0.013	4.28	0.031	3.44
33	4.20	0.039	3.64	0.038	2.96	85	4.82	0.033	4.36	0.055	3.34
34	4.29	0.036	3.82	0.031	3.18	86	4.88	0.049	4.34	0.012	3.34
35	4.45	0.032	3.79	0.042	3.35	87	4.82	0.039	4.39	0.046	3.44
36	4.42	0.046	3.76	0.036	3.29	88	4.95	0.029	4.46	0.018	3.54
37	4.59	0.049	4.13	0.028	3.80	89	4.79	0.039	4.32	0.046	3.44
38	4.64	0.050	3.93	0.039	3.59	90	4.86	0.045	4.46	0.048	3.54
39	4.70	0.016	4.03	0.044	3.77	91	4.89	0.053	4.50	0.046	3.58
40	4.79	0.046	4.05	0.024	3.77	92	4.84	0.047	4.51	0.047	3.54
41	4.73	0.040	4.43	0.046	4.10	93	4.82	0.034	4.63	0.037	3.62
42	4.74	0.019	4.59	0.057	4.23	94	5.05	0.046	4.80	0.039	4.30
43	4.81	0.033	4.56	0.054	4.21	95	4.57	0.022	4.23	0.015	3.69
44	4.91	0.013	4.60	0.046	4.29	96	4.52	0.031	4.22	0.025	3.85
45	4.87	0.034	4.61	0.048	4.18	97	4.50	0.029	4.24	0.020	3.79

46	4.87	0.034	4.59	0.052	4.07	98	5.06	0.041	4.88	0.048	4.41
47	4.34	0.033	4.06	0.034	3.81	99	5.06	0.041	4.94	0.049	4.26
48	4.38	0.053	4.17	0.042	3.85	100	5.07	0.021	4.92	0.039	4.62
49	4.35	0.054	4.12	0.031	3.84	101	4.85	0.030	4.46	0.027	3.19
50	4.60	0.024	3.88	0.042	3.33	102	4.75	0.035	4.34	0.018	3.12
51	4.55	0.031	3.80	0.048	3.31	103	3.76	0.025	3.63	0.053	2.43
52	4.58	0.035	3.76	0.037	3.47	104	5.15	0.047	5.02	0.034	4.97

To be continued

Table 2: Ultrasonic pulse velocity test results (continued)

No.	Av. V km/sec	SDD km/sec	Av. V_s km/sec	SDS km/sec	f_r MPa	No.	Av. V km/sec	SDD km/sec	Av. V_s km/sec	SDS km/sec	f_r MPa
105	5.51	0.029	5.13	0.031	5.06	155	3.57	0.019	3.52	0.012	2.51
106	5.66	0.050	5.18	0.038	5.09	156	3.55	0.030	3.52	0.023	2.48
107	5.45	0.036	5.30	0.045	5.06	157	3.61	0.023	3.34	0.024	2.20
108	4.76	0.036	4.20	0.038	3.17	158	3.63	0.034	3.38	0.021	2.06
109	4.90	0.043	4.05	0.031	3.39	159	3.61	0.020	3.36	0.015	2.01
110	4.85	0.051	4.06	0.054	3.22	160	4.86	0.027	4.45	0.045	3.88
111	4.85	0.038	4.05	0.042	3.61	161	4.79	0.045	4.44	0.035	3.61
112	4.84	0.034	3.97	0.040	3.30	162	4.85	0.042	4.38	0.035	3.87
113	4.91	0.042	4.00	0.041	3.69	163	4.64	0.025	3.60	0.032	3.12
114	4.37	0.041	3.94	0.027	3.13	164	4.73	0.040	3.60	0.015	3.17
115	4.36	0.025	3.94	0.043	3.07	165	4.91	0.044	3.94	0.044	3.54
116	4.46	0.030	3.95	0.045	3.07	166	4.38	0.037	3.71	0.013	3.29
117	4.45	0.025	3.96	0.021	3.09	167	4.36	0.032	4.10	0.028	3.37
118	4.36	0.016	3.94	0.041	2.93	168	4.36	0.020	4.09	0.024	3.57
119	4.44	0.041	3.92	0.027	2.98	169	4.33	0.029	4.11	0.029	3.53
120	4.46	0.012	4.02	0.048	3.07	170	3.94	0.037	3.56	0.034	2.86
121	4.35	0.050	3.95	0.050	2.96	171	3.95	0.020	3.56	0.030	2.96
122	4.38	0.035	3.88	0.046	3.02	172	4.04	0.037	3.54	0.027	2.97
123	5.44	0.019	4.85	0.037	4.81	173	4.85	0.054	4.38	0.052	4.07
124	4.41	0.030	3.91	0.035	3.17	174	4.89	0.041	4.28	0.044	3.90
125	4.39	0.023	3.94	0.037	3.39	175	4.90	0.039	4.28	0.047	3.98
126	4.35	0.025	3.99	0.052	3.23	176	4.75	0.039	4.30	0.056	3.82
127	5.20	0.018	5.03	0.025	4.88	177	4.80	0.023	4.34	0.016	3.97
128	5.21	0.031	5.03	0.050	4.98	178	4.95	0.041	4.34	0.013	4.02
129	5.21	0.027	4.95	0.017	4.91	179	4.22	0.040	4.01	0.021	3.03
130	4.90	0.040	4.10	0.040	4.07	180	4.19	0.025	4.01	0.041	3.06
131	4.61	0.035	4.13	0.047	4.18	181	4.19	0.029	4.02	0.018	3.04
132	4.46	0.017	4.10	0.017	4.18	182	3.97	0.017	3.47	0.041	2.35
133	4.93	0.043	4.85	0.044	4.24	183	3.96	0.038	3.54	0.033	2.51
134	4.81	0.042	4.81	0.049	4.30	184	3.96	0.032	3.51	0.038	2.37
135	4.87	0.043	4.95	0.039	4.36	185	4.94	0.050	4.53	0.051	3.53
136	4.66	0.026	4.27	0.042	3.78	186	5.32	0.027	4.73	0.047	4.27
137	4.75	0.049	4.29	0.046	3.62	187	5.49	0.051	4.78	0.041	4.39
138	4.66	0.020	4.30	0.040	3.66	188	4.91	0.026	4.53	0.024	4.29
139	3.09	0.040	2.66	0.057	1.66	189	4.98	0.027	4.52	0.042	4.30
140	2.92	0.023	2.63	0.042	1.61	190	4.99	0.040	4.53	0.027	4.36
141	3.00	0.025	2.63	0.055	1.64	191	4.64	0.014	3.60	0.032	3.23
142	3.65	0.035	2.92	0.026	2.12	192	4.75	0.047	3.60	0.015	3.28
143	3.68	0.027	2.83	0.047	2.17	193	4.91	0.035	3.94	0.044	3.58

144	3.65	0.012	2.70	0.035	2.04	194	4.78	0.031	4.46	0.028	3.77
145	5.05	0.051	4.44	0.032	4.37	195	4.89	0.040	4.52	0.013	4.05
146	5.07	0.036	4.51	0.034	4.46	196	4.81	0.031	4.49	0.032	3.94
147	5.15	0.045	4.48	0.052	4.37	197	4.91	0.033	4.51	0.029	3.88
148	3.93	0.035	3.28	0.021	2.34	198	4.79	0.006	4.48	0.030	4.11
149	4.02	0.055	3.34	0.030	2.46	199	4.89	0.022	4.46	0.038	4.05
150	3.95	0.030	3.54	0.054	2.44	200	5.49	0.044	4.78	0.026	4.43
151	4.99	0.016	4.53	0.024	4.16	201	4.41	0.041	4.09	0.046	3.20
152	5.05	0.038	4.52	0.042	4.18	202	4.41	0.030	4.11	0.037	3.22
153	5.06	0.046	4.53	0.027	4.24	203	4.45	0.023	4.21	0.033	3.29
154	3.47	0.025	3.48	0.030	2.47						

Av. V: average direct ultrasonic pulse velocity in km/sec, Av. V_s: average indirect (surface) ultrasonic pulse velocity in km/sec, SDD: standard deviation for direct velocity in km/sec, SDS: standard deviation for indirect (surface) velocity in km/sec and f_r = concrete flexural strength in MPa.

These acceptable ranges of standard deviation and coefficient of varaition indicate that good control on the use of testing machine was achieved during the testing program.

The results of direct and surface velocities shown in Table2 were plotted againest the flexural strength in two seperated diagrams. One diagram is for direct test method (Fig. 3) and the other for indirect test method (Fig. 4). For each diagram, the data were submitted to a regression process to produce two mathematical correlations for direct and surface ultrasonic pulse test methods. The feature of curve fitting equations was carefully sellected to gain a maximum coefficient of determinaton (R^2). Eq.2 and eq.3 are the correlation results of the above regression process:

1. Direct pulse test method:

$$f_r = 0.439\, exp^{0.447V} \quad (R^2 = 0.881) \qquad (2)$$

2. Indirect (surface) pulse test method:

$$f_r = 0.596\, exp^{0.420V_s} \quad (R^2 = 0.879) \qquad (3)$$

Where,
V: average direct ultrasonic pulse velocity in km/sec,
V_s: average indirect (surface) ultrasonic pulse velocity in km/sec and
f_r = concrete flexural strength in MPa.

It is clear that both equations eq.2 and eq.3 have simillar feature. The differece is in multiplier and the power of expoenential function. Dividing eq.2 by eq.3 produces eq.4 which is a relationship between direct and indirect pulse velocities of the same concrete. This relation was plotted in Fig.(5).

$$\frac{0.439}{0.596}\left(\frac{exp^{0.447V}}{exp^{0.420V_s}}\right) = 1 \qquad (4)$$

$$V = 0.94V_s + 0.685$$

The regression equation of direct UPV (eq.2) was compared with that proposed by Raouf and Ali (1983), the well known correlation used in Iraq although it concerned with prediction of cube compressive strength. This was done by estimating the flexural strength from the vaules computed from Raouf and Ali's equation and converted to cylinder compressive strength using eq.5 that proposed by ACI 209-Committee.

$$f_r = 0.0135[wf_c']^{0.5} \qquad (5)$$

Where,
w = unit weight of concrete in kg/m^3 which was assumed 2400 kg/m^3.
f_c' = cylinder compressive strength (MPa) = $0.8\,f_{cu}$.
f_{cu} = cube compressive strength (MPa).
The comparison was plotted in (Fig. 6) from which a good agrement between the two proposed equations can be indicated.

4. CONCLUSIONS

The following conclusions can be drawn:
1. The proposed two equations (eq.2 and eq.3) can be used in estimating the flexural strength of plain concrete members such as precast kerb units. The method of test may be applied in situ where the units are errected.
2. The application of the proposed method can be extended to cover the other concrete units that should satisfy a specified flexural strength like

concrete roof tiles and terrazo tiles. This extension should be conditioned by using appropriate types of transducers to create suitable ultrasonic pulses for these thin members.

3. The concluded relationship between direct and indirect (surface) pulse velocities (eq.4) may be used in other ultrasonic applications e.g. compressive strength estimation.

4. The two equations (eq.2 and eq.3) cannot be used in estimating the flexural strength of reinforced concrete members because the existance of reinforcement steel has an important role in UPV measurments.

REFERENCES:

ACI Committee 209, "Prediction of creep, shrinkage and temperature effects in concrete structures". (ACI 209R-92). American Concrete Institute, Detroit, 1999.

ASTM C597 (2002). "Standard test method for pulse velocity through concrete". Annual Book of ASTM Standards, vol.04.02. New York, USA.

British Standards Institution (2004). EN12504-4 "Testing concrete determination of ultrasonic pulse velocity".

Abdul-Salam, M.A. (1992). "Ultrasonic pulse velocity versus strength for concrete in Qatar". Engineering Journal of Qatar University, vol.5, pp.87-93.

Ali, B.A. (2008). "Assessment of concrete compressive strength by ultrasonic non-distructive test". MSc. Thesis, Baghdad University.

Carino, N.J. (1994). "Nondestructive testing of concrete: history and challenges". ACI SP-144, Concrete Technology: past, present and future, P.K. Mehta, Ed., American Concrete Institute, Detroit, MI, pp. 623-678.

C.N.S. Electronics ltd. (1979). "PUNDIT manual for use with the portable ultrasonic non-destructive degital indicating tester". London.

Elevery, R.H. and Ibrahim, L.A(1976). "Ultrasonic assessment of concrete strength at early ages". Magazine of Concrete Research, vol. 28 no. 97 pp.181-190.

Hobbs, B.M. and Tchoketch, K. (2007). "Non-destructive testing techniques for the forensic engineering ivestigation of reinforced concrete buildings". Forensic Sci. Int. 167(2-3), pp.167-172.

Jassim, A.K. (2012). " Prediction of Compressive Strength of Reinforced Concrete Structural Members by Using Combined Non-Destructive Tests". MSc. Thesis, Baghdad University.

Jones, R. (1962). " Non-destructive testing of concrete". MSc. Thesis, Cambridge University, London.

Krautkramer, J. and Krautkramer, H. (1969). "Ultrasonic testing of materials". Journal of Sound

Vibration, 11(1), pp.157-158.

Lawson, I., Denso, K.A., Odoi, H.C., Adjei C.A., Quashie, F.K., Mumuni, I.I. and Ibrahim, I.S. (2011). "Non-destructive evaluation of concrete using ultrasonic pulse velocity". Research Journal of Applied Sciences, Engineering and Technology 3(6) pp.499-504. Maxwell scientific organization.

Malhorta, S. and Carino, N. (2004). "Handbook on non-destructive testing", ASTM International, 2nd edition, pp.181-197.

Nash't, I.H., A'bour, S.H. and Sadoon, A.A. (2005). "Finding an unified relationship between crushing strength of concrete and non-destructive tests". www.ndt.ne, 3rd MENDT, Midle East Non-destuctive testing Conference & Exhibition, 27-30Nov., Bahrain, Manama.

Raouf, Z. and Ali, Z.M. (1983). "Assessment of concrete characteristics at an early age by ultrasonic pulse velocity". Journal of Building Reasearch, vol.2 no.1, pp.31-44.

Shariati, M., Sulong, N.H., Arbnejad, M.M., Shafigh, P. and Sinaei, H. (2011). "Assessing the strength of reinforced concrete structures through ultrasonic pulse velocity and Schmidit rebound hammer tests". Scientific Research and Essays vol.6(1), pp.213-220, Kuala Lumpur, Malaysia.

Solis-Carcano, R. and Moreno, E. (2008). "Evaluation of concrete made with crushed limestone aggrgate based on ultrasonic pulse velocity". Construction Building Materials, 22(6), pp.1225-1231.
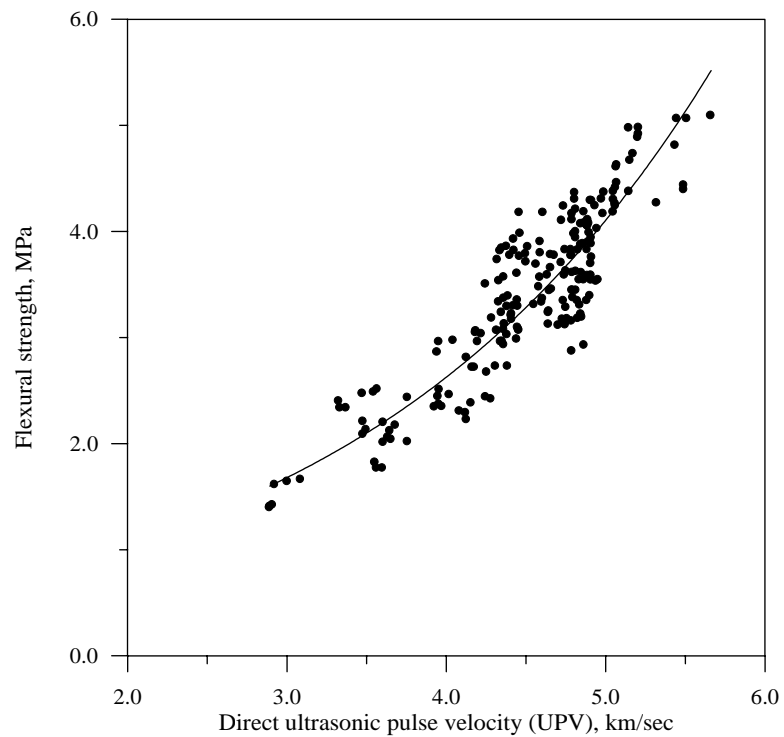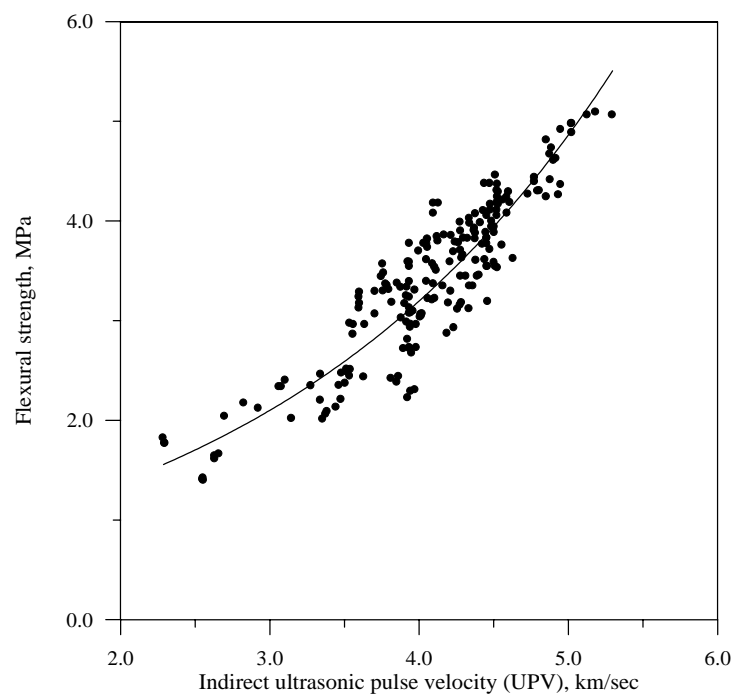
(a)

(b)

(c)

(d)

Fig. 1: Ultrasonic pulse velocity test method

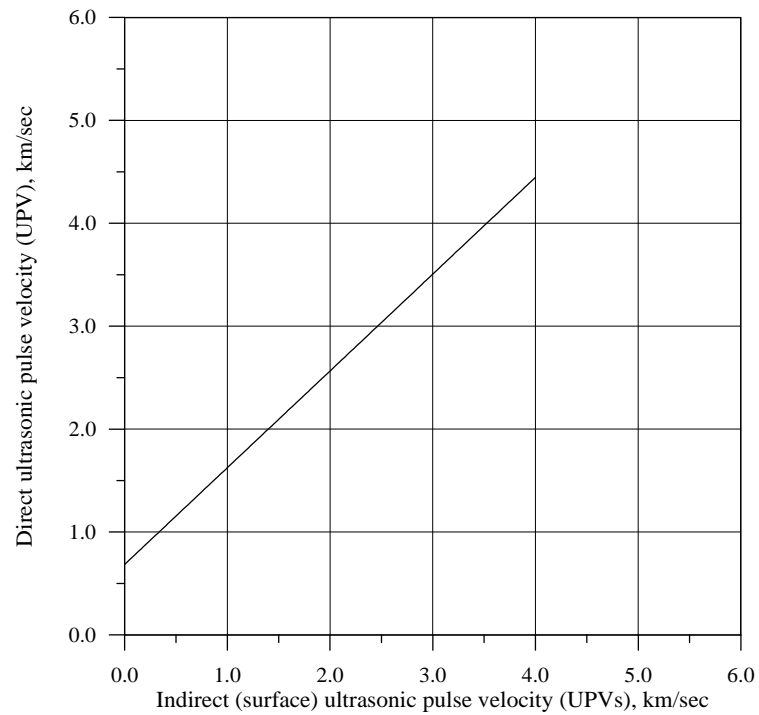**Fig. 2: Flextural strength test**

204

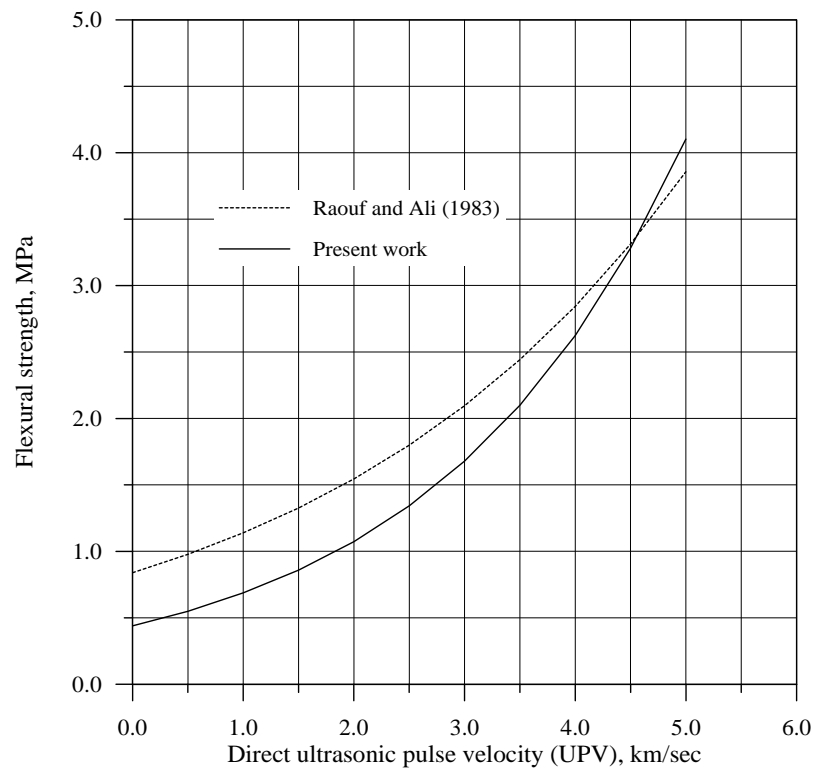**Fig. 3: Direct pulse velocity-flexural strength relationship**

Fig. 4: Indirect (surface) pulse velocity-flexural strength relationship

Fig. 5: Direct –indirect ultrasonic pulse velocity relationship

Fig. 6: Comparison between Raouf and Ali (1983) and present work

Traveling Wave Cylindrical Induction Heating System

Prof. Dr. Jafar Hamid Alwash	**M.Sc. Riyadh Kamil Chillab**
Electrical Engineering Department	**Electrical Engineering Department**
College of Engineering, University of Baghdad	**College of Engineering, University of Baghdad**
jalwash@yahoo.com	inductionm@yahoo.com

ABSTRACT

The paper deals with the traveling wave cylindrical heating systems. The analysis presented is analytical and a multi-layer model using cylindrical geometry is used to obtain the theoretical results.

To validate the theoretical results, a practical model is constructed, tested and the results are compared with the theoretical ones. Comparison showed that the adopted analytical method is efficient in describing the performance of such induction heating systems.

KEY WORDS: induction heating, cylindrical heating systems.

نظام التسخين الحثي الاسطواني ذو الموجة المنتقلة

م.م. رياض كامل جلاب　　　　**أ.د. جعفر حميد علوش**

الخلاصة

يوضح هذا البحث الدراسة النظرية و العملية لتحليل أنظمة التسخين الحثي ذات الموجة المنتقلة لقطع معدنية إسطوانية الشكل. تم بناء و تشغيل نموذج عملي لأتمام الفحوصات المختبرية لهذا النوع من المسخنات.

إن الطريقة التي تم إستخدامها نظريا لتحليل هذا المسخن هي طريقة تحليلية صرفة تعرف بنظرية الطبقات المتعددة بإستخدام المحاور الإسطوانية.

تمت المقارنة بين النتائج النظرية و المختبرية، و أظهرت هذه المقارنة كفاءة الطريقة المستخدمة نظريا لإستقراء إداء هذا النوع من المسخنات الحثية.

الكلمات الرئيسية : التسخين الحثي، أنظمة التسخين الاسطواني.

LIST OF PRINCIPAL SYMBOLS

B	magnetic flux density, T
E	electric field strength, V/m
H	magnetic field strength, A/m
k	wave length factor $= 2\pi/\lambda$
P_w	power induced in the charge, W
P	number of poles
I_{max}	peak of phase current, A
J'	amplitude of line current density, A
l	axial coil length, m
m	number of phases
N_{eff}	effective number of series turns per phase
Z_t	terminal impedance, Ω
F	supply frequency, Hz
r,θ,z	subscripts for cylindrical coordinates
s	Slip
λ	wavelength of exciting wave, m
μ	permeability, H/m
σ	conductivity, s/m
ω	equal to $2\pi f$

1. INTRODUCTION

The primary object of this work is to propose a general mathematical model for the system Fig.(1) using the actual topology for three-phase excitation with any number of poles in the axial direction. As a second object, the paper employs the multi-layer approach with an appropriate current sheet representation to calculate the flux density

Prof. Dr. Jafar Hamid Alwash
M.Sc. Riyadh Kamil Chillab

Traveling Wave Cylindrical Induction Heating System

components, induced power in the charge, terminal impedance and electromagnetic force in the direction of the traveling field.

The primary coil construction may be explained in a similar manner with the aid of Fig.(2) which shows the cylindrical windings in its tubular form with multi-polar system distributed axially. The model shown in Fig.(2-a) has two axial poles, and Fig.(2-b) has six axial poles.

2. MATEHMATICAL MODEL

A general multi-region problem is analyzed. The model is taken to be a set of infinitely long concentric cylinders, with a radialy infinitesimally thin and axially infinite current sheet excitation of radius r_g. It is further assumed that magnetic saturation is neglected.

Maxwell's equations for any region in the model are

$$\text{curl } H = J \qquad (1)$$

$$\text{curl } E = -\frac{\partial B}{\partial t} \qquad (2)$$

$$\text{div } E = 0 \qquad (3)$$
$$\text{div } B = 0 \qquad (4)$$
$$\text{div } J = 0 \qquad (5)$$
$$J = \sigma E \qquad (6)$$
$$B = \mu H \qquad (7)$$

Assumptions

Maxwell's equations are solved using cylindrical coordinates system subject to the following assumptions and boundary conditions.
 1. The induction heating system is infinitely long in the axial z- direction.
 2. Displacement currents are considered negligible at the frequencies used.
 3. All field quantities decay to zero at sufficiently large radial distances from the induction heating system axis of symmetry.
 4. The radial component of flux density (B_r) is continuous across a boundary.
 5. The radial component of line current density (J_r) is assumed to be zero.
 6. The axial component of magnetic field strength (H_z) is continuous across a boundary, but allowance for the current sheet should be taken into account.
 7. Longitudinal end effects are neglected.

3. THEORETICAL ANALYSIS

3.1 The primary current density

The primary winding considered is of cylindrical geometry and the excitation wave produced is assumed to be a perfect sinusoidal traveling wave. The line current density may be represented as

$$J_\theta = Re\left[J' e^{j(\omega t - kz)}\right] \qquad (8)$$

Where

$$J' = \frac{4mN_{eff}I_{max}}{\lambda \cdot P}$$

The field produced will link all regions (1) to (N).

3.2 The field equations of a general region

As a first step in the analysis, the field components of a general region are derived. Assuming that all fields vary as $e^{j(\omega t) - kz}$ [2], and omitting this factor for shortness from all the field expressions that follow.

Taking only the radial component form both sides of equation (2) gives

$$\frac{\partial E_\theta}{\partial z} = j\omega\mu H_r$$

or

$$H_r = -\frac{kE_\theta}{\omega\mu} \qquad (9)$$

Taking only the z-component form both sides of equation (2), one can get

$$\frac{1}{r}\frac{\partial rE_\theta}{\partial r} = -j\omega\mu H_z \qquad (10)$$

Using equation (1) and (6) and taking only the θ-component from both sides, gives,

$$\frac{\partial H_r}{\partial z} - \frac{\partial H_Z}{\partial r} = \sigma E_\theta \qquad (11)$$

After rearranging, equation (11) may be written in the form

$$r^2\frac{\partial^2 E_\theta}{\partial r^2} + r\frac{\partial E_\theta}{\partial r} - \left(\alpha^2 r^2 + 1\right)E_\theta = 0 \qquad (12)$$

The solution is given by

$$E_\theta = AI_1(\alpha r) + DK_1(\alpha r) \qquad (13)$$

Where

$$\alpha^2 = k^2 + j\omega\mu\sigma$$

and ω is replaced by (sω) for any region with slip s. I_1 and K_1 are the modified Bessel functions of the first order and of general complex argument. A and D are arbitrary constants to be determined from boundary conditions.

Using equations (2), (7) and (13), it can be shown that

$$H_z = j\frac{\alpha}{\omega\mu}\left[AI_0(\alpha r) + DK_0(\alpha r)\right] \qquad (14)$$

3.3 Field calculation at the region boundaries

Fig.(3-a) shows a general region n, where $E_{\theta,n}$ and $H_{z,n}$ are the field components at the upper boundary of the region, and $E_{\theta,n-1}$ and $H_{z,n-1}$ are the equivalent values at the lower boundary.

From equation (13) and (14), it can be shown that

$$E_{\theta,n} = AI_1(\alpha_n r_n) + DK_1(\alpha_n r_n) \qquad (15)$$

and

$$H_{z,n} = j\frac{\alpha_n}{\omega\mu_n}\left[AI_0(\alpha_n r_n) - DK_0(\alpha_n r_n)\right] \qquad (16)$$

Equivalent expressions for $E_{\theta,n-1}$ and $H_{z,n-1}$ can be found by replacing (r_n) in the above expressions by (r_{n-1}).

Now, for regions where n $\neq$ 1 or N,

$$\begin{bmatrix} E_{\theta,n} \\ H_{z,n} \end{bmatrix} = [T_n] \cdot \begin{bmatrix} E_{\theta,n-1} \\ H_{z,n-1} \end{bmatrix} \qquad (17)$$

Where $[T_n]$ is the transfer matrix [3,4] for region n, and is given by

$$[T_n] = \begin{bmatrix} a_n & b_n \\ c_n & d_n \end{bmatrix} \qquad (18)$$

Expressions for the transfer matrix elements are given in the appendix. Hence, given the values of E_θ and H_z at the lower boundary of a region, the values of E_θ and H_z at the upper boundary can be found using the transfer matrix. At boundaries where no excitation current sheet exists E_θ and H_z are continuous. Thus, for example, if two regions are considered to have no current

sheet at their common boundary, knowing the values of E_θ and H_z at the beginning of the first region, values of E_θ and H_z at the end of the second region can be found by successive use of two transfer matrices.
Now, considering the current sheet to be at radius r_g, then

$$H'_{r,n} = H_{z,n} \qquad\qquad n \neq g \qquad (19)$$

and

$$H'_{r,n} = H_{z,n} - J' \qquad n = g \qquad (20)$$

Where $H_{z,n}$ is the axial magnetic field strength immediately below a boundary, and $H'_{z,n}$ is the magnetic field strength immediately above a boundary. Bearing in mind the boundary conditions, it is apparent that for the model under consideration, it can be written that

$$\begin{bmatrix} E_{\theta,N-1} \\ H_{z,N-1} \end{bmatrix} = [T_{N-1}] \cdot [T_{N-2}] \cdots \cdots [T_{g+1}]\begin{bmatrix} E_{\theta,g} \\ H_{z,g} - J' \end{bmatrix} \quad (21)$$

and

$$\begin{bmatrix} E_{\theta,g} \\ H_{z,g} \end{bmatrix} = [T_g] \cdot [T_{g-1}] \cdots \cdots [T_2]\begin{bmatrix} E_{\theta,1} \\ H_{z,1} \end{bmatrix} \qquad (22)$$

If region N is now considered, Fig. (3-b), then

$$I_1(\alpha r) \to \infty \text{ as } (r \to \infty).$$

Therefore, from equation (15) and (16) one may obtain that (A=0) and

$$E_{\theta,N-1} = DK_1(\alpha_N r_{N-1}) \qquad (23)$$

and

$$H_{z,N-1} = -j\frac{\alpha_N}{\omega\mu_N}DK_0(\alpha_N r_{N-1}) \qquad (24)$$

Considering the first region (1), then

$$K_1(\alpha r) \to \infty \text{ as } (r \to 0)$$

Therefore, from equation (15) and (16) one may obtain that (D=0) and

$$E_{\theta,1} = AI_1(\alpha_1 r_1) \qquad (25)$$

and

$$H_{z,1} = j\frac{\alpha_1}{\omega\mu_1}AI_0(\alpha_1 r_1) \qquad (26)$$

It should be appreciated that equations (23 … 26) describing the field components at the boundaries of regions (1) and (N) still contain arbitrary constants. However, the ratios of E_θ to H_z at these boundaries contain no arbitrary constants, and it is only

these ratios that are needed for a complete solution. The next section shows how this may be accomplished. The ratios of E_θ to H_z have been termed the surface impedance [5].

3.4 Surface impedance calculations

The surface impedance looking outwards at a boundary of radius r_s is defined as [6],

$$Z_{s+1} = \frac{E_{\theta,s}}{H'_{z,s}} \qquad (27)$$

and the surface impedance looking inwards a boundary is defined as

$$Z_s = -\frac{E_{\theta,s}}{H_{z,s}} \qquad (28)$$

Using the method given in [6] with the values of $E_{\theta,N-1}$, $H_{z,N-1}$, $E_{\theta,1}$, $H_{z,1}$ and that of (a_n, b_n, c_n and d_n) as given in the appendix, it can be shown that

$$Z_{in} = \frac{Z_g Z_{g+1}}{Z_g + Z_{g+1}} \qquad (29)$$

Where Z_{in} is the input surface impedance at the current sheet, and Z_{g+1} and Z_g are the surface impedances looking outwards and inwards at the current sheet.
Substituting for Z_g and Z_{g+1} using equations (28) and (27) respectively, and with rearranging to get

$$Z_{in} = \frac{-E_{\theta,g}}{H_{z,g} - H'_{z,g}} \qquad (30)$$

From equation (20)

$$H'_{z,g} = H_{z,g} - J'$$

Substituting this in equation (30)

$$Z_{in} = \frac{-E_{\theta,g}}{J'} \qquad (31)$$

Thus, the input impedance at the current sheet (Z_{in}) has been determined. This means that all the field components can be found by making use of this and equations (28), (21) and (22).

3.5 Terminal impedance

The terminal impedance per phase can be derived in terms of Z_{in} [7], as

$$Z_t = \frac{16 \cdot m \cdot \pi \cdot N_{eff}^2 \cdot r_g \cdot Z_{in}}{\lambda \cdot P} \qquad (32)$$

3.6 Power calculations

Having found E_θ and H_z at all boundaries, it is then a simple matter to calculate the power entering a region through the concept of pointing vector. The time average power passing through a surface is given [7], as

$$P_{in} = \frac{1}{2}Re\left(\overline{E}_\theta \times \overline{H}_z^*\right) \quad (\text{w/m}^2) \qquad (33)$$

Using equations. (28), (31) and (33), it can be shown that the total charge power is

$$P_w = \frac{1}{2}\left|J'\right|^2 Re(Z_{in})(2\pi r_g l) \quad (\text{w}) \qquad (34)$$

3.7 Axial force

It follows that the axial acting force on the region [8] is

$$F_z = \frac{P_w}{\lambda f} \quad (\text{N}) \qquad (35)$$

4. EXPERIMENTAL MODEL

4.1 Model description

Fig.(4) shows the experimental test rig. The coils (primary winding) were wound circularly on a plastic tube, and held in positions through using circular guides. These guides were fixed on the tube in such away to make ditches between them. These ditches represent the slots of the primary circuit. Since the core has no backing iron then the primary circuit is of the open type. Each slot

(which is open) is filled with a coil, and the coils are connected in star to a variable voltage supply. It is worth mentioning that these star connected coils represent the heating part of the system (heater). The heater was then mounted and fixed on a board using a suitable mechanical structure. This enables fine adjustment for a uniform air-gap surrounding the workpiece that represents the load (charge). The type of the charge used is a solid aluminum cylinder.The magnetic circuit for this material provides the required flux paths. The conductivity of the charge was measured using standard DC measurement. Table 1 shows the parameters of the experimental model.

To calculate the magnetic flux density on the charge surface, simple type of independent probe (search coil) was used. The magnetic flux density in the axial direction was measured using a (B – probe), as will be explained in the next section.

4.2 B – probe

A search coil is used to investigate the axial component of magnetic flux density at different positions on the surface of the charge. Five identical B-probes, displaced (5 cm) from each other, were used to measure the magnitude of the magnetic flux density. Each probe consists of (200) turns of thin wire of size (SWG 30) wound around the cylindrical charge, of ($\pi \cdot r_w^2$) area. The coil ends were twisted together and connected to a digital voltmeter.

Using Faraday's law, the induced voltage V_C across the search coil is

$$V_C = n_c \cdot \omega \cdot A_c \cdot B \qquad (36)$$

Where

r_w : radius of the charge, (mm)

n_c : number of turns of the search coil.

A_c : cross sectional area of the charge around which search coil is wound, (m^2)

4.3 Load power measurement

The load power was measured experimentally as follows:

a. The input power to the heater was measured by using two wattmeter method.

b. Primary phase current was measured using an ammeter. Then, the copper loss for the three-phase primary winding (coils) was calculated, as

$$P_{cs} = 3I_{ph}^2 R_{ph} \qquad (w) \qquad (37)$$

Where

P_{cs} : Copper loss of coil conductors, (w).

I_{ph} : Primary phase current, (A).

R_{ph} : Resistance of primary coil per phase, (Ω)

c. The load power in charge was found by subtracting the copper losses from the input power, as follows

$$P_{ch} = P_t - P_{cs} \qquad (w) \qquad (38)$$

Where

P_{ch} : Load power in charge, (w).

P_t : Total input power, (w).

4.4 Axial force measurement

An experimental measurement of the axial force has been implemented using the experimental set-up shown in Fig.(5). Each point was found, by adjusting the suspended mass (M_z), to balance the force produced by the system. The force is then calculated using the following equation

$$F_z = M_z \times g_a \qquad (N) \qquad (39)$$

Where

F_z : Axial force, (N).

M_z : Mass, (Kg).

g_a : Acceleration of gravity = 9.81 m/sec^2.

5. RESULTS

Theoretical and experimental results were executed with different number of poles. Variable three-phase current excitation was used at a test frequency of 50 Hz.

Prof. Dr. Jafar Hamid Alwash
M.Sc. Riyadh Kamil Chillab

Traveling Wave Cylindrical Induction Heating System

Fig. (6), and (7) show the variation of charge power with exciting current per phase for 2,and 6 poles respectively.

From the results, it is clear that increasing number of poles reduces the power induced in the charge. This of course is to be expected since increasing the number of poles is accompanied by reducing the effective number of turns per pole per phase.

The layer theory approach has been used for the analysis of induction heating system with rotational symmetry with three-phase excitation. The analysis presented is quite general in that it lends itself to the analysis of traveling wave induction heating systems with any number of poles.

The displayed results show clearly that the theoretical results correlate well with the experimental ones. This may be considered as fair justification to the method adopted for the analysis in this work.

6. Conclusions

The layer theory approach has been used for the analysis of induction heating system with rotational symmetry with three-phase excitation. The analysis presented is quite general in that it lends itself to the analysis of traveling wave induction heating systems with any number of poles.

The displayed results show clearly that the theoretical results correlate well with the experimental ones. This may be considered as fair justification to the method adopted for the analysis in this work

7. Appendixes

7.1 Transverse matrix elements

$$a_n = \alpha_n r_{n-1} \left[I_1(\alpha_n r_n) K_0(\alpha_n r_{n-1}) + I_0(\alpha_n r_{n-1}) K_1(\alpha_n r_n) \right]$$
(40)

$$b_n = j\omega\mu_n r_{n-1} \left[I_1(\alpha_n r_{n-1}) K_1(\alpha_n r_n) - I_1(\alpha_n r_n) K_1(\alpha_n r_{n-1}) \right]$$
(41)

$$c_n = j \frac{\alpha_n^2 r_{n-1}}{\omega\mu_n} \left[I_0(\alpha_n r_n) K_0(\alpha_n r_{n-1}) - I_0(\alpha_n r_{n-1}) K_0(\alpha_n r_n) \right]$$
(42)

$$d_n = \alpha_n r_{n-1} \left[I_0(\alpha_n r_n) K_1(\alpha_n r_{n-1}) + I_1(\alpha_n r_{n-1}) K_0(\alpha_n r_n) \right]$$
(43)

REFERENCES

- Freeman, E.M., and Smith, B. E.; "Surface impedance method applied to multilayer cylindrical induction devices with circumferential exciting currents"; Proc. IEE, vol. 117, No. 10, pp 2012-2013, Oct. 1970.
- Alwash, J. H.; "Analysis and Design of Linear Induction Machines"; Ph.D. Thesis, Imperial College, London University, U. K., 1972.
- Greig, J., and Freeman, E.M.; "Traveling wave problem in electrical machine"; Proc. IEE, vol. 114, pp. 1681-1683, Nov. 1967.
- Freeman, E.M.; "Traveling waves in induction machines: input impedance and equivalent circuits"; Proc. IEE, vol. 115, No. 12, pp. 1772-1776, Dec. 1968.
- J. H. H. Alwash, A. D. Muhsen and A. S. Abdi; "Helical motion tubular induction motor"; IEEE Trans. Energy Conv., vol. 18, No. 3, pp. 362-369, Sep. 2003.
- Eastham, J. F., and Alwash, J. H.; "Transverse-flux tubular motors"; Proc. IEE, vol. 119, No. 12, pp. 1709-1718, Des. 1972.
- Mohssen, A. D.; "Predicting the performance of helical winding induction motors"; M.Sc. Thesis, College Engineering, Baghdad University, Baghdad 1996.
- Al-shammari, R. K.; "Analysis of traveling wave cylindrical induction heating systems"; M.Sc. Thesis, Elect. Eng. Dept., College of Engineering, University of Baghdad, 2009.
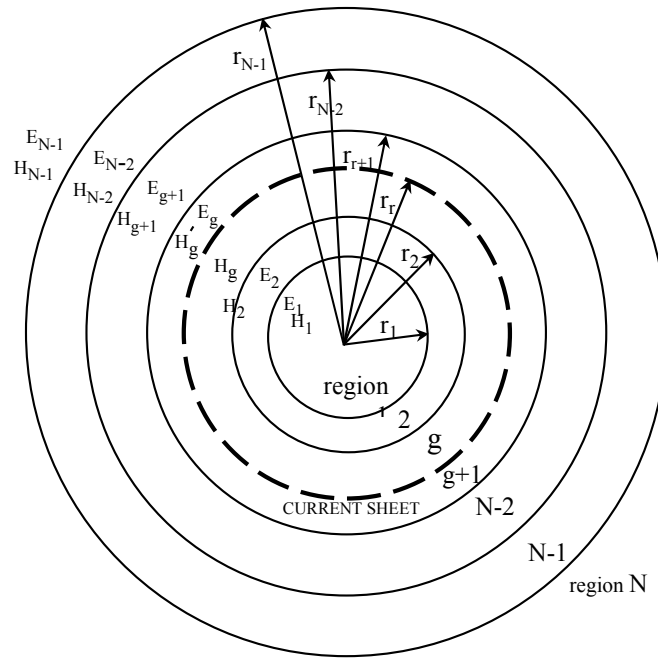
Fig.(1)
Cross-sectional view through multi-cylindrical induction heating system
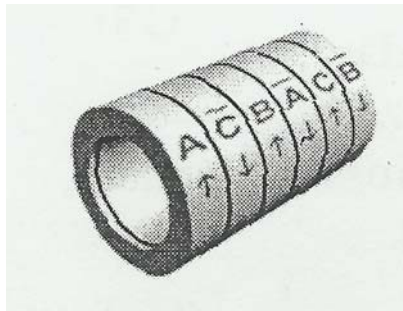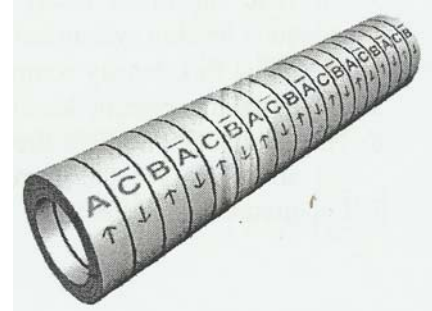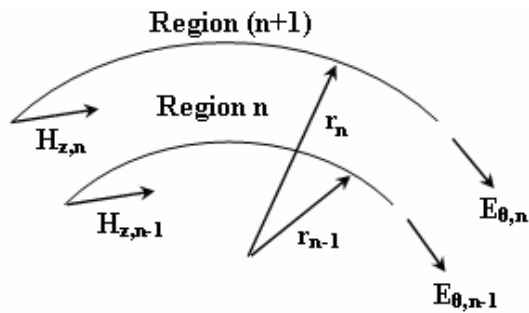

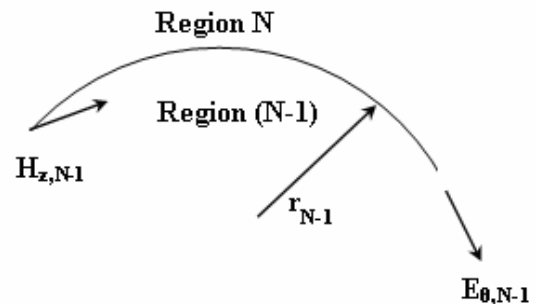**(a)**   **(b)**

Fig.(2): Three-phase windings form of induction heater with different number of poles
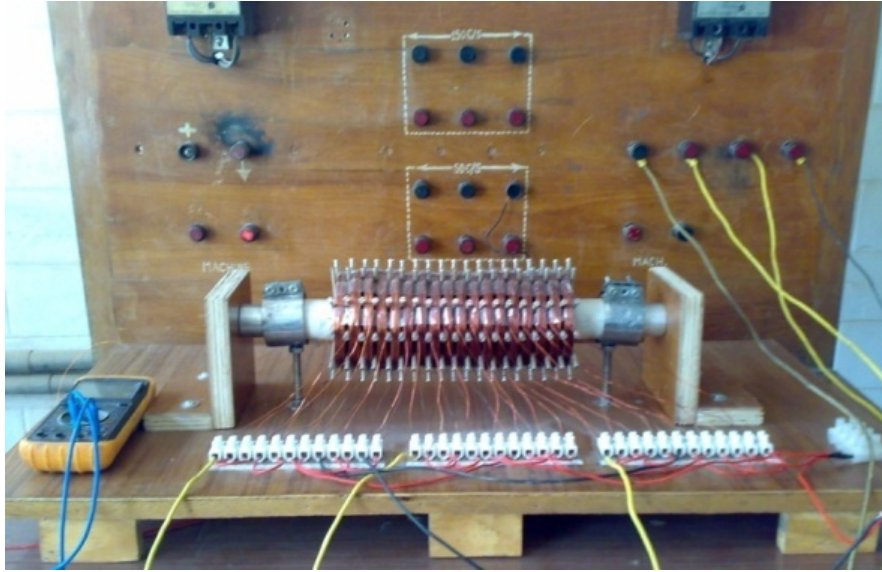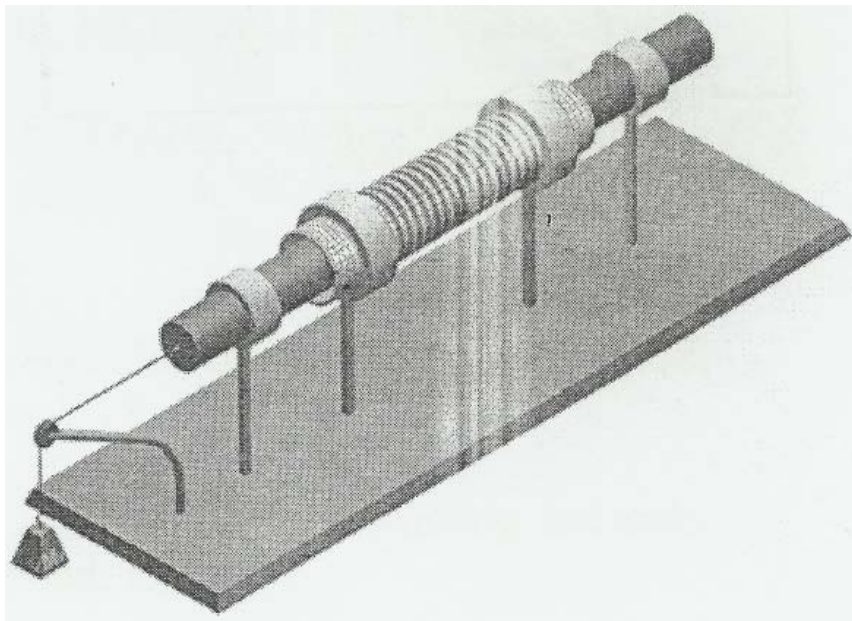**(a) 2-poles connection   (b) 6-poles connection**

(a)   **(b)**

Fig.(3): Mathematical model
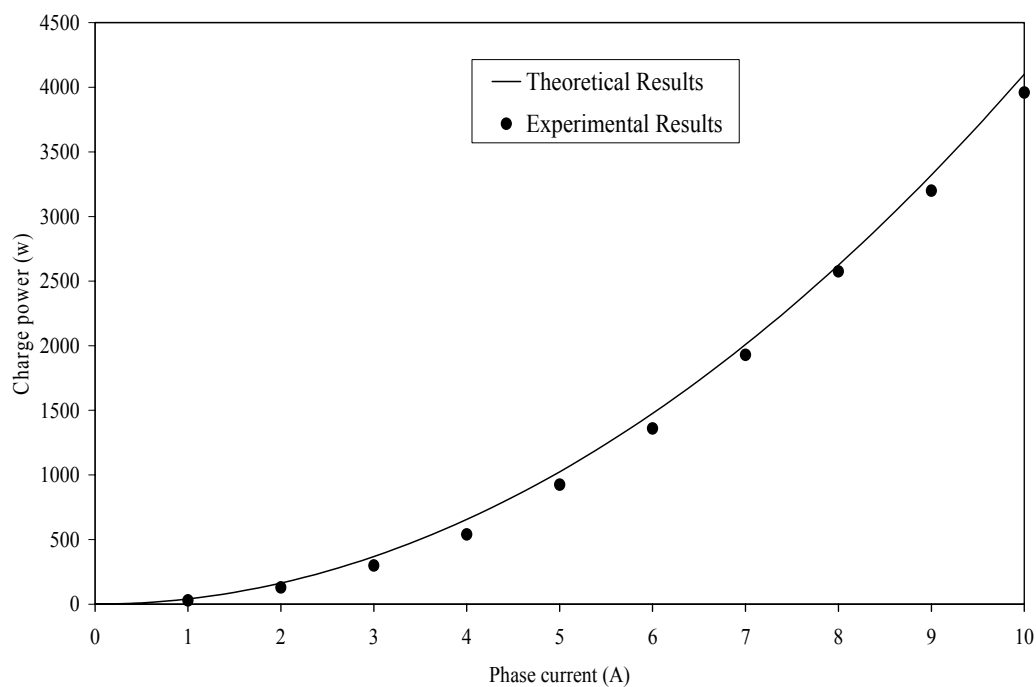**(a) General region n   (b) End region N**

Fig.(4)
Photograph of the experimental model

Fig.(5)
Experimental set-up for measuring the axial force

Fig.(6)
Variation of charge power with phase current (2-pole connection)
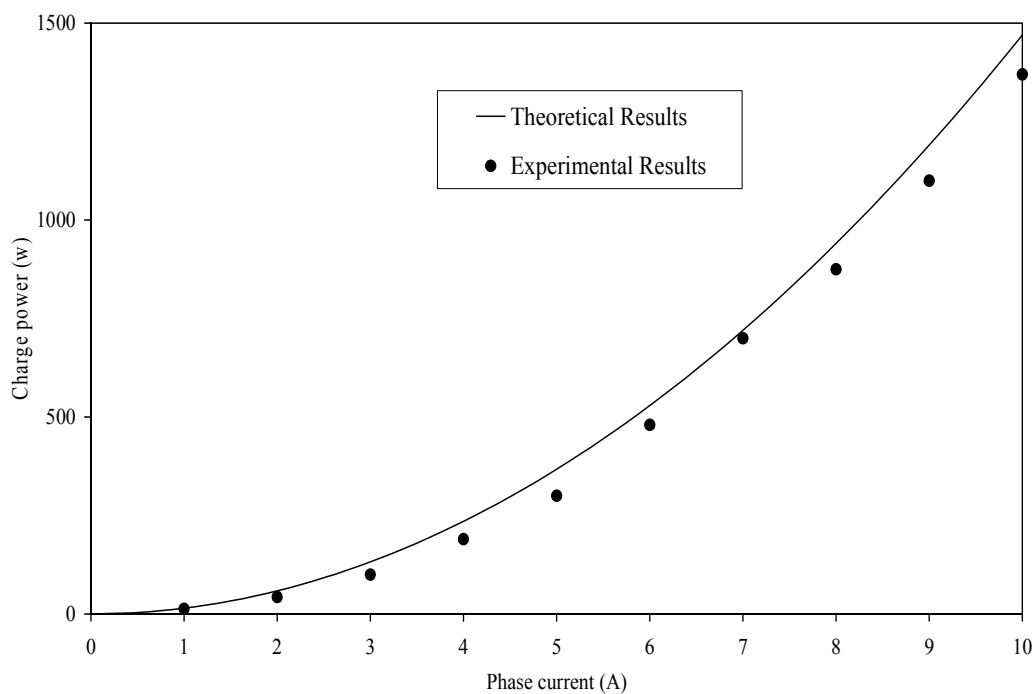
Fig.(7)
Variation of charge power with phase current (6-pole connection)

215

Table 1
Experimental model parameters

Parameter/Characteristic	Value
Phases	3
Axial poles	2,6
Number of slots (coils)	18
Turns per coil	260
Coil inner diameter (mm)	50
Slot width (mm)	10
Slot pitch (mm)	16
Slot depth (mm)	37
Frequency (Hz)	50
Air-gap length (mm)	5
Primary conductor wire gauge	SWG 19.5
Charge length (mm)	294
Charge radius (mm)	20
Charge conductivity (s/m)	3.4×10^7
Charge relative permeability	1
Exciting phase current (A)	Variable

Improvement of Resistance Spot Welding by Surfaces Treatment of AA1050 Sheets

Dr. Qasim Mohammed Doos Al-Attaby	**Dr. Moneer Hammed Al Saadi**	**Ihsan Kadhom Abbas Al Naimi**
Professor	Assistance Professor	Ph.D.
Mechanical Engineering	Welding Department	Mechanical Engineering
Baghdad University	Technical College-Baghdad	Baghdad University
Kasim_daws@yahoo.com	monerht@yahoo.com	Ihsan_kad@yahoo.com

ABSTRACT

Resistance spot welding (RSW) aluminum alloys has a major problem of inconsistent quality from weld to weld, because of the problems of the non-uniform oxide layer. The high resistivity of the oxide causes strong heat released which influence significantly on the electrode lifetime and the weld quality. Much effort has been devoted experimentally to the study of the sheet surface characteristics for as-received sheet and surface pretreatment sheet by pickling in NaOH and glass-blasted with three thicknesses (0.6, 1.0, and 1.5 mm) of AA1050. Three different welding process parameters energy setup as a low, medium, and high were carried. Tensile-shear strength tests were performed to indicate the weld quality. Moreover, microhardness tests, macro/micrographs, and SEM/EDS examinations were carried out to analyze, compare, and evaluate the effect of surface conditions on the weldability. The as-received sheet showed a higher electrical contact resistance because of its thicker and non-uniform oxide layer. In contrast, the glass-blasted sheet showed lower value, since it has a roughest surface, which leads to easy breakdown the oxide layer. The highest average values and least scattering of the maximum load fracture are with treated sheet by pickling in NaOH, these values are 760, 1193, and 2283 N for 0.6, 1.0, and 1.5 mm sheet thickness respectively for medium input energy. In contrast, the minimum values with glass-blasted sheet are 616, 1008, and 2020 N for 0.6, 1.0, and 1.5 mm sheet. The microhardness profiles of the fusion zone and HAZ is the lower than the base metal for all cases. Numerical simulation with SORPAS$^{®}$ was used to simulate and optimize the process parameters, and it has given good results in prediction when they compared with experiments.

Keywords: RSW   Oxide Film   Roughness   Macro/Micrograph   SEM/EDS   AA1050   SORPAS$^{®}$

Dr. Qasim Mohammed Doos Al-Attaby
Dr. Moneer Hammed Al Saadi
Ihsan Kadhom Abbas Al Naimi

AA1050

أ. د. قاسم محمد دوس العتابي   أ. م. د. منير حميد طلفيح السعدي   إحسان كاظم عباس النعيمي

.

.

(0.6   1.0   1.5   )

AA1050   .

    –   .

)

(

.

760   1193   2283

0.6   1.0   1.5   .

616   1008   2020   0.6   1.0   1.5   .

.

SORPAS®

.

الكلمات الرئيسية :

INTRODUCTION

Todays, World is faced with an energy crisis. It is therefore essential to find cost-effective solutions to this issue. Therefore, there has been a significant trend in the automobile industry by economic and political pressure to make lighter vehicles in order to reduce fuel consumption and CO_2 emission. Because of their lightweight and high specific strength (strength-to-weight ratio), the application of aluminum alloys in automobile industry is being increased and popularity. The advantages of weight saving up to 46% [Wheeler, 1987] and resistance of corrosion are considerable.

Resistance Spot Welding (RSW) has been the dominant process in sheet metal joining, particularly in automobile industry. Because of its low cost, flexible, easy automated and maintains, fast, and minimum skill labor requirements. Moreover, it is a well-established process in the automotive industry [Brown, 1995 and Cho, 2006]. The process is also applied in manufacture of other transportation, kitchen utensils, and more. Modern small vehicles contain (2000-5000) spot welds [Chao, 2003]. Annual production of automobiles in the world is measured in tens of millions units; therefore, each welded spot has its own importance not only with regard to quality but also for production issue. Steel and aluminum alloys share many of the same process attributes for RSW. However, the productivity of aluminum spot welding is lower than of steel especially those alloys with low strength (series 1xxx). This is because aluminum alloys have higher thermal and electrical conductivity, higher coefficient of expansion, narrow plastic temperature range, and oxide film problems, which forms on the surface of the aluminum and has high electrical resistance and

a high melting temperature (2050℃), as the oxide

film grows the effective contact resistance of the aluminum changes. Therefore, the control of weld quality is much more difficult and requires tighter controls [Kim, 2009]. In general, aluminum's high thermal and electrical conductivity require higher current, shorter weld time, about (2-3) times the amount of current and (¼) weld time compared to spot welding steel. Accurate control and

synchronization of current and electrode force is required due to the narrow plastic temperature range [RWMA, 2003]. Aluminum is highly reactive to oxygen and will within 100 picoseconds form thin protective oxide layer (Al_2O_3) on its surface and is often considered be a uniform ceramic coating or layer. This layer is beneficial as it protects the base metal from corrosion. While this may be close to reality for high-purity aluminum, the oxide layer on the aluminum alloy sheets for automotive bodies is much more complex [Patrick, 1984]. The oxide layer is important because its thickness is an influential parameter in the electrical resistance [Sun, 1982]. The high resistivity of the oxides causes strong heat release. Fusion of the low melting alloy takes place not only at the sheet-to-sheet interfaces but also at the sheet-to-electrode contacts, resulting in unacceptable electrode wear.

RSW is a welding process that joint sheet metal together by applying pressure and passing a large quantity of current through localized area generating heat by Joule ohmic heating law while weld nugget growth is initiated here and the sheets are permanently fixed together. Thereby, electrical contact resistance is one of the most critical parameters in resistance welding. A large contact resistance is advantageous for the formation of a single spot weld. As discussed by Browne, et al. [Browne, 1995] contact resistance plays an important role in the RSW process for aluminum. It has drawn the attention of many researchers since several decades ago, [Studer, 1939] carried out many experiments to demonstrate the influences of the pressure, temperature, and materials and its state on the contact resistance. With assistance of Gleeble system, contact resistance was experimentally investigated dynamically by [Song, 2005]. They demonstrated that interface normal pressure has great influence on the contact resistance and it decreases with increased normal pressure, in contrast, the influence of temperature on contact resistance is less pronounced as pressure increases.

Surface roughness along with elastic-plastic properties of the materials; also influence the electrical contact resistance [Dzekster, 1990]. The effect of surface roughness and oxide film thickness on the electrical contact resistance of aluminum were carried out by [Crinon, 1997], they illustrated

That the effect of the oxide film is greatest in the specimen with smoothest surfaces.

Expulsion, which can be observed frequently during RSW, happens at either the faying surface or

the electrode/work piece interfaces. The latter may severely affect surface quality and electrode life. The risk of expulsion is especially high in spot welding of aluminum alloys due to the very dynamic and unstable character of the process, relating to the application of a high current in a short welding time as compared to welding steels [Senkara, 2004 and Mathers, 2002].

RSW of aluminum alloys has two major problems: short electrode tip life and inconsistent weld quality [Williams, 1984]. Spot welding in AA1050 is less stable and the electrodes will stick to the sheet after 50 welds because of the oxide film problems [Pederson, 2010].

In this study, the influence of oxide film pretreatment on the strength of the weldments, which had done by RSW process was compared and evaluated. The pretreatment of the strips surfaces of AA1050 was done by both glass blast (mechanical mean) and pickling with NaOH (chemical mean).

EXPERIMENTAL PROCEDURE

The experiments were conducted at Technical University of Denmark (DTU), using 0.6, 1.0, and 1.5 mm sheet thicknesses of low-strength aluminum alloy AA1050, which were spot-welded on TECNA, the specifications of the welding machine are listed in **Table 1**. The Controller of the machine is TE-180 type with 16 functions. The electrode tips (Female Cap) used during the experiments are type A0 according to ISO 5821-2009, [RWMA, 2003]. They were made of Zirconium copper alloy with the following chemical compositions; Cr: 0.7-1.2%, Zr: 0.06-0.15% and the remainder is Cu. The configuration of them is radius type (A), diameter of 16 mm, end surface of 40 mm radius. The electrodes were drilled near the tips end with 1.5 mm diameter to insert copper wires in order to measure the secondary voltage. The current measurements from Rogowski coil together with a

Pre-calibrated TECNA-1430 conditioner and a piezoelectric force sensor with Kistler-5015 transducer were acquired by a DAQ BNC-2110 from National Instruments and then passed to LabVIEW software programmer to treatment the signals .The properties and nominal compositions (performed by spectrum analyzer) of the sheets are shown in **Table 2**, the samples were cut from the sheets into 16×115 mm, the rolling direction with

the longitudinal dimension and they joined as a lap joining, to prepare the tensile-shear test. The parameters of the RSW process were calculated for each experiment, RMS current I (A), welding time C (cycle), and the electrode force P (kN). The tensile-shear tests were carried out using a 100 kN (22.5 kIb$_f$) AMSLER universal testing machine at a deformation rate 2mm/min at room temperature to demonstrate the strength of the weld S (N). The microhardness test were performed using FUTURE-TECH-CORP FM-700 using the Vickers scale at an applied load of 50 g, they were taken on each samples in longitudinal direction along the diameter of the nugget at intervals of 0.5 mm. The macro/micrographs of the weldments were carried out using light optical microscope (LOM) type a Neophot 30 (Zeiss, Jena) with a Cool Snap CCD camera. Moreover, for high-resolution images electron microscope (SEM) a JEOL JSM-5900 with LaB6 filament applying secondary electron (SE) at 20 kV, and electron-dispersion x-ray spectroscopy (EDS) part of a SEM facility an Oxford Instruments for quantitative chemical analysis were used.

The pretreatment of the surfaces of the strips were done by two methods: mechanical and chemical. The mechanical means was carried out by glass blast with grain size of 100 µm; each strip was subjected to 30 seconds of blast treatment at air pressure of 200 kPa. The experiments were done on both sides of the strips and other experiments were performed only on one side of the strips. The latter were welded with two directions; the pretreatment surfaces of the strips were the faying surfaces, and the alternative direction was the pretreatment surfaces with electrodes interface. The chemical means was done by pickling with sodium hydroxide (NaOH), the procedure of this approach was performed by sink the strips in solution 60 g of NaOH with one liter of ionized clean water within 2 minutes only, the temperature of the solution was

60°C. Then, the strips by hot water and ethanol were

rinsed and cleaned for the both means to be ready for welding.

Aluminum is high affinity of oxygen, an oxide layer is always present at its surface and will immediately reform if surface pretreatment mechanically or chemically. For the stability of the oxide film, and repeating the experiments with the same conditions; the pretreatment strips were prepared within 3 hours before spot welding. This time was chosen depending on the **Fig. 1**, which was expected to have fresh, thin, and uniform oxide layer, while the as-received sheet would have thicker and non-uniform oxide layer.

The experiments were designed as a general factorial with three replicates per condition [Cho, 2006]. The factors and their associated parameters are given in **Table 3**. During welding, expulsion and sticking were observed and recorded.

RESULTS AND DISCUSSION

PICKLING IN NaOH

The electrical contact resistance at the interfaces sheet-to-sheet and sheet-to-electrode is the main source of heat during RSW of aluminum alloys, unlike steel, which the source of heat is the bulk resistance of the sheets. This electrical contact resistance depends strongly on the tribological characteristics of the contacts at the two interfaces. The significant factor impression tribological feature of aluminum sheets is the oxide layer. **Fig. 2** illustrates SEM image with EDS analyzer for as-received spot-welded strips, which show unambiguously the high amount of oxygen (3.6, 4.6, and 2.9%) near the area of strips separation. In the second importantly are the surface roughness and the presence of the foreign materials such as dirt, lubricant, chemical, water vapor, and others [Studer, 1939, Crinon, 1997, and Rashid, 2011]. Although of all care to maintain uniform surface conditions, the electrical contact resistance is almost different when another time measured in the same region. Therefore, the quality of RSW of aluminum alloys is inconsistent.

During pickling of aluminum alloy sheets in basic or acidic solutions the surface oxides or hydroxides are dissolved. The pickling rate is dependent on many variables including; 1- solution agent and concentration, 2- solution temperature, 3- composition of the surface sheet, 4- velocity of solution movement around the sheet (rpm). In earlier of this work, 5 minutes was chosen to sink the strips in the pickling agent (NaOH). However, it clearly seems that the corrosion rate of aluminum is much higher than the dissolution rate of the oxide layer. The formula of dissolution is:

$$Al_2O_3 + 2OH^- + 3\,H_2O \rightarrow 2Al(OH)_4^- \quad (1)$$

When the metal is bared; immediately corrodes according to this formula:

$$Al + 3H_2O + OH^- \rightarrow Al(OH)_4^- + \tfrac{3}{2}H_2 \quad (2)$$

The last formula shows that H_2 is evolved during dissolution of aluminum even in basic agent [Rönhult, 1980]. Consequently, the metal is corroded by pitting as soon as the protecting layer of oxide film has been dissolved in some areas. Investigation by SEM shows strip exposure to NaOH within 5 minutes gave severe pitting corrosion of the surface, as shown in **Fig. 3**. Severe expulsions and sticking with electrodes were occurred during spot welding with these strips, due to the decreasing of electrical contact resistance in electrode sheet interface in spite of sheets interface especially with those of 0.6 mm strips. Therefore, all experiments latter were performed by exposure the strips to NaOH only within 2 minutes to minimize expulsion and sticking occurring.

SURFACE ROUGHNESS

Surface roughness measurements were carried out in this work on a Taylor/Hobson, Precision-SURTRONIC-25 instrument for various types of the strips to analyze and compare. Five measurements randomly on each of three strips for each surface condition and the average of all of them were recorded. **Table 4** shows these values of the centerline average (Ra) of as-received and pretreatment strips. It clearly seems that pretreatment sheets with glass blast show high values of roughness and the roughest surface is 1.0 mm sheet with glass blast (Ra = 4.703 μm), as seen

in **Fig. 4,** in contrast the smoothest surface is 1.5 mm as-received sheet (Ra = 0.238 μm). Chemical

Surface pretreatment (pickling in NaOH) shows the lowest value in standard deviation (s) when measured the surface roughness, and therefore it will be the most consistent in the weld strength. In contrast, the pretreatment strips with glass-blast show higher values in standard deviation although the attempt to control the removing surface layer precisely due to the manual process, and therefore it will be more scattering in welding strength as illustrated later.

The large variance between the smoothest and the roughest surfaces were clearly affected the strength of the weldments when were tested on the shear-tensile test. The glass-blasted strips show much lower contact resistance between sheet interfaces in spot welding causes less heat generated in this region, therefore small size nugget were produced, thus were affected the strength of the weldments. In the same sense, these strips show much lower sticking with electrodes, due to the lower heat generation since lower contact resistance in the region between sheet and electrode. Therefore, some experiments were conducted only on one side with glass-blast associated with sheet-to-electrode interface, and it shows as expected good weldability especially no sticking with electrodes and high strength with same process parameter.

Although there was a not high difference of roughness level between as-received and chemical treatment strips, there was a large difference in consistent of the welding quality between them. These results clearly demonstrate that the surface roughness is not the unique factor controlling the electrical contact resistance, but the oxide layer thickness and its configuration, which was similar to that found by other researchers [Patrick, 1984, Studer, 1939, Crinon, 1997, and Pouranvari, 2010]. It seems likely this result of surface roughness were associated with easier breaking down the oxide film in roughest surfaces when applying the electrode force during spot welding causes much lower contact resistance.

Fig. 5 shows LOM images, which confirm the variance of the surface roughness of the as-received

sheet and the pretreatment sheet with pickling in NaOH and glass-blast.

TENSILE-SHEAR TESTS

Tensile-shear tests carried out on the welded joints indicated their strength and the failure mode. In this work, direct comparisons of the as-received surface with those of the pretreatment surface by pickling in NaOH and glass-blasted were established. **Fig. 6** shows the maximum fracture load for the spot welds as a function of welding input energy as mentioned in **Table 3** while other parameters are kept constant. The data point, which was represented in the figure, is the average of three specimens test. It is seen in general that with increasing energy input the maximum fracture load of spot welding increases. Moreover, the mode of failure is recorded and it is classified in three types; 1st interfacial failure (nugget fracture in shear), 2nd plug failure (nugget pull out), 3rd failure occurs in the heat affected zone (HAZ) where failure is a result of breaking this region throughout the width of the strip. The failure of spot welding could be seen as a competitive process, i.e. any failure occurs in a mode require least load [Newton, 1994]. These three types of the mode of failure were occurred usually as follows, the first type with low input energy, the second type with medium input energy, and finally the third type were occurred with high input energy for the three thicknesses sheets due to overheating and softening the region near the nugget perpendicular to strip width. A few anomalous specimens that have been observed during the testing did not fall under these types of failure. In line with other studies [Senkara, 2004, Mathers, 2002, and Ma, 2008], expulsion was occurred beyond the high input energy as well as of sever sticking sheet with electrodes. Furthermore, the fracture was usually in the form of ductile tearing around the nugget. Only a few weak welding failed in a brittle manner through the interface, and this was especially observed at low input energy.

The second observation, the scattering in maximum load fracture in tensile-shear tests is less in the pretreatment surfaces sheet with pickling in NaOH due to the new uniform less thickness of oxide layer. In addition, more scattering is with glass-blasted sheet due to the not good controlling manual process of removing the oxide layer. However, the maximum scattering values is with as-received sheet due to the non-uniform oxide layer,

which can scarcely be controlled without putting the samples in a vacuum.

The most important result obtained is that the average of maximum load fracture was the highest value in chemically treated with all thickness sheets. These values are 760, 1193, and 2283 N for 0.6, 1.0, and 1.5 mm sheet thickness respectively for medium input energy. In contrast, the minimum values of the maximum load fracture are in the glass-blasted sheet due to the lowest values of electrical contact resistance that lead in turn to be a small nugget size and thus small values of maximum load fracture. The electrical contact resistance of the roughest surface becomes lower value when electrode force is applied, due to the more breaking of the oxide layer, which is electrical insulating and this is a good agreement with many researchers as [Crinon, 1997]. These values are 616, 1008, and 2020 N for 0.6, 1.0, and 1.5 mm respectively. However, there is an interesting observation, which there is a significant increase in the maximum load fracture corresponding with glass-blasted treated strips on one side, which is the interface of the electrodes and the other faying surfaces remain untreated. The reason is higher heat generation due to higher electrical contact resistance at the faying surfaces and it is lower at the sheet-electrode interface and therefore less sticking with electrodes with increasing electrodes life. These values are 775, 1147, and 2408 N for 0.6, 1.0, and 1.5 mm sheet thickness respectively for the medium input energy.

MICROHARDNESS TESTS AND MICROSTRUCTURE EXAMINATIONS

Microhardness characteristics of the RSW are one of the most important factors affecting their failure behavior. Typically, the microhardness profile of the nugget of steel exhibit a significant hardness increase from the base metal due to the increasing of the martensite forming, and it is being more with alloy steel due to the content of alloying elements. An example of this behavior was recorded by [Hayat, 2011] with DP600 steel. With aluminum alloys, the microhardness values obtained from the fusion zone proved the existence of hard and brittle intermetallic phases due to the high content of the alloying elements thereby cause increasing of the hardness in that region. However, with low content of alloying elements as AA1050 the profile of

microhardness is completely different, since the lower hardness is in the fusion zone. It is somewhat lower than the base metal, which can be attributed to its cast microstructure and the presence of coarse columnar grains. Moreover, the effect of the prior work hardening is completely removed in the fusion zone because of the melting.

Fig. 7 illustrates the variations of the microhardness profile for the pretreatment surfaces by mechanical (glass-blasted) and chemical (pickling in NaOH) and the as received of 1.0 mm sheets, which carried out on the cross section of the nugget to show the microhardness of the weld metals, HAZ region, and the base metals. The first important observation of profiles is that the microhardness of the fusion zone and HAZ is lower than the base metal for all cases, since these points were affected by the heat generated of welding, which were completely removed all previous work hardening especially in the fusion zone and its cast microstructure as mentioned above. The second observation, there are points with values of relatively low microhardness. These points are close to the voids defects result of the expulsion was occurred due to the high welding current (32 kA) for this sheet thickness, such as points 6 in glass-blasted sheet, point 7 in chemical pretreatment sheet, and point 5 in as-received sheet, which are observed in macrostructures were obtained by LOM. In contrast, there are a few points with relatively high values. Since, they are located on small grains and formed from intermetallic compounds, such as points 2, 2, and 8 in in glass-blasted, chemical pretreatment, and as-received sheet respectively, see the microstructures of these points as shown in **Fig. 7** (**a**), (**b**), and (**c**). Therefore, there is not a constant microhardness profile along the nugget.

In general, the microhardness measurements in fusion zone and HAZ of pretreatment surfaces with glass-blasted show highest values than the others, due to of the treatment by this means, which causes a few work hardening result of the hitting of the surface by glass grains during the oxide remover. In contrast, the microhardness measurements of as-received sheet show a lower values than the other pretreatment sheets due to the more heat generated at the faying surfaces since of the highest value of electrical contact resistance, as shown in **Fig 7** (**d**). Moreover, the microhardness of pretreatment

Surfaces by pickling in NaOH of the base metal show a lower value than the others due to the uniform fresh small thickness of oxide layer which consider as a harder material.

The macrographs show variations across the joints between the as-received sheets and the pretreatment surface sheets. The nugget size of the as-received weldments is larger than the pretreatment surfaces in the both means, since they are much lower contact resistance in the region of the faying surfaces, therefore lower heat generated. As an example, the nugget sizes are 5.1, 5.0, and 4.7 mm of 1.0 mm, 7.0, 6.54, and 5.35 mm of the 1.5 mm for as received, pickling in NaOH, and glass-blasted sheets respectively. The minimum size is with glass-blasted sheet that are less electrical contact resistance, which generates less heat.

The structures of aluminum weldments are usually not clearly distinguishable as in steel weldments, and the HAZ is significantly narrower for an aluminum weldments. These make the identification of various zones difficult. **Fig. 8** shows the micrographs of the 1.5 mm strips, which were welded with 32 kA welding current and 5 cycles welding time and the sheet were treated by pickling in NaOH. There are recrystallized small equiaxial grains and insoluble particles of $FeAl_3$ (black) in the oval nugget, and there are narrow zone of the columnar grains in the edge of the nugget and this zone is interfacial with the HAZ, which are formed of the dendritic grains. Moreover, some porosity (large, black area) is evident due to the splashes were occurred because of relatively high current was used. There are not a significant variation in the microstructures in the nugget and the HAZ of the weldments between the as received and the pretreatment sheets since the pretreatment is on the surfaces and not in the region which are heat affected. View of non-repetition, has not been discussed the microstructures of the other cases of the sheet condition that are not being a large variance from this case.

SEM AND EDS EXAMINATIONS

Further micrographs were carried out on SEM including secondary-electron images (SEI) to observe the nugget size, microstructures, surfaces profile, and together with X-ray spectroscopy (EDS) including high resolution mapping analyzing

the chemical composition in the area of the interest. As-received sheet including non-uniform thick oxide layer caused indentation of the electrodes into the strips when spot-welded leading to degradation of the electrodes rapidly due to the pitting on the surface of the electrodes and dissolving or alloying the copper into the base metal of the aluminum or vice versa in this region. The reason of these problems is the high electrical resistance and a brittle nature of oxide layer causing relatively high heat generated in this region. The reason of few defects in the case of treated sheet might probably lie in the presence of the pitting on the electrodes surface because of the previous welding, as shown in **Fig. 9**.

The white color areas in the SEM images indicate the presence of the aluminum bronze with copper alloying element, as shown in the EDS analyzer table.

NUMERICAL SIMULATION

Commercial finite element numerical program SORPAS® [SWANTEC] was used in this work. It is well known and most widely used as a numerical tool for simulation, optimization, and planning features of the resistance welding processes. It is based on mechanical, electrical, thermal, and metallurgical models. In order to analyze and compare the experiments with the numerical modeling scheme, SORPAS® has been used to simulate a RSW of AA1050 with as-received sheet and the pretreatment sheet. Weld schedule specifications (WSS) is a new update input window included in the new version (10) of the program for optimized weld current, weld force, weld time, and hold time. **Table 5** indicates the WSS of the weld planning to optimize the RSW process parameters for as-received sheets. Furthermore, the process parameters for pretreatment sheets have been optimized in order to compare with as-received sheet. The value of electrical resistance at 20℃ in the materials database of the program was only changed to lower value, for the purpose of compatibility with oxide layer treatment. Only one result has changed that is the value of the welding current, which has become lower about 2 kA.

Fig. 10 shows the simulated joint for pretreatment by glass blast of 1.0 mm sheet

compared with experimentally macro etched cross-section nugget result welded with 29 kA welding current and 5 cycles welding time. It can be seen that the shape of the weld is predicted relatively a very fine correlation with the actual weld nugget, as well as the HAZ zone.

CONCLUSIONS

The experiments showed that weldability is improved when the oxide layer is properly removed. However, the resistance of an oxide layer is beneficial for the localized heating required to form the weld nugget, but this resistance should be as low as possible in order to minimize the heat generated at the interface between the electrodes and the sheets. The significant conclusions drawn from this experimental work are as follows:

1. The surface condition of aluminum sheet has a significant influence on the weldability and the electrode lifetime.
2. The optimum time immersing the strips in the solution of NaOH is 2 minutes at temperature of 60 °C.
3. In line with [Rashid, 2011] conclusions, the surface roughness affects the contact resistance by decreasing it where surface roughness increase, as it occurred with glass-blasted sheet, since it breakdown the oxide layer.
4. Treated sheet with pickling in NaOH gives highest average values of the maximum load fracture as shear-tensile test with all sheet thicknesses, as well as the scattering in the maximum load fracture is the least in this sheet, due to the fresh uniform oxide layer.
5. Less electrode sticking has occurred with one side surface treated that is electrode-sheet interface, in spite of good welding (maximum load fracture).
6. The microhardness profiles of the fusion zone and HAZ is the lower than the base metal for all cases where were completely removed all previous work hardening.
7. By examining macrographs of the welds, there are recrystallized small equiaxial grains and insoluble particles of $FeAl_3$ in the nugget and a narrow zone of columnar grains in the edge of it and this zone is interfacial with the HAZ, which are formed of dendritic grains.
8. SEM and EDS examinations confirm the presence of dissolving/alloying of the copper

(electrode material) with aluminum (base sheet metal) in each other in as-received sheet more than the pretreatment sheet. Therefore, it is leading to degradation of the electrodes rapidly due to the pitting on the surface of the electrodes.
9. Numerical simulation with SORPAS® has given good results in predicted process parameters and the nugget size when they compared with experiments.

REFRENCES

Brown, D. J., Newton, C. J., and Boomer, D. Optimization and Validation of a Model to Predict the Spot Weldability Parameter lobes for Aluminum Automotive Body Sheet. Advanced Technologies & Processes, IBEC, pp. 100-106, 1995.

Browne, D. J., Chandler, H. W., Evans, J. T., and Wen, J. Computer Simulation of Resistance Spot Welding in aluminum, part one, Welding Journal 74(10), pp. 339-344, 1995.

Browne, D. J., Chandler, H. W., Evans, J. T., James, P. S., Wen, J., and Newton, C. J. Computer Simulation of Resistance Spot Welding in aluminum, part two, Welding Journal 74(12), pp. 417-422, 1995.

Chao, Y. J. Ultimate Strength and Failure Mechanism of RSW Subjected to Tensile, Shear, and combined tensile/Shear Loads. ASME journal of Engineering Materials and Technology, Vol. 125, 125-13, 2003.

Cho, W., Li, and Hu, Design of Experiment Analysis and Weld Lobe Estimation for Aluminum Resistance Spot Welding. Supplement to the Welding Journal, sponsored by the American

Welding Society and the Welding Research Council, 2006.

Crinon, E., Evans, J. T., The Effect of Surface Roughness, Oxide Film Thickness and Interfacial Sliding on the Electrical Contact Resistance of Aluminum. Material Science and Engineering Journal, A242, pp. 121-128, 1998.

Dzekster, N. N., and Ismailov, V. V. Some methods for Improving Aluminum Contacts. Proceeding of 36th Annual Holm conference on Electrical Contacts, Illinois Institute of Technology, Chicago III. pp. 518-520, 1990.

Hayat, F. The Effects of the Welding Current on Heat input, Nugget Geometry, and the Mechanical and fractural Properties of Resistance Spot Welding on Mg/Al Dissimilar Materials. Materials and Design, 32, 2476-2484, 2011.

Kim, D. C., Park, H. J., Hwang, I. S., Kang, M. J., RSW of Aluminum alloy sheet 5J32 Using SCR type and Inverter Type Power Supplies. International Scientific Journal, Vol. 38, Issue 1, Pages 55-60, 2009.

Ma, C., Chen, D. L., Bhole, S. D., Boudreau, G., Lee, A., Biro, E. Microstructure and Fracture Characteristics of Spot-Welded DP600 Steel. Materials Science and Engineering, 485, 334-346, 2008.

Mathers, G. The Welding of Aluminum and its alloys. Book published by Woodhead Publishing Limited, Cambridge CB1 6AH, England, 2002.

Newton, C. J., Browne, D. J., Thornton, M. C., Boober, D. R., and Keay, B. F. The Fundamental of Resistance Spot Welding Aluminum. Sheet Metal Conference VI, Paper E2, 1994.

Patrick, E. P., Auhl, J. R., and Sun, T. S. Understanding the Process Mechanism is Key to Reliable Resistance Spot Welding Aluminum Auto Body Components. SAE Technical Paper 840291, 1984.

Pederson, K. R. Resistance Welding of Aluminum Alloys. MSc. thesis, DTU, Department of Mechanical Engineering, Denmark, 2010.

Pouranvari, M. Prediction of Failure Mode in AISI 304 Resistance Spot Welds. Association of Metallurgical Engineers of Serbia, AMES, UDC: 621.791.763, PP. 23-29, 2010.

Rashid, M. Some Tribological Influences on the Electrode-Worksheet Interface during Resistance Spot Welding of Aluminum Alloys. Journal of Materials Engineering and Performance, Vol. 20(3), pp. 456-462, 2011.

RWMA, Resistance Welding Process. Resistance Welding Manuals, printed by George H. Buchman, Bridgeport, Nj USA, 2003.

Rønhult, T., Rilby, U., and Olefjord, I. The Surface State and Weldability of Aluminum Alloys. Material Science and Engineering, 42, pp. 329-336, 1980.

Senkara, J., Zhang, H., and Hu, S. J., Expulsion Prediction in Resistance Spot Welding. Welding Research, Welding Journal, pp. 123-132, 2004.

Song, Q., Zhang, W., and Bay, N. An Experimental Study Determines the Electrical Contact Resistance in Resistance Welding. Sponsored by AWS and WRC, Welding Journal, pp. 73-76, 2005.

Studer, F. J. Contact Resistance in Spot Welding. Welding Journal, Vol.18, Iss. 10, pp. 374-380, 1939.

Sun, T. S. Electrode Deterioration Mechanisms in Resistance Spot Welding of Aluminum. Aloa Internal Report No. 53-82-3, 1982.

SWANTEC Software and Engineering ApS. SORPAS®, Version 10.6, www.swantec.com.

Wheeler, M. J., Sheasby, P. G., and Kewley, D. Aluminum Structured Vehicle Technology. A comprehensive approach to vehicle design and manufacturing aluminum, SAE, Technical Paper 870146, 1987.

Williams, N. T. Suggested topics for Future Research in Resistance Welding. Welding in the World 22 (1/2), pp. 28-34, 1984.

ABBREVIATIONS

AA   : Aluminum Alloy
EDS   : Energy Dispersive Spectroscopy
HAZ   : Heat Affected Zone
HV   : Hardness Vickers
LOM   : Light Optical Microscope
Ra   : Arithmetic Mean Value of Roughness
rpm   : Revolution Per Minute
RSW   : Resistance Spot Welding
RWMA: Resistance Welder Manufacturers'
          Alliance
std   : Standard Deviation
SE   : Secondary Electron
SEI   : Scanning Electron Images

SEM   : Scanning Electron Microscope
SORPAS   : Simulation and Optimization of
          Resistance Projection and Spot Welding
SWANTEC   : Scientific Welding and Numerical
          Technology
WSS   : Weld Schedule Specifications
wt-%   : Weight Percentage

Table 1 Resistance spot welders Specifications

Specifications	Values	Specifications	Values
Controller	TE-180, 16 Functions	Max. welding Power	810 kVA
Supply Voltage	380 V	Nominal power at 50%	250 kVA
Frequency	50 Hz	Phases	1
Max. welding current	68 kA	Supply pressure	6.5 bar
Max. welding force	18.85 kN	Electrode force per 1 bar	3.14 kN
Throat depth	250 mm	Net weight	1000 kg
Water cooling	12 ℓ / min		

Table 2 Strip material specifications

Trade name	Thickness (mm)	Tensile (MPa)	Hardness (HV)	Nominal composition (wt-%)				
				Fe	Si	Mn	Others	Al
AA1050	0.6	105	30	0.255	0.173	0.021	0.051	99.5
AA1050	1.0	105	30	0.378	0.100	0.018	0.004	99.5
AA1050	1.5	127	45	0.350	0.070	0.010	0.070	99.5

Table 3 Experiments setup (factors and their associated values)

Sheet (mm)	Welding Energy input					
	Low		Medium		High	
	Cycles	Current (kA)	Cycles	Current (kA)	Cycles	Current (kA)
0.6	2	20	5	23	9	26
1.0	2	23	5	26	9	29
1.5	2	26	5	29	9	32
Electrode Force 1.85-2.45 kN						

Table 4 Surface roughness values

Sheet (mm)	As-Received		Pickling in NaOH		Glass-Blast	
	R_a (µm)	std.	R_a (µm)	std.	R_a (µm)	std.
0.6	o.287	0.046	0.339	0.011	2.650	0.115
1.0	0.300	0.051	0.385	0.037	4.703	0.987
1.5	0.238	0.039	0.411	0.028	3.230	0.453

Table 5 WSS of weld planning optimization SORPAS®

Sheet	As-Received (mm)			Pretreatment (mm)		
	0.6	**1.0**	**1.5**	**0.6**	**1.0**	**1.5**
Welding Current (kA)	23.9	26.27	31.64	22.87	24.58	27.26
Welding Time (cycles)	2	4	5	2	4	4
Electrode Force (kN)	1.16	1.44	1.78	1.04	1.44	1.49
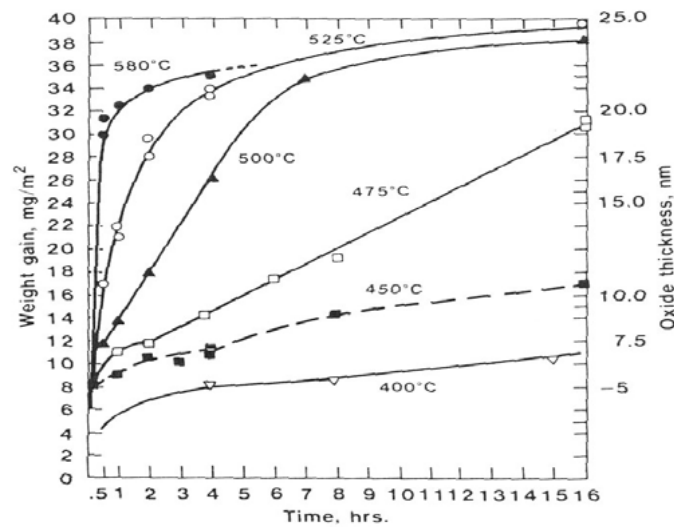
Fig. 1 Growth of oxide film for different temperatures [Pederson, 2010]

Processing option : All elements analysed (Normalised)				
Spectrum	In stats.	O	Al	Total
1	Yes	3.6	96.4	100.0
2	Yes	4.6	95.4	100.0
3	Yes	2.9	97.1	100.0
Mean		3.7	96.3	100.0
Std. deviation		0.8	0.8	
Max.		4.6	97.1	
Min.		2.9	95.4	

All results in weight%
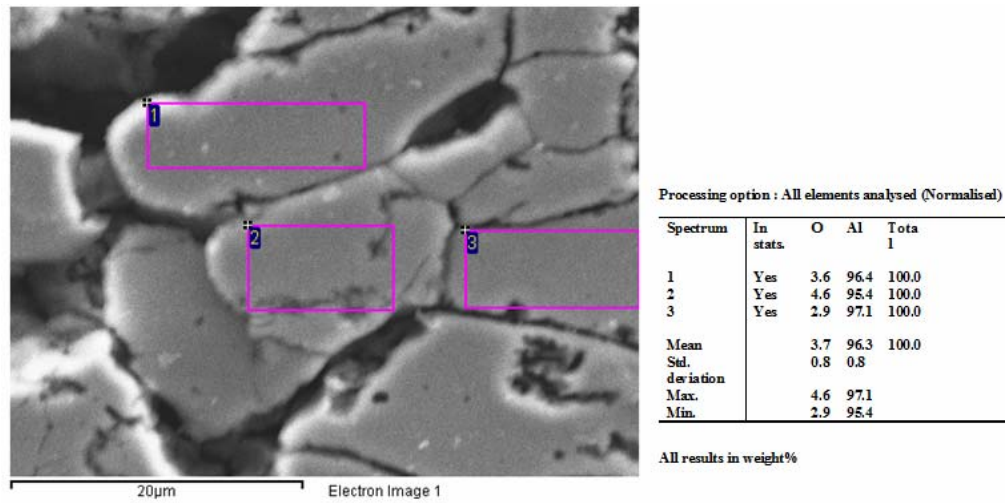
Fig. 2 SEM image and EDS analyzer for as-received spot-welded

(a)   **(b)**
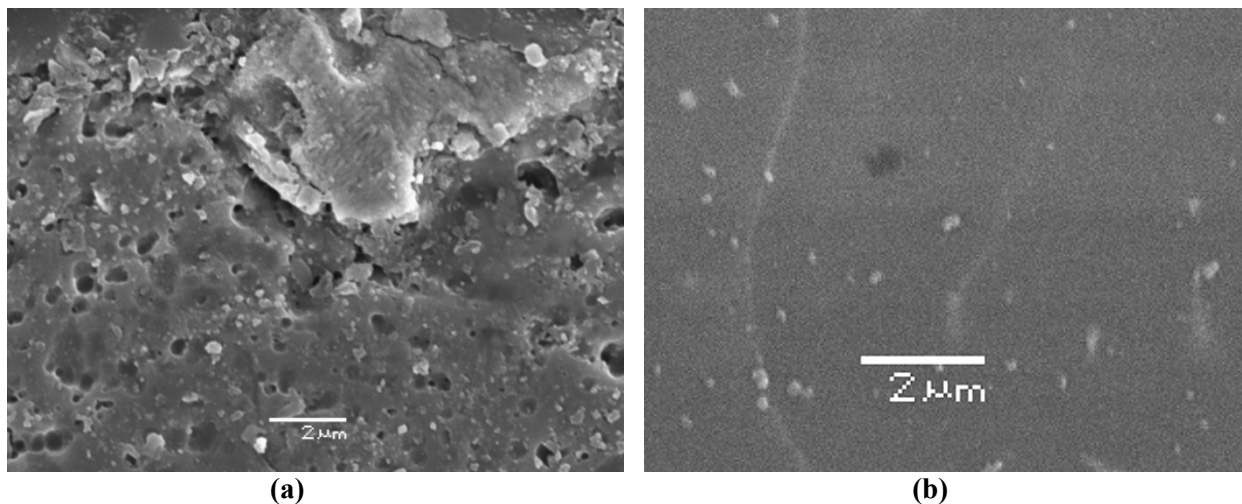
Fig. 3 SEM images the sheets exposure to NaOH solution agent; **(a)** 1.0 mm within 5 minutes, **(b)** 1.5 mm sheet within 2 minutes
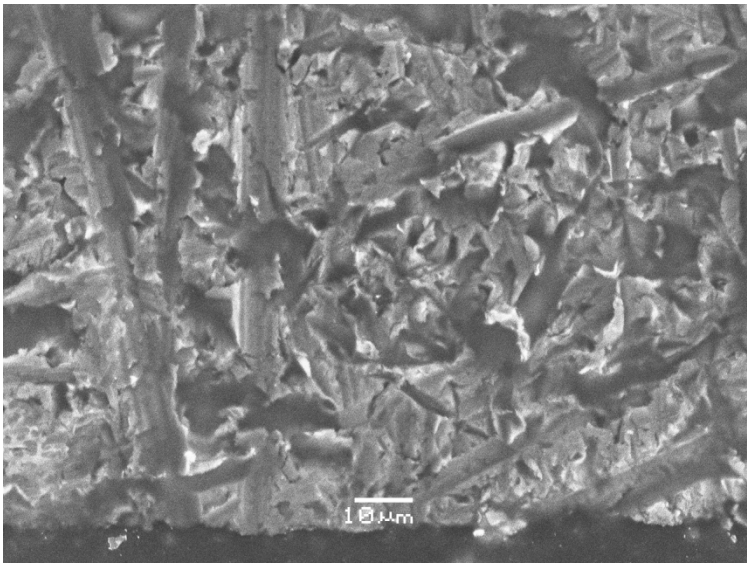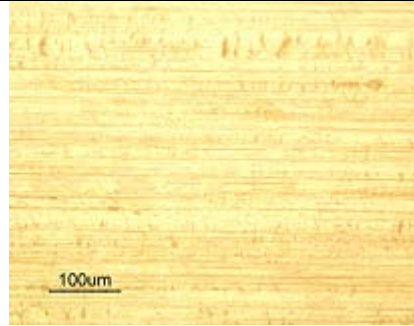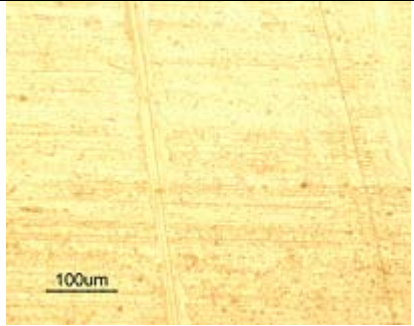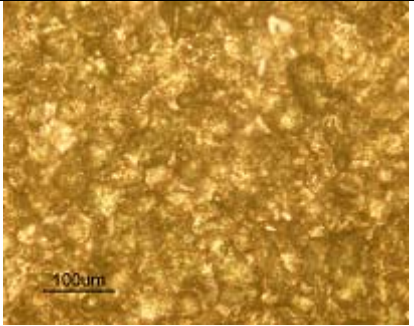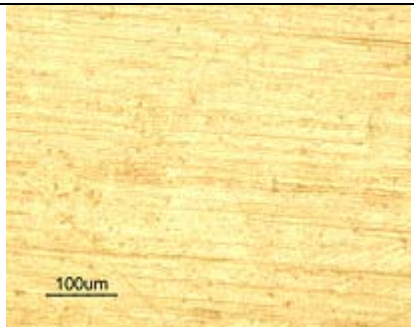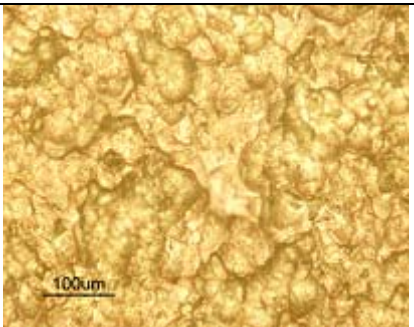
Fig. 4 SEM image RSW 1.0 mm glass blast sheet 29 kA, 5 cycles

Sheet	As-Received	Pickling in NaOH	Glass-Blast
0.6 (mm)			
1.0 (mm)			
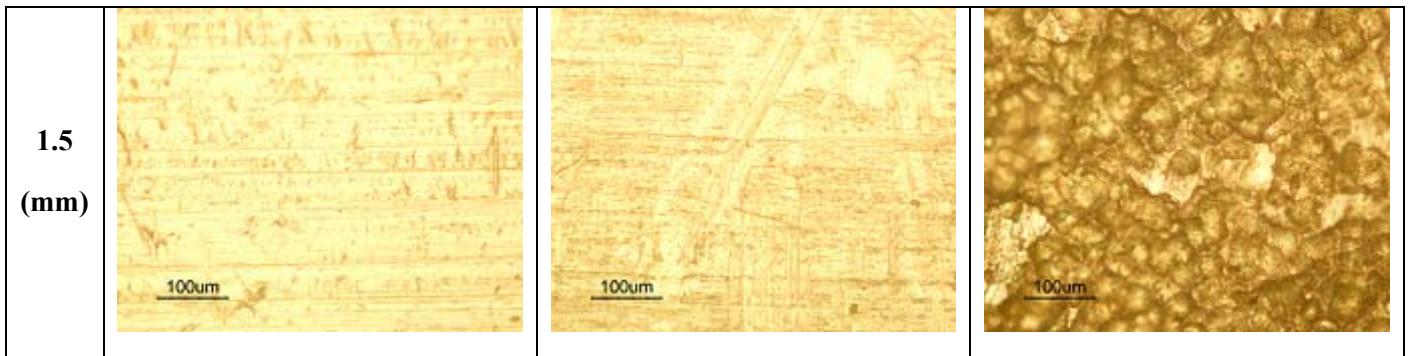
| 1.5 (mm) | | | |

Fig. 5 LOM images, surface roughness of various type strips 200x
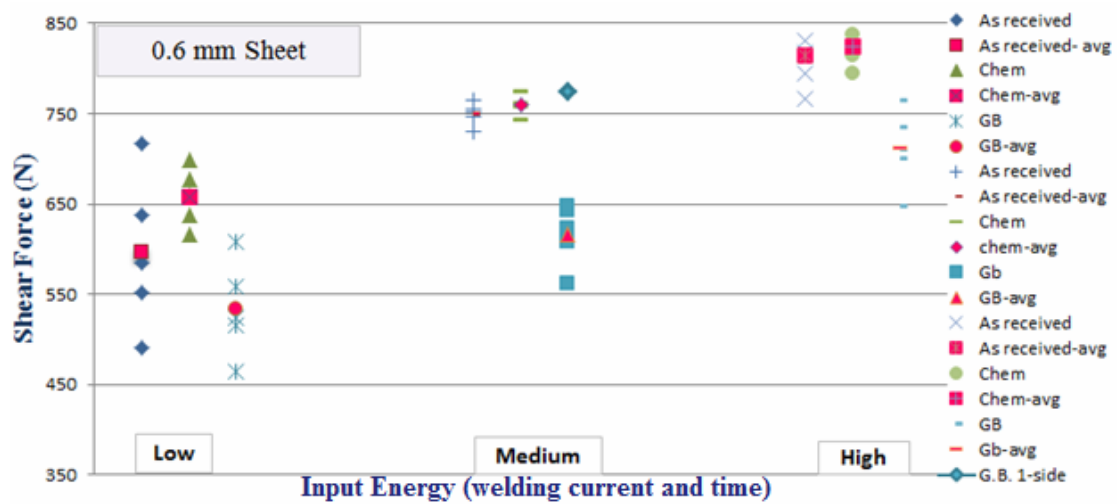
(**a**) 0.6 mm sheet
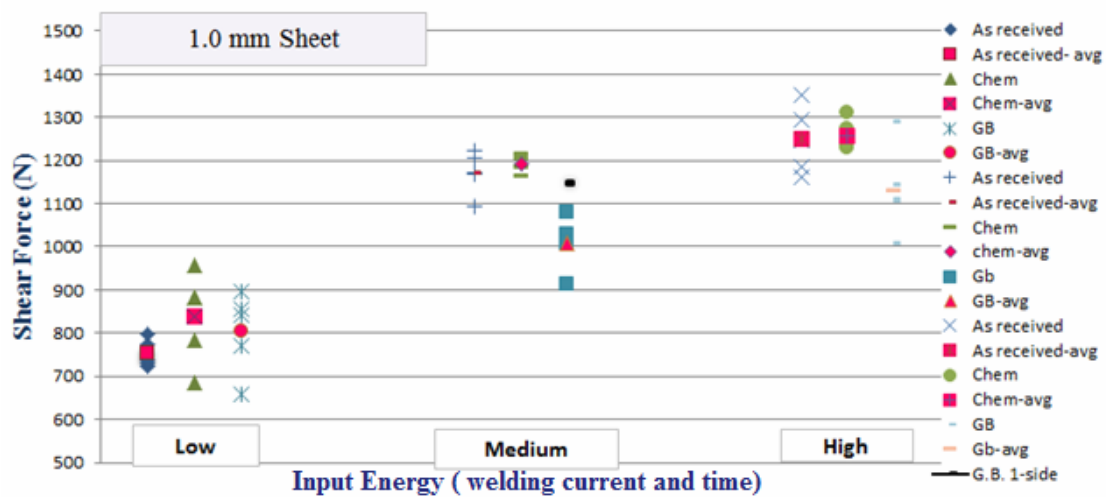
(**b**) 1.0 mm sheet
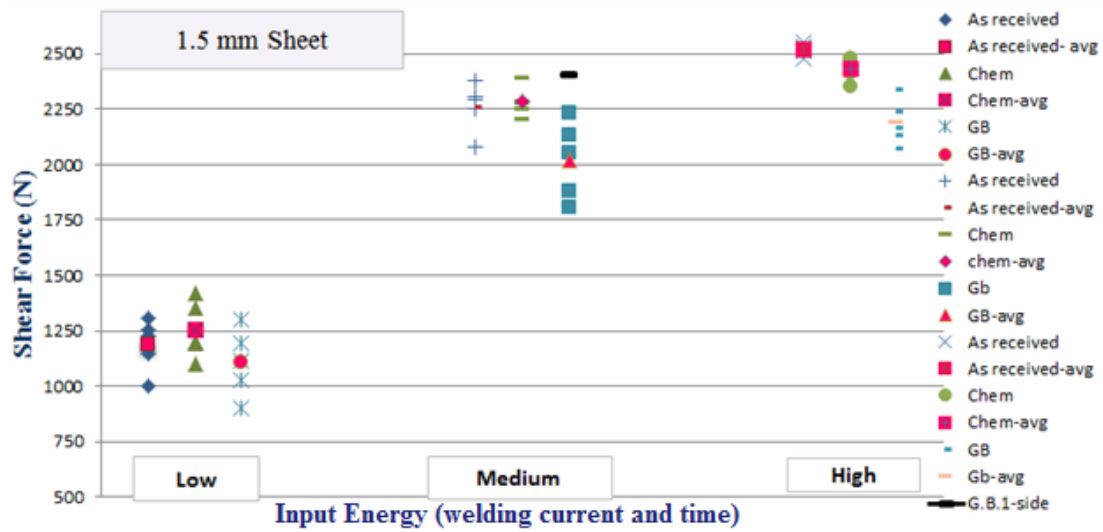
(**c**) 1.5 mm sheet

Key; avg: average, Chem: Chemical (Pickling in NaOH), GB: Glass blast

Fig. 6 Maximum fracture load versus the welding input energy in the tensile-shear tests
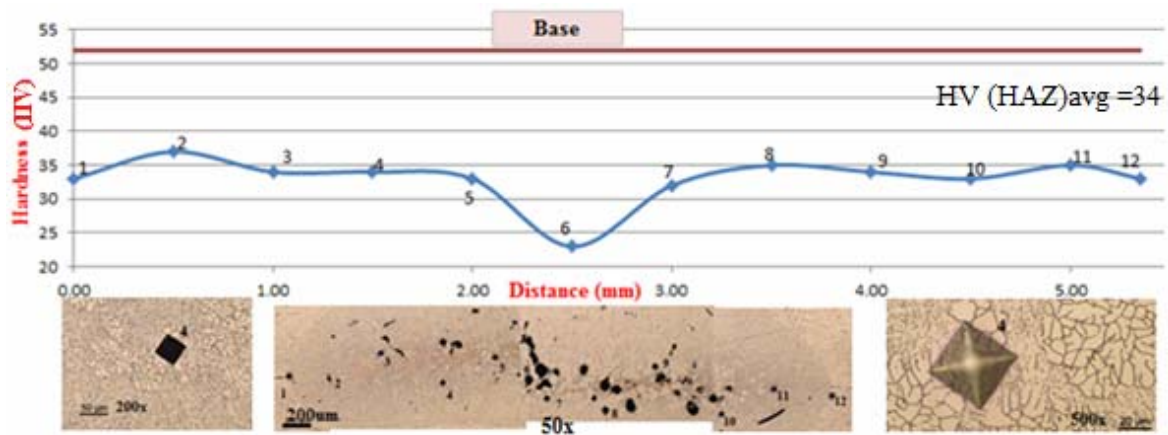
(**a**) Glass-blasted pretreatment surfaces
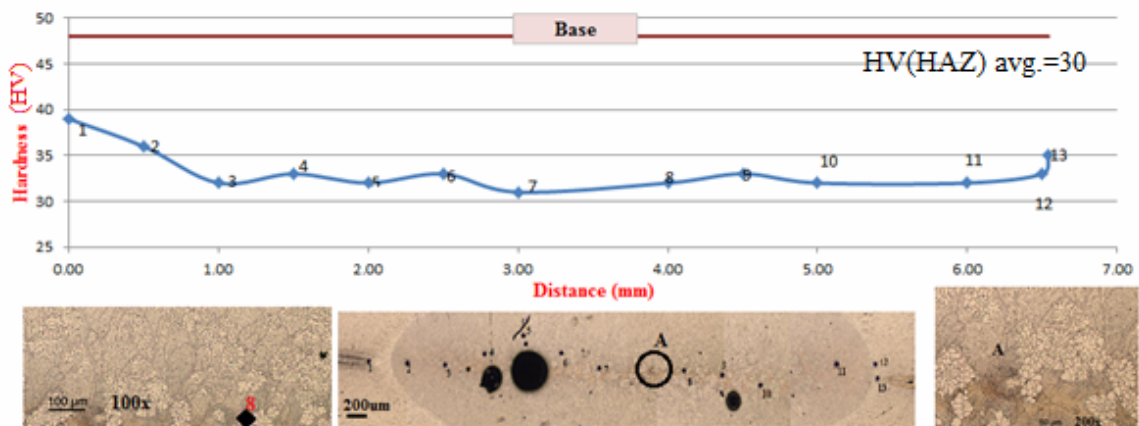
(**b**) Pickling in NaOH pretreatment surfaces
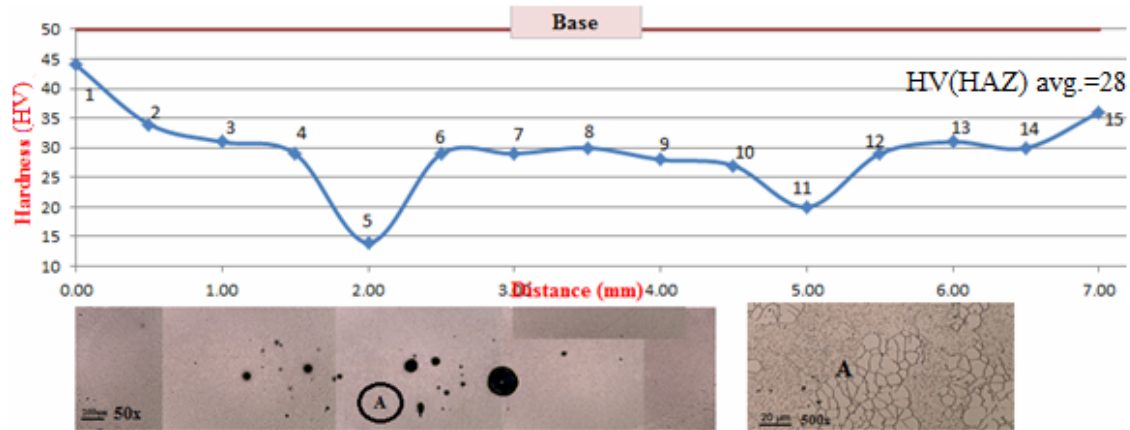
(**c**) As-Received sheet
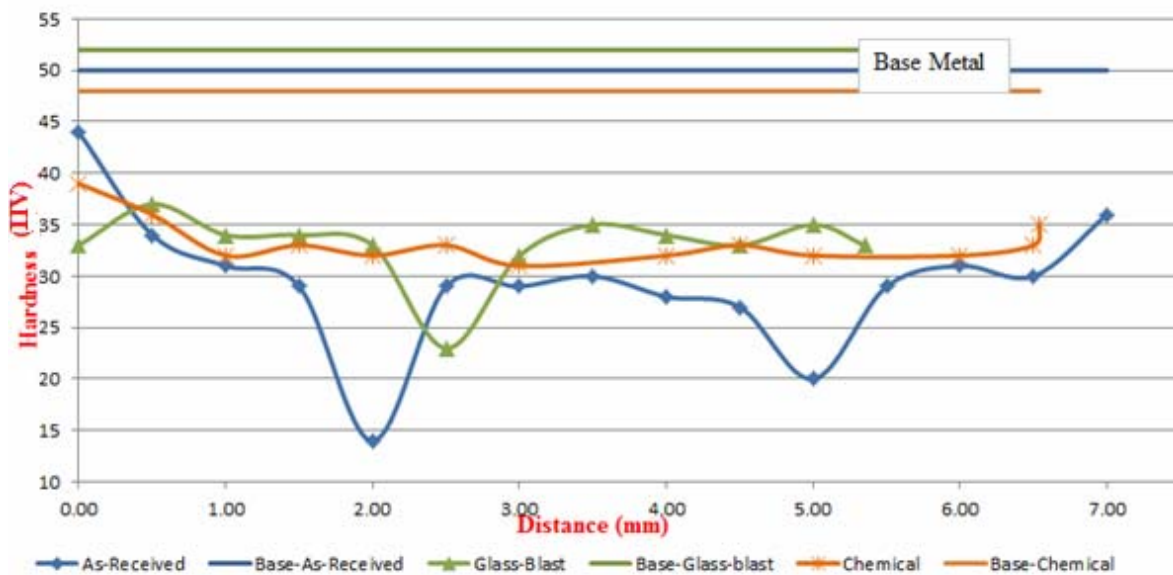
(**d**) All conditions sheets

Fig. 7 Microhardness profiles of 1.5 mm sheet, welding parameters (32 kA, 5 cycles)

233
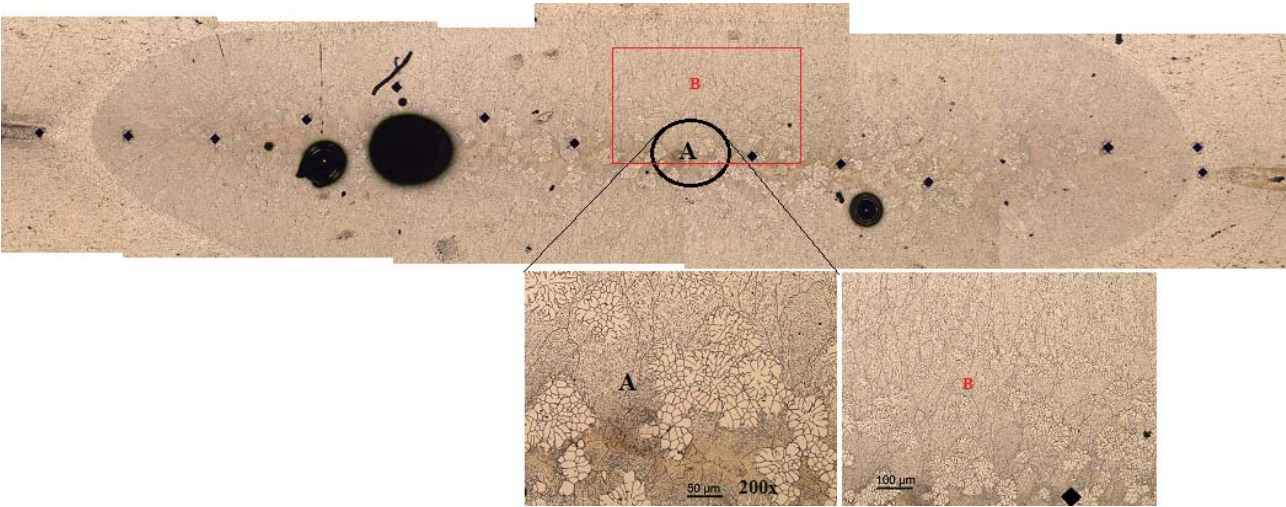
Fig. 8 Macro-Micrographs of RSW of 1.5 mm sheet, welding parameters (32 kA, 5 cycles)
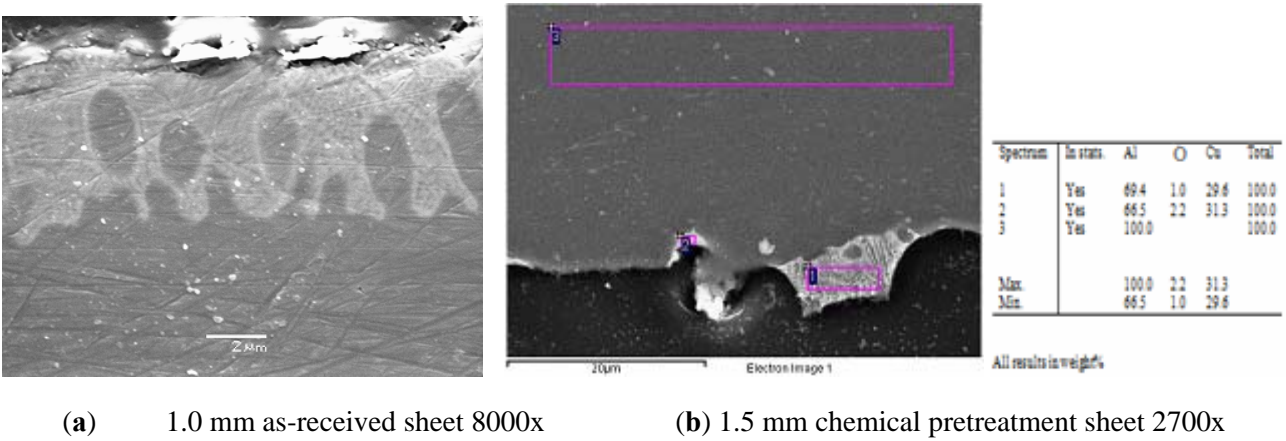
(**a**) 1.0 mm as-received sheet 8000x   (**b**) 1.5 mm chemical pretreatment sheet 2700x

Fig. 9 SEM images RSW
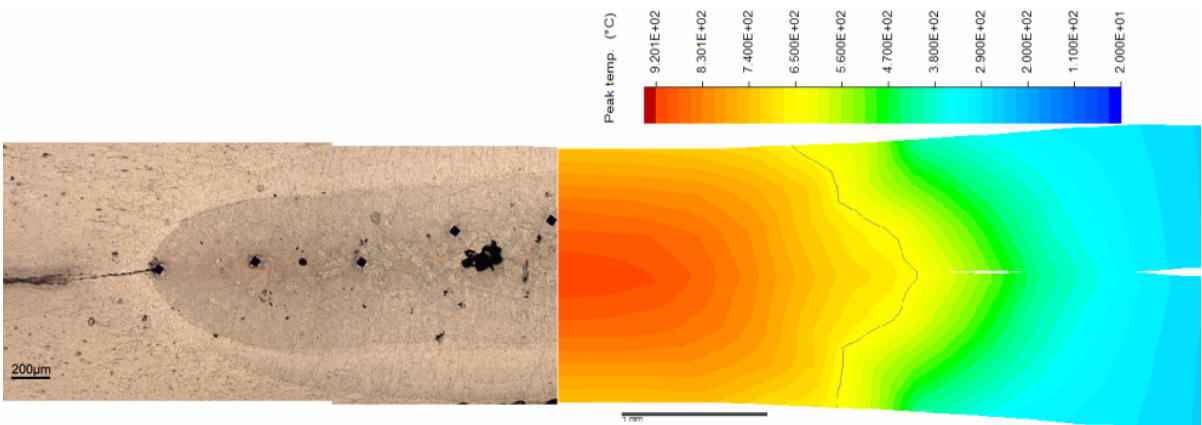
Fig 10 Comparison between SORPAS® simulation and a metallographic experimental result

Parallel Routing in Wireless Sensor Network

Prof.Dr.Kais Al Sabbagh

Computer Engineering Department

Engineering College, Baghdad University

Kais_1946@yahoo.com

Dr. Zainab Tawfeeq Baqer

Electrical Engineering Department

Engineering College, Baghdad University

zainab_alisa@yahoo.com

ABSTRACT

The limitations of wireless sensor nodes are power, computational capabilities, and memory. This paper suggests a method to reduce the power consumption by a sensor node .This work is based on the analogy of the routing problem to distribute an electrical field in a physical media with a given density of charges. From this analogy a set of partial differential equations (Poisson's equation) is obtained. A finite difference method is utilized to solve this set numerically. Then a parallel implementation is presented. The parallel implementation is based on domain decomposition, where the original calculation domain is decomposed into several blocks, each of which given to a processing element. All nodes then execute computations in parallel, each node on its associated sub-domain. With this method power consumption by the central node which is responsible to compute routing in the network is reduced.

Keywords- sensor network; electrostatic theory; finite difference method; successive over relaxation; domain decomposition;

التوجيه المتوازي للشبكات التحسس اللاسلكية

.

.

.

. (Poisson   )   .

.

.

.   .

:

INTRODUCTION

A wireless sensor network (WSN) is a wireless network consisting of spatially distributed autonomous devices (several hundred to several thousand devices) that use sensors to monitor physical or environmental conditions. These autonomous devices, or nodes, combine with routers and a gateway to create a typical WSN system. The distributed measurement nodes communicate wirelessly to a central gateway, which provides a connection to the wired world where data measurement can be collected, processed, analyzed, and presented. To extend distance and reliability in a wireless sensor network, routers can be used to gain an additional communication link between end nodes and the gateway. The primary areas in which these networks are environmental observations, military monitoring, building monitoring and health care [Vijay 2007].

In many applications the sensors perform measurements of specific metrics such as temperature, pressure, movements or other physical values, and it is desired to collect the data of sensors in a specific station for processing, archiving and other purposes. This station is a data sink, and it has enough processing power, storage space, and capability of communicating with the sensors. For the purpose of communication to the sink, the sensors relay the packets of each other in a multi-hop way.

A novel approach for the routing problem in wireless ad hoc networks was introduced [Kalantari 2004]. This approach is based on the analogy of the routing problem to the distribution of electric field in a physical media with a given density of charges. Then this approach is used in wireless sensor network [Kalantari 2006]. The mathematical model is explained in the following section briefly with some assumptions and consideration. Mathematical details formulation is given by Kalantari [2006] . The work presented in this paper is based on this approach. A Poisson's equations are obtained from this approach. These equations are solved numerically using the finite difference method. This method is parallelized. Because the energy is very important, partitioning the computations between more than one node in the sensor network will achieve better performance. One node needs more time for calculations and distributions the results to the other nodes. So, to reduce this time more nodes are utilized.

MATHMATICAL MODEL

Consider a network with N wireless nodes that can communicate with each other through radio links. The

nodes are randomly placed in a region A in the plane. Assume there are M source-destination pairs, denoted $s_1 ... s_M$. Source-destination pair s_i has a bandwidth demand which we refer to as its *weight* and denote by W_i. Suppose that one or more paths in the plane are chosen for each s_i. Each path starts at the source node and ends at the destination node of s_i. The weight W_i is partitioned into amounts that are assigned to the paths. The weight assigned to a particular path indicates the amount of demand that is desired to follow that path. It should be noted that the chosen paths are not constrained by the location of intermediate nodes. Instead, the paths are 'abstract' paths in the plane that represent desired paths for the transit of packets. For communication to occur, each abstract path must be approximated by an actual path consisting of a piecewise linear multihop path connecting the source and destination through a sequence of intermediate nodes. Given a set of weighted (abstract) paths for each source-destination pair, define a vector field on A which refers to as the *load density* vector field and denote by $\vec{D}$. $\vec{D}$ represents the flux density of the weighted paths for the source-destination pairs. Given a

point $(x, y) \in A$, a small area element at (x, y) is

chosen. For each path that intersects S, we take the tangent vector to the path and scale it so it has magnitude equal to the weight of the path. Adding up these scaled tangent vectors, dividing by the area of S, and letting the area element go to zero gives the value of $\vec{D}$ at (x, y). A problem with this definition is that since there are only finitely many source-destination pairs, and hence

only finitely many paths $\vec{D}$ will be 0 except on a set of measure zero.

For optimal $\vec{D}^*$ a set of partial equations can be written

$$\vec{\nabla}.\vec{D}^* = \rho \qquad \vec{\nabla} \times \vec{D}^* = 0 \qquad (1)$$

ρ represents the density of sources in the network and $\vec{\nabla}$ is defined as:

$$\vec{\nabla} = \frac{\partial}{\partial x}\hat{i} + \frac{\partial}{\partial y}\hat{j} \qquad (2)$$

The above equations are similar to Maxwell's equations in the electrostatic theory. It is proved that the vector field D can be expressed as the gradient of a scalar field. In other wards:

$$\vec{D} = \vec{\nabla} U \qquad (3)$$

in which U is a scalar function known as the potential function. Then the set of equations defined by (1) reduces to:

$$\nabla^2 U = \rho \qquad (4)$$

in which the operator ∇^2 is defined as:

$$\nabla^2 = \frac{\partial^2}{\partial x^2} + \frac{\partial^2}{\partial y^2} \qquad (5)$$

The partial differential equation defined by (4) is known as the Poisson equation. The potential function gives a rough idea of how much effort by the network is needed to send data from a source to the destination. This effort is proportional to the potential difference of the source and the destination. In addition, the potential function gives insight into the routing. Based on (3), the routing is done in the direction of the gradient of the potential function.

FINITE DIFFERENCE METHOD

The finite differenc method is a numerical analysis technique for obtaining approximate solutions to a wide variety of engineering problems. In many engineering problems, it is difficult to find the analytical solution. So several approximate numerical analysis methods have evolved over the years such as the finite difference method which is a powerful and a versatile numerical technique for handling problems involving complex solution regions. It involves three steps:

(1) Dividing the solution region into a grid of nodes (Fig.1).
(2) Approximating the given differential equation by finite difference equivalent that relates the dependent variable at a point in the solution region to its values at the neighboring points.
(3) Solving the difference equations subject to the prescribed boundary conditions and/or initial conditions.

More information on finite difference method can be found in [Sadiku 2001]. As explained in section II, it is desired to solve the following equation:

$$\nabla^2 U = \frac{\partial^2 U}{\partial x^2} + \frac{\partial^2 U}{\partial y^2} = \rho \qquad (6)$$

The function U(x,y) in a 2-D domain, x in [0,1] and y in [0,1] is solved. The boundary conditions (U (0, y), U (1, y), U(x, 0), and U(x, 1)) are given. In addition, the function U(x,y) can also be specified on specific points in the interior domain. The source ρ (x,y) is taken to be a simple Gaussian in what follows for simplicity.

The domain is discretized on a 2-D numerical lattice, with $x_i = i*h$, $y_j = j*h$ and $h = \frac{1}{N}$.

N is the number of grid points in both directions and h is the mesh size. In this work different size of grids is utilized. The Poisson equation is re-written in finite difference form (five stencil form):

$$\frac{1}{h^2} = (U_{i+1,j} + U_{i-1,j} + U_{i,j+1} + U_{i,j-1} - 4*U_{i,j}) = \rho_{i,j}$$

$$(7)$$

$U_{i,j}$ is the value of U at node (i,j) in the mesh for Poisson's equation (**Fig.1**).

This leads to a large set of linear equations to solve for the field values $U_{i,j}$ on the grid within the domain, keeping $U_{i,j}$ fixed at the boundary. This set of equations can be solved by an iterative method, whereby

$$U_{i,j}^{k+1} = \frac{1}{4}(U_{i+1,j}^k + U_{i-1,j}^k + U_{i,j+1}^k + U_{i,j-1}^k - h^2\rho_{i,j})$$

$$(8)$$

is iterated until the changes in $U_{i,j}$ become less than some predefined tolerance criteria. An arbitrary guess for $U_{i,j}$ is assumed to start with. We choose $U^0_{i,j} = 0$, or can be the average of U at the fixed node. The old and new values of $U_{i,j}$ are mixed to accelerate the convergence, leading to the "Successive Over Relaxation" scheme [Azali 2009]. It may define residual $R_{i,j}$ as:

$$R_{i,j}^k = (U_{i+1,j}^k + U_{i-1,j}^k + U_{i,j+1}^k + U_{i,j-1}^k - 4U_{i,j}^k - h^2\rho_{i,j})$$

$$(9)$$

$$U_{i,j}^{k+1} = U_{i,j}^k + \frac{w}{4}R_{i,j}^k \qquad (10)$$

The relaxation factor *w* is selected such that $1 < w < 2$. The choice of a proper value of *w* is problem dependent and is often determined by trial and error. In this paper, *w*=1.5.

The value of the potential function U at each node in the mesh is computed as shown in **Fig.2**. Let us assume that the source of packets in the middle of the network ($node_{60,60}$) and it (source) want to broadcast its packets (assuming all the other nodes destinations). The number of nodes in the network=14400 (120x120). In this simulation, the time is recorded for different number of nodes as shown in **Fig.3** with different values of tolerance. As shown, the time is

increased when the number of nodes in the network is increased. More accurate results are obtained due to the increases of nodes. Of course increasing the number of nodes gives an accurate results but the time increases. Requiring more time in wireless sensor network make the sensor nodes consume more power. So in this work the original domain is divided into sub-domains in order to distribute the computation between nodes as described in the following section.

PARALLELIZATION STRATEGY

Parallelism in this system is to sub-divide the data structures into sub-domains and assign each sub-domain to one processor. In this case, the same code runs on all processors with its own set of data. By dividing the computational domain into four sub-domains as shown in **Fig.4**, it is possible to spread the workload between four different processors. However, it is important to note that, in order to compute the variables for each nodal point, the variables at its neighboring points are required. Thus, in order to calculate the variables at the points close to the interface between sub-domains, one processor will require information stored in the memory of a neighboring processor. This requires communication at regular intervals, which may slow down the computation. In general, the computation procedure involves three steps (1) partitioning of the solution domain; (2) performing computations on each processor to update its own data set; (3) communicating data between processors. This technique is called domain decomposition. The key for an efficient computation is to maintain the communications between processors to a minimum level, as well as, to divide the workload equally between processors.

In this work, domain decomposition coordinate bisection is used [Andreas 2010]. This method divides the number of points equally between processors, but makes no attempt to obtain a domain division that minimizes the communication between processors, i.e., a division with the smallest number of nodal points in boundaries between sub-domains. Therefore, coordinate bisection may produce sub-domains with long interfaces that will lead to a large

amount of communication. This can be partly overcome by recursive application of alternate x, y bisections. The grid is first divided into 2 grids using bisection of the x-length of the calculation domain. Then to each of the resulting domains, y bisection is applied, resulting in four blocks (or sub-domains).The procedure can be continued to obtain eight blocks, sixteen blocks, thirty two blocks, etc. Once a multi-block domain has been established, calculations on each block can begin in parallel if the boundary conditions of these blocks are known. This may be either a physical boundary condition or an internal boundary condition generated as a consequence of the domain decomposition. The physical boundary data of each block, if any, are provided by the user, while the internal boundary data must be received from neighboring blocks, which may reside on different processors. Internal boundary data are hold by buffers on the boundary of each block as shown in **Fig. 4**, which illustrates a calculation sub-domain and the buffer cells used to store the overlap data. Once the buffer data has been received from all sides of a block, the computation of this block can start, using the sequential algorithm. On completion of the solution for the block, the data at its boundaries is sent to the neighboring blocks. Calculation in this block then waits for the buffer update provided by this block's neighbors, after which the next computation cycle can start. The information exchange across sub-domains can be performed using the message passing interface standard, MPI (Message Passing Interface). The use of MPI ensures portability across different computing platforms.

If the communication time is ignored for this method, the time will be decreased with increasing the number of processing elements as shown in **Table 1**. If the suggested model is divided into two sub-domains the time will halved, and if the division into four sub-domains the time will be quarter its origin value and so on as shown in **Fig. 5**. This is true if the communication time is ignored. In fact, with increasing the number of processing elements, the time will be decreased to some threshold value then will be increased due to the overhead appended for communication between the processing elements.

In this work the task is divided into n equal subtasks, each of which can be executed by one processing element. If ts is the time to perform a task by a single processor, tm is the time taken by each processor.

$$tm = ts / n \tag{11}$$

$$\text{Speed up} = ts / tm = n \tag{12}$$

This is true when the communication overhead is ignored. With communication overhead:

$$tm = ts / n + tc \tag{13}$$

where tc is the communication time, So :

$$\text{Speed up} = ts / tm = ts / (ts / n + tc)$$

$$= n / (1 + n* tc / ts) \tag{14}$$

For each block or subtask, calculations can begin in parallel if the boundary conditions of these blocks are known. Boundary conditions are sent by the processor element using message passing interface functions. The potential $U_{i,j}$ is updated repeatedly (eq.(10)). In addition, to the potential, the residual is also updated repeatedly (eq.(9)). To compute the potential at node i,j, the potential from the neighboring nodes are needed to be transferred. As an example, to compute potential at node i,j at *k+1* step :

send $U_{i,j}^{k}$ to all neighbors

             (using MPI_Send function)

receive $U_{i+1,j}^{k}, U_{i-1,j}^{k}, U_{i,j+1}^{k}, U_{i,j-1}^{k}$ from neighbors

(using MPI_Rec function)

Compute $R_{i,j}$ using eq.(9)

Compute $U_{i,j}^{k+1}$ using eq.(10)

As shown from the above computations, for each potential updated at a boundary node, an additional time is added to the computation delay. This time is increased with increasing the number of blocks (processor element), increasing tolerant and increasing the number of nodes in the domain. So the division of the data domain into sub blocks is limited by the communication time.

Prof.Dr.Kais Al Sabbagh
Dr. Zainab Tawfeeq Baqer

CONCLUSIONS

Wireless sensor network have many limitations. One of these important limitations is the power consumption. This work suggested a method to reduce this power. This work is based on the analogy of the routing problem to the distribution of electrical field in a physical media with a given density of charges. From this analogy a set of partial differential equation is obtained. A finite difference method is utilized to solve this set numerically. Then, a parallel implementation is presented. The parallel implementation is based on domain decomposition, where the original calculation domain is decomposed into several blocks, each of which is given to a processing element. All nodes then execute computations in parallel, each node on its associated sub-domain. The time to compute routing in the network is reduced with increasing the number of the nodes (communication time is ignored). Of course the power consumption will decrease when the time is decreased.

REFRENCES

Andreas Adelmann1, Peter Arbenz, and Yves Ineichen1;"Improvements of a Fast Parallel Poisson Solver on Irregular Domains ".July 2010.

Azali Saudi1 and Jumat Sulaiman"Path Planning for Mobile Robot with Half-Sweep Successive Over Relaxation Iterative Method".Symposium on Progress in Information & Communication Technology 2009.

Mathew N.O Sadiku,"Numarical Techniques in Electromagnatics", second eddition, 2001.

M. Kalantari and M. Shayman, "Routing in Multi-Commodity Sensor Networks Based on Partial Differential Equations" IEEE ,2006, pp.402-406.

M. Kalantari and M. Shayman, "Routing in Wireless Ad Hoc Networks by Analogy to Electrostatic Theory" IEEE, 2004,pp. 4028-4033.

Vijay K. Garg "Wireless Communictions and Networking"© 2007 by Elsevier.

http://www.mhpcc.edu/training/workshop/mpi/Main.html parallel Programming Workshop_ Message Passing Interface.
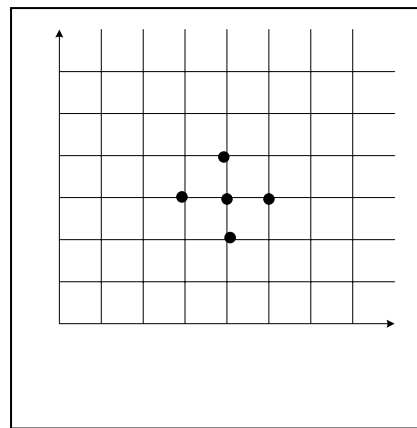
Figure 1 Finite difference mesh for two independent variables X and Y
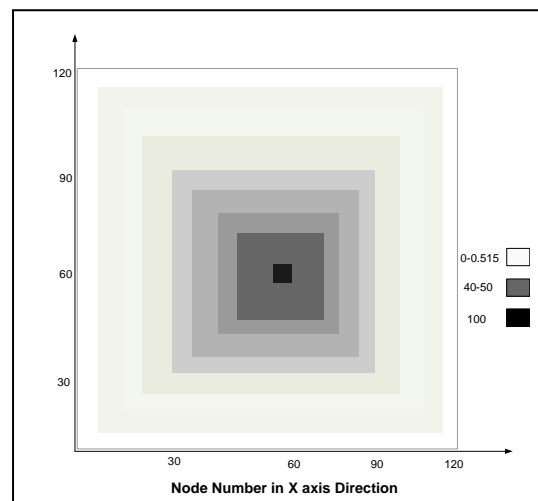
Figure.2 The value of the potential function *U*
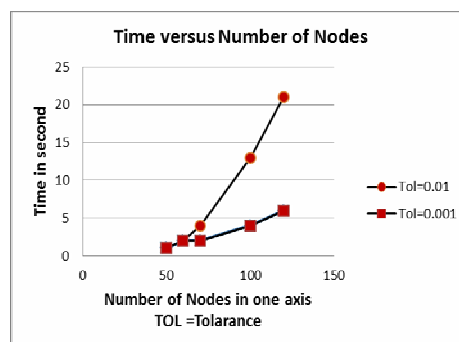
Figure 3 Execution time obtained with different mesh size and different tolerance.

Y

I,j+1

I-1,j

mber in Y axis Direction
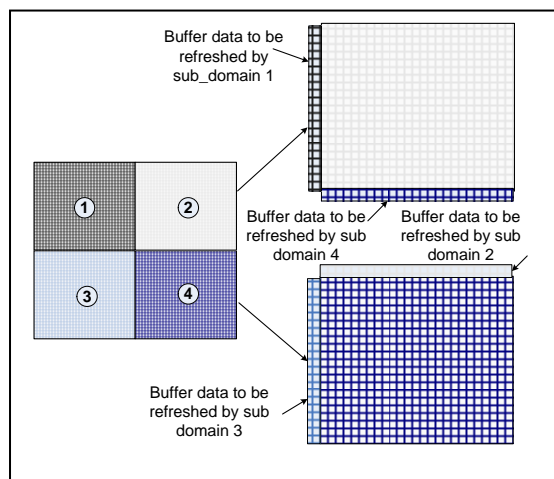
Figure 4 Schematic representation of a calculation sub-domain divided into four subdomains, indicating the buffer cells used to store the internal boundaries data
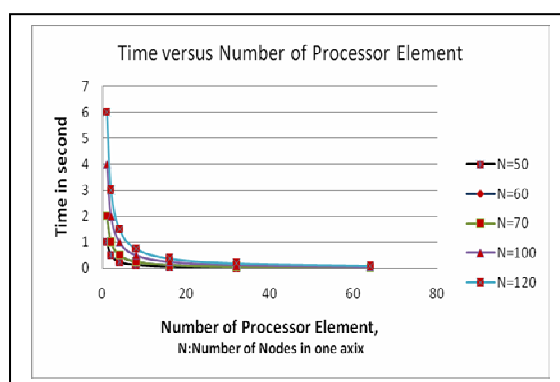
Figure 5.Execution time for different meshes size (50x50, 60x60, 70x70, 100x100, 120x120) with different number of processing element.

Table 1. Execution time for different meshes size (N number of nodes in one axis) with different number of processing element neglegting the communication time.

No of Processing elements	N=50	N=60	N=70	N-=100	N=120
1	1	2	2	4	6
2	0.5	1	1	2	3
4	0.24	0.5	0.5	1	1.5
8	0.12	0.25	0.25	0.5	0.75
16	0.06	0.125	0.125	0.25	0.375
32	0.03	0.0625	0.0625	0.125	0.1875
64	0.015	0.03125	0.03125	0.0625	0.09375

Statistical Model for Predicting the Optimum Gypsum Content in Concrete

Dr. Zena Kudair Abbas
Civil Engineering Department
Baghdad University
zka_abbas@yahoo.com

Prof. Dr. Riyadh S. Al-Rawi
Civil Engineering Department
Baghdad University

Dr. Ali H. Al-Neaime
Civil Engineering Department
Baghdad University

ABSTRACT

   The problem of internal sulfate attack in concrete is widespread in Iraq and neighboring countries. This is because of the high sulfate content usually present in sand and gravel used in it. In the present study the total effective sulfate in concrete was used to calculate the optimum SO_3 content. Regression models were developed based on linear regression analysis to predict the optimum SO_3 content usually referred as (O.G.C) in concrete.

The data is separated to 155 for the development of the models and 37 for checking the models. Eight models were built for 28-days age. Then a late age (greater than 28-days) model was developed based on the predicted optimum SO_3 content of 28-days and late age. Eight developed models were built for all ages. The important results obtained from the developed models are the positive effect of C_3S, C_3A and C_4AF on optimum SO_3 content. The effect of C_3A on optimum SO_3 content is about twice that of C_4AF. The study also showed a trend of positive and important effect of the fineness of cement except in some models and this is due to statistical overlap.

Key wards: Optimum SO_3 content (O.G.C), total effective SO_3 content, 28-day age model, late age model, all age model

<div dir="rtl">

نماذج أحصائية لتخمين نسبة الجبس المثلى في الخرسانة

أ.د. رياض شفيق الراوي   د. علي حسين النعيمي   د. زينة خضير العنبوري

الخلاصة

   مشكلة مهاجمة الكبريتات الداخلية في الخرسانة منتشرة في العراق و البلدان المجاورة. هذا يعزى الى النسبة العالية لاملاح الكبريتات الموجودة في الرمال و الحصى المستخدم فيها. دراستنا الحالية أستعملت القيمة الكلية المؤثرة(الفعالة) للكبريتات في الخرسانة و التي تستعمل لحساب النسبة المثلى للكبريتات. تم تطوير نماذج رياضية بأستعمال طرق تحليل الانحدار ، للتنبؤ بنسبة الكبريتات المثلى و التي تعرف ب (O.G.C). البيانات قسمت الى 155 تدخل في بناء النموذج و 37 لتدقيق النموذج. صممت (8) نماذج لعمر 28-يوم. ثم طور نموذج للاعمار المتأخرة (أكبر من 28-يوم) و المعتمد على القيمة المثلى المتوقعة للكبريتات من عمر 28-يوم و الاعمار المتأخرة الاخرى. تم تصميم (8) نماذج أخرى و لكل الاعمار.

وكان من أهم النتائج التي تم التوصل اليها التأثير الايجابي ل (C_3A،C_3S) و C_4AF) و كان تأثير (C_3A) حوالي ضعف تأثير (C_4AF). كما أظهرت الدراسة التأثير الايجابي و الفعال لنعومة السمنت على نسبة الكبريتات المثلى الا في بعض النماذج و هذا يعزى الى التداخلات الاحصائية.   :   28

.

الكلمات الرئيسية: النسبة المثلى للجبس ، النسبة الكلية الفعالة للاملاح ، الموديلات بعمر 28 يوم ، الموديلات بالاعمار المتأخرة ، الموديلات بكل الاعمار

</div>

Dr. Zena K. Abbas
Prof. Dr. Riyadh S. Al-Rawi
Dr. A.H. Al-Neaime

**Statistical Model for Predicting the
Optimum Gypsum Content in Concrete**

1. DETERMINATION OF THE STATISTICAL MODEL VARIABLES
1.1 Collecting Data

In order to build a regression predictive model, there should be sets of data that cover a wide range of variation of the independent variable. A survey was carried out to obtain the required data has been chosen to cover locally published literature from (1977 to 2002) as presented in Table 1.

1.2 The Independent Variables

The Followings are the selected data of the independent variables; the data were processed to obtain the information listed below and as presented in Table 2.
1. Total alkalis as equivalent Na_2O.
2. Main compounds of cement.
3. Cement surface area (Blaine fineness).

1.3 The Dependent Variables

The value of optimum SO_3 content has to be predicted from the relationship between compressive strength and different SO_3 content as detailed in the presented research items as shown in Table 3. The decision was based on the observed variation of SO_3 content with maximum compressive strength and the change of SO_3 content with age of the same mix.

1.4 Preliminary Statistical Analysis

The analysis focused on the calculation of the following measures of central tendency and dispersion of data and the number of data equal to 178.
1. Mean, median and mode (central tendency)
2. Minimum and maximum, range and standard deviation (dispersion).
The calculated measures of central tendency and dispersion are presented in Table 4.

1.5 Correlation Analysis

Two types of correlation coefficient obtained which were Person and Spearman [SPSS manual] between dependent and independent variables are presented in Table 5 and 6 respectively. First one is used for linear relationship while the second coefficient for non

User   Page 244   1/13/2013linear relationships. This is achieved by comparison between calculated (r_c) and the critical correlation coefficient (r_c) at a specified level of significance [Bland (1985)] and can be calculated using the equation given below.

$$r_c = \frac{t_{\alpha/2}}{\sqrt{t_{\alpha/2}^2 + n - 2}}$$

Where: r_c= the critical correlation coefficient α = the level of significance, t = the standard t variable, n = number of sample data pairs.

2. DEVELOPED REGRESSION MODELS FOR CONCRETE
2.1 28-days model

Developments of predictive models for concrete are made in two stages based on age of the product. The first stage focused on data for the age of (28- days) and the second stage for late ages higher than 28-days. First descriptive statistic analysis presented in Table 7. The calculated coefficient for Person and Spearman correlation are presented in Tables 8 and 9 respectively.

Comparison between the values in the two Tables (8) and (9) and indicates that there is a high correlation between the independent variables. From the partial correlation presented in Table 10, it could be concluded in general that the coefficients of correlation of the linear relationship are higher than the critical coefficient of correlation except for the relation with total alk. , C_4AF and fineness Blaine, which is lower than the critical value and it is higher than the nonlinear relationship so the multiple linear regression analysis is used for model development.

Eight models were built for 28-days age presented in Table 11 and the number of data is equal to 33 when ignoring Abdul-Latif ` data (1997-2001) and this means no missing value for total alkalies for model (1-A,2-A,3-A) and 42 when used for models (1-B,2-B,3-B,4 and 5). The missing values for total alkalies were replaced by the average value for all other data.

Table 12 presents the ANOVA, R^2, root mean square of error, Durbin-Watson and $\sum$residual$\times$predicted SO_3% for all models.
From Tables 11 and 12 the followings can be concluded:

1. The best statistical model is (1-A) since, it has the highest coefficient of determination, R^2 (0,992), lowest root mean square of error (0.3424) and the Durbin- Watson value within the accepted range of (1.5-2.5) although the T- value is not the best but it is still low despite that some independent variables not on the line of concrete technology.

2. For model 2-A, 2-B, the effect of L.O.I is removed because it is less effective in concrete, the following can be concluded:
   - Some independent variables not in the line of concrete technology.
   - High coefficient of determination, R^2 of (0,985 and 0.974), low root mean square of error (0.458 and 0.5816), and the Durbin- Watson is not within the ranges (1.36 and 0.952) and T-value is low value (-0.24 and 0.22).

3. For model 3-A and 3-B the effect of L.O.I and MgO are removed. The reason is that the collected data below the values mentioned in the ASTM specification (6%). Furthermore, examinations of the model suggest the following:
   - Some of the independent variables effect is not consistent with the current knowledge of concrete technology.
   - Low coefficient of determination R^2 of (0.954 and 0,952) in comparison with the other developed models. This is in addition to the high root mean square of error (0.7851 and 0.7753),and the Durbin-Watson statistic is not within the ranges(1.331 and 0.788) and T- value is low value (-0. 81 and 0.01).

4. For model 4 , The effect of total alkalies is removed in order to include Abdul- Latf's data (1997 -2001) , so the model become with no missing values

.From this model the following can be observed :
- High coefficient of determination R^2 of (0.987), low root mean square of error (0.417), and the Durbin- Watson is not in within the rang but it is closest to the rang and T- value is the lowest value (0. 01).

5. For model 5 in general the independent effect is consistent with the current knowledge of concrete technology, but the shortcoming is on the statistical concept, it has low coefficient of determination R^2 of (0.952) compared with other model, the low root mean square of error (0.7686), and the Durbin- Watson is not within the range (0.726) despite the low T- value (-0. 01).

From the presented as above analysis it can be concluded that it is so difficult to choose the best acceptable model which satisfies the conditions of concrete science and regression analysis. Therefore, the decision was selected of 1-A, 3-B and 4 for more examination.

Examination of the scatter plots for C_3A and optimum predicted SO_3 versus the residuals are presented in Figs. 1 and 2 for model 1-A, Figs. 3 and 4 for model 3-B and Figs 5 and 6, indicates that model 3-B does not adequately represent the obtained data. Therefore this model is ignored in the following analysis.

Further statistical analysis is made to find the best model among those described as above. The relationship between the observed and predicted SO_3 are presented in Fig. 7 and Fig. 9 for models 1-A and 4 respectively. The conclusion is that the developed models result in minimal random error. By contrast, Fig**.** 8 for model 3-B is less articulate.

Moreover, the distribution of residuals presented in Figs 10 ,11 and 12 for model 1-A , 3-B and 4 respectively provide further evidence to support the conclusion that model 3-B is not a

Dr. Zena K. Abbas
Prof. Dr. Riyadh S. Al-Rawi
Dr. A.H. Al-Neaime

**Statistical Model for Predicting the
Optimum Gypsum Content in Concrete**

reliable model. To conclude this section, it was decided that the data presented in Fig 12 provide the best fit between observed and predicted SO$_3$ values. The implication is that model 4 is the best to describe the obtained data.

2.2 Late Ages models (Greater Than 28-Days)

Following the development of 28-days models, a late age (greater than 28-days) model was developed based on the predicted optimum SO$_3$ content of 28-days and late age. The number of data is equal to 77.

Descriptive statistical analysis is presented in Table 13. The predicted models for late ages are presented in Table 14.

Optimum SO$_3$ %(Late ages)-model **4**= $0.976 \times$ SO$_3$ (predicted for 28-days) +1.251E-$03 \times$ Time (late ages)   eq. (1)

Table 15 shows that the standard error of estimate (R^2) is (0.97). This has the implication that 97.0% of the observed scatter in the data is explained by the adopted model. This conclusion is consistent with result of comparison of the calculated F (1206.493) with the tabulated critical F value of (3.127) at the 95% level of confidence.

Moreover, the calculated Durbin-Watson value is (1.939) which is within the range (1.5-2.5) and hence, a minimal random error would be expected. The value of T-statistics equal to (T= 0.08).

A prove to the conclusion that the developed model result is in a minimal random error can found by examination of Fig. 13.

Examination of Figs.14 and 15 which shows scatter plots of predicted optimum SO$_3$ and MgO, variables versus the residual. The presented data suggest the existence of random variation between variable values and its residual values.

Finally the distribution of the residuals is shown in Fig. 16, from this figure it is clear that the residuals are almost normally distributed.

From all statistical analysis presented above, it is also difficult to select model 4 as the best model for 28-days model since it contain some

independent variables not in the line of concrete technology. So all age model may be the alternative model.

2.3 All- Age Concrete Models

Eight development models were built for all ages, and the number of data is equal to 132 when Abdul-Latif `s data (1997-2001) were ignored and 155 when entering them. The results of the preliminary descriptive statistical analysis are presented in **Table 16**.

Results of linear and non linear (Pearson and Spearman) correlation analysis are presented in the form of a matrix in Tables 17 and 18 respectively.

The data presented suggest that in general the linear model provides better fit for the data between the compounds and there are highly correlated with each other.

From the partial correlation presented in Table 19, in general the coefficients of correlation of the linear relationship are higher than the critical coefficient of correlation except for MgO and C$_3$A. For nonlinear relationship all independent variables are less than the critical value. Based on this result it was decided to use linear multiple regression technique for the developed required statistical model.

The regression equation coefficient obtained, t-value and the decision are presented in Table 20.

From Tables 20 and 21 we can conclude:
1. The best statistical model is (1-A) since ,it has the highest R^2 , lowest root mean square of error and the Durbin- Watson value within the range although the T-value is not the best but it is still a low value despite that some independent variables not on the line of concrete technology .
2. The model (1-B) may be selected as the best model for the following reasons:

- In general the regression coefficient is in the line of concrete technology except for total alkalies and this is because that we replace the value of Latif`s data (1997 and 2001) by mean value and this effect the final result.

- High coefficient of determination R^2 of (0.98) , low root mean square of error (0.4821) and the Durbin – Watson is not

within the range , but it is still near the range and with low T- value (-0.49).
- The model includes all independent variables.
3. For model 2-A, 2-B ,3-A and 3-B it is clear from the Table presented above there is a shortcoming either in the statistical concept or that some independent variables contains all expected positive and negative factors and values .
- High coefficient of determination, R^2 (0.98), low root mean square of error (0.417), and the Durbin- Watson is not within the ranges but it is closest to the ranges and T- value is the lowest value
 (-0.08).
- The model including all independent variables except total alkalies.
5.   For model 5 despite all independent variables are in the line of concrete technology ,but the shortcoming is on the statistical concept, it has low coefficient of determination , R^2 (0.962)compared with other model , the highest root mean square of error , and the Durbin- Watson is not within the rang despite the low T- value (0.08) .
Examination of Figs. 17 and 18 for model 4 and Figs.19 and 20 for model 5 which shows scatter plots for C_3S, C_3A, Blaine and age versus the residuals of each variable. The data presented suggest the existence of random variation between variable values and its residual values. The data presented provides further confirmation to the conclusion that the developed model 4 can be considered as the best selected model.
A proof to the conclusion that the developed model results in minimal random error can found by examination of Fig. 21 for model 4. The distribution of the residuals is shown in Fig 22 from this figure it is clear that the residuals are almost normally distributed.

3. CONCLUSIONS
3.1 Development of Models for (28 Days – Late Age And All Age Model) of Concrete:
1. The examination of the data presented for all variables indicates that the coefficients of correlation for linear

not in the line of concrete technology and this due to high correlated between the independent variables .
4. Model 4 is the best model for the following reasons:
- All independent variables is on the line with concrete technology understanding , as it
relationship are substantially higher than that for nonlinear relationship.
2. In general, statistically, it was also found that the MgO content of cement positively affects the optimum SO_3 content.
3. Increasing the SO_3 content in sand affects the optimum SO_3 content of concrete and this effect is more significant than that due to increasing the SO_3 content in coarse aggregate, so total effective SO_3 in concrete is preferred.

3.2 28 Days – Late Age Models:
In the 28-days model the relationship between the independent variables themselves and the optimum SO_3 content is overlapped resulting in the high correlation between them. From the presented regression analysis it is difficult to choose the best model because the regression models are either in the line of concrete technology or best statistical analysis. According to the results obtained from the models of 28-days, the following could be concluded:
1. In general, the trend for both C_3S and C_2S are positive and this is due to the positive influence effect for both C_3S and C_2S on 28-days strength.
2. For more confidence for the above conclusion, the value of regression coefficient C_2S is less than for C_3S in all positive effect models (1-b, 2-B, 3-B, 4, and 5).
3. It was proved statistically that the effect of C_3A is positive.
4. In general, the effect of C_4AF is positive.
5. In general the effect of C_3A is about double that of C4AF except for 1-A, 2-A and 3-A and this due to the combined effect between Abdul – Latif `s data and other authors data.
5. The trend of Blaine fineness is not clear, so it needs more study.

Dr. Zena K. Abbas
Prof. Dr. Riyadh S. Al-Rawi
Dr. A.H. Al-Neaime

Statistical Model for Predicting the
Optimum Gypsum Content in Concrete

6. It is proved statistically that the optimum SO_3 content increases with increase of age in late age model.

3.3 All Age Models

For our best models 4 and 5, the following could be concluded:

1. The effect of C_3S is positive and of C_2S is negative.

2. The effects of C_3A and C_4AF are positive.

3. The effect of C_3A is about twice the effect of C_4AF.

4. The effects of C_3A and C_4AF are higher than the effects of C_3S and C_2S.

5. The positive effect of fineness Blaine.

6. The positive effect of time led to increase in optimum SO_3 content with increase of age.

7. Blaine fineness and C_3A were found as the major factors affecting the optimum SO_3 content.

REFRENCES

Abdul-Latif, A.M. (1997)

" ",

. 57 39-34

Abdul-Latif, A.M. (2001), "Optimum gypsum content in cement mortar and concrete", Ph.D. Thesis, College of Engineering, University of Baghdad.

Abood , S.H. (1989) , " Creep of concrete with sulfate contaminated aggregate " Ms.C. Thesis , College of Engineering , University of Baghdad , pp.110-112,81,100.

Ali, N.H. (1981), "Effect of sulfates content on concrete with different gypsum content cements", Ms.C Thesis, College of Engineering, University of Baghdad, pp.145-149,128,137.

Al-Qissi, A.W. (1989),

" فاعلية الكبريتات الملوثة للركام الناعم في الخرسانة " ، رسالة ماجستير ، كلية الهندسة ، جامعة بغداد .

Al-Rawi, R.S. (1977), "Gypsum content of cement used in concrete cured by accelerated method ", ASTM Journal of Testing and Evaluation, Vol.5, No. 3, pp.231-237.

Al-Rawi, R.S. , Al-Salihi ,R.A. and Ali , N.H. (2002)-A " Effective sulfate content in concrete ingredient " , Challenges of concrete construction Symposium , University of Dundee , Scotland , U.K.

Al-Salihi , R.A. (1994) , "Proposed revision of Iraqi specifications for concrete ingredients to cope with post war era " , Ms.C thesis , College of Engineering , University of Baghdad , pp.20,37,60-63,97-102.

Drapper, N. R. and Smith, H. (1981), "Applied regression analysis ", John Wiley, New York, pp. 709.

Montgomery, D.C. and Peack, E.A., (1992)," Introduction to linear regression analysis ", 2nd Edition, John Wiley and Sons, Inc., New York.

SPSS manual, (1992), Statistical package for social science, version 10, electronic help file.

Yousif , S.H. (1980) , " Effect of sulfate on lean and medium richness concrete " , Ms.C Thesis , College of Engineering , University of Baghdad, pp.93,98-101 .

Zari, A.S. (1981), "Role of aggregate in sulfate effect on cement mixes", Ms.C Thesis, College of Engineering, University of Baghdad, pp.151-155,137.

Table 1: The collected data from published literature

Author	No. of data	Type of cement
Al-Rawi (1977)	3	Approximately the same chemical composition and different in Blaine.
Ali (1980)	5	Same chemical composition with 1:2:4 mix and different SO_3 level
Yousif (1981)	6	(3-OPC with 1:2:4,1:3:6 and1:4:8 mix) and (3-SRPC with 1:2:4,1:3:6 and1:4:8 mix)
Zari (1981)	16	(8-OPC with 1:2, 1:3, 1:4, 1:5 mix) and (8-SRPC with 1:1:2, 1:1.33:2.68, 1:2:4 and 1:3:6 mix).
Abood (1988)	2	Same chemical composition with (1:2.75:3.18 and 1:1.84:2.46) mix
Al-Qissi (1989)	1	Chemical composition
Al-Salihi (1994)	7	Different chemical composition with schedule mixes
Abdul-latif (1997)	7	Different chemical composition
Abdul-latif (2002)	5	Different chemical composition

Table2: Selected independent variables, total alkalis, main cement compounds and surface published literatures.

Author	Serial No. of selected data set	Calculated					
		Total Alk. (%)	C_3S (%)	C_2S (%)	C_3A (%)	C_4AF (%)	Surface area(cm^2/gm)
Ali (1980)	1-5	0.94	41.10	34.8	8.8	8.5	3000
Yousif (1981)	1-3	0.86	34.00	38	10	9	3103
	4-6	0.65	49.00	26	2	16	2533
Zari (1981)	1-4	0.53	49.53	20.12	8.76	10.16	3278
	5-8	0.35	61.96	13.7	1.1	15.1	3124
Al-Rawi (1977)	1	0.34	62.00	13	12	11	2500
	2	0.34	62.00	13	12	11	3500
	3	0.34	62.00	13	12	11	4500
Al-Qissi (1989)	1	0.74	47.80	24.2	9.7	9.12	3125
Abood (1988)	1-2	0.58	58.44	15.83	5.22	9.39	3471
Al-Salihi (1994)	1-7	0.80	34.48	36.07	8.87	9.12	3420
Abdul-Latif (1997)	1	-	36.03	36.75	2.55	15.2	3660
	2	-	36.28	33.8	12.91	8.32	3840
	3	-	54.85	19.09	7.71	8.48	3600
	4	-	60.63	13.87	2.65	16.29	4000
	5	-	38.22	34.64	2.57	15.2	3540
	6	-	21.15	51.38	14.79	2.18	3660
	7	-	30.1	39.04	9.52	10.33	3350
Abdul-Latif (2002)	1	-	43.85	32.28	1.61	14.85	2620
	2	-	43.59	31.9	2.3	13.98	2750
	3	-	48.45	26.51	8.53	7.54	2600
	4	-	37.74	36.91	7.66	9.48	2570
	5	-	52.02	21.55	8.02	9.6	2470

Dr. Zena K. Abbas
Prof. Dr. Riyadh S. Al-Rawi
Dr. A.H. Al-Neaime

Table 3: Optimum SO₃% of concrete at different ages (by weight of cement) from published literature.

Author	Serial	Optimum SO$_3$ content (%) Time in days							
		7-days	14-days	28-days	56-days	90-days	120-days	181-days	365-days
Al-Rawi (1977)	1	.	.	2.00	.	.	.	2.00	.
	2	.	.	2.00	.	.	.	2.00	.
	3	.	.	2.00	.	.	.	5.70	.
Ali (1981)	1	1.50	.	1.5	2.5	2.00	.	.	1.50
	2	2.00	.	2.00	3.00	2.00	.	.	2.50
	3	2.50	.	2.50	2.20	2.50	.	.	3.00
	4	2.45	.	2.45	2.45	2.45	.	.	2.45
	5	2.70	.	2.70	2.70	2.70	.	.	2.70
Yousif (1981)	1	2.83	.	2.83	.	2.83	.	.	2.83
	2	3.1	.	3.1	.	3.1	.	.	3.1
	3	3.37	.	3.37	.	3.37	.	.	4.44
	4	2.53	.	2.53	.	2.53	.	.	3.07
	5	2.80	.	2.80	.	2.80	.	.	2.80
	6	3.07	.	3.07	.	3.07	.	.	4.14
Zari (1981)	1	.	4.22	4.22	4.22	4.22	.	.	.
	2	.	4.22	4.22	4.22	3.72	.	.	.
	3	.	3.47	4.22	4.22	3.74	.	.	.
	4	.	4.2	4.22	4.22	4.22	.	.	.
	5	.	3.72	4.22	3.72	4.22	.	.	.
	6	.	4.22	4.22	4.22	4.22	.	.	.
	7	.	3.72	3.72	3.72	3.72	.	.	.
	8	.	4.22	4.22	4.22	4.22	.	.	.
	9	.	3.22	3.22	3.47	3.22	.	.	.
	10	.	3.22	3.22	3.22	3.22	.	.	.
	11	.	3.2	3.22	3.72	4.22	.	.	.
	12	.	3.22	3.22	3.22	3.22	.	.	.
	13	.	3.22	3.22	3.47	3.22	.	.	.
	14	.	3.22	3.22	3.22	3.22	.	.	.
	15	.	3.22	3.47	3.22	3.47	.	.	.
	16	.	3.22	3.22	3.22	3.22	.	.	.
Abood (1988)	1	.	3.35	3.35	.	.	.	.	.
	2	.	3.20	3.20	.	.	.	.	.
Al-Qissi (1989)	1	3.39	.	3.94	.	.	3.94	.	.
Al-salihi (1994)	1	2.96	.	2.33	2.96	2.96	.	2.96	.
	2	2.54	.	2.54	3.09	3.09	.	3.09	.
	3	2.89	.	23.24	3.41	3.41	.	3.41	.
	4	3.24	.	3.24	3.24	3.24	.	3.73	.
	5	3.56	.	3.56	3.56	3.56	.	3.56	.
	6	3.88	.	3.88	3.88	3.88	.	3.88	.
	7	4.17	.	4.17	4.17	4.17	.	4.17	.
Abdul-Latif (1997)	1	3.4	.	3.4	.	.	3.4	.	.
	2	3.81	.	3.81	.	.	3.81	.	.
	3	4.47	.	4.47	.	.	4.47	.	.
	4	4.58	.	4.58	.	.	3.34	.	.
	5	3.24	.	3.24	.	.	3.24	.	.

	6	4.96	.	4.39	.	.	4.96	.	.
	7	4.12	.	4.52	.	.	4.12	.	.
Abdul-Latif(2001)	1	.	.	3.52	.	.	.	.	3.87*
	2	.	.	3.23	.	.	.	.	3.90*
	3	.	.	4.00	.	.	.	.	4.00*
	4	.	.	3.55	.	.	.	.	3.90*
	5	.	.	3.30	.	.	.	.	3.97*

* For 300 – days

Table 4: Descriptive statistics analysis for cement mortar (all data)

Compound	Central tendency			Dispersion			
	Mean	Median	Mode	Std. deviation	Range	Minimum	Maximum
MgO%	3.3153	3.400	4.110	0.831	3.300	0.9	4.20
Total Alk.[1]%	1.158	1.160	1.160	0.271	0.690	0.86	1.55
C_3S%	45.053	41.100	34.480	11.148	40.8	21.15	62.00
C_2S%	27.732	34.640	36.070	10.221	38.30	13.0	51.38
C_3A%	7.407	8.800	8.870	3.528	13.60	1.1	14.79
C_4AF%	10.551	9.120	9.120	2.768	14.10	2.18	16.29
L.O.I%	1.399	1.610	1.620	0.614	2.500	.20	2.70
Blaine gm/cm^2	3235.7	3201.0	3420.0	297.23	2030	2470	4500
Total eff. SO_3%	3.375	3.240	3.220	0.708	4.20	1.5	5.70

Table 5: Correlation matrix for dependent and independent variables (Person correlation)

Variable	MgO	Total Alk.	C_3S	C_2S	C_3A	C_4AF	L.O.I	Blaine	Ages	SO_3%
MgO	1.00	.239**	-.194**	.066	.255**	-.389**	.150	-.074	-.115	.379**
Total Alk.	.239**	1.00	-.901**	.957**	.593**	-.733**	-.430	-.078	.236**	-.334**
C_3S	-.194**	-.901**	1.00	-.974**	-.624**	.657**	-.048	.157*	-.159*	.101
C_2S	.066	.957**	-.974**	1.00	.541**	-.608**	-.084	-.161*	.191**	-.240**
C_3A	.255**	.593**	-.624**	.541**	1.00	-.919**	-.105	-.119	.084	.048
C_4AF	-.389**	-.733**	.657**	-.608**	-.919**	1.00	.098	.197**	-.080	-.040
L.O.I	.150	-.430	-.048	-.084	-.105	.098	1.000	.201	-.115	.539
Blaine	-.074	-.078	.157*	-.161*	-.119	.197**	.201	1.00	-.050	-.048
Ages	-.115	.236**	-.159*	.191**	.084	-.080	-.115	-.050	1.00	.040
SO_3%	.379**	-.334**	.101	-.240**	.048	-.040	.539	-.048	.040	1.00

Dr. Zena K. Abbas
Prof. Dr. Riyadh S. Al-Rawi
Dr. A.H. Al-Neaime

Statistical Model for Predicting the
Optimum Gypsum Content in Concrete

Table 6: Correlation matrix for dependent and independent variables (Spearman correlation)

Variable	MgO	Total Alk.	C_3S	C_2S	C_3A	C_4AF	L.O.I	Blaine	Ages	$SO_3\%$
MgO	1.00	.090	-.093	.060	.133	-.265**	.317	.364**	-.055	.471**
Total Alk.	.090	1.00	-.868**	.867**	.595**	-.874**	-.359	-.207**	.077	-.380**
C_3S	-.093	-.868**	1.00	-.987**	-.709**	.595**	-.050	-.148*	-.058	.122
C_2S	.060	.867**	-.987**	1.00	.666**	-.583**	.024	.079	.068	-.143*
C_3A	.133	.595**	-.709**	.666**	1.00	-.703**	-.060	.298**	.067	-.085
C_4AF	-.265**	-.874**	.595**	-.583**	-.703**	1.00	.113	-.055	-.049	.129
L.O.I	.317	-.359	-.050	.024	-.060	.113	1.000	.524	-.052	.521
Blaine	.364**	-.207**	-.148*	.079	.298**	-.055	.524	1.00	-.104	.190**
Ages	-.055	.077	-.058	.068	.067	-.049	-.052	-.104	1.00	.070
$SO_3\%$	.471**	-.380**	.122	-.143*	-.085	.129	.521	.190**	.070	1.00

**, Correlation is significant at the 0.01 level (2-tailed)*, Correlation is significant at the 0.05 level (2-tailed)
$r_c = 0.118$ for N= 192 for all variable except for total Alk. $r_c = 0.1875$ for N= 113

Table 7: Descriptive statistics analysis for concrete (28-days)

Variables	Mean	Stan. deviation	Minimum	Maximum
MgO%	3.106	0.959	0.900	4.200
Total Alk. %	0.617	0.215	0.340	0.940
$C_3S\%$	46.956	11.326	21.150	62.000
$C_2S\%$	26.101	10.375	13.000	51.380
$C_3A\%$	7.022	3.857	1.100	14.790
$C_4AF\%$	10.931	3.115	2.180	16.290
L.O.I%	1.424	0.623	0.200	2.700
Blaine gm/cm^2	3193.47	408.900	2470.00	4500.00
Total eff. $SO_3\%$	3.209	0.684	1.500	4.220

No. of data = 42 for all variables except for total Alk. No. of data = 33

Table 8: Person correlation values for 28-days for concrete

Variables	MgO	Tot. AlK.	C_3S	C_2S	C_3A	C_4AF	L.O.I	Blaine	$SO_3\%$
MgO	1.000	0.114	-0.054	-0.015	-0.004	-0.172	0.194	0.343*	0.527**
Tot. AlK.	0.114	1.000	-0.913**	0.912**	0.508**	-0.854**	-0.279	-0.174	-0.222
C_3S	-0.054	-0.913**	1.000	-0.985**	-0.615**	0.642**	-0.136	-0.093	0.048
C_2S	-0.015	0.912**	-0.985**	1.000	0.555**	-0.613**	0.138	0.006	-0.074
C_3A	-0.004	0.508**	-0.615**	0.555**	1.000	-0.698**	-0.047	0.242	-0.156
C_4AF	-0.172	-0.854**	0.642**	-0.613**	-0.698**	1.000	0.032	-0.021	0.031
L.O.I	0.194	-0.279	-0.136	0.138	-0.047	0.032	1.000	0.328	0.559
Blaine	0.343*	-0.174	-0.093	0.006	0.242	-0.021	0.328	1.000	0.095
$SO_3\%$	0.527**	-0.222	0.048	-0.074	-0.156	0.031	0.559	0.095	1.000

**, Correlation is significant at the 0.01 level (2-tailed): *, Correlation is significant at the 0.05 level (2-tailed)

Table 9: Spearman correlation values for 28-days for concrete

Variables	MgO	Tot. AlK.	C_3S	C_2S	C_3A	C_4AF	L.O.I	Blaine	$SO_3\%$
MgO	1.000	0.257	-0.124	0.006	0.057	-0.223	0.133	0.174	0.493**
Tot. AlK.	0.257	1.000	-0.907**	0.951**	0.532**	-0.712**	-0.332	-0.116	-0.262
C_3S	-0.124	-0.907**	1.000	-0.977**	-0.598**	0.646**	-0.16	-0.062	0.078
C_2S	0.006	0.951**	-0.977**	1.000	0.520**	-0.601**	0.061	-0.017	-0.208
C_3A	0.057	0.532**	-0.598**	0.520**	1.000	-0.891**	-0.051	0.242	-0.044
C_4AF	-0.223	-0.712**	0.646**	-0.601**	-0.891**	1.000	-0.142	-0.142	-0.039
L.O.I	0.133	-0.332	-0.16	0.061	-0.051	0.0021	1.000	0.108	0.626*
Blaine	0.174	-0.116	-0.062	-0.017	0.242	-0.142	0.108	1.000	-0.063
$SO_3\%$	0.493**	-0.262	0.078	-0.208	-0.044	-0.039	0.626*	-0.063	1.000

**, Correlation is significant at the 0.01 level (2-tailed):   *, Correlation is significant at the 0.05 level (2-tailed)
r_c = 0.304 for N=42 for all variables except for total Alk. r_c = 0.3442 for N=33

Table 10: Partial correlation for concrete model (28-days) between optimum $SO_3\%$ and other compounds

Variables	Person correlation	Spearman correlation
MgO	0.4829	0.0508
Total alkalies	0.1719	0.0000
C_3S	0.6765	0.0220
C_2S	-0.6841	-0.0150
C_3A	-0.3044	-0.0805
C_4AF	-0.0155	0.0000
L.O.I	0.4554	0.0000
Blaine	-0.078	-0.0768

No.of data = 42 for all variables except for total Alk. No. of data = 33

Table 11: Regression equation coefficients and other statistical measures for concrete (28-days).

Model	1-A			1-B		
Independent variable	Regression coefficient	t- vale	Decision (5%)	Regression coefficient	t- vale	Decision (5%)
MgO%	-0.150	-0.718	Accept	0.380	4.644	Reject
Total Alk%	4.417	2.773	Reject	-0.167	-0.22	Accept
$C_3S\%$	3.307E-02	0.914	Accept	3.008E-02	2.562	Reject
$C_2S\%$	-7.458E-02	-1.400	Accept	1.003E-02	0.570	Accept
$C_3A\%$	3.344E-02	0.616	Accept	6.843E-02	1.691	Accept
$C_4AF\%$	-7.394E-02	-0.529	Accept	2.964E-02	0.614	Accept
L.O.I%	1.649	4.64	Reject	0.730	5.739	Reject
Blaine gm/cm^2	-8.779E-05	-0.379	Accept	-4.344E-04	-2.434	Reject
Model	2-A			2-B		
Independent variable	Regression coefficient	t- vale	Decision (5%)	Regression coefficient	t- vale	Decision (5%)
MgO%	0.751	07.302	Reject	0.557	5.321	Reject
Total Alk%	3.728	1.757	Reject	-2.390	-2.695	Reject
$C_3S\%$	-8.954E-02	-2.706	Reject	3.266E-02	2.013	Reject
$C_2S\%$	-0.171	-2.613	Reject	5.322E-02	2.416	Reject
$C_3A\%$	0.210	4.064	Reject	7.724E-02	1.545	Accept
$C_4AF\%$	0.445	3.978	Reject	6.222E-02	0.938	Accept
L.O.I%	-	-	-	-	-	-

Dr. Zena K. Abbas
Prof. Dr. Riyadh S. Al-Rawi
Dr. A.H. Al-Neaime

Statistical Model for Predicting the
Optimum Gypsum Content in Concrete

Blaine gm/cm^2	1.787E-04	0.596	Accept	-3.705E-04	-1.504	Accept
Model		3-A			3-B	
Independent variable	Regression coefficient	t- vale	Decision (5%)	Regression coefficient	t- vale	Decision (5%)
MgO%	-	-	-	-	-	-
Total Alk%	3.067	0.844	Accept	-0.663	-606	Accept
C$_3$S%	-5.880E-02	-1.045	Accept	4.284E-02	2.005	Reject
C$_2$S%	-0.109	-0.979	Accept	3.901E-02	1.345	Accept
C$_3$A%	8.392E-02	1.004	Accept	2.429E-02	0.374	Accept
C$_4$AF%	0.258	1.379	Reject	-8.292E-03	-0.096	Accept
L.O.I%	-	-	-	-	-	-
Blaine gm/cm^2	1.065E-03	2.266	Accept	1.563E-04	0.523	Accept
Model		4			5	
Independent variable	Regression coefficient	t- vale	Decision (5%)	Regression coefficient	t- vale	Decision (5%)
MgO%	0.371	5.26	Reject	-	-	-
Total Alk%	-	-		-	-	
C$_3$S%	2.942E-02	1.425	Accept	3.845E-02	1.530	Accept
C$_2$S%	6.903E-03	0.658	Accept	2.57E-02	1.37	Accept
C$_3$A%	6.786E-02	1.206	Accept	2.496E-02	0.388	Accept
C$_4$AF%	2.945E-02	0.69	Accept	-1.204E-03	-0.014	Accept
L.O.I%	0.745	2.934	Reject	-	-	-
Blaine gm/cm^2	-4.277E-04	-1.465	Accept	1.745E-04	0.592	Accept

Table 12: General statistical concept for concrete (28-days)

Model					ANOVA	R^2	Root mean square of error	Durbin-Watson	$\sum Re. \times$ predicted SO_3%
	Source	D.F.	Sum of squares	Mean square	F value				
1-A	Model(Reg.)	8	355.491	44.436	379.004	0.992	0.3424	1.549	0.07
	Error(Res.)	25	2.931	0.117					
	Total	33	358.422						
1-B	Model(Reg.)	8	445.716	55.714	311.736	0.987	0.4228	1.313	0.12
	Error(Res.)	34	6.077	0.179					
	Total	42	451.792						
2-A	Model(Reg.)	7	352.967	50.424	240.334	0.985	0.4580	1.360	-0.24
	Error(Res.)	26	5.455	0.210					
	Total	33	358.422						
2-B	Model(Reg.)	7	439.830	62.833	183.839	0.974	0.5846	0.952	0.22
	Error(Res.)	35	11.962	0.342					
	Total	42	451.792						
3-A	Model(Reg.)	6	341.781	56.963	92.420	0.954	0.7851	1.331	-0.81
	Error(Res.)	27	16.642	0.616					
	Total	33	358.422						
3-B	Model(Reg.)	6	430.154	71.692	119.278	0.952	0.7753	0.788	0.01
	Error(Res.)	36	21.638	0.601					
	Total	42	451.792						
4	Model(Reg.)	7	445.707	63.672	366.205	0.987	0.417	1.327	0.01
	Error(Res.)	35	6.085	0.174					
	Total	42	451.792						
5	Model(Reg.)	5	429.934	85.987	145.551	0.952	0.7686	0.726	-0.01
	Error(Res.)	37	21.858	0.591					
	Total	42	451.792						

Table 13: Descriptive statistics analysis for concrete (Late age) for model 4

Compound	Mean	Standard deviation	Minimum	Maximum
Time (Late age)-days	148.64	119.96	56	365
Total eff. SO$_3$%	3.3487	0.6952	1.5	5.7
Opt. SO$_3$% predicted(28-days)	3.2155	0.5656	1.61	4.08

No. of data for model 4= 77

Table 14: Regression equation with standard error for each compound

Independent variable	Regression coefficient	Standard error
Time (late ages)-days	1.251E-03	0.031
Opt.SO$_3$(predicted for 28-days)%	0.976	0.001

Table 15: General statistical concept for concrete models (late age) for model 4

Source	D.F.	Sum of squares	Mean square	ANOVA F value	R^2	Root mean square of error
Model(Reg.)	2	873.058	436.529	1206.493	0.97	0.6015
Error(Res.)	75	27.136	0.362			
Total	77	900.195				

Table 16: Result of descriptive statistical analysis for concrete (All ages)

Variables	Mean	Stan. deviation	Minimum	Maximum
MgO%	3.259	0.872	0.900	4.200
Total Alk.%	0.643	0.216	0.340	0.940
C$_3$S%	46.113	11.047	21.150	62.00
C$_2$S%	26.811	10.124	13.000	51.380
C$_3$A%	7.011	3.731	1.100	14.790
C$_4$AF%	10.904	3.044	2.180	16.290
L.O.I%	1.396	0.606	0.200	2.700
Blaine gm/cm^2	3197.194	345.864	2470.000	4500.000
All ages-days	82.000	103.964	7.000	365.00
Total eff. SO$_3$%	3.273	0.671	1.500	5.700

No. of data = 155 for all variables except for total Alk. No. of data =132

Dr. Zena K. Abbas
Prof. Dr. Riyadh S. Al-Rawi
Dr. A.H. Al-Neaime

Statistical Model for Predicting the
Optimum Gypsum Content in Concrete

Table 17: Person correlation values for all ages concrete data

Variables	MgO	Total Alk.[1]	C_3S	C_2S	C_3A	C_4AF	L.o.I	Blaine	All ages	$SO_3\%$
MgO	1.000	.051	-.036	-.013	.048	-.163*	.318**	.383**	-.053	.446**
Tot.AlK[1]	.051	1.000	-.877**	.876**	.646**	.67**	.018	.076	.068	-.189*
C_3S	-.036	-.877**	1.000	-.987**	-.756**	.67**	-.026	-.142	-.059	.167*
C_2S	-.013	.876**	-.987**	1.000	.702**	-.639**	.018	.076	.068	-.189*
C_3A	.048	.646**	-.756**	.702**	1.000	-.738**	-.04	.256**	.060	-.114
C_4AF	-.163*	-.89**	.67**	-.639**	-.738**	1.000	.148	.011	-.060	.162*
L.O.I	.318**	-.401**	-.026	.018	-.04	.148	1.000	.537**	-.044	.565**
Blaine	.383**	-.218*	-.142	.076	.256**	.011	.537**	1.000	-.117	.263**
All ages	-.053	.079	-.059	.068	.06	-.06	-.044	-.117	1.000	.085
$SO_3\%$	.446**	-.405**	.167*	-.189*	-.114	.162*	.565**	.263**	.085	1.000

Table 18: Spearman correlation values for all ages concrete data

Variables	MgO	TotalAlk	C_3S	C_2S	C_3A	C_4AF	L.O.I	Blaine	All ages	$SO_3\%$
MgO	1.000	.195*	-.152	.026	.19*	-.297**	.129	.24**	-.124	.324**
Tot. AlK.[1]	.195*	1.000	-.904**	.957**	.632**	-.755**	-.473**	-.086	.250**	-.394**
C_3S	-.152	-.904**	1.000	-.974**	-.69**	.715**	-.035	-.131	-.163*	.158*
C_2S	.026	.957**	-.974**	1.000	-.609**	-.67**	-.098	.037	.195*	-.294**
C_3A	.190*	.632**	-.69**	-.609**	1.000	-.922**	-.052	.276**	.099	.036
C_4AF	-.297**	-.755**	.715**	-.67**	-.922**	1.000	.076	-.198*	-.097	-.004
L.O.I	.129	-.473**	-.035	-.098	-.052	.076	1.000	.272**	-.12	.552**
Blaine	.240**	-.086	-.131	.037	.276**	-.198*	.272**	1.000	-.177*	.146
All ages	-.124	.25**	-.163*	.195*	.099	-.097	-.120	-.177*	1.000	.032
$SO_3\%$	.324**	-.394**	.158*	-.294**	.036	-.004	.552**	.146	.032	1.000

No. of data = 155;   [1], means number of data =132
r_c = 0.1565 for No. of data =155 , r_c =0.1694 for No. of data =132 .
**, Correlation is significant at the 0.01 level (2-tailed):   *, Correlation is significant at the 0.05 level (2-tailed)

Table 19: Partial correlation for concrete model (all ages) between optimum $SO_3\%$ and other compounds

Variables	Person correlation	Spearman correlation
MgO	0.0678	-
Total alkalies[1]	0.2685	0.0000
C_3S	0.4806	0.0421
C_2S	-0.4979	0.0250
C_3A	-0.0194	0.0639
C_4AF	0.1598	0.000
L.O.I	0.1995	0.0000
Blaine	0.3144	-
Ages	0.2173	0.1556

No. of data = 155   , [1] means No. of data = 132   , r_c = 0.1565 for No. of data =155 , r_c =0.1694 for No. of data =132 .

Table 20: Regression equation coefficients and other statistical measures for concrete (all age).

Model	1-A			1-B		
Independent variable	Regression coefficient	t- vale	Decision (5%)	Regression coefficient	t- vale	Decision (5%)
MgO%	-0.112	-0.81	Accept	0.275	5.096	Reject
Total Alk%	4.32	3.952	Reject	-0.568	3.28	Reject
$C_3S\%$	-3.071E-02	-1.188	Accept	2.580E-02	0.51	Accept
$C_2S\%$	-0.126	-3.519	Reject	5.910E-03	1.605	Accept
$C_3A\%$	8.164E-02	1.177	Accept	9.341E-02	1.29	Accept
$C_4AF\%$	0.116	1.202	Accept	4.275E-02	6.607	Reject
L.O.I%	1.001	4.187	Reject	0.581	-1.523	Accept
Blaine gm/cm^2	7.603E-04	1.657	Accept	1.982E-04	0.959	Accept
Time(All ages)-days	9.014E-04	2.433	Reject	1.164E-03	-1.127	Accept
Model	2-A			2-B		
Independent variable	Regression coefficient	t- vale	Decision (5%)	Regression coefficient	t- vale	Decision (5%)
MgO%	0.416	6.841	Reject	0.404	2.225	Reject
Total Alk%	3.585	1.235	Accept	-2.601	2.759	Reject
$C_3S\%$	-0.111	-6.091	Reject	1.912E-02	1.534	Accept
$C_2S\%$	-0.183	-5.175	Reject	3.341E-02	2.361	Reject
$C_3A\%$	0.198	7.363	Reject	0.112	0.517	Accept
$C_4AF\%$	0.451	1.65	Accept	8.528E-02	2.976	Reject
L.O.I%	-	-	-	-	-	-
Blaine gm/cm^2	9.936E-04	3.24	Reject	4.995E-06	-5.523	Reject
Time(All ages)-days	9.307E-04	1.021	Accept	1.349E-03	1.641	Accept
Model	3-A			3-B		
Independent variable	Regression coefficient	t- vale	Decision (5%)	Regression coefficient	t- vale	Decision (5%)
MgO%	-			-		
Total Alk%	3.594	2.677	Reject	-1.568	3.263	Reject
$C_3S\%$	-0.107	-5.027	Reject	3.257E-02	1.608	Accept
$C_2S\%$	-0.174	-4.196	Reject	2.754E-02	4.914	Reject
$C_3A\%$	0.156	5.732	Reject	0.144	1.113	Accept
$C_4AF\%$	0.381	5.113	Reject	9.049E-02	-0.523	Accept
L.O.I%	-	-	-	-	-	-
Blaine gm/cm^2	1.639E-03	0.796	Accept	-5.930E-06	1.435	Accept
Time(All ages)-days	5.599E-04	1.226	Accept	7.448E-04	-2.926	Reject
Model	4			5		
Independent variable	Regression coefficient	t- vale	Decision (5%)	Regression coefficient	t- vale	Decision (5%)
MgO%	0.245	5.2	Reject	-	-	-
Total Alk%	-	-	-	-	-	-
$C_3S\%$	2.432E-02	3.133	Reject	1.377E-02	1.396	Accept
$C_2S\%$	-4.311E-03	-0.598	Accept	-1.311E-02	-1.399	Accept
$C_3A\%$	8.911E-02	1.631	Accept	9.77E-02	2.951	Reject
$C_4AF\%$	3.909E-02	1.184	Accept	6.824E-02	1.6	Accept
L.O.I%	0.641	9.099	Reject	-	-	-
Blaine gm/cm^2	1.78E-04	1.379	Accept	4.628E-04	1.043	Accept
Time(All ages)-days	1.11E-03	1.365	Accept	8.815E-04	1.672	Accept

Dr. Zena K. Abbas
Prof. Dr. Riyadh S. Al-Rawi
Dr. A.H. Al-Neaime

Table 21: General statistical concept for concrete (All ages)

Model	Source	D.F.	Sum of squares	Mean square	ANOVA F value	R^2	Root mean square of error	Durbin-Watson	∑Re.> predicted SO₃%
1-A	Model(Reg.)	9	1475	163.907	939.65	0.986	0.4177	1.725	-4.45
	Error(Res.)	123	21.45	0.174					
	Total	132	1496.6						
1-B	Model(Reg.)	9	1696.7	188.472	812.33	0.98	0.4817	1.223	-0.49
	Error(Res.)	146	33.874	0.232					
	Total	155	1730						
2-A	Model(Reg.)	8	1472.1	184.013	930.81	0.984	0.4446	1.474	-15.05
	Error(Res.)	124	24.514	0.198					
	Total	132	1496.6						
2-B	Model(Reg.)	8	1686.0	210.759	703.36	0.975	0.5474	0.912	2.59
	Error(Res.)	147	44.04	0.3					
	Total	155	1730						
3-A	Model(Reg.)	7	1462.8	208.979	773.63	0.977	0.5197	1.216	-2.05
	Error(Res.)	125	33.766	0.270					
	Total	132	1496.6						
3-B	Model(Reg.)	7	1667.7	238.251	565.44	0.962	0.6491	0.66	-0.69
	Error(Res.)	148	62.361	0.421					
	Total	155	1730.1						
4	Model(Reg.)	8	1695.95	211.994	912.035	0.98	0.4821	1.246	-0.08
	Error(Res.)	147	34.169	0.232					
	Total	155	1730.12						
5	Model(Reg.)	6	1666.8	277.809	654.26	0.962	0.6516	1.021	0.08
	Error(Res.)	149	63.267	0.425					
	Total	155	1730.1						

Model 1-A
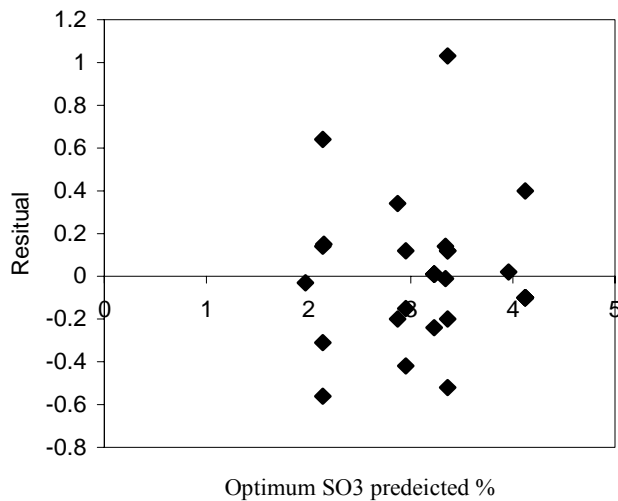
Fig. 1:Relationship between optimum SO3-
predicted and resituals
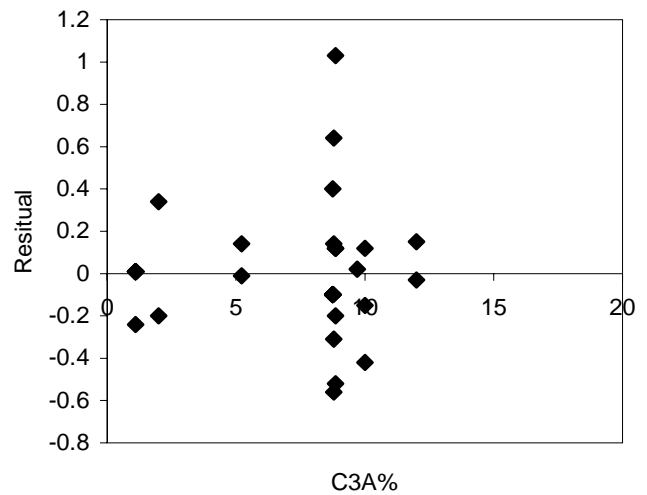
Fig. 2 :Relationship between C3A and resituals

Model 3-B
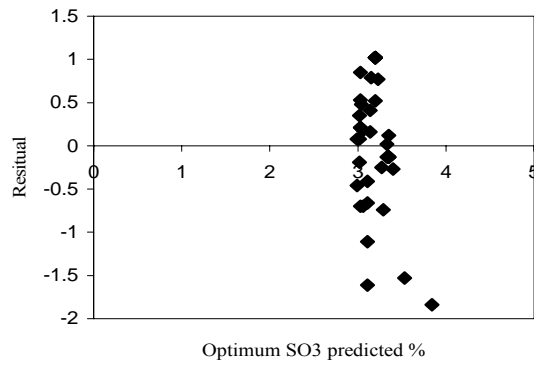
Fig. 3 :Relationship between optimum
SO3-predicted and resituals
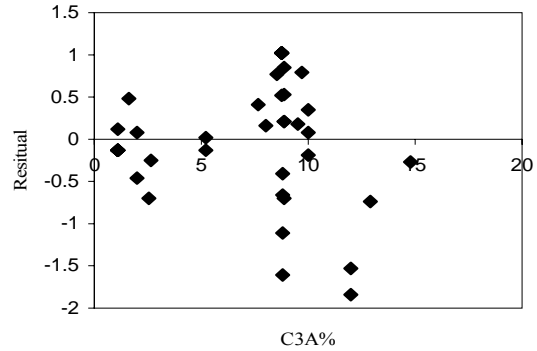
Fig. 4:Relationship between C3A
and resituals
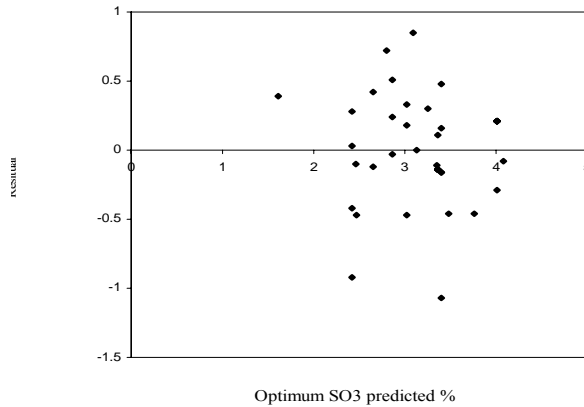
Model 4

Fig. 5 :Relationship between optimum SO3-
predicted and resituals
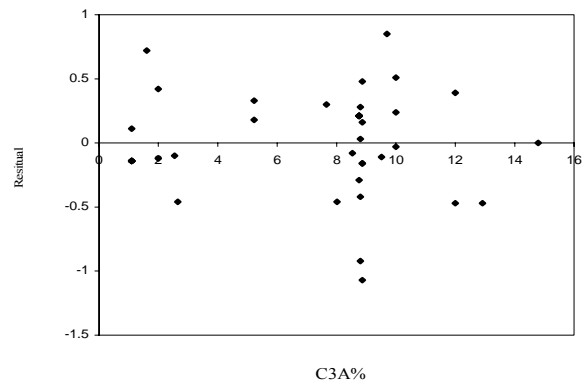
Fig. 6 :Relationship between C3A
and resituals

optimum SO3-predicted%
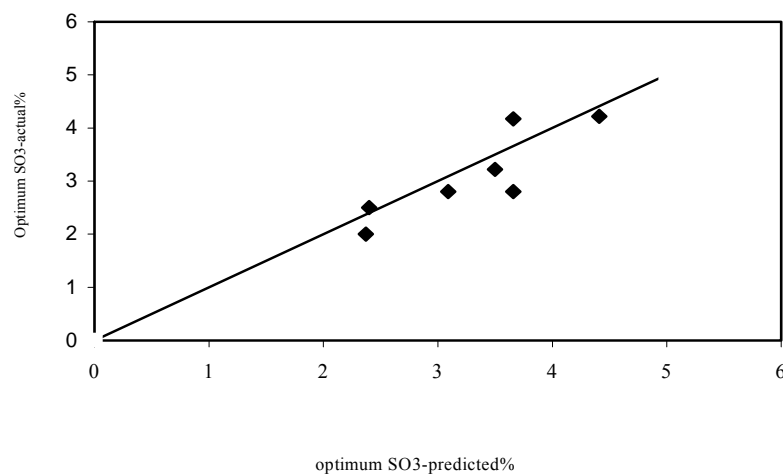
Fig. 7 : Relationship between optimum SO3-predic
and actual for concrete model -28-days (1-A model)

Dr. Zena K. Abbas
Prof. Dr. Riyadh S. Al-Rawi
Dr. A.H. Al-Neaime
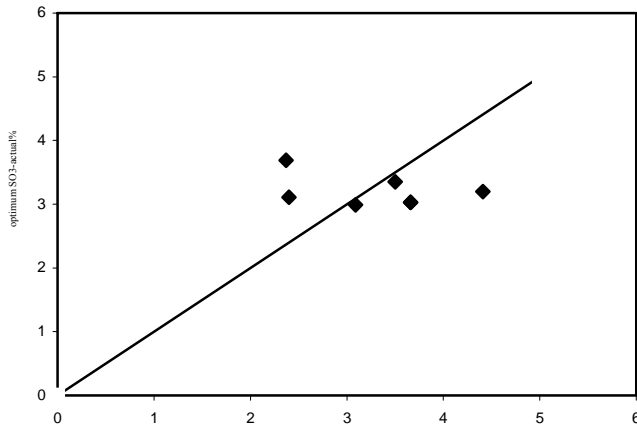
Fig. 8 : Relationship between optimum SO3-predicted and actual for concrete model -28-days (3-B model)
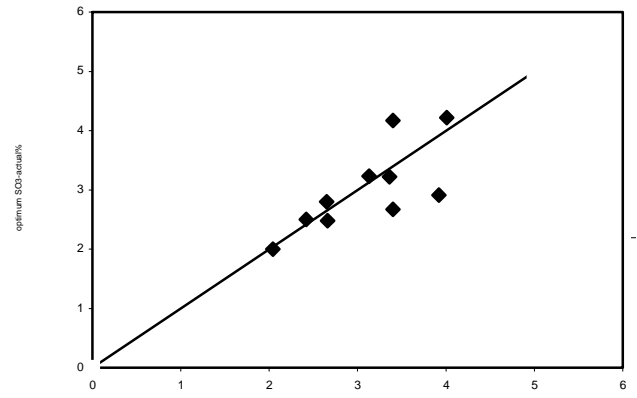
Fig. 9 : Relationship between optimum SO3-predic and -actual for concrete model -28-days (4 model)
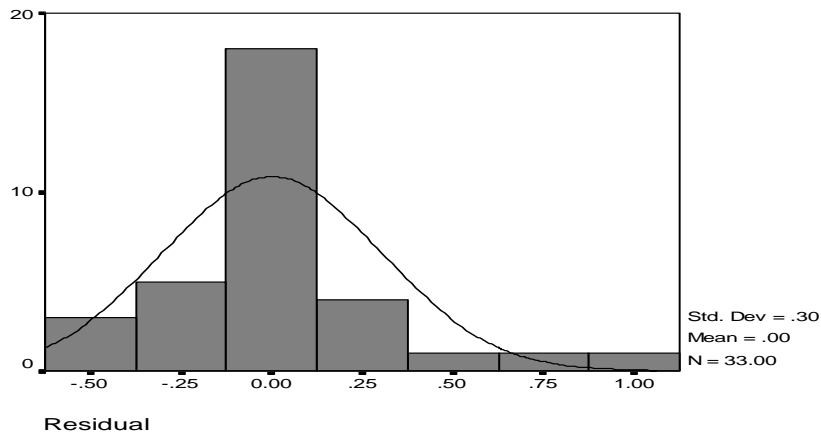
Fig. 10: Residual distribution for 28-days model (1-A)
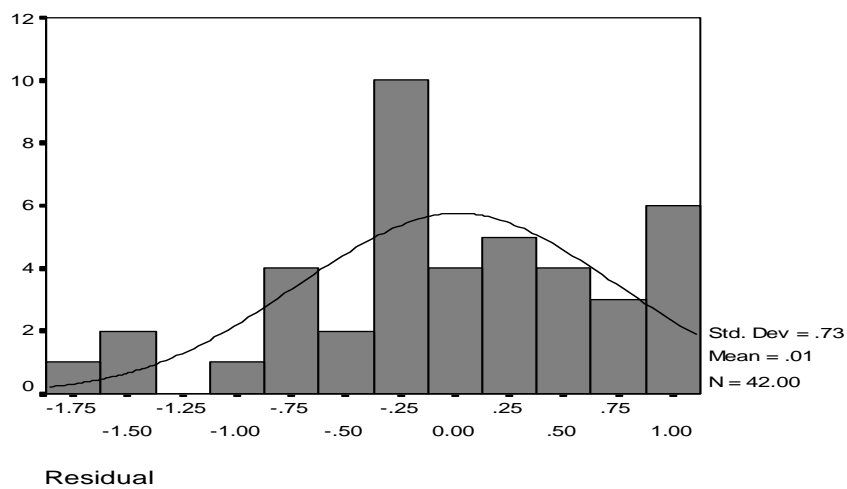
Fig. 11: Residual distribution for 28-days (3-B)
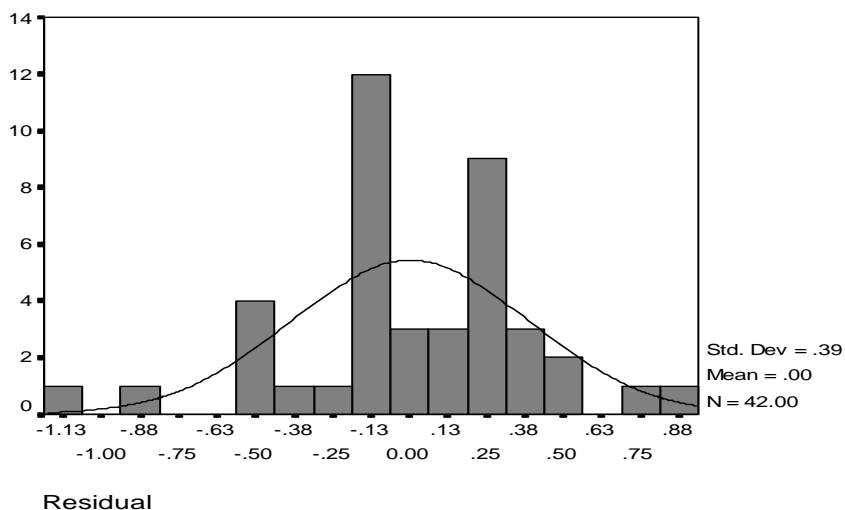
Fig. 12: Residual distribution for 28-days model (4)
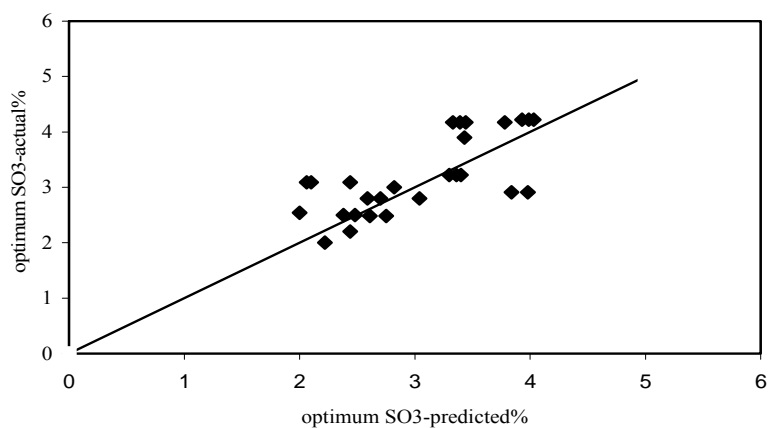
**Fig. 13 : Relationship between optimum SO3-predic
and actual for concrete model -late ages-model 4**
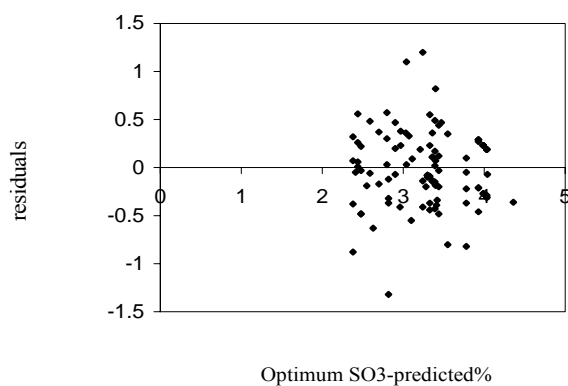
Fig. 14: Relationship between
optimum predicte SO3 and residuals
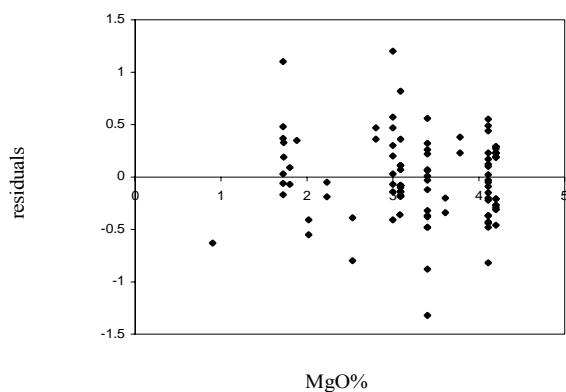
Fig. 15: Relationship between MgO
and residuals

261

Dr. Zena K. Abbas
Prof. Dr. Riyadh S. Al-Rawi
Dr. A.H. Al-Neaime

Statistical Model for Predicting the
Optimum Gypsum Content in Concrete
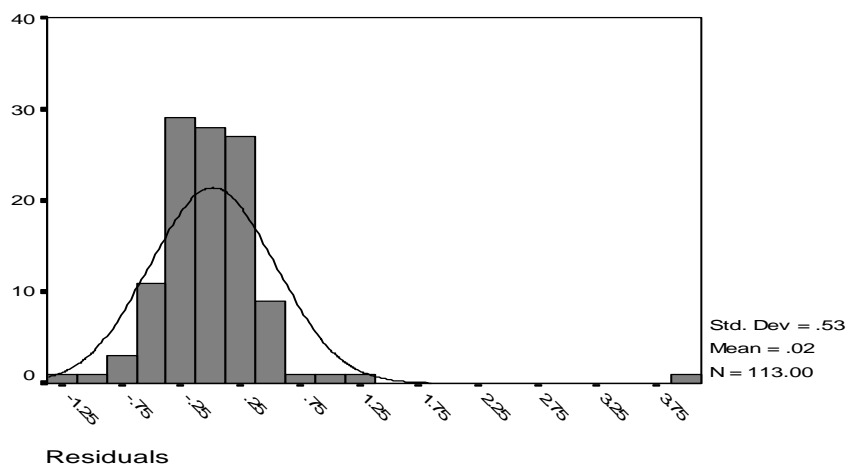
Fig. 16: Residual distribution for any age concrete model NO. 4
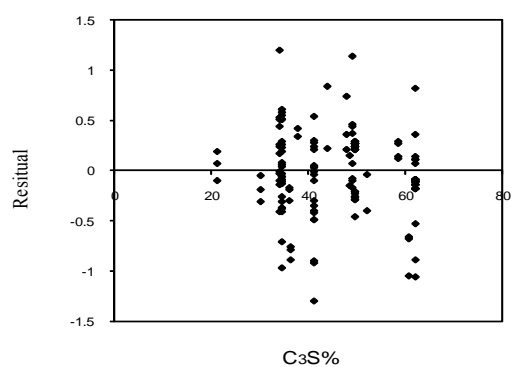
Fig. 17:Relationship between C₃S and resituals
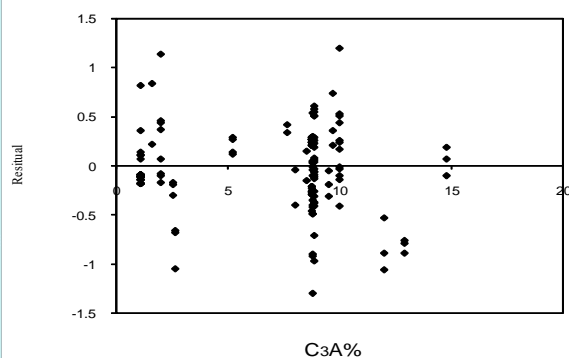
Fig. 18:Relationship between C3A and resituals
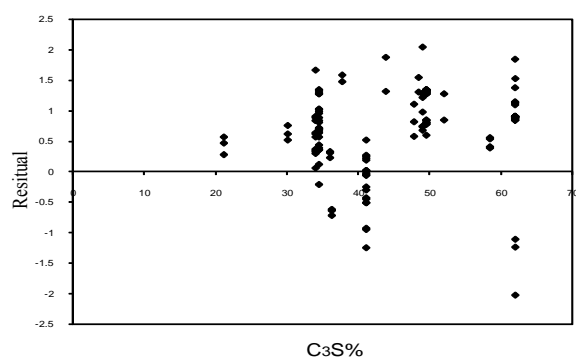
Model 4:

Fig. 19:Relationship between C₃S and resituals
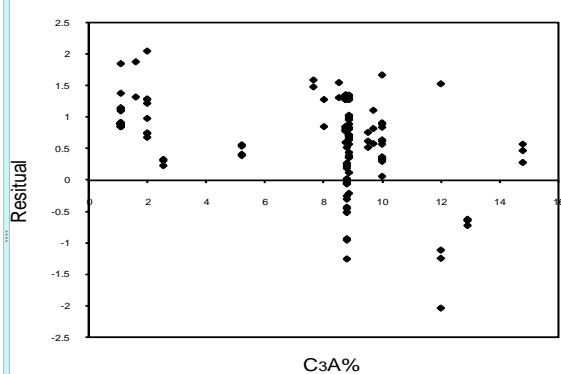
Fig. 20:Relationship between C3A andresituals
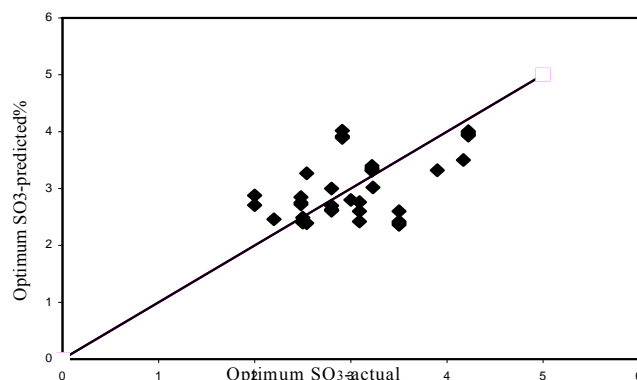
Model 5:

Fig. 21:Relationship between optimum SO3
actual and predicted
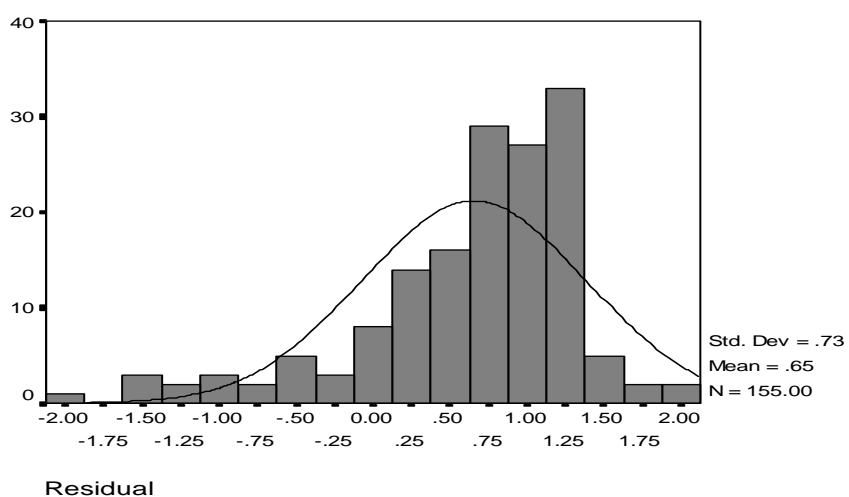
Fig. 22: Residuals distribution for concrete (all Age) - model 4

Application of Wavelet Packet and S Transforms for Differential Protection of Power Transformer

Waad Noori Taboor
M.Sc student
Waad_nori@yahoo.com

Dr. Adel Ahmed Obed
Lecturer
adelrazan@yahoo.com

Dr. Majed Abdul Nabi Alwan
Lecturer
altimimee@yahoo.com

Department of Electrical Engineering, Basrah University

ABSTRACT:

The differential protection of power transformers appears to be more difficult than any type of protection for any other part or element in a power system. Such difficulties arise from the existence of the magnetizing inrush phenomenon. Therefore, it is necessary to recognize between inrush current and the current arise from internal faults. In this paper, two approaches based on wavelet packet transform (WPT) and S-transform (ST) are applied to recognize different types of currents following in the transformer. In WPT approach, the selection of optimal mother wavelet and the optimal number of resolution is carried out using minimum description length (MDL) criteria before taking the decision for the extraction features from the WPT tree. In ST approach, the spectral energy index and the standard deviation (STD) are calculated from the S-matrix obtained by discrete S-transform. The two approaches are tested for generating a trip signal and disconnecting the transformer supply experimentally using 1KVA, 220/110V, 50Hz, Δ / Y three-phase transformer. The experimental results show that the trip signal is initiated faster in WPT approach while the transformer is disconnected from the supply after a delay of 10-15msec in the two approaches due to computer interface and the relay circuit used.

Keywords: differential protection, wavelet packet transform, S-transform, inrush and fault Currents recognition

<div dir="rtl">

استخدام تحويليتي ربطة المويجة وربطة المويجة المعدلة في الحماية التفاضلية لمحولة القدرة

د. ماجد عبد النبي علوان   د. عادل احمد عبيد   وعد نوري طابور
مدرس   مدرس   طالبة ماجستير

الخلاصة:

تبدو الحماية التفاضلية لمحولات القدرة أصعب من أية حماية لأي جزء أو عنصر في نظام القدرة. إن هذه الصعوبة تكمن من نشوء ظاهرة تيار التدفق المغناطيسي لحظة التشغيل. لذلك من الضروري التمييز بين تيار التدفق والتيارات الناشئة من تيارات الخطأ الداخلية. في هذا البحث تم استخدام طريقتين للتمييز بين تيار التدفق وتيارات الخطأ الداخلية اعتمادا على تحويله ربطة المويجة وتحويله ربطة المويجة المعدلة. في الطريقة الأولى تم اختيار المويجة الأم وأفضل مستوى حل باستخدام دالة الطول الأصغر قبل اتخاذ قرار استخلاص المعالم من شجرة تحويله المويجة. في الطريقة الثانية تم حساب دليل الطاقة الطيفية والانحراف القياسي من مصفوفة S التي حسبت من تحويله ربطة المويجة المعدلة. اختبرت كلا الطريقتين لتوليد إشارة عزل المحولة من المصدر عمليا باستخدام محولة ثلاثية الطور   50Hz ,220/110V ,1KVA Y / Δ. أظهرت النتائج العملية بأن إشارة العزل تتولد أسرع في الطريقة الأولى بينما تنعزل المحولة عن المصدر بعد تأخير زمني من 10-15 ملي ثانية في كلا الطريقتين بسبب توصيلة الحاسبة ودائرة المرحل المستخدمة.

الكلمات المفتاحية: الحماية التفاضلية، تحويله ربطة المويجة، تحويله S، تمييز تيارات الخطأ وتيارات التدفق.

</div>

1- INTRODUCTION:

The protection of power transformer has been always in a challenge due to the problem of rapid discriminating between the inrush and internal fault currents. A possibility for false tripping of differential relay may be caused by the magnetizing inrush current during energization. Such wrong-operation of differential relays can affect both reliability and stability of the whole power system [S. A. Saleh, et. al., 2005].

The conventional methods use the second harmonic components to restrain operation of the differential relay during magnetizing inrush conditions. The main idea of the harmonic restraint differential relays is to extract the fundamental, the second and sometimes the fifth harmonics and to compare the ratio of the second and fifth harmonics with the fundamental to predefined threshold value. However, sometimes, the magnitude of second harmonic components in the internal fault current can be close to or greater than the magnitude of inrush currents. This may be due to saturation and the new low-loss amorphous core material in modern power transformer [B. A. Sykes, et., al., 1972 and M. R. Zaman, 1996].

The previous methods on power transformer protection include other approaches, among these approaches; calculation of transformer inductance during saturation, artificial neural network (ANN), flux and voltage restraints and fuzzy logic [L. D. Periz, et., al., 1994, A. Wiszniewski, et., al., 1995, M. R. Zaman, 1996, A. L. Oville, et., al., 2001, M. C. Shin, et., al., 2003, H. Khorashadi, 2006].

Recently, signal processing has been reported on use of time frequency localization for current signal recognition. Wavelet (WL) decomposition is ideal for studying transient signals and obtaining a much better current characterization and a more reliable recognition. It allows the decomposition of the signal into different levels of resolution. The mother wavelet function is dilated at low

Frequencies and compressed at high frequencies so that large windows are used to obtain the low frequency components of the signal, while small windows reflect discontinuities. Therefore, from small windows, a certain features can be extracted to recognize between inrush and internal fault currents [S. A. Saleh, et. al., 2005, A. Rahmati, 2010, S. A. Saleh, et. al., 2010]. In WL analysis, a proper mother wavelet function and a level of decomposition should be chosen which are sometimes difficult, thereby the computation time may increase. These limitation can be overcome using the modified WL transform named S-transform (ST). The S-transform is an invertible time frequency spectral localization technique that combines element of WL transform and short time Fourier transform (STFT) [P. K. Dash, et., al., 2003, S. R. Samantaray, et., al., 2007, Q. Zhang, et., al., 2009, S. Jiao., et., al., 2010, G. Mokryani, et., al., 2010 and A. A. Obed, et., al., 2011].

The main objective of this paper is to develop and implement two approaches to recognize inrush current from faults based on wavelet packet transform (WPT) and S-transform. The MDL criterion is used to select both the mother wavelet and the level of decomposition for the WPT algorithm used. A signatures which represent the values and the time locations of the coefficients depend on the second level details ad^2 and dd^2 are considered in this algorithm. In the second approach, the spectral energy index and the STD are calculated from the S-matrix and used as an extraction features for signal recognition. The two approaches are examined experimentally on 1KVA, 220/110V, 50Hz, Δ / Y three-phase transformer and the results revel fast, accurate and reliable methods to recognize different current following in the transformer.

2- APPLICATION OF SIGNAL PROCESSING IN DIFFERENTIAL ROTECTION OF POWER TRANSFORMER

The application of signal processing in power system transient has become increasingly popular in recent years due to its effectiveness in capturing short term transients. Basically, STFT transform, wavelet transform and S-transform are a means of obtaining a representation of both time and frequency contents of a differential current signal used in differential protection of power transformer. In this work, a short brief for WPT and ST are given.

2.1 Wavelet Packet Transform

Wavelet packet transform is a type of wavelet-based signal processing in a way that each level of resolution (octave) j consists of 2^j boxes generated by a tree of low pass filter (LPF) and high pass filter (HPF) operations. The frequency bandwidth of a box decreases with growing octave number i.e. with increasing octave number, the frequency resolution becomes higher while the time resolution is reduced. Starting with a discrete signal f[n] with length N, the first level, j=1, decomposition produces two subbands discrete signals $a^1[N/2]$ and $d^1[N/2]$ as follows [G. Stang , et., al., 1996 and M. A. S. K. Khan, et., al., 2007]

$$a^1[n] = \sum_{k=0}^{N-1} g(k)\, f(n-k) \qquad (1)$$

$$d^1[n] = \sum_{k=0}^{N-1} h(k)\, f(n-k) \qquad (2)$$

where $a^1[n]$ and $d^1[n]$ are the first level approximations and details respectively, k is an integer and g(n), h(n) are the LPF and HPF associated with a selected mother wavelet function respectively. The output of both LPF and HPF are downsampled by two at the end of each filtering stage in order to increase the frequency resolution and to ensure the time localization of each frequency subband. The second level of decomposition will produce four subbands due to the decomposition of both $a^1[N/2]$ and $d^1[N/2]$ using the same set of filters. These subbands are $aa^2[N/4]$ $ad^2[N/4]$, $da^2[N/4]$ and $dd^2[N/4]$ as follows

$$aa^2[n] = \sum_{k=0}^{\frac{N}{2}-1} g(k)\, a^1(n-k) \qquad (3)$$

$$ad^2[n] = \sum_{k=0}^{\frac{N}{2}-1} h(k)\, a^1(n-k) \qquad (4)$$

$$da^2[n] = \sum_{k=0}^{\frac{N}{2}-1} g(k)\, d^1(n-k) \qquad (5)$$

$$dd^2[n] = \sum_{k=0}^{\frac{N}{2}-1} h(k)\, d^1(n-k) \qquad (6)$$

A higher level of decomposition can be produced in the same procedure above.

The main advantage of WPT over continuous and discrete wavelet transform is better, more accurate and more detailed representation of the decomposed signals [G. Stang, et., al., 1996]. Also, wavelet packet basis functions are localized in time offering better signal approximation and decomposition. These basis functions are generated from one base function at scale s, dilation a and translation b as follows

$$w_{s,a,b}(n) = 2^{j/2}\, W_a(2^{-j}(n-b)) \qquad (7)$$

where $W_a(n)$ is the wavelet function coefficient matrix. In WPT, a discrete signal f[n] is represented as a sum of orthogonal

Wavelet basis functions $w_{s,a,b}(n)$ as follows:

$$f[n] = \sum_s \sum_a \sum_b w_{s,a,b}[n] W_a[n] \qquad (8)$$

The implementation procedure of the WPT for two levels is shown in the decomposition tree of Fig.1.

2.2 The Extended Wavelet Transform: S-Transform

The S-transform, is an extension to the ideas of wavelet transform, and is based on a moving and scalable localizing Gaussian window. From the S-matrix, an important information in terms of magnitude, phase and frequency can be extracted. Further, feature extraction is done by applying standard statistical techniques onto the S-matrix.

Many features such as amplitude, variance, mean, standard deviation and energy of the transformed signal are widely used for proper classification. The S-transform is fully convertible from the time domain to two-dimensional (2-D) frequency translation domain and to then familiar Fourier frequency domain. The amplitude frequency- time spectrum and the phase-frequency- time spectrum are both useful in defining local spectral characteristics.

The S- transform produces a time frequency representation of a time varying signal by uniquely combining the frequency depended resolution with simultaneously localizing the real and imaginary spectra. The S-transform is similar to the wavelet transform but with a phase correction and here both the amplitude and phase spectrum of the signal are obtained. Since the S-transform provide the local spectrum of a signal, the time averaging of the local spectrum gives the Fourier transform [P. K. Dash, et., al., 2003 and M. V. Chilukuri, et., al., 2004].

CONTINUOUS S- TRANSFORM

It is well known that information is contained in the phase of the spectrum, as well as in the amplitude. In order to utilize the information contained in the phase of the continuous wavelet transform (CWT), it is necessary to modify of the mother wavelet. The CWT $W(\tau, a)$ of a function f(t) is given as

$$W(\tau, a) = \int_{-\infty}^{\infty} h(t) \; W(t - \tau, a) \, dt \qquad (10)$$

where $W(\tau, a)$ is a scaled replica of the fundamental mother wavelet, the dilation a determines the width of the wavelet and this controls the resolution. The S-transform is obtained by multiplying the CWT with a phase factor as [S. Sendilkumar, et., al., 2009, P. K. Dash, et., al., 2003 and M. V. Chilukuri, et., al., 2004].

$$S(\tau, f) = \exp(i2\pi f\tau). \; W(\tau, a) \qquad (11)$$

where f is the frequency, and the quantity τ is a parameter which controls the position of Gaussian window on the t-axis and a is the dilation factor. The mother wavelet for this particular case is defined as

$$w(t, f) = \frac{|f|}{\sqrt{2\pi}} . \; \exp(\frac{-t^2 f^2}{2}).\exp(-i2\pi ft) \qquad (12)$$

In the equation above, the dilation factor "a" is the inverse of the frequency f. Thus, the final form of the continuous S-transform is obtained as

$$S(\tau, f) = \int_{-\infty}^{\infty} h(t). \frac{|f|}{\sqrt{2\pi}} \exp(\frac{-(\tau-t)^2 f^2}{2}).\exp(-i2\pi ft) dt$$
$$(13)$$

and the width of the Gaussian window $\sigma(f)$ is

$$\sigma(f) = T = \frac{1}{|f|} \qquad (14)$$

DISCRETE S-TRANSFORM

The signal h(t) can be expressed in a discrete from as h(kT), k=0,1,……...,N-1 and T is the sampling time interval. The discrete Fourier transform of h(kT) is obtained as [P. K. Dash, et., al., 2003 and M**.** V. Chilukuri, et., al., 2004]

$$H\left[\frac{n}{NT}\right] = \frac{1}{N}\sum_{k=0}^{N-1} h(kT).\exp\left(\frac{-i2\pi nk}{N}\right) \qquad (15)$$

where n=0, 1,……...., N-1. Using eq. (13), the S-Transform of a discrete time series h(kT) is obtained by making $f = n/NT$ and $\tau = jT$ as

$$S\left[jT,\frac{n}{NT}\right] = \sum_{m=0}^{N-1} H\left[\frac{m+n}{NT}\right] G(m,n)\exp(2\pi mj/N)$$
$$(16)$$

and

$$G(m,n) = \exp(-2\pi^2 \, m^2 / n^2) \qquad (17)$$

where j, m =0, 1, 2,…......, N-1, and n= 1, 2,…......, N-1. For n=0

$$S(jT,0) = \frac{1}{N}\sum_{m=0}^{N-1} h\left(\frac{m}{NT}\right) \qquad (18)$$

Equation 18 gives the constant average of the time series into zero frequency, so that the amplitude of the S-matrix over the time results in Fourier spectrum. The amplitude and phase of the S-transform are obtained as

$$\left|S\left[jT,\frac{n}{NT}\right]\right|, \tan^{-1}\left\{Imag\left(S\left[jT,\frac{n}{NT}\right]\right)/Real\left(S\left[jT,\frac{n}{jT}\right]\right)\right\}$$

The multiresolution S-transform output is a complex matrix, the row of which is the frequency and the columns are the time values. Each column thus represents the "local spectrum" for that point in time. Also, frequency-time contours which have the same amplitude spectrum are obtained to detect, and localize signal disturbance events. A mesh

three-dimensional (3-D) of the S-transform output yields frequency-time, amplitude-time, and frequency-amplitude plots.

3. EXPERIMENTAL SETUP AND DATA COLLECTION

The initial and important step in this work is to setup the protected transformer with all necessary equipments to accurately collect the needed data for analytical purpose and then to protect the transformer from internal faults. Figure 2 shows the schematic diagram for the implemented protection system given in Fig.3. The system is applied to 1KVA, 220/110V, 50Hz, Δ / Y three-phase transformer. Three identical current transformer (CTs) are connected in Y on the Δ connected primary side while another three identical CTs are connected in Δ on the Y connected secondary side. The ratios of the primary side CTs and the secondary side CTs are chosen in a manner that guarantees a negligible value of the differential current under steady state operation conditions. The differential current signal of the three phases passes through 1Ω resistor combination. Theses signals are sent into personal computer (PC) through analogue to digital circuit (LabJack-U3-HV), shown in Fig.4. The LabJack can operate also as digital to analogue converter.

The collected data consists of the differential current of different magnetizing inrush current, different external fault currents and different internal current under load and noload conditions. For the case of collecting data, a conductor, timer and switch (switching circuit), as shown in Fig.5, is used to isolate the transformer after ten cycles from the running instant to avoid damage in the transformer and the equipments used.

When the decision features are extracted and the algorithm of WPT and ST are ready to use, the tripping signal, if initiated, is used to isolate the supply by a relay circuit connected instead of the switching circuit. The schematic and the implemented relay circuits are shown in Figs. 6 and 7. The digital trip signal

Generated from the recognition algorithms is converted to analogue by the LabJack and sent

to the relay circuit to use it for the complete system protection.

The data for different operating conditions is sampled at 6.4kHz, 128 samples per cycle and stored to be processed for constructing the features in the two mentioned algorithms.

4. DECISIONS FOR EXTRACTION FEATURES

In order to detect any fault following a disturbance, it is necessary to build an extraction features. A successful feature involves the identification of abnormal conditions by the mathematical modeling of the complete system or the analysis of the fault current signature resulting from different transient disturbances. A signature analysis method is used in the two approaches used in this work.

4.1. WPT Approach

Three various conditions from the collected data are used for the analysis of selecting the optimal mother wavelet filter and the number of level of decomposition. These various conditions are; unloaded magnetizing inrush current, primary double line to ground internal fault loaded and single line to ground external fault loaded.

The optimal mother wavelet filter can be selected by calculating the MDL index using the following formula [N. Saito, 1994 and S. A. Saleh, et. al., 2005]

$$MDL_x(k, j) = \min \left\{ \frac{3}{2} k \log N + \frac{N}{2} \log \left\| \overline{\alpha}_{xj} - \overline{\alpha}_{xj}^{(k)} \right\|^2 \right\}$$

(19)

Where $0 \leq k < N$ which represents the length of the signal $f[n]$, $1 \leq j < M$ the total number of wavelet filter (level of resolution) used for the decomposition of the signal $f[n]$, $\overline{\alpha}_{xj} = W_{xj} f[n]$ denotes to the vector of

decomposition coefficients of $f[n]$ up to level j, $\overline{\alpha}_{xj}^{(k)} = \theta^{(k)} W_{xj} f[n]$ denotes to the vector that contains k non-zero elements and $\theta^{(k)}$ is the hard threshold operation that keeps the k largest elements of $\overline{\alpha}_{xj}$ in absolute value intact and set all other elements to zero. The first term of the MDL criteria index represents the penalty function that is increasing linearly with the number of the retained wavelet coefficients k, while the second term describes the logarithmic energy residual between $\overline{\alpha}_{x,j}$ and $\overline{\alpha}_{x,j}^{(k)}$. It should be noted that the residual energy decreases as k increases. The number of coefficients k for which the MDL function reaches the minimum value, is considered as an optimal one.

The MDL index is calculated up to the second level of decomposition for five types of orthogonal and bi-orthogonal mother wavelet functions. The results for the three conditions are given in Tables 1, 2 and 3. From the these tables, it can be noted that Daubechies (db4) has the smallest value of MDL index in the first level. Therefore it can be considered the optimal mother wavelet function. These low values of MDL(1) may be due to the jumps of the data at the switching instant and some missing data. Thus, MDL(1) may not provide accurate indication and the higher levels of resolution will include more detailed representation of the signal. The optimal level of decomposition j is reached when MDL(j) is less than levels of higher j. Table 4 presents four levels of MDL index using db4 mother wavelet. The second level has the lowest values of MDL index. Therefore, the second level is selected as the optimal level of decomposition.

To extract features for the WPT algorithm, the signals of the different differential currents are decomposed up to the second level of resolution by WPT using the selected mother wavelet function (db4). [S. A. Saleh, et. al., 2005] proposes an algorithm for the same features depends on the second level high

frequency details (dd^2). This approach looks at the second level high and low frequency details (dd^2 and ad^2) for different current signals. These details are given in Fig. 8.

The values of these coefficients and their time locations represent the needed signatures to recognize the type of the investigated current. It is clear that the normal (inrush) current and the external fault current do not have any high frequency details components in the second level dd^2 and a threshold value for low frequency details in the second level. When an internal fault occurred, the details dd^2 and ad^2 show a threshold value frequency components, which can be used as a features extraction recognition. Therefore, the WPT algorithm is depended on the identification of dd^2 and ad^2 components or coefficients in the second level.

4.2 S-Transform Approach

The computation of the discrete S-transform can be outlined as follows.

1. Denote n/NT, m/NT, kT, and jT as n, m, k, and j respectively, for all of the computations.
2. Obtain discrete Fourier transform H[n] of the original time-varying signal h[k], with N points and sample interval T, using DFT routine from eq. (15).
3. Compute the localizing Gaussian G[n,m] for the required frequency n using eq. (17).
4. Shift the spectrum H[n] to H[m+n] for the frequency n by using convolution theorem.
5. Obtain the product of H(m+n) and G(m+n) and take inverse Fourier transform of the product to get S transform as eq. (16).

The multiresolution S-transform output is a complex matrix, the row of which is the frequency and the columns are the time values. Each column thus represents the "local spectrum" for that point in time. Also, frequency-time contours which have the same amplitude spectrum are obtained to detect, and localize signal disturbance events. A mesh

three-dimensional (3-D) of the S-transform output yields frequency-time, amplitude-time, and frequency- amplitude plots.

To illustrate the use of multiresolution S-transform for nonstationary signal analysis, a sample of inrush current waveform in a data window of eight cycles (using a sampling rate of 128 samples/ cycle) is considered. The three-dimensional (3-D) mesh for the signal shown in Fig. 9(a) is shown in Fig. 9(b). From the 3-D plot, one can find the magnitude, frequency, and time information's to detect, localize, and visually classify the event. Also, it is observed that the increase or decrease of the signal magnitude can be deduced from the innermost (or the lowest level) contour. Similar plots are shown for a sample of internal fault current waveform in Fig. 10. It is mentioned here that the time axis is replaced by the number of samples.

After the signal is retrieved, S-transform is used to process the signal samples to provide the relevant features for identifying the type of fault. The energy of inrush current and fault current are computed through Parseval's theorem [M. O. Oliveira, et., Al., 2008] from S-matrix output. On the other hand, the standard deviation is directly applied to the S-matrix output to derive the Standard Deviation (STD) values for the corresponding phase, for example, the feature extraction of energy and standard deviation of S-transform contour are obtained from Matlab functions as [S. Sendilkumar, et., al., 2009]

Energy a = (S-matrix a) ^ 2   (20)
S-matrix a = S-matrix of phase a and
STD a = std (abs (S-matrix a))   (21)

Table 5 shows the spectral energy and the STD for different inrush, internal and external fault current for different connections of the three-phase transformer. It can be seen from this table that the values of energy vector and STD are able to be differentiable effectively between them or as pattern recognition to discriminate between inrush, external and internal fault current. This pattern is used to

Waad Noori Taboor
Dr. Adel Ahmed Obed
Dr. Majed Abdul Nabi Alwan

Implement the S-transform algorithm used in this work.

5. ALGORITHMS IMPLEMENTATION AND EXPERIMENTAL RESULTS

The two algorithms are implemented experimentally to examine the ability of recognition between the internal fault currents and the current of inrush and external faults. Figure 11 shows the flowcharts for the software implementation of the two algorithms. In WPT algorithm, the three-phase differential current is read through the CTs and root summed squared together into one value before being passed to low and high pass filters to construct the first level d^1 and a^1. The output is downloaded by two and then passed through another low and high pass filter to construct dd^2 and ad^2. If the absolute value of dd^2 and ad^2 are higher than threshold, then it generates a trip signal in order to disconnect the transformer from the supply.

In ST algorithm, the S-matrix is calculated for each phase current. The energy and the standard deviation are also calculated. If E and STD are greater than the threshold, then a trip signal is initiated. Otherwise, a restrain signal is appear.

Several magnetizing inrush currents, external and internal fault currents both in load and noload cases are used to test the two algorithm with the hardware of the complete protection system. Three cases differ from that used in MDL calculation. Figure 12 shows the three-phase differential current and the trip signal generated by WPT algorithm (Fig. 12 a) and by ST algorithm (Fig. 12 b) for the case of magnetizing inrush current with a balanced Y-connected full load unity power factor. The two algorithms used do not generate any trip signal. Figure13 shows the same results for the case of loaded external three-phase to ground fault current after energization. The trip signal status is also not changed.

Two cases of different internal faults are considered to show the ability of disconnecting the transformer from the supply. Figures 14 and 15 show the results unloaded secondary three-phase to ground fault and unloaded secondary internal two-phase to ground fault respectively. In the two cases, the trip signal is generated

6. CONCULSIONS

This paper presents and applies two approaches for differential protection of power transformer based on WPT and S transforms. The main function of these approaches is how to recognize between (internal faults) and (inrush and external faults). The two approaches do not need any kind of training or harmonic analysis. The WPT method must select the optimal for both the mother wavelet filter and the number level of resolution. This limitation is overcome using S-transform but WPT is fast for recognition of current type. The two methods are quite simple to implement and easy to be coded with a small amount memory for storage and compilation. The two methods are applied with hardware implementation of the overall system and the experimental results are accurate, prompt and can be used for differential protection of power transformer.

7- REFERENCES
A. L. Oville-Fernandez, N. K. J. Ghonaim, and J. A. Valencia, "A FIRANN as a Differential Relay for Three Phase Power Transformer Protection", IEEE Trans. Power Delivery, Vol.16, No. 2, PP. 215-218, 2001.

A. Rahmati "An Adaptive Differential Relay for CT Saturation Based on Wavelet Transform" IEEE, PES T&D, PP1-6, 2010.
A. A. Obed, M. A. Alwan and W. N. Taboor, "A Wavelet Packet Transform-Based Technique for the Discrimination of Inrush Currents from Faults in Three-Phase Transformer" Journal of Basrah Researches, Vol. 37, No. 4A/15, PP 1-14, Aug. 2011.

A.Wiszniewski and B. Kasztenny, "A multi criteria differential transformer relay based on fuzzy logic, IEEE Trans.Power Delivery, 10 (4), 1786-1792, 1995.

B. A. Sykes and I. F. Morrison, "A Proposed Method of Harmonic Restraint Differential

Protection of Transformers by Digital Computer," IEEE Trans. Power App. Syst. vol. PAS-91, pp. 1266-1272, May 1972.

G. Stang and T. Nguyen, "Wavelet and Filter Banks" Wellesley,   MA: Wellesley-Cambridge, 1996.

G. Mokryani, M. R. Haghifam, H. Latafat , P. Aliparast, and A. Abdollahy, "Detection of Inrush Current Using S-Transform and Probabilistic Neural Network", Transmission and Distribution conference and Exposition, pp.1-6, IEEE PES, 2010.

H. Khorashadi, "Fuzzy-Neuro Approach to Investigating Transformer Inrush Current," Transmission and Distribution Conference and Exhibition, pp. 1302-1306, May, 2006.

L. D. Periz, A. J. Flechsig, J. L. Mendor, and Z Obradovic, " Training of Artifical Neural Network to Discriminate between Magnetizing Inrush and Internal Faults", IEEE Trans. Power Delivery, Vol. 9, No. 1, PP.434-441, 1994.

M. R. Zaman, "Artificial Neural Network Based Protection of Power Transformer", Ph.D thesis, Memorial University of Newfoundland, St. John's, NF, Canda, 1996

M. V. Chilukuri and P. K. Dash, "Multiesolution S-Transform-Based Fuzzy Recognition System for Power Quality Events" IEEE Tran. Power Delivery., Vol. 19, No. 1, pp.323-330, January, 2004.

M. A. S. K. Khan, T. S. Radwan and M. A. Rahman, "Real Time Implementation of Wavelet Packet Transform Based Diagnosis and Protection of Three-Phase Induction Motors" IEEE Trans. Energy Conversion, Vol. 22, No. 3, Sep., 2007.

M.C.Shin, C.W.Park and J.H.Kim, "Fuzzy Logic - Based Relaying for Large Power Transformer Protection", IEEE Trans.Power Delivery, 18 (3), 718-724, 2003.

M. O. Oliveira, R. H. Salim and A.S. Bretas, "Wavelet Transform Approach for Differential Protection of Three-Phase Transformers", 2008

43rd International universities power Engineering conference, pp.1-5, 2008.

N. Saito, "Simultaneous Noise Suppression and Signal Compression using a Library of Orthogonal Basis and the Minimum Description Length Criterion" in Wavelet in Geophysics. E. Foufoula-Georgiou and Kumar, Eds. New York: Academic, PP. 299-324, 1994

P. K. Dash, B. K. Panigrahi, and G. Panda "Power Quality Analysis Using S-Transform" IEEE Tran. Power Delivery., vol. 18, No. 2,pp.406-411, April 2003

Q. Zhang, S. Jiao and S. Wang, "Identification Inrush Current and Internal Faults of Transformer Based on Hyperbolic S-transform", IEEE Conference on Industrial Electronics and Applications, pp. 258-263, 2009.

S. A. Saleh and M. A. Rahman, "Modeling and Protection of a Three-Phase Power Transformer using Wavelet Packet Transform", IEEE Trans. Power Del., Vol. 20, No. 2, pp. 1273–1282, Apr. 2005.

S. R. Samantaray, B. K. Panigrahi, P. K. Dash and G. Panda, "Power Transformer Protection using S-transform with Complex Window and Pattern Recognition Approach" IET Gener. Transm. Distrib., pp. 278–286, 2007.

S. A. M. Salah and M. A. Rahman "Testing of a Wavelet-Packet-Transform-Based   Differential Protection for Resistance-Grounded Three-Phase Transformers" IEEE Trans. On Industry Applications, Vol. 46, No. 3, pp.1109-1117, May/June 2010.

S. A. Saleh, B. Scaplen, and M. A. Rahman, "A New Implementation Method of Wavelet-Packet-Transform Differential Protection for Power Transformers", IEEE Trans. Industry Application., Vol. 47, No. 2, March/April 2011.

S. Jiao and H. Huang, "Research on Identification Between Inrush Current and Internal Faults of Power Transformer Based on H-S Transform," 3rd International congress on Image and signal processing, pp. 3619-3624,2010.

Waad Noori Taboor
Dr. Adel Ahmed Obed
Dr. Majed Abdul Nabi Alwan

S. Sendilkumar, B. L. Mathur and Joseph Henry, "A New Technique To Classify Transient Events in Power Transformer Differential Protection Using S-Transform" Third International

Conference on Power Systems, Kharagpur, INDIA December 27-29, 2009.

LIST OF SYMBOLS AND APPREVIATIONS

ANN: Artificial Neural Network
CT: Current Transformer
CWT: Continuous Wavelet Transform
db: Daubechies mother wavelet
DFT: Discrete Fourier Transform
G(m,n): Gaussian Function

$H\left[\dfrac{n}{NT}\right]$: discrete Fourier transform function

HPF: High Pass Filter
I: current
LPF: Low Pass Filter
KVA: Kilo Volt Amper

MDL: Minimum Description Length
PC: Personal Computer
R: Relay

$S\left[jT,\dfrac{n}{NT}\right]$: S transform function of the discrete signal

$S(\tau,f)$: S transform function of the continuous signal
ST : S Transform
STD: STandard Deviation
STFT: Short Time Fourier Transform
WL: WaveLet
WPT: Wavelet Packet Transform
$W(\tau,a)$: continuous wavelet transform function

α_N : vector of the decomposition coefficients of f

$\alpha_N^{(k)}$: vector of the continuous nonzero elements

$\theta^{(k)}$: hard-threshold
$\sigma(f)$: Gaussian window
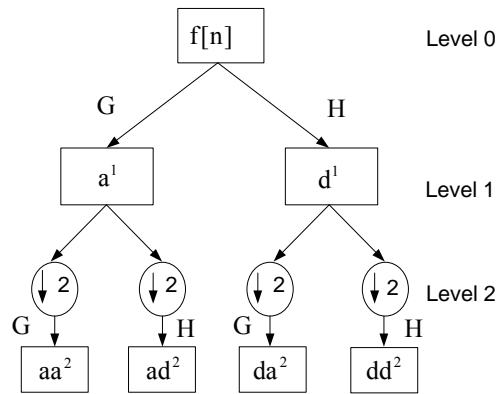
Fig.1 Two levels of decomposition by WPT
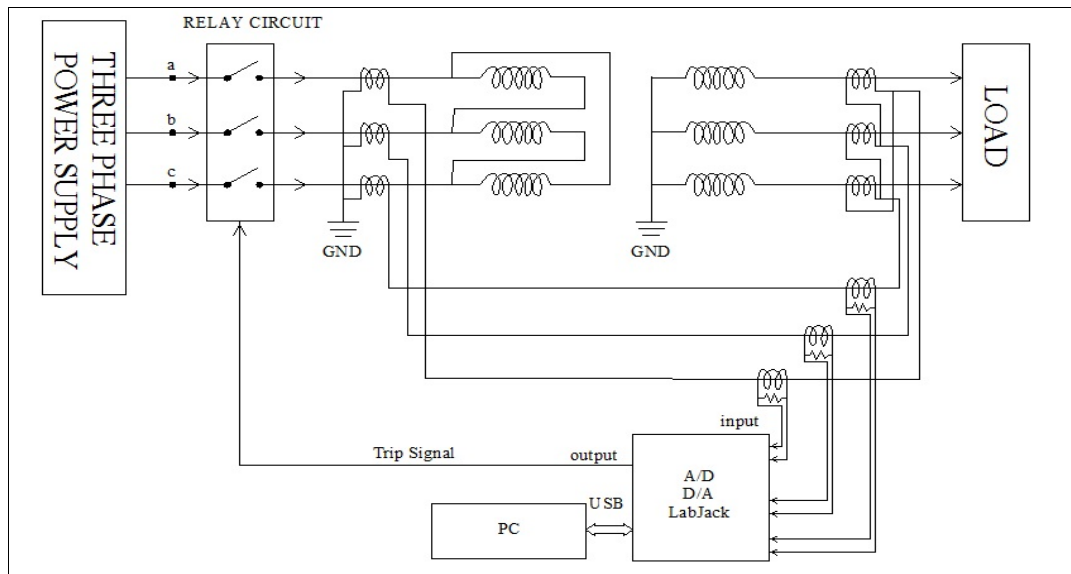
Fig.2 Schematic diagram for differential protection of the three- phase power transformer
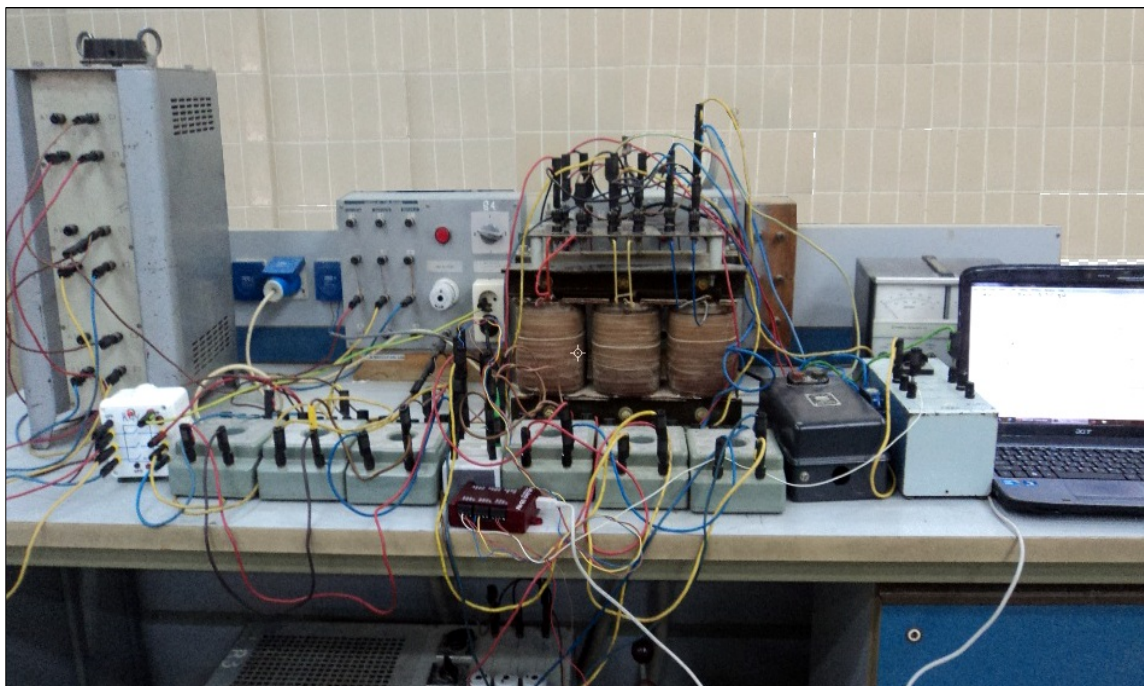
Fig.3 Implemented system for differential protection of the three- phase power transformer

Waad Noori Taboor
Dr. Adel Ahmed Obed
Dr. Majed Abdul Nabi Alwan
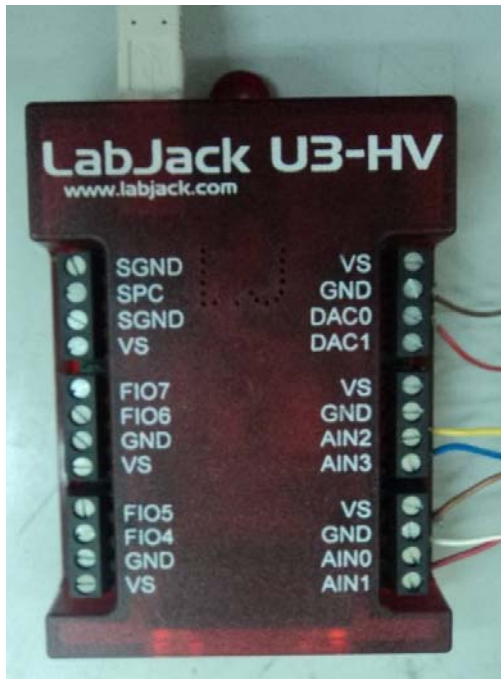
Fig.4 (Lab Jack U3-HV) circuit

Fig. 5 The switching circuit
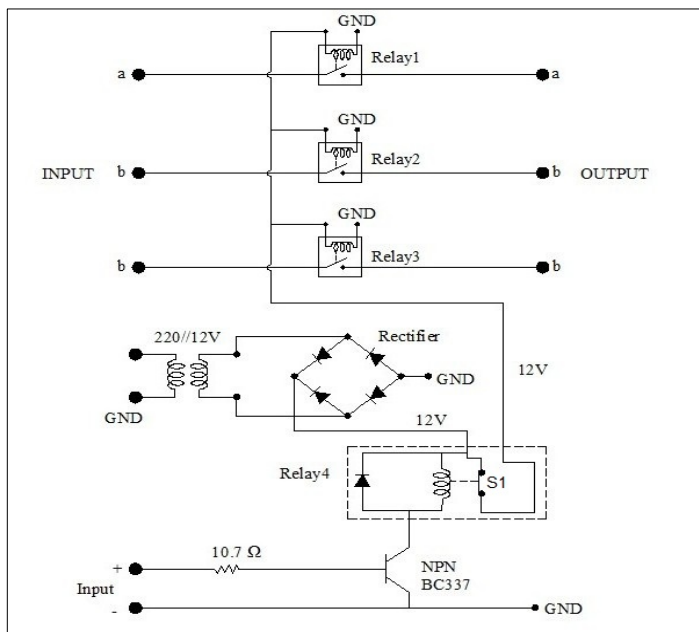
Fig. 6 Schematic diagram of relay circuit Circuit

Fig.7 The implemented relay

ad^2

ad^2

ad^2

dd^2

dd^2

dd^2

(a)

(b)

(c)
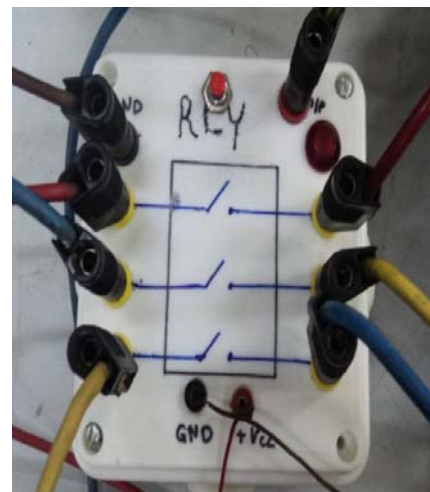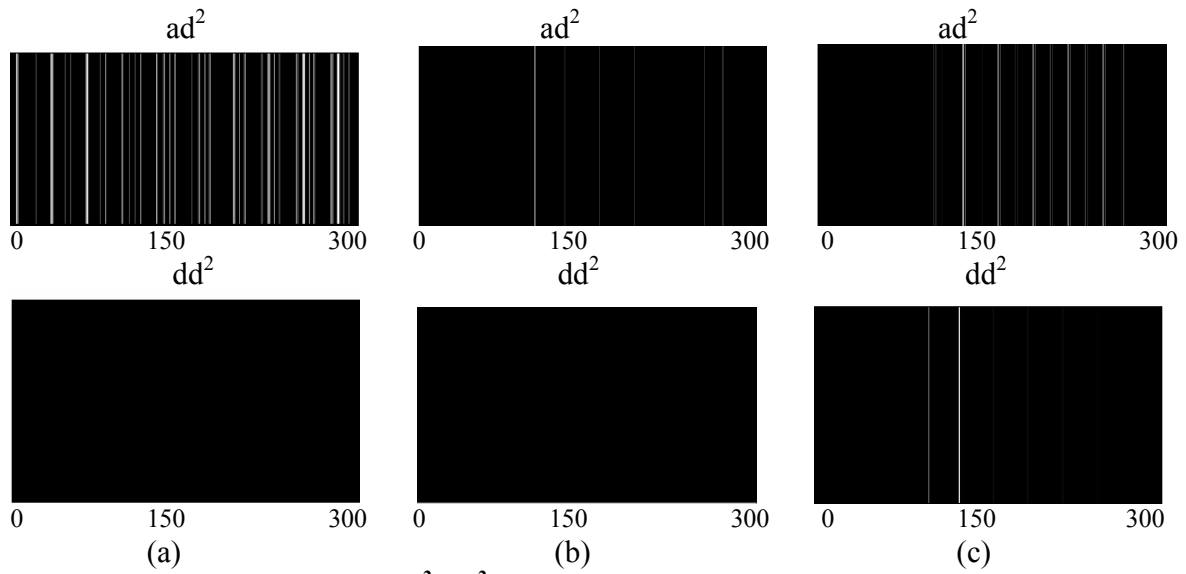
Fig. 8 Second level coefficients ad^2, dd^2, (a) inrush current, (b) external fault, (c) internal fault.
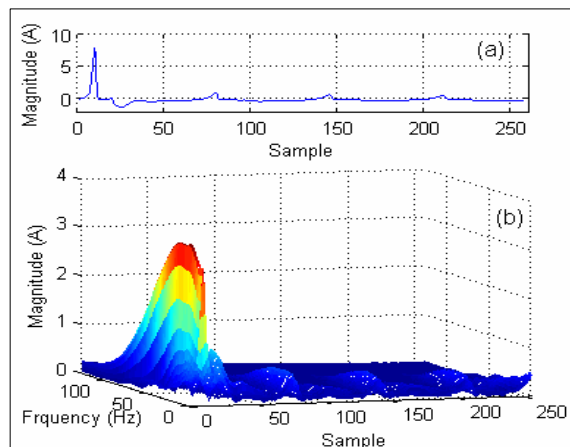
**Fig. 9: (a) Inrush current (b) 3-D S-
      Transform plot**
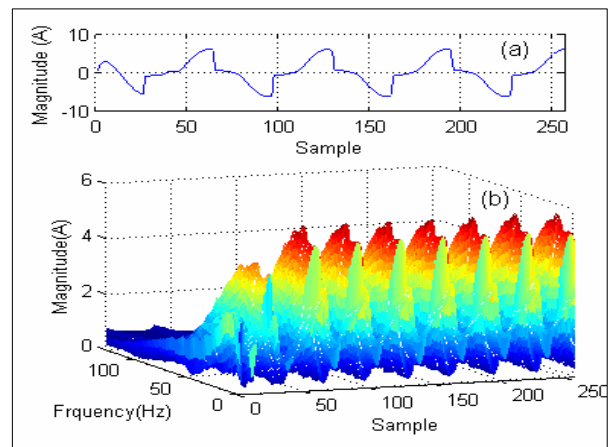
**Fig. 10 (a) Internal fault current (b) 3-D
      S transform**
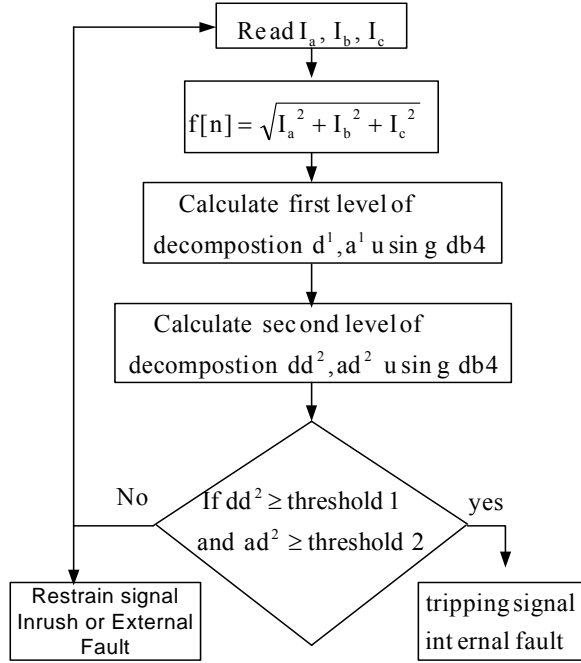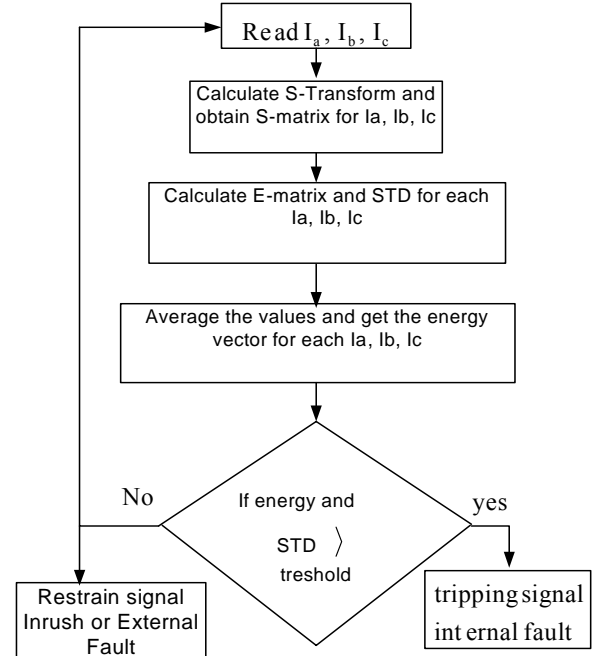
(a)   (b)

Fig. 11 Flowchart for software implementation for (a) WPT algorithm (b) ST algorithm
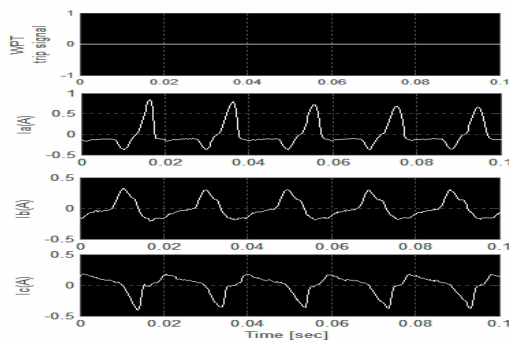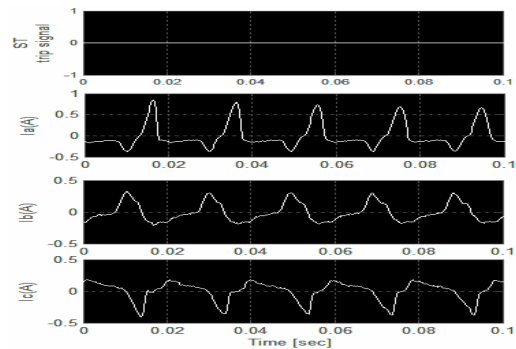
(a)   (a)

**Fig.12 Three-phase differential current and the trip signal for the case of loaded inrush current
before energization (a) by WPT algorithm, (b) by ST algorithm**

(a)   (b)
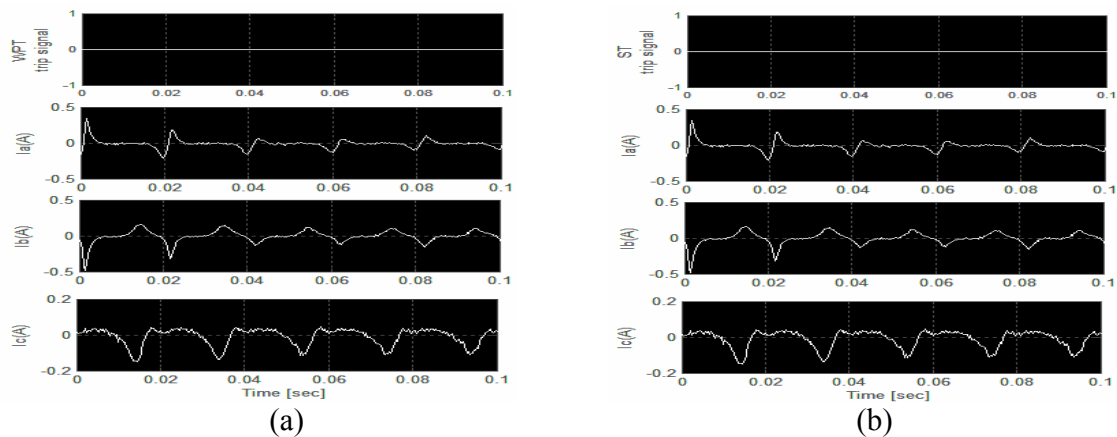
Fig.13 Three-phase differential current and the trip signal for loaded external 3-ph to ground fault current after energization (a) by WPT algorithm (b) by ST algorithm.

(a)   (b)
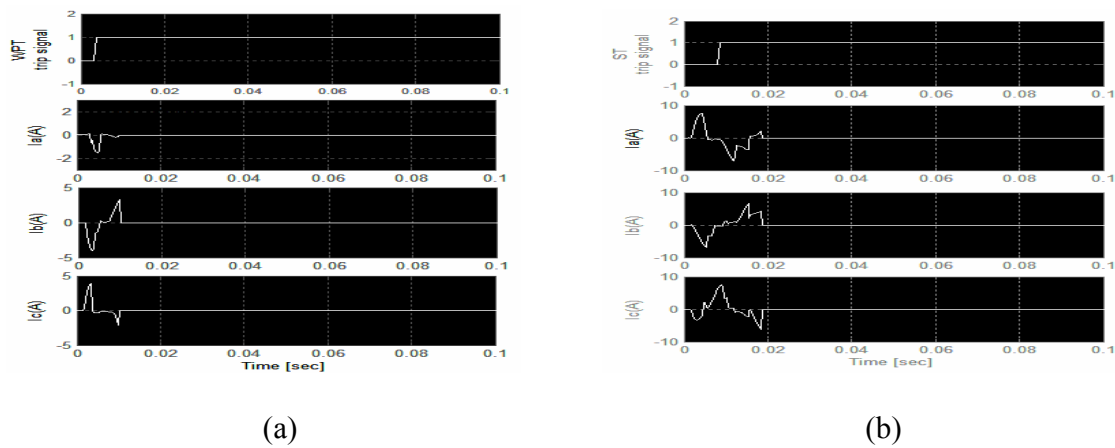
Fig.14 Three-phase differential current and trip signal for secondary unloaded internal 3-ph to ground fault after energization (a) by WPT algorithm (b) by ST Algorithm

(a)   (b)
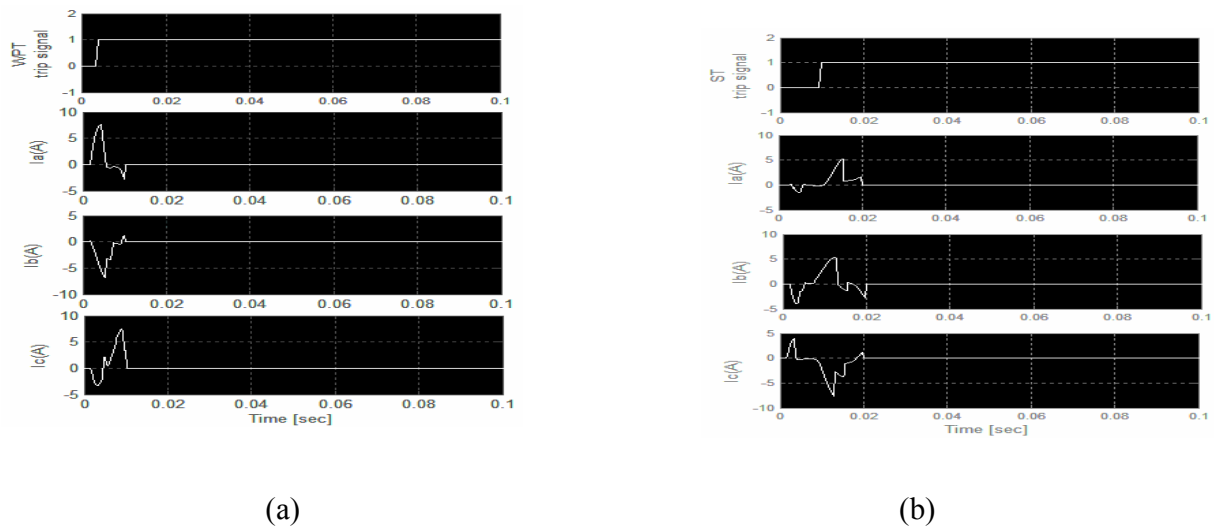
Fig. 15 Three-phase differential current and trip signal for unloaded secondary internal two-phase to ground fault (a) by WPT algorithm (b) by ST Algorithm

Table 1, MDL index for inrush current

Mother Wavelet	MDL(1)	MDL(2)
db4	1.5399	0.9865
coif1	5.68	4.7957
sym2	20.8061	1.8741
bior1.1	112.7782	11.1746
db10	10.1095	7.5879

Table 2. MDL index for internal fault

Mother Wavelet	MDL(1)	MDL(2)
db4	3.3744	1.0476
coif1	70.7034	7.8594
sym2	62.5534	0.1653
bior1.1	174.3035	38.151
db10	4.592	3.3369

Table 3, MDL index for external fault

Mother Wavelet	MDL(1)	MDL(2)
db4	3.1112	0.6934
coif1	6.0301	4.4436
sym2	15.4894	0.2691
bior1.1	184.4074	2.0319
db10	6.345	3.465

Table 4, Four levels MDL index

Current data	MDL(1)	MDL(2)	MDL(3)	MDL(4)
Unloaded inrush	1.5399	0.9865	2.3746	1.8191
Primary DLG fault	3.3744	1.0476	1.7611	1.8733
External SLG fault	3.1112	0.6934	2.5005	1.7593

Table 5 Energy and standard deviation for inrush and fault currents

INRUSH /FAULT	ENERGY	STD
Inrush loaded		
Inrush-a-(Δ-Y)	0.0091	0.0203
Inrush-b-(Δ-Y)	0.0024	0.0055
Inrush-c-(Δ-Y)	0.0025	0.0056
Internal Fault		
Fault Δ-Y bc-g(b)	0.8197	1.7759
Fault Δ-Y bc-g(c)	0.8608	1.92333
Fault Δ-Y abc-g(a)	1.0967	2.3607
Fault Δ-Y abc-g(b)	1.1464	2.4688
Fault Δ-Y abc-g(c)	0.8596	1.8503
External Fault		
Fault Δ-Y abc (a)	$2.9049*10^{-4}$	$6.5615*10^{-4}$
Fault Δ-Y abc (b)	$8.5276*10^{-4}$	$1.8751*10^{-3}$
Fault Δ-Y abc (c)	$2.9049*10^{-4}$	$6.5615*10^{-4}$

Experimental Investigation Utilizing Thermal Image Technique to the Heat Transfer Enhancement Using Oscillated Fins

Prof. Dr. Ihsan Y. Hussain
Mechanical Engineering Department
University of Baghdad
drihsan@uobaghdad.edu.iq
dr.ihsanyahya1@yahoo.com

Asst.Prof. Dr.Karima E.Amori
Mechanical Engineering Department,
University of Baghdad
drkarimaa@yahoo.com

Asst.Lecturer. Dheya G. Mutasher
Mechanical Engineering Department,
University of Technology
dheya_ghanim@yahoo.com

ABSTRACT

Heat transfer around a flat plate fin integrated with piezoelectric actuator used as oscillated fin in laminar flow has been studied experimentally utilizing thermal image camera. This study is performed for fixed and oscillated single and triple fins. Different substrate-fin models have been tested, using fins of (35mm and 50mm) height, two sets of triple fins of (3mm and 6mm) spacing and three frequencies applied to piezoelectric actuator (5, 30 and 50HZ). All tests are carried out for (0.5 m/s and 3m/s) in subsonic open type wind tunnel to evaluate temperature distribution, local and average Nusselt number (Nu) along the fin. It is observed, that the heat transfer enhancement with oscillation is significant compared to without oscillation for low air inlet velocity. Higher thermal performance of triple fins is obtained compared to the single rectangular fin, also triple fins with (height=50mm and fin spacing=3mm) gives better enhancement as compared to other cases. This work shows that the piezoelectric actuator when mounted on the rectangular fins shows great promise for enhancing the heat transfer rate.

KEYWORDS: laminar flow; forced convection; thermal image; enhancement of heat transfer; oscillating fins.

<div dir="rtl">

دراسة عملية باستخدام تقنية الكامرا الحراريه لزيادة معدلات انتقال الحرارة باستخدام الزعانف المتذبذبة

م.م. ضياء غانم مطشر
قسم الهندسة الميكانيكية
جامعة بغداد/طالب دكتوراه

أ.م.د. كريمة اسماعيل عموري
قسم الهندسة الميكانيكية
جامعة بغداد

أ.د.احسان يحيى حسين
قسم الهندسة الميكانيكية
جامعة بغداد

الملخص:

(Piezoelectric Actuator)

(6   3)   (50   35)

3   / 0.5)   .(50 30 5)   (Piezoelectric Actuator)

(/

</div>

Prof. Dr. Ihsan Y. Hussain
Asst.Prof. Dr.Karima E.Amori
Asst.Lecturer. Dheya G. Mutasher

(35= 50 =)

(Piezoelectric Actuator) .

:

.

INTRODUCTION

Heat transfer enhancement has become a target in the miniaturization of electronic components. Enhanced heat transfer surfaces can be designed through a combination of factors that include increasing fluid turbulence, generating secondary fluid flow patterns, reducing the thermal boundary layer thickness and increasing heat transfer surface area (David 2010). One of the most difficult challenges in modern power electronics is obtaining sufficient cooling for the components. The operating temperature of the components is an extremely important factor affecting their reliability. The heat sink typically consists of a base plate and a stack of fins. In addition, as the dissipated heat of the components grows, a fan or a pump is needed to obtain higher rates of heat transfer by forced convection. The design process of a heat sink for a given set of electronic components is a very complicated task involving many contradicting optimization criteria (Antti 2005). Numerous methods have been proposed to enhance heat transfer rate of a heat body. These methods can be classified into the passive and active methods. Examples of the former one are treated surfaces and swirl flow devices, while examples of the active methods are surface vibration, fluid vibration, injection and suction (Wu-Shung 2007).Active methods require external power to enhance heat transfer on the contract to passive methods. Extended surfaces or fins are example of passive methods that are commonly used in variety of industrial applications to enhance the rate of heat transfer between primary surface (heat sink) and ambient fluid (M.R.Shaeri 2009). In addition to numerous methods have been proposed to enhance heat transfer rate by using block moving back and forth on a heated surface in a channel flow, this phenomena causes the heat transfer rate of the heat surface to be enhanced because it destroys and suppresses the velocity and thermal boundary layers on the heat surface periodically, studied by (Wu-

Shung 2000, 2001, 2007, 2010). (Tae 2008) introduced a novel heat sink with moving fins inserted between cooling fins for electronics cooling application. In this heat sink, they replace the fan module by moving fins inserted in the intervals of fixed fins (cooling fins) for generating fluid flow. The relative motion of the moving fins to the cooling fins, causes a heat dissipation from the cooling fins to the coolant and discharge of the heated coolant. Experimental results show that measured flow rates of the coolant are almost linearly proportional to the rotating speed of the moving fins. The thermal performance of the scroll heat sink is compared to that of an equivalent plate-fin heat sink under the same Reynolds number. The scroll heat sink has at least 14% lower thermal resistance than that of the equivalent plate-fin heat sink in the range 0.135m/s V 0.56m/s. (H.K. Ma 2009) proposed innovative vibrating fins and successfully built three-dimensional transitional models to investigate design performance. The basic fins, with dimensions of 30mm in length, 1mm in thickness, and 100mm in width, are designed on a 2mm thick finned base. The displacement ratio and frequency of the vibrating fins are 0.9 and 10 HZ. The results showed that the performance of the vibrating fins is strongly affected by dimensions, vibrating frequency, pitch, and amplitude of the fins. As gravity parallels the surface of the finned base, the vibrating fins can perform better than traditional fins on heat dissipation due to the lower convective obstacle. (Subhrajit 2009) carried out a numerical investigation using finite volume method for a 3D oscillating fin to disturb the thermal boundary layer to enhance forced convection heat transfer from conventional heat sink. The fin dimensions were (0.5" *1"*0.01") and substrate was (1"*1"). The power supplied to the substrate was 20W. It was found that such oscillations lead to tip-leakage vortices from the fins. A local up wash is presented on the fin lateral surfaces, hence increasing the overall heat transfer rate. This enhancement in heat transfer was demonstrated

through an increase in the time-averaged Nusslet number (Nu) on the fin surface. The objective of this work is to design, manufacture and test a new cooling system. This system is formed of piezoactuated plate fins integrated with a hot substrate subjected to forced convection. The cooling of hot electronic devices integrated with fixed fins may be failed for high heat generation rate, so oscillating these fins will disturb the development of boundary layer and enhances the heat dissipation effectively and reliably from hot substrate to the stream wise flowing fluid. The dependence of temperature distribution, and local Nusselt number of fixed or oscillated fin   is quantified on parameters like free stream velocity, fin height, fin spacing and frequency of oscillation of the fin. The impact of the presence of single or triple fixed and oscillated fins has also been highlighted.

EXPERIMENTAL TEST RIG

A designed manufactured experimental model used in this study is consist of: square copper substrate of (100mm, long, 100 mm wide and 11 mm thickness); copper flat plate fin of (0.075mm) thickness and (100mm) long, and heating unit. A schematic diagram of the experimental model is shown in Fig.(1). The effect of single fin and triple fins is investigated for: fins height (H=35mm and 50 mm), fins spacing (W=3mm and 6mm). The piezoelectric actuators in the form of a rectangular shape pair are mounted on each end of the fin surfaces by a heat tape and supported from bottom. The fin oscillation disrupts the growth of the thermal boundary layer and serves to bring about heat transfer enhancement between the fluid and the fin surfaces. A four cartridge electrical heaters are built in the substrate to obtain constant heat flux. The input power to the heater is controlled by a variac transformer and measured by an in-line digital power and energy monitor. A PID controller type WATLOW EZ-ZONE was used to adjust the electrical current supplied to the cartridge heater. The heater output power is 1200 W at (voltage of 250V and current of 4.8A).   The substrate-fin assembly is tested for different velocities in a subsonic open type wind tunnel of rectangular cross sectional test section. The test section walls are made of 5mm thickness of plexi-glass and its' dimensions are (340mm height, 340mm wide and 600mm long) is shown in fig. (2) . The wind tunnel

used in this work consists of: filter, nozzle with flow straightners, test section, damping chamber, diffuser, and an AC fan. A thermal image camera (H2600) series has the infrared detector of 640*480 pixels is used to view and record the temperature distribution on both the fin and the substrate is shown in figs. (3 and 4) for different frequencies. Isofrax paper (1260°c k=0.073 W/m K) has been used to thermally insulate the bottom surface of the substrate followed by Insulfrax blanket (k = 0.07 W/m K) of 80 mm thickness. The experiments of the fluid flow and heat transfer were carried out for each tested model for seven values of Reynolds number based on hydraulic diameter of test section (1.0886*104 to 1.3*105). A hot-wire anemometer is used to measure air velocity and temperature at inlet of test section. Power supply is used to generate and amplify signals sent to the piezoelectric actuator to oscillate the plate fin. The range of input signal frequency to the piezoelectric actuator was (5HZ to 50HZ).
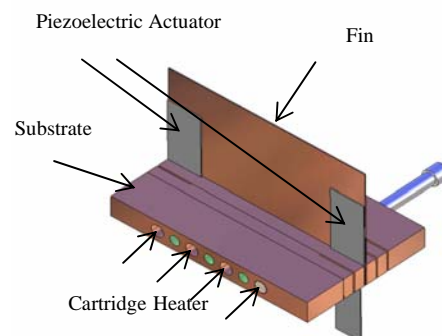
Fig. (1): The structure of oscillating fin.
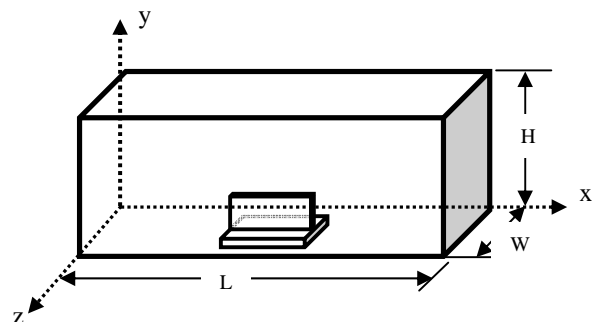
Fig. (2): Geometry of the Problem

Prof. Dr. Ihsan Y. Hussain
Asst.Prof. Dr.Karima E.Amori
Asst.Lecturer. Dheya G. Mutasher

Experimental Investigation Utilizing Thermal Image Technique
to the Heat Transfer Enhancement Using Oscillated Fins
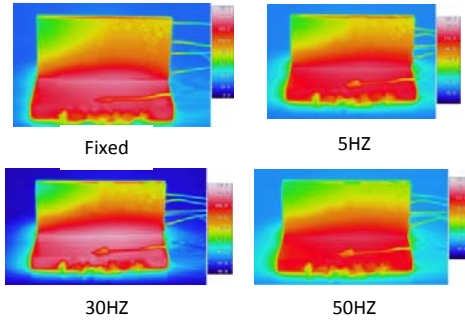
Fig. (3): Thermal Image , I.P=50W and
u=0.5m/s
(h=50mm and dis.=3mm)
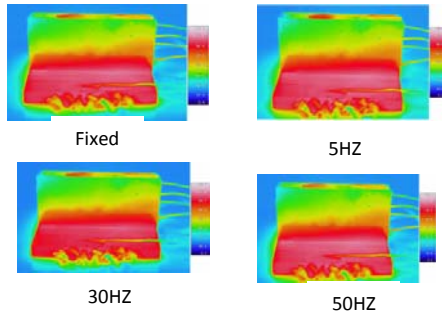
Fig. (4): Thermal Image , I.P=50W and
u=0.5m/s
(h=50mm and dis.=6mm)

DATA REDUCTION

In order to investigate the convection heat transfer in the test section, the heat transferred to the air is required to be determined. Considering the energy balance, the total heat flux q_{tot} generated by the heated plate is dissipated into the convective heat flux from the test section to the air q_{conv}, conductive heat loss through the insulation materials q_{cond} and radiant heat loss from the test section q_{rad}, as shown below (Saad 2002):

$$q_{tot} = q_{conv} + q_{cond} + q_{rad}, \qquad (1)$$

The essential quantities, which are obtained in the study of heat transfer are; the convective heat transfer (q_c), the local Nusselt number over the tested fins ($Nu_{x,f}$), the Average Nusselt number (Nu_f). The total heat generated from the heater (q_t) is distributed into the heat transferred by convection to the flowing air (q_c) and the heat losses through the insulation surrounds and under the tested model (q_L) as follows:

$$q_c = q_t - q_L \qquad (2)$$
$$q_L = q_s + q_p + q_b + q_{ft} + q_r \qquad (3)$$

Where q_s, heat lost by conduction in the stream-wise (X) direction (W); q_p, heat lost by conduction in the spanwise (Z) direction, (W); q_b, heat lost by conduction from the bottom surface of the base plate, (W); q_{ft}, heat lost from the fin tips surface (W); q_r, heat lost by radiation (W). Then, the value of losses is small compared with the heat input value and it can be neglected. Consequently the total heat transferred by convection to the flowing air (q_c) equals the heat generated by the heater (q_t):

$$q_c = q_t \qquad (4)$$

The heat transferred by convection to the air stream is divided into two parts:
The convection heat transfer from fins (q_{cf}) which can be calculated as

$$q_{cf} = q_c \ A_{ct,f}/A_{ct} \qquad (5)$$

where
$A_{ct,f}$, total cross-sectional area of fins at the base (sum of surface area of the fins tip) (m^2)
Act, is the total cross-sectional area of the base plate and fins (m^2), and the convection heat transfer through one fin (q_f) is given by
$$q_f = q_{cf}/N \qquad (6)$$

where N is Number of fins
The convection heat transfer from substrate area which exposed to flowing air (without fins) (q_{cb}) which can be calculated as

$$q_{cb} = q_c \ A_{cb,f}/A_{ct} \qquad (7)$$

Where

$A_{cb,f}$, total free surface areas of the base plate (without fins), (m^2).
The local heat transfer coefficient over the tested fins can be calculated by applying the Newton's law (F.B. Incropera 1985)

$$h_{x,f} = q_f/A_{sf}\,(T_f - T_i) \tag{8}$$

where

T_f , Local fin temperature (^oC); T_i, air inlet temperature (^oC); q_f , convection heat transfer through one fin (W); A_{sf} , total surface area of the tested fin (m^2).

$$Nu_{x,f} = h_{x,f}\ .x/k_a \tag{9}$$

where

$h_{xf,x}$, is local heat transfer coefficient over the tested fins (W/m^2. ^oC); ka, is air thermal conductivity at T_i (W/m. ^oC).
The fin-average Nusselt number can be defined as

$$Nu_f = h_f L/K_a \tag{10}$$

where h_f is fin average heat transfer coefficient which is calculated as:

$$h_f = 1/A_{sf} \int_A h_{f,x} dA_{sf} \tag{11}$$

Newton Raphson Method is used to calculate the average heat transfer coefficient over the tested fins such that:

$$h_f = \tfrac{h}{3}[h_{f,o} + 4\sum_{i=1,3,5}^{n-1} h_{f,i} + 2\sum_{i=2,4,6}^{n-2} h_{f,i} + h_{f,n} \tag{12}$$

where h is division size of the fin length = L/n

RESULTS AND DISCUSSION

The presented temperature distribution has been extracted from thermal image taken for substrate integrated with fixed and oscillated fins. The following cases have been studied in this work:

Case 1: fixed triple fins (height =50mm and fin spacing =3mm)Case 2: oscillated triple fins (height =50mm and fin spacing =3mm)

Case 3: fixed triple fins (height =35mm and fin spacing =3mm)

Case 4: oscillated triple fins (height =35mm and fin spacing =3mm)

Case 5: fixed triple fins (height =50mm and fin spacing =6mm)

Case 6: oscillated triple fins (height =50mm and fin spacing =6mm)

Case 7: fixed triple fins (height =35mm and fin spacing =6mm)

Case 8: oscillated triple fins (height =35mm and fin spacing =6mm)

Case 9: single fixed fin (height =50mm)

Case 10: single oscillated fin (height =50mm)

1- TEMPERATURE DISTRIBUTION

The front view of the fin is divided into four rows and five columns as shown in Fig.s (5and 6). The coordinate of each node has been transformed from the thermal image to digital value of temperature using thermal image camera software.
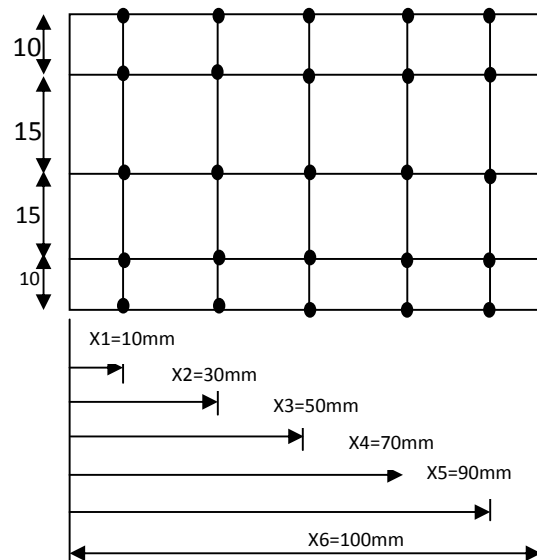
Fig. (5): Locations of temperature measured by thermal image (fin height =50 mm)

Prof. Dr. Ihsan Y. Hussain
Asst.Prof. Dr.Karima E.Amori
Asst.Lecturer. Dheya G. Mutasher

Experimental Investigation Utilizing Thermal Image Technique
to the Heat Transfer Enhancement Using Oscillated Fins
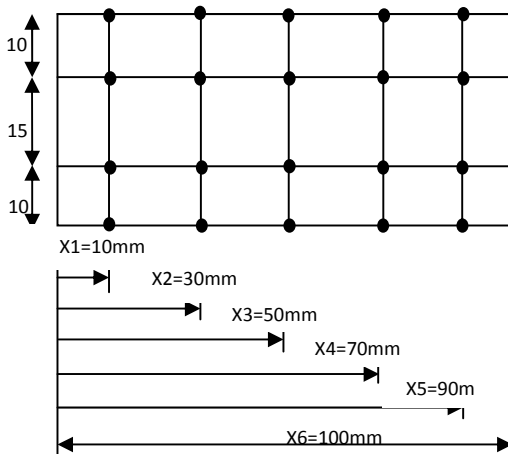
Fig.(6): Locations of temperature measured by thermal image (fin height =35 mm)

Figures (7, and 8) show the temperature distribution along the front fin height (when the substrate integrated with triple fins) for air free stream velocity of 3m/s and fins spacing =3mm. It is clear that the temperature decreases toward the tip of the fin. There is inconsiderable change in temperature variation for oscillated fin compared with that for fixed one except for H=35mm. Increasing the fin spacing from 3mm to 6mm has little Impact on the values of temperature distribution. The temperature distribution along the fins is shown in Fig.s (9 and 10). The fin leading edge (near the tip) was the coldest region while the fin root near the trailing edge was the hottest. Figure (11) shows the same trend of temperature distribution along the single fin height with approximately constant stream wise temperature variation. Quantitatively colder temperatures are indicated with increasing number of fins as shown in Figures (9 a, b) (10 a, b) and (11 c, d).

2) NUSSELT NUMBER

The calculated local heat transfer coefficient is increased toward the fin tip as shown in Fig. (12). Fin oscillation enhances the heat transfer as shown in this figure. Higher values of local Nusselt No. are found near the fin trailing edge as presented in Fig. (13). From this figure it is clear that stimulation the fins to oscillate rises the value of hf,x. Increasing

the inter-fin spacing causes an increase of mass flow rate between fins and good washing for the fins wall takes place, hence an increase of local Nusselt No. was obtained consequently as indicated in Fig.s (12 and 14). Fig.(15) shows the same trend of local Nusselt No. on single fixed and oscillated fin.

Figures (16 and 17) show a considerable increase in average Nusselt number (Nu) on the frontal fin is obtained with increasing inlet air velocity from 0.5m/s to 3m/s. Nusselts number increases at the tip of the fin much more than fins' root. Also an enhancement in heat transfer is obtained with increasing the frequency. For 0.5m/s, the best performance for oscillation was at frequency 50HZ, while for 3m/s it was at frequency 30HZ. The static fin develops convection driven thermal boundary layer on either side of the fin. It acts as a resistance to further heat dissipation. This layer is expected to rupture under the influence of local cross wise perturbation in the form of sinusoidal motion imposed on the fin by the piezoelectric actuator. As the fin starts to oscillate, one of the lateral surfaces of the fin behaves as the pressure side with the opposite surface being as the suction side. This gets reversed every half time period. As the fin is on its way to move, the fluid close to the fins' pressure surface is pushed by the fin and flows transversely to the stream wise direction. As a result, the heat transfer is enhanced. Conversely, the fluid near the opposite surface of the fin simultaneously replenishes the vacant space induced by the movement of the fin. Most of the fluid near the suction surface of the fin is difficult to catch up to this surface of the fin simultaneously, hence a small recirculation zone is developed, and a re attachment flow is presented. As a result a heat transfer enhancement is obtained. It is clear from Fig.s (16,and 17) that for cases 3, 4, 6 and 7, no significant effect of oscillation frequency on average Nusselt number is found. For cases 1, 2, 5 and 6, the results show obviously an increase in average Nusselt number exists with increasing the frequency, especially with 50HZ. For case 9 and case 10, the results show the increase of the average Nusselt number with increasing the frequency is very low for higher air velocity.
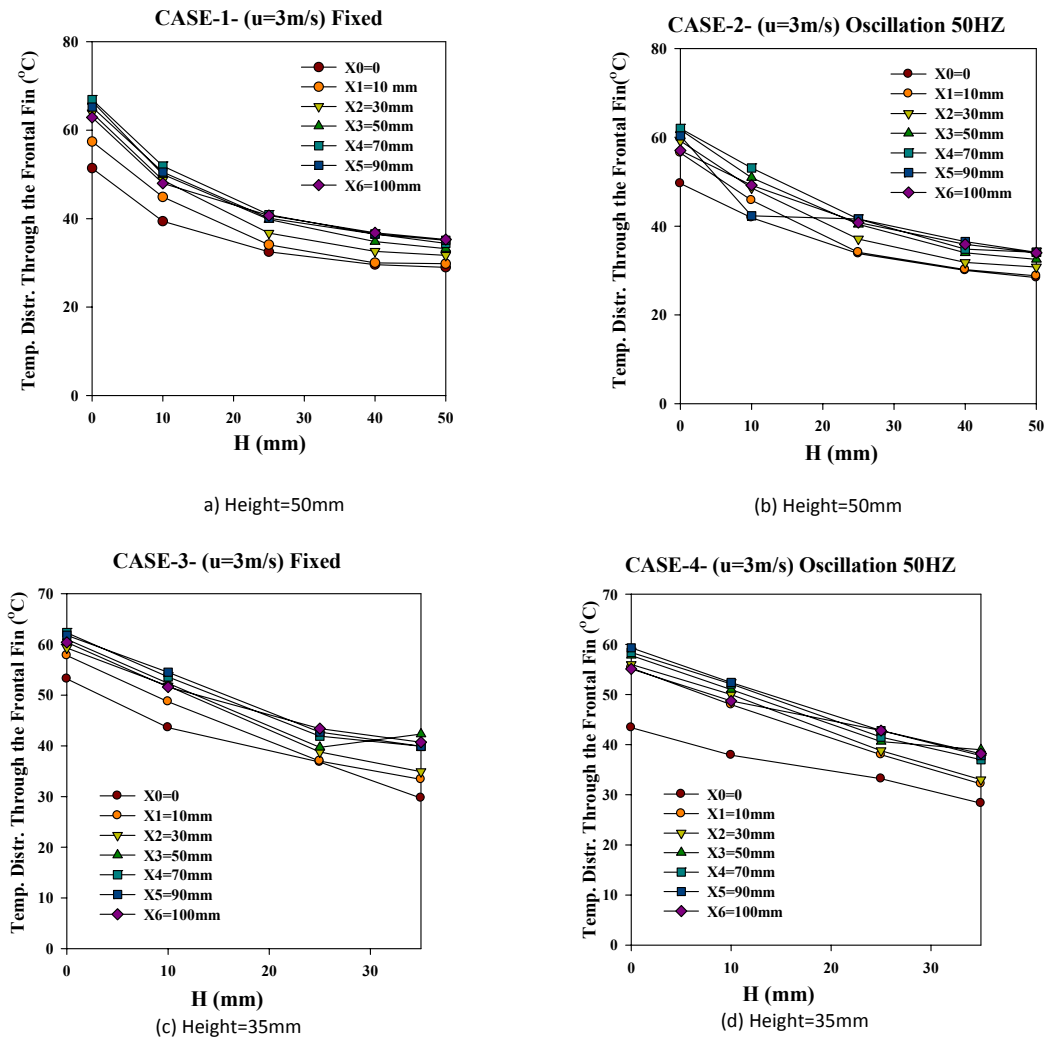
Fig. (7): Temperature distribution along the height of the frontal fin for (fins spacing=3mm).

Prof. Dr. Ihsan Y. Hussain
Asst.Prof. Dr.Karima E.Amori
Asst.Lecturer. Dheya G. Mutasher

**Experimental Investigation Utilizing Thermal Image Technique
to the Heat Transfer Enhancement Using Oscillated Fins**
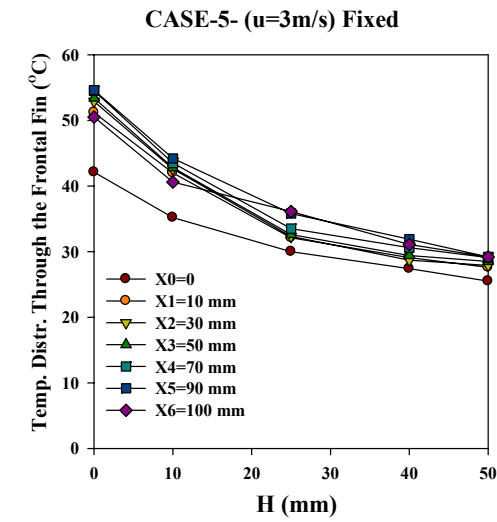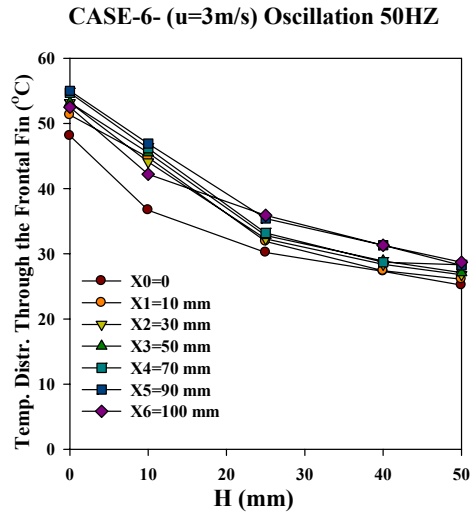
(a) Height=50mm

(b) Height=50mm
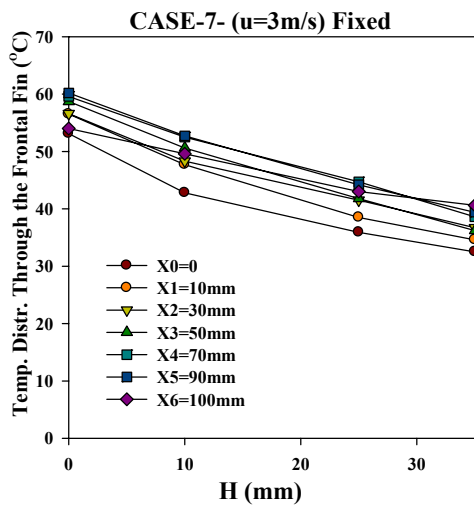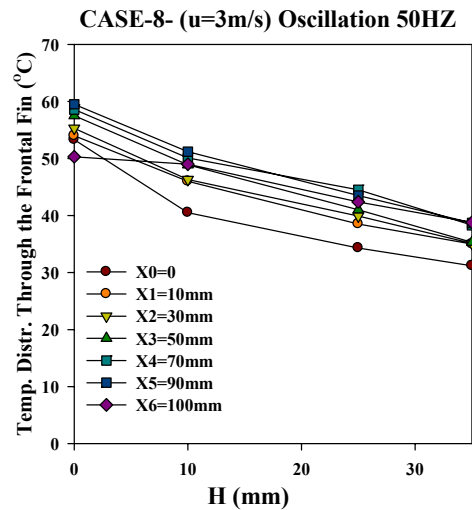
(c) Height=35mm

(d) Height=35mm

Fig.(8): Temperature distribution along the height of the frontal fin for (fins spacing=6mm).

Fig. (9): Temperature distribution along the frontal fin for (fins spacing=3mm).
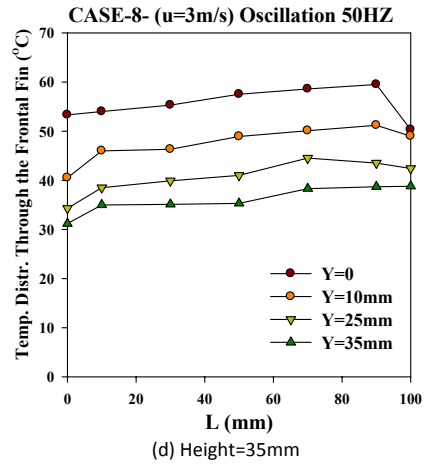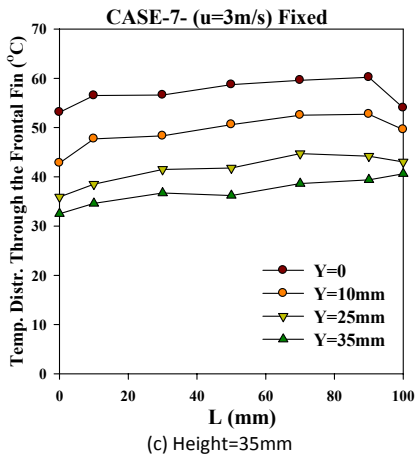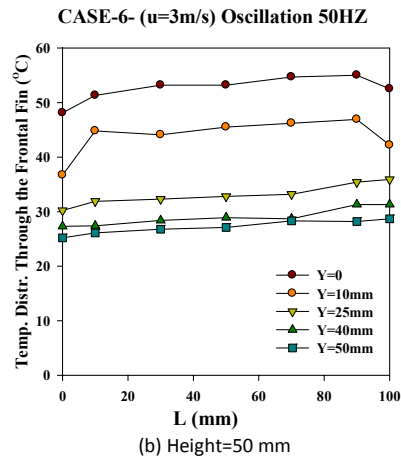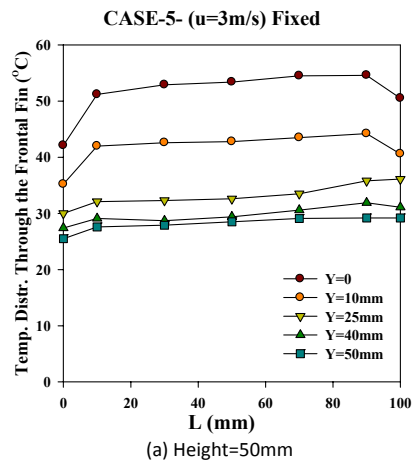
Prof. Dr. Ihsan Y. Hussain
Asst.Prof. Dr.Karima E.Amori
Asst.Lecturer. Dheya G. Mutasher

Experimental Investigation Utilizing Thermal Image Technique to the Heat Transfer Enhancement Using Oscillated Fins

(a) Height=50mm

(b) Height=50 mm

(c) Height=35mm

(d) Height=35mm

Fig. (10): Temperature distribution along the frontal fin for (fins spacing=6mm).

(a)Single fixed fin

(b) Single oscillated fin

(c) Single fixed fin

(d) Single oscillated fin
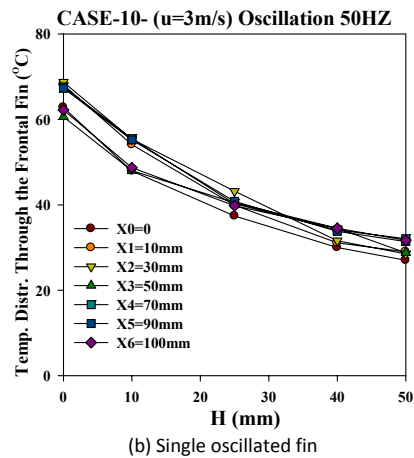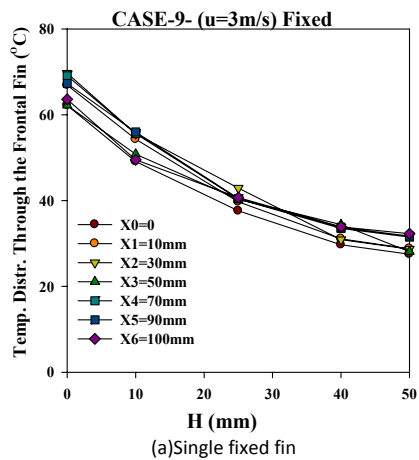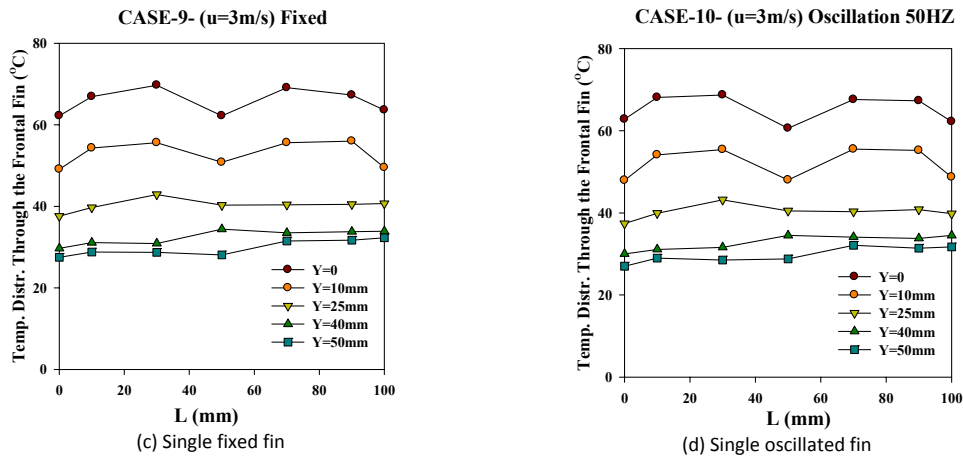
Fig.(11): Temperature distribution along the fin; a,b) height; c,d) length

(a) Height=50mm

(b) Height=50mm

(c) Height=35mm

(d) Height=35mm
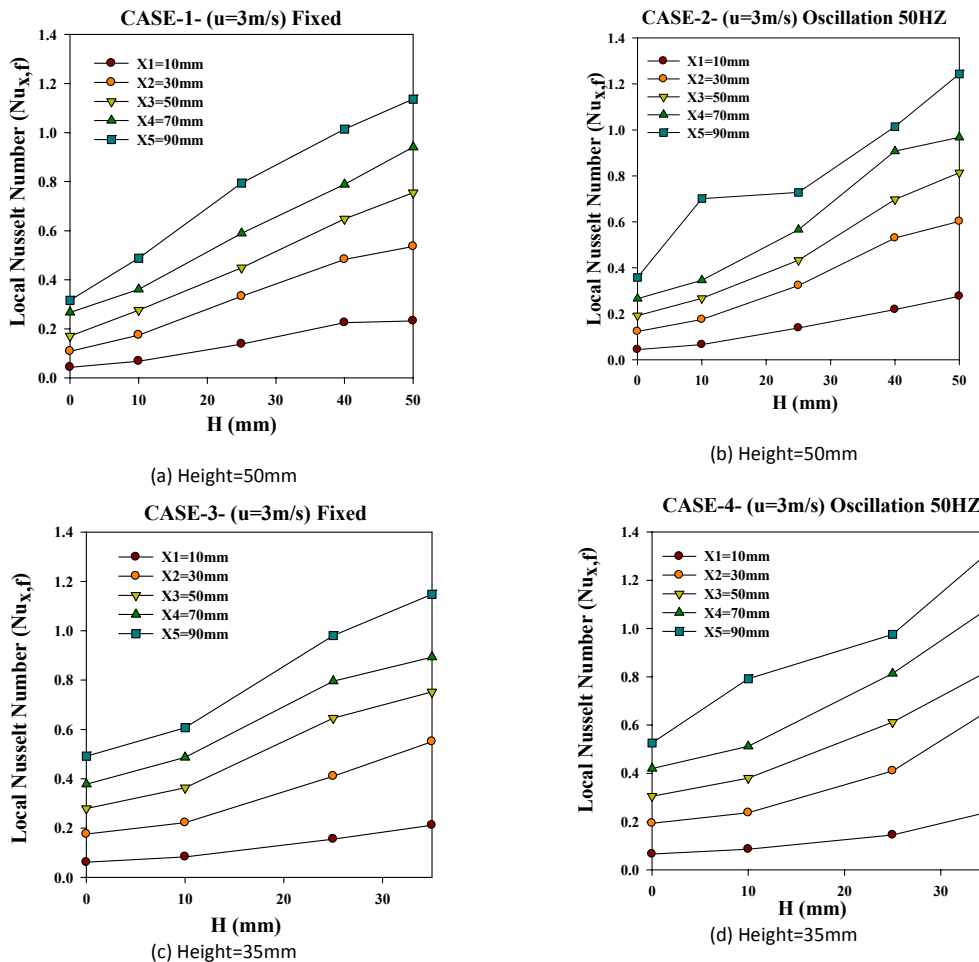
Fig. (12): Variation of local Nusselt number along the height of the frontal fin (fins spacing=3mm).

Prof. Dr. Ihsan Y. Hussain
Asst.Prof. Dr.Karima E.Amori
Asst.Lecturer. Dheya G. Mutasher

**Experimental Investigation Utilizing Thermal Image Technique
to the Heat Transfer Enhancement Using Oscillated Fins**

(a) Height=50mm

(b) Height=50mm

(c) Height=35mm

(d) Height=35mm
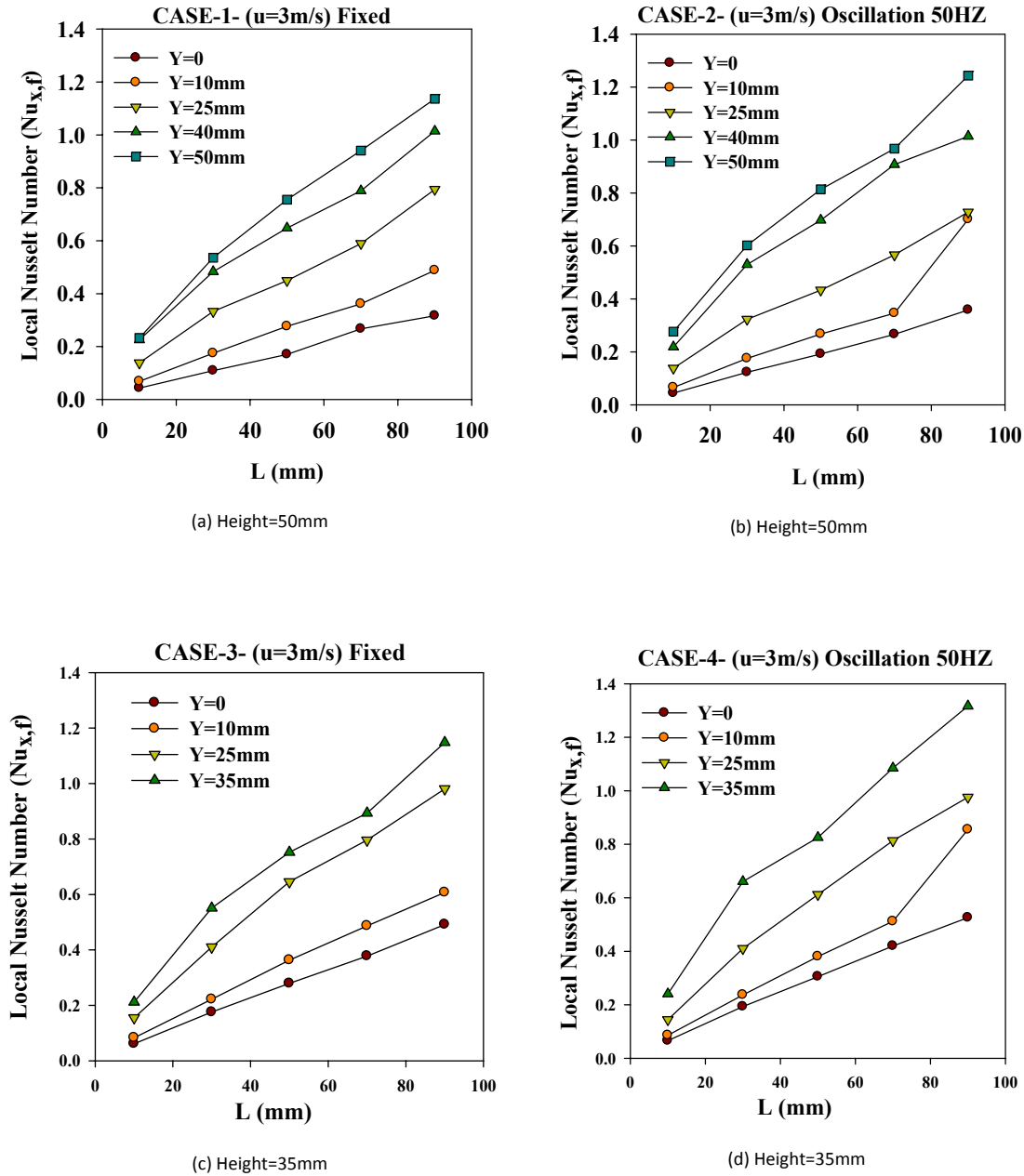
Fig.(13): Variation of local Nusselt number along the frontal fin (triple fins with fins spacing=3mm).
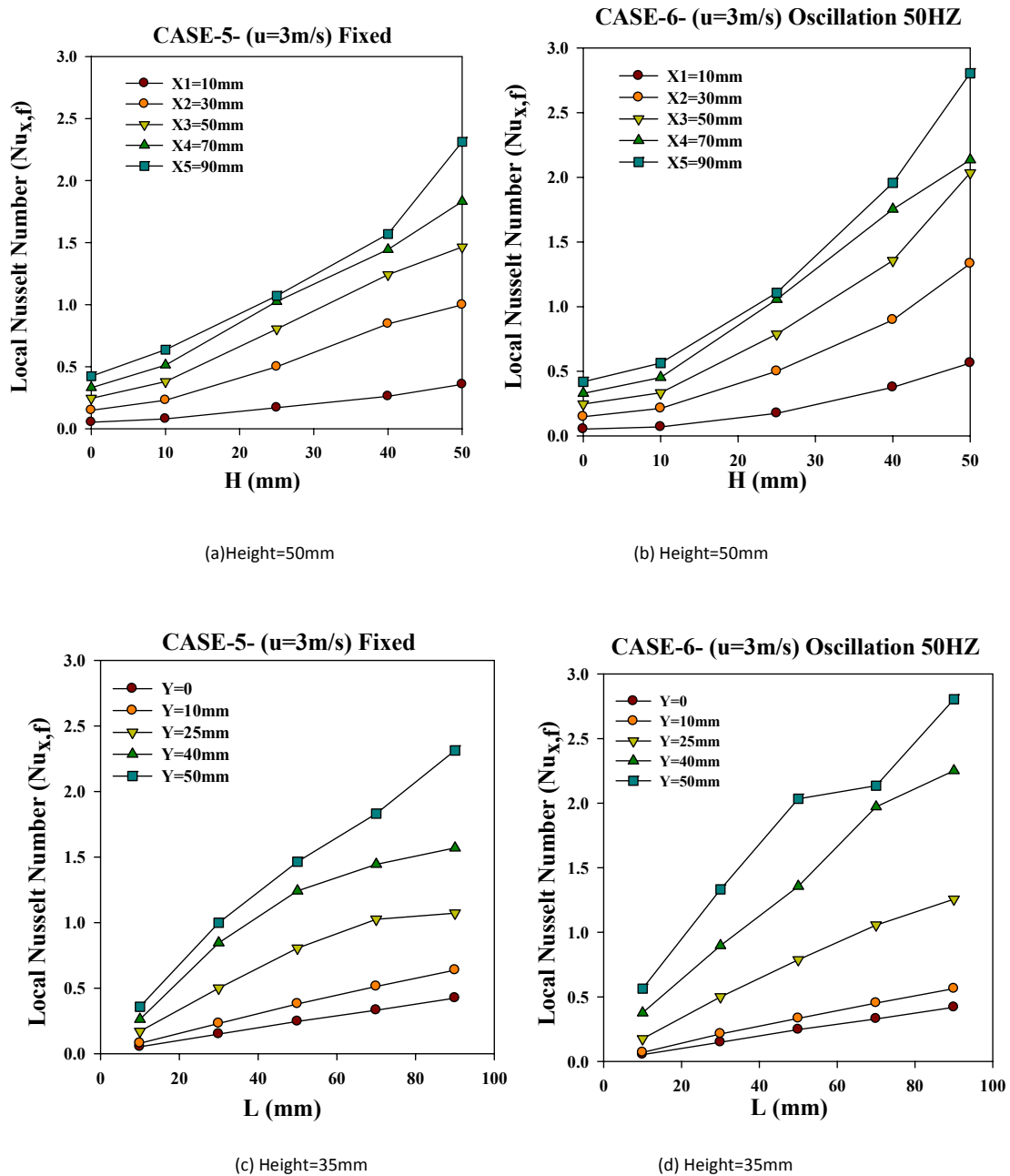
Fig.(14): Variation of local Nusselt number along the frontal fin (fins spacing=6mm).

Prof. Dr. Ihsan Y. Hussain
Asst.Prof. Dr.Karima E.Amori
Asst.Lecturer. Dheya G. Mutasher

**Experimental Investigation Utilizing Thermal Image Technique
to the Heat Transfer Enhancement Using Oscillated Fins**

CASE-9- (u=3m/s) Fixed   **CASE-10- (u=3m/s) Oscillation 50HZ**

(a)   (b)
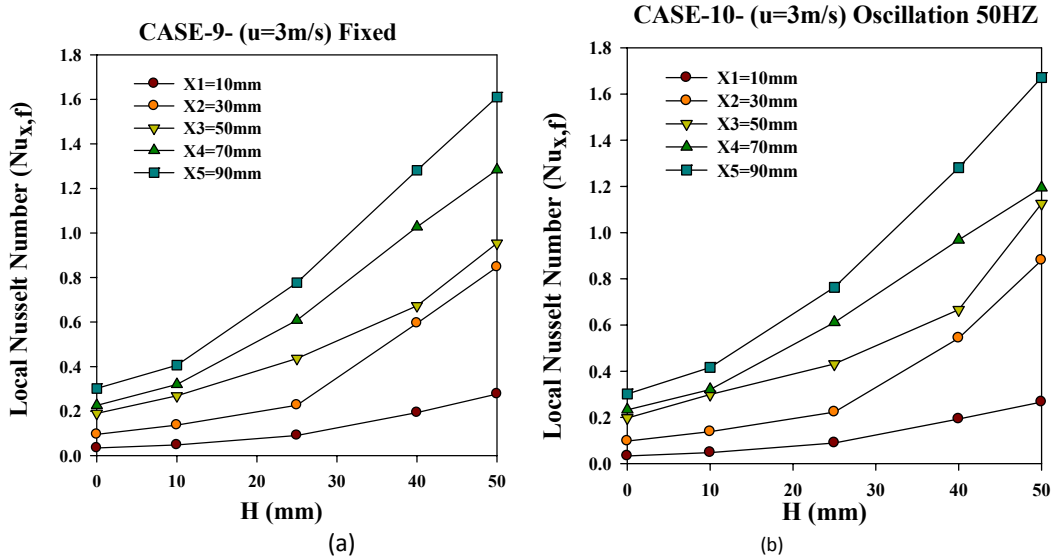
Fig. (15): Variation of local Nusselt number along the height of a) single fixed fin; b) single oscillated fin.

(a)   Single fin, u=0.5 m/s

(b)   Single fin, u=3 m/s
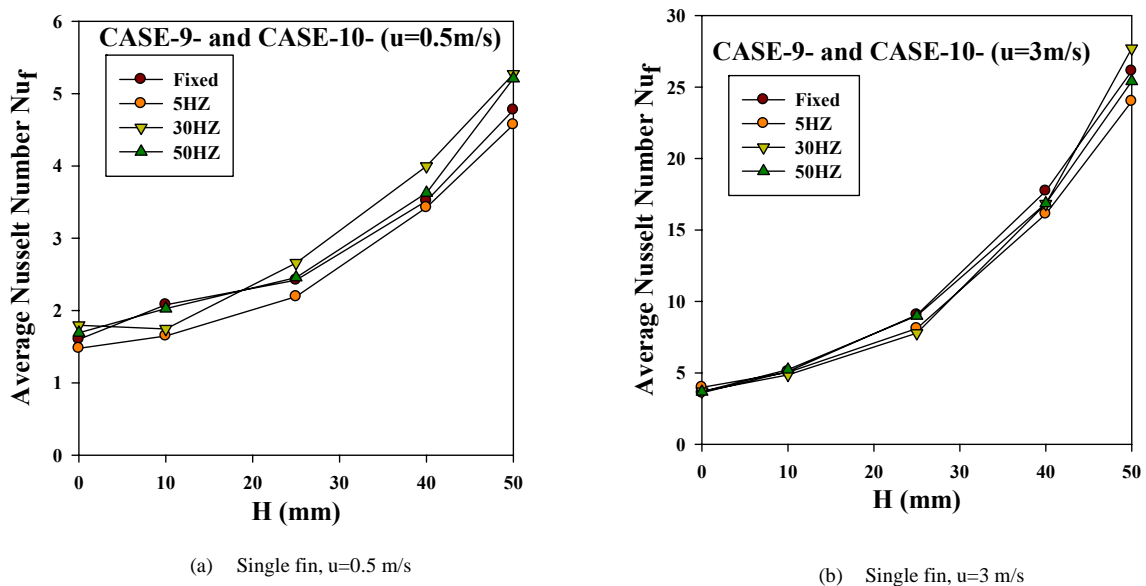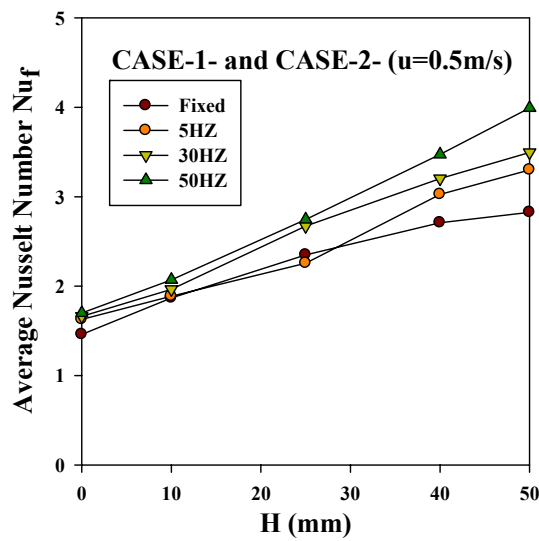
(c) Triple fins, u=0.5 m/s, spacing=3mm
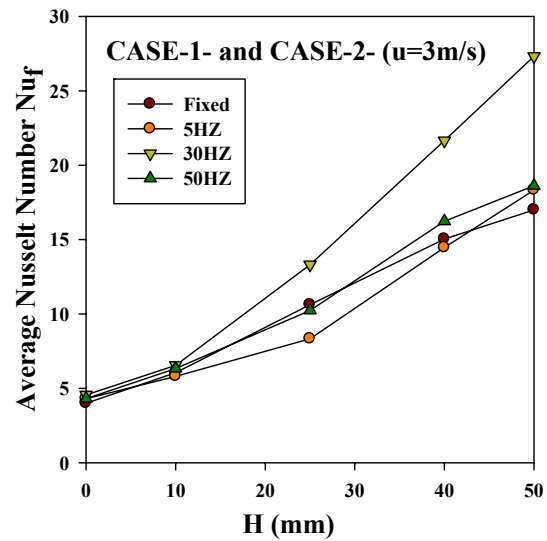
(d) Triple fins, u=3 m/s , spacing=3mm
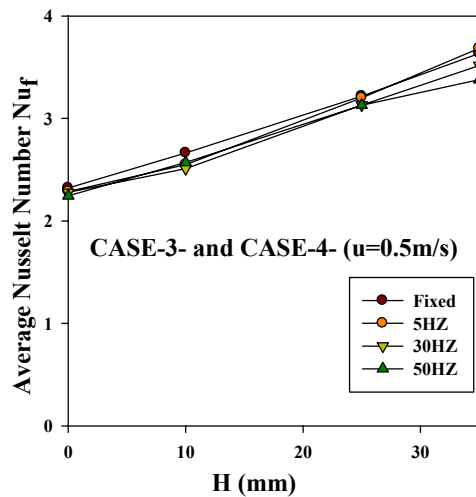
(e) Triple fins, u=0.5 m/s , spacing=6mm
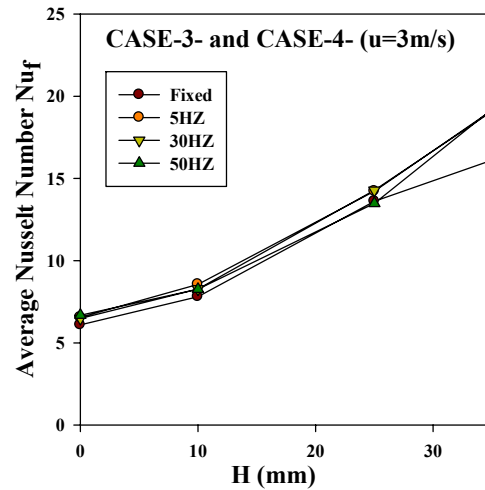
(f) Triple fins, u=3 m/s , spacing=6mm

Figure (16): Variation of average Nusselt number along fins' height for different frequencies
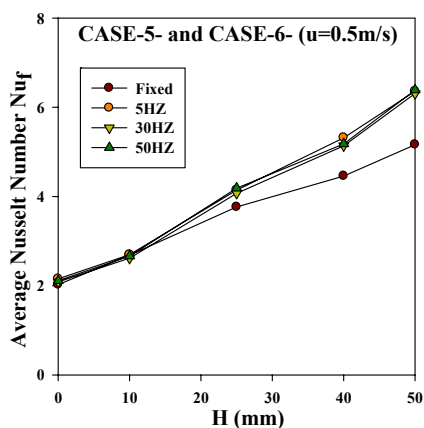
(a) Triple fin, u=0.5 m/s, spacing=6mm,H=50mm
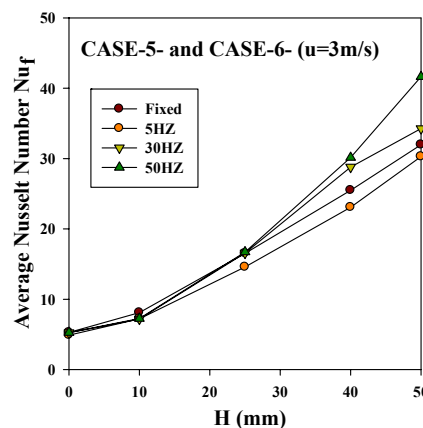
(c)   Triple fin, u=3 m/s, spacing=6mm, H=50mm

Prof. Dr. Ihsan Y. Hussain
Asst.Prof. Dr.Karima E.Amori
Asst.Lecturer. Dheya G. Mutasher

Experimental Investigation Utilizing Thermal Image Technique
to the Heat Transfer Enhancement Using Oscillated Fins
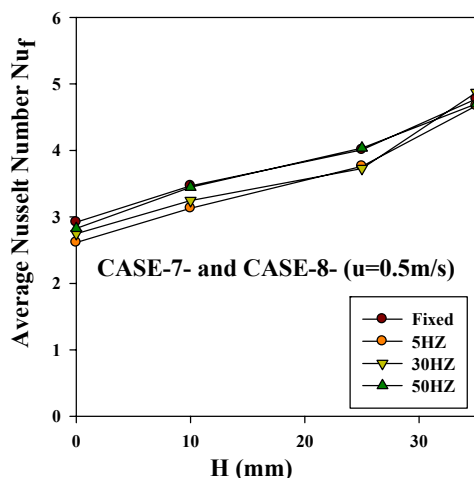
(c) Triple fins, u=0.5 m/s, , spacing=6mm,H=35mm
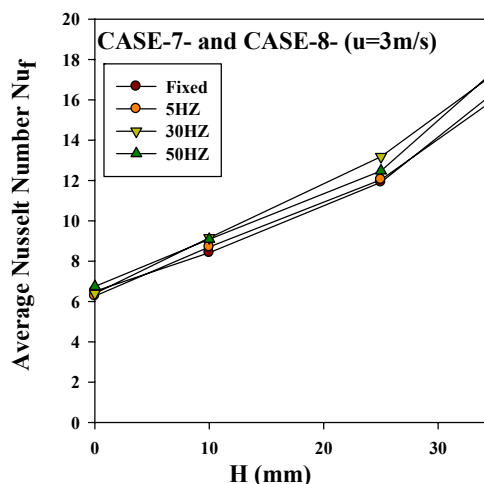
(d) Triple fins, u=3 m/s , spacing=6mm,H=35mm

Fig. (17): Variation of average Nusselt number along fins' height for different frequencies

CONCLUSION

According to the previous discussion the following conclusions can be extracted:

1. There is an effect for the height, Reynolds number, frequency and distance between the fin on heat transfer.

2. Triple fin (case 1) is the best case for enhancing heat transfer and the triple fin (case 2) gives minimum heat transfer with respect to other height.

3. Heat transfer increases with increasing frequency and stream wise air velocity.

4. Maximum heat transfer occurs at fins leading edge near it tip i.e X/L=0, Y/H=1 for all investigated heights.

5. Average heat transfer through the middle fin is enhanced by (4-25) % by oscillating the fin with 50HZ.

6. More effective enhancement of heat transfer utilizing fin oscillation is obtained for low stream wise air velocity (0.5m/s to 2m/s).

7. Increasing stream wise air velocity attenuates the enhancement in heat transfer due to oscillation because the air works as a damper to the oscillation.

8. The enhancement of heat transfer increases significantly with increasing oscillation frequency from 5HZ to 50HZ for all cases, except for height 35mm, because this fin height is not effective with oscillation, while, this height is found an optimal height with fixed fin only.

9. The effect of the inter-fin space obviously appears in the thermal image, especially with a distance of 6mm, the heat transfer through the surface of the frontal fin is improved due to the increase of flow rate between fins.

ACKNOWLEDGEMENT

REFERENCES

Antti Lehtinen (2005): "Analytical Treatment of Heat Sinks Cooled by Forced Convection" Ph.D thesis, Tampere University of Technology.Publication 579.

David J.Kukulka, Kevin G. Fuller, (2010): "Development of an Enhanced Heat Transfer Surface" 20th European Symposium on Computer Aided Process Engineering-ESCAPE20, Elsevier B.V.

F.B. Incropera, D.P. Deitt (1985): "Fundamentals of Heat and Mass Transfer" second ed., John Wiley and Sons, New York, 1985

H.K. Ma, B.R. Chen, H.W. Lan, K.T. Lin, and C.Y. Chao (2009): "Study of an LED Device with Vibrating Piezoelectric Fins" 25th IEEE SEMI-THERM Symposium.

M.R.Shaeri,   M.Yaghoubi   (2009):   "Thermal Enhancement from Heat Sinks by Perforated Fins" Energy Conversion and Management 50 PP 1264-1270.
Subhrajit Dey and Debapriya Chakrbrty, (2009): "Enhancement of Convective Cooling Using Oscillating Fins" Int. Communications in Heat and Mass Transfer 36 pp. 508-512.

Saad A. El-Sayed, Shamloul M. Mohamed, Ahmed M. Abdel-latif, Abdel-hamid E. Abouda, (2002): "Investigation of Turbulent heat transfer and fluid flow in longitudinal rectangular-fin arrays of different geometries and shrouded fin array" Experimental thermal and fluid Science 26 . pp. 879-900.

Tae Young Kim, Dong-Kwon Kim, Sung Jin Kim (2008): "Scroll Heat Sink: A Heat Sink with the Moving Fins Inserted Between the Cooling Fins" School of Mechanical, Aerospace and System Engineering. IEEE.

W.-S. Fu, S.-J.Yang, (2000): "Numerical Simulation of Heat Transfer Induced by a Body Moving in the Same Direction as Flowing Fluids" Int. J. heat mass transfer, 36, pp.257-264.

Wu-Shung Fu and Suh-Jenq Yang, (2001): "Heat transfer Induced by a Body Moving in Opposition to a Flowing Fluid" Int. J. heat mass transfer, 44, pp.89-98.

Wu-Shung Fu, Shih-Fa Chen and Ke-Nan Wang, (2001): "Effect of Moving Distance of a Moving Block on Heat Transfer in a Channel Flow" Int. J. heat mass transfer, Vol. 28, No.3, pp. 411-426.

Wu-Shung Fu, Ching-Chi Tseng, Chien-Ping Huang, Ke-Nan Wang (2007): "An Experimental Investigation of a Block Moving Back and Forth on a Heat Plate under a Slot Jet". Int. J. heat and mass transfer, Vol. 50, PP3224-3233.

Wu-Shung Fu, Jieh-Chau Huang, Chung-Gang Li (2010): "Enhancement of Forced Convection Heat Transfer in a Three-Dimensional Laminar Channel Flow with Insertion of a Moving Block" Int. J. heat mass transfer, 53, pp. 3887-3897.

Prof. Dr. Ihsan Y. Hussain
Asst.Prof. Dr.Karima E.Amori
Asst.Lecturer. Dheya G. Mutasher

Experimental Investigation Utilizing Thermal Image Technique
to the Heat Transfer Enhancement Using Oscillated Fins

Nomenclature

$A_{ct,f}$	Total Cross-Sectional Area of Fins at the Base (m^2)
Act	Surface Area of the Base Plate (m^2)
$A_{cb,f}$	Total Free Surface Areas of the Base Plate (m^2)
A_{sf}	Surface Area of the Tested Fin (m^2)
dis.	Distance Between the Fin (mm)
Distr.	Distribution
$h_{x,f}$	The Local Heat Transfer Coefficient ($W/m^2.^oC$)
$h_{xf,x}$	Local Heat Transfer Coefficient over the Tested Fins ($W/m^2.^oC$)
h_f	the Average Heat Transfer Coefficient over the Fin ($W/m^2.^oC$)
H	Height of the Fin (mm)
Ka	Thermal Conducyivity of the Air (W/m.k)
$Nu_{x,f}$	Local Nusselt Number over the Tested Fins
Nu_f	The Fin-average Nusselt number
N	Number of fins
q_{tot}	the Total Heat Flux (W)
q_{conv}	Convective Heat Flux (W)
q_{cond}	Conductive Heat Loss (W)
q_{rad}	Radiant Heat Loss (W)
q_c	the Convective Heat Transfer (W)
q_t	The Total Heat Generated from the Heater (W)
q_L	the Heat Losses (W)
q_s	Heat Lost by Conduction in the Stream-Wise (X) Direction (W)
q_p	Heat Lost by Conduction in the Spanwise (Z) Direction (W)
q_b	Heat Lost by Conduction From the Bottom Surface of the Base Plate (W)
q_{ft}	Heat Lost From the Fin Tips Surface (W)
q_r	Heat Lost by Radiation (W)
q_{cf}	the Convection Heat Transfer Through the Fins (W)
q_f	the Convection Heat Transfer Through one Fin (W)
q_{cb}	the Convection Heat Transfer Through the Free Area (W)
t	Thickness of the Fin (mm)
T_f	Temperature of the Fin at (x) (^oC)

297

قائمة المحتويات

-      -

:

.

%30   .

"

.(C.H.L)

.

Critical Evaluation of City Streets

Al_Talib Prof. Talib Hameed   altalib_ta@yahoo.com
Asst. Lec. Huda Sabah Fakher Al_deen   h_dream_7@yahoo.com

ABSTRACT

   The diverse urban spaces of the streets is an important part of the city's physicist configuration and a link between architectural and civilizational communication through time starting from the historic towns down to the contemporary cities, within the proposals of the future cities.

   From general observations and literature review a research problem is crystallized as some directions not arbitrary rational when expansion and the growth of cities, and other measures wrong or the existence of some incorrect actions and processes related to the cities planning as a categorizing the goals and priorities in city plan.The streets were constitute a high proportion of the total area of cities, where up to over 30% in major cities. These faults are primarily a result of considering city streets as mere path for vehicular movement While pedestrian movement comes as a left over consideration.

And a clear hypothesis search through the streets and designs which are formulated in accordance with the basis of geometric and mathematical equations to achieve the highest traffic density possible per hour (C.H.L).

The research paper exposes some international considerations and improvement methods in converting vehicular streets to pedestrian streets which considers step to revitalize the city street life as a social place that responds to the active and passive human needs.

:_____

(   )

.

.

.   "

(   )

                              "

                                                   ..

                                                       :

                              .

                              .

            :

      .

:   .

.

"   :

:   -1.1

.

.

"

.

(Gallion,1969,p.284)   ··

"

.

(Favro,1994,p.1)   -2.1   :

:

:   .

:

(7   1988   ).

.

(8) (7) (6) (5) (4) (3) (2) (1)

.

"

(2)

http;//www.coursesite.uhcl.edu

:

.

:
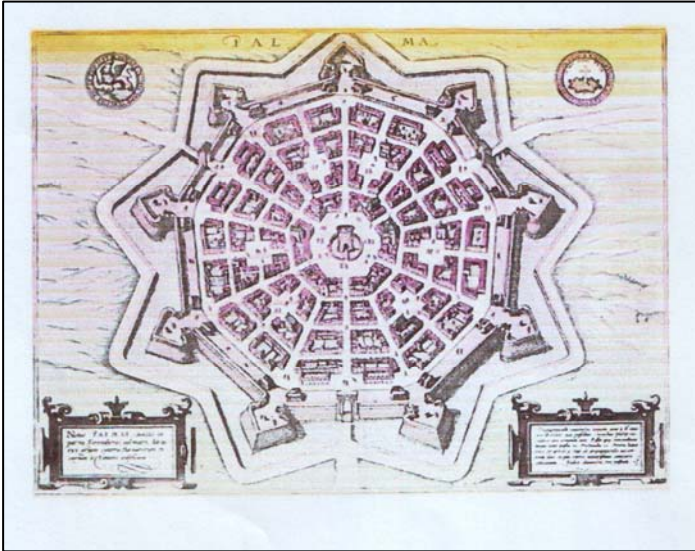
Social rooted   -
                                          Values

Economically   -
rooted Values

Public rooted   -
                                          Values

:

(3)
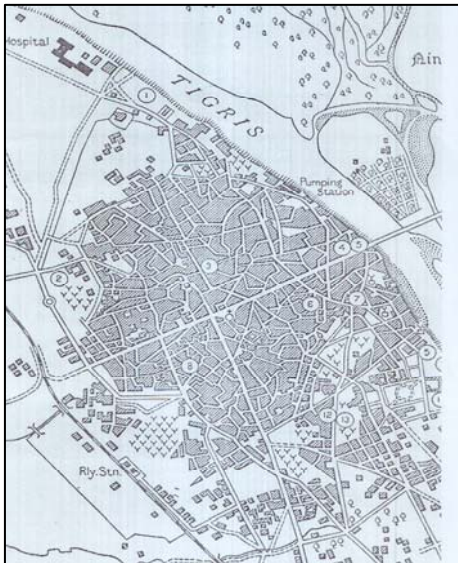
http;//www.lib.utexas.edu/ mosul

"   "

.

(1)

(Gallion,1969,p.289)

22

(5)

http;//www.rodshot.com

(4)

http;//www.lib.utexas.edu/ mosul

(7)

http;//www.lib.umd.edu

(6)

http;//www.boklife.com

(8)

http://www.sanftieben.com
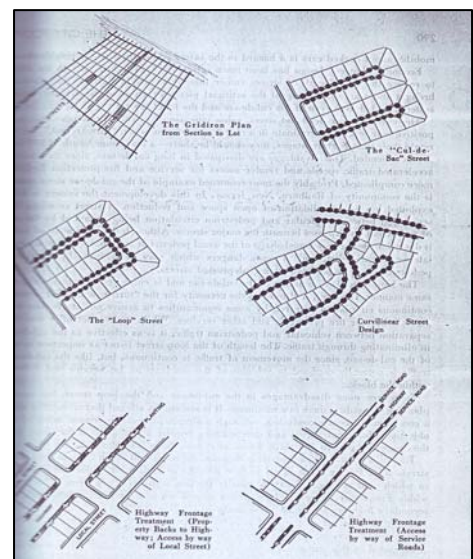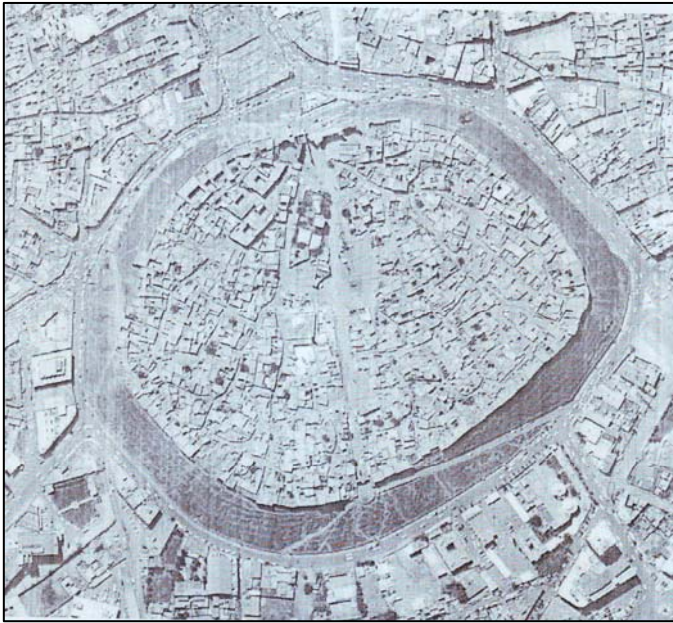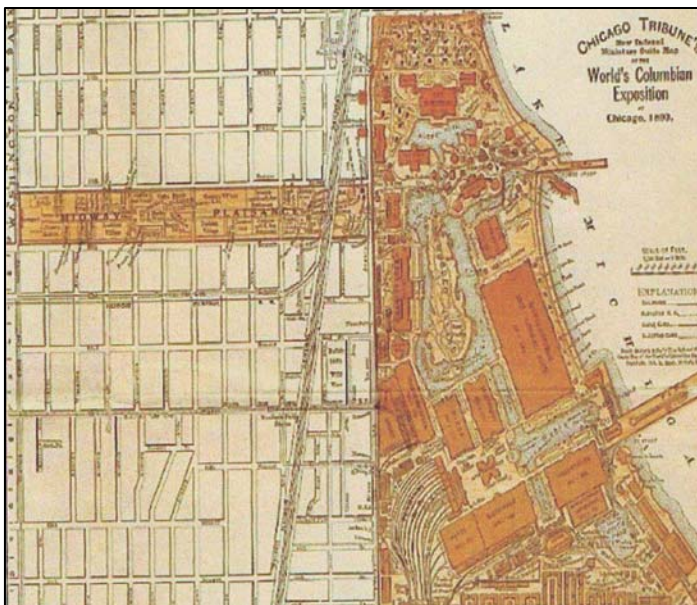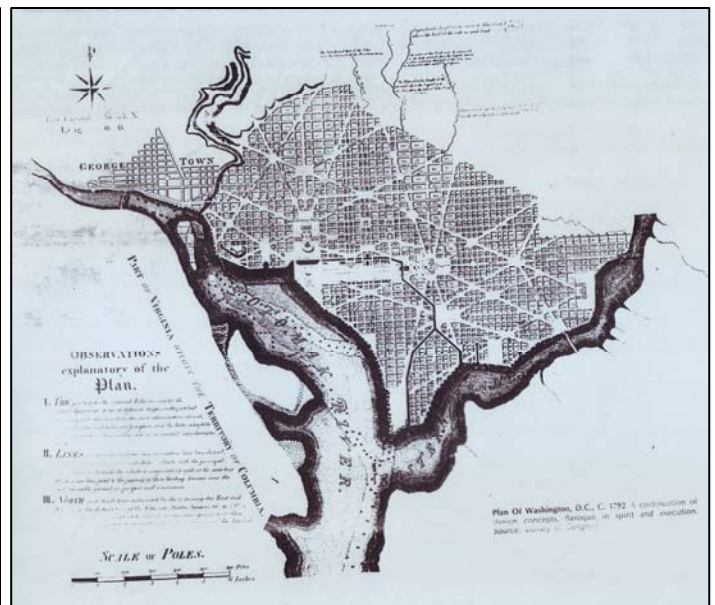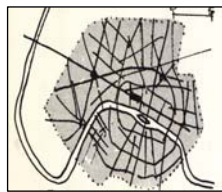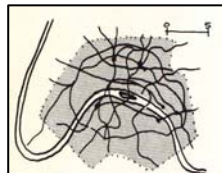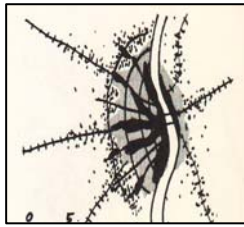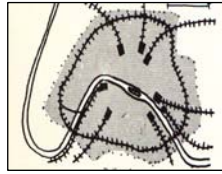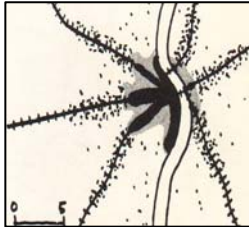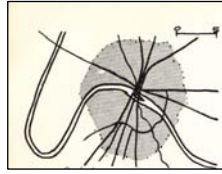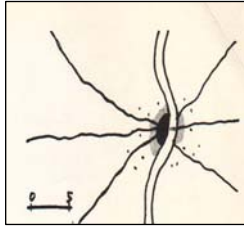
(10)   (9)

(Spreiregen,1965,p160,161)

3.1–   :

"

"   "

.

(10) (9)

"
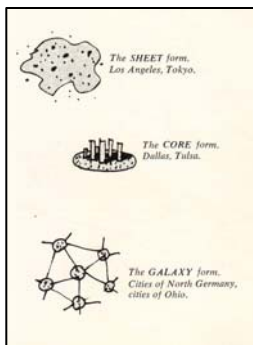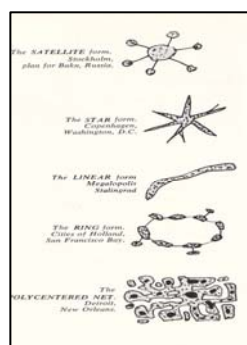
(12) (11)

(12)   (11)

(Spreiregen,1965,p171,172)
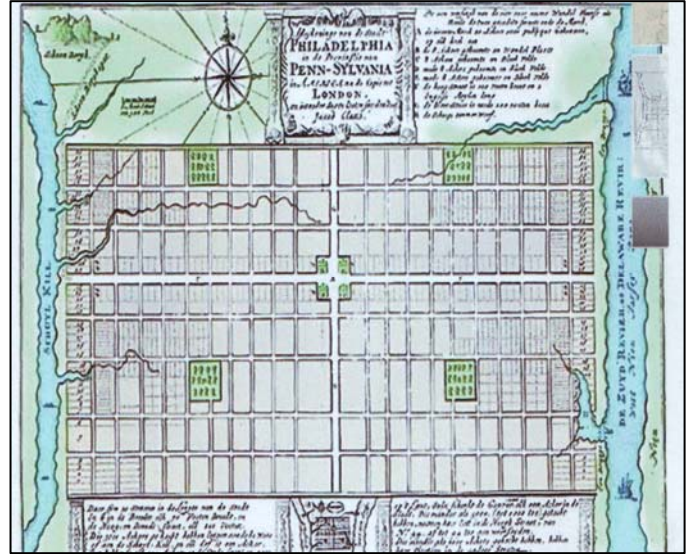
(14)   (13)

(Spreiregen,1965,p160,161)

!

(15)

.(16) (15) (14) (13)

"

"
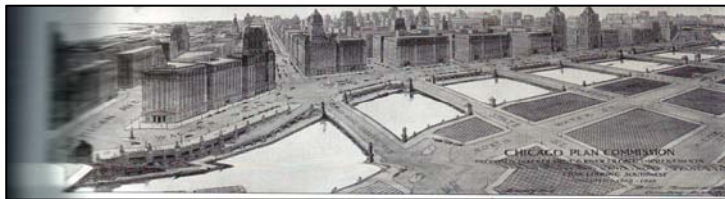
(16)
(16) (15) (14) (13)
(Favro,1994,p.259,262,265,266)

"

.
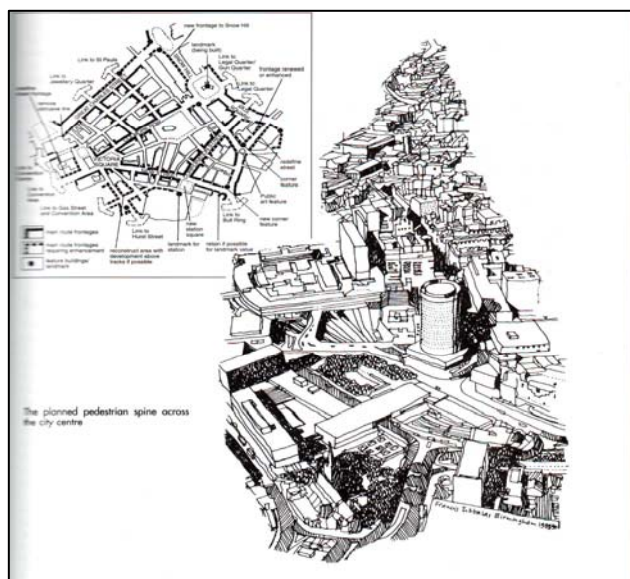
(17)
(19) (18) (17)
(Parfect,1997,p.164,177,185)

"   "

(31 29   2012   ).

"

(18) (17)

.(19)

.

:

2.1–   Identity:

.

.

(18)

.

.

(19)

:

.

.

.

.

.

.

.

.

.

26

.

.
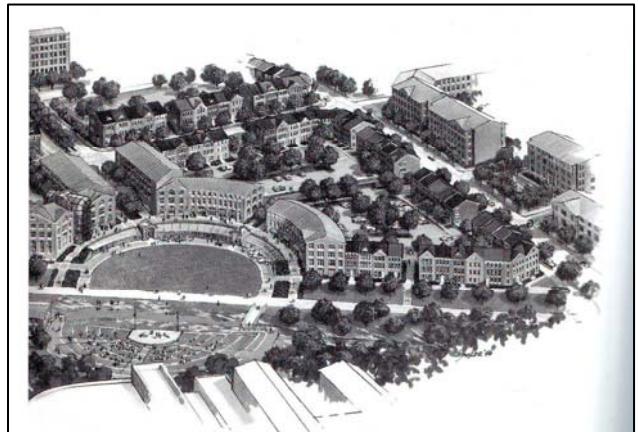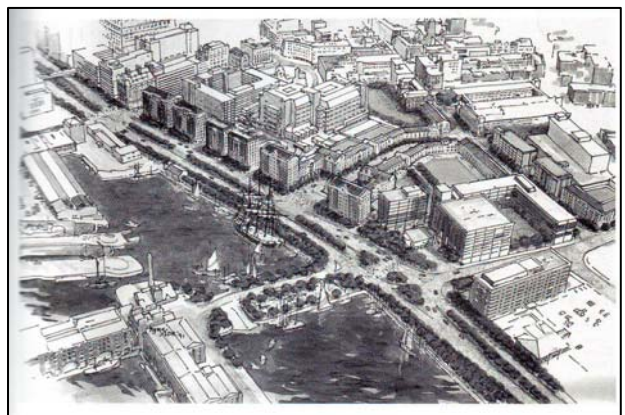
(Doxiadis,1974,p22-24)

.

.   .

(   )   :

.

"

" .

"
.

(Lynch,1972,p47-50)

"   "

.   :

(Lynch,1972,p2-8)   .

.   ...

.

:

(31 30   2012   ) .

Street Physical   2.2-

Construct:

.

.

.

.

.

.

Hegeman,   !   "

Peets

.

"   "

(Hegeman,1922, p187) .

.

(Module)

28

(Jone Wood the Elder)   .

1739-1728   (Arcade)   (Colonnaded)

(Jone Wood the Younger)

(The Royal Crecent)

(26) (25) (24) (23)   1774-1767   .

.

(www.localhistory,p15) .

Street Artistic   -3.2   .

:Construct   (Cliff Moughtin,2003, p145)

"   "

.

(21)   (20)

(22)

.

(Giorgio Vasari)

(Piazza delgi Uffizi)

.   -1560   (Medichi)

1574

(Bacon,1975,p112)

:

:

.

:   :

.   (Circus)

.   .

(432-   .

(447

(27) (28) (29)

(Phidias)

.   .

.   .

67

.

.(Kenza,2004,p3-10)

"

.   .

Kimberly Elam

.

2570 .   .

.(1.618/1)   .

(Kimberly Elam,p6)

(Paramidiology)   .

(21)

(22)

(20)   (21)   (22)

http://www.flicker.com/photos

(23)

(24)

(25)

(20)

.

.

.

.

.

.

.

(26)

(23) (24) (25) (26)

–

http://www.flicker.com/photos

(27)

.

(28)

.

( ) :

.

.

2.4– **Street Furniture:**

(29)

.

(27) (28) (29)

.
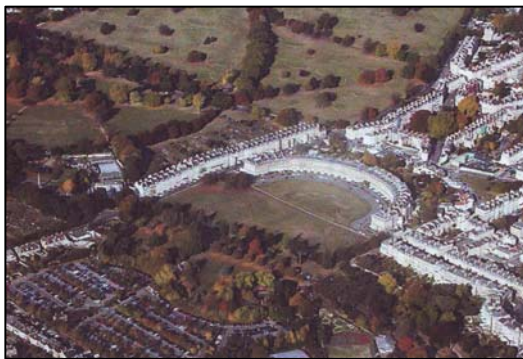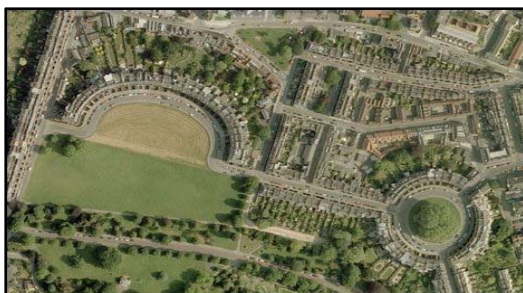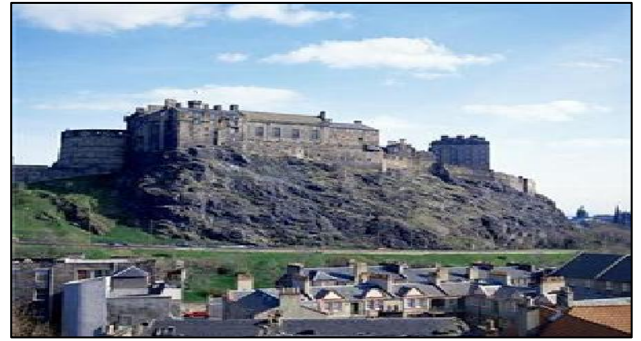
32

:   (Gibed,1955,

.

" "

(47)

(Gibed)

…

.

1933   .   .
(CIAM)

(Congress Internationaux d'Archtectur
                        Moderne)

(Function)   :
              (Structure)   p199) .

(Standardization)   (Jacobs,1961,p39-40) .

.

(Smithson,1967,   p130) .

(Lynch,1972, p3) .   .

"   "The street is not only a means
of access, but also an arena for
social interaction,"
(Jane Jacobs)

(Doxiadis,1974, p21).

:

.

"

:

.

3.1-   Pedestrian Street:

.

)

"

.

.

(

Effective Eye on the Street

.

.

"

.

.

Stroget

.

Times Square   (Newman,1972,p169)

(52) (51) (50) (49) (48)   .   :

(53)

(40)

(46) (45) (44) (43) (24) (41)   Macro Economics

A   -   –

nation on wheels   (38) (37) (36) (35)   .

57   (39)

"   (en.wikipedia , p 1-20)

:

.

.

.

(13   1986   ).

<u>:   –2.3</u>

:

.

(120 –117   1985   ).   .

(   )

)

.

.

Utopias

(

(111   1987   ) (30)

"

Garden City

Ebenezer Haward   Corbusier   "

"   "

.   .   24

60

.   .

%5

.

.

.

.   "   "   "   "   "   "

(34)   (33)   .

5-

%12   .

(Gallion,1969,p360-362)   .

.

:   .

.   .

(31)   .

"   (Spreiregen,1965,p.36)   (32)

Le
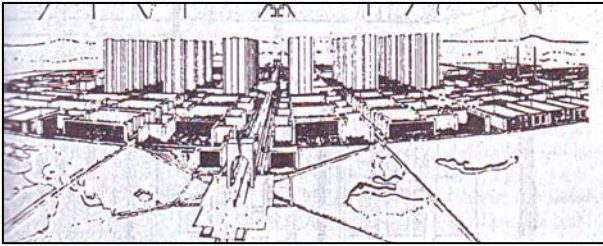
(34)

(Gallion,1969,p.361)

(35)
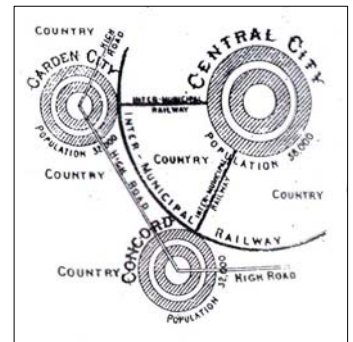
http://3bpblogspot.com

(30)

(107   1987   )

(31)

(Spreiregen,1965,p.36)

(36)

http://whatsonsanya.com

(32)

(Spreiregen,1965,p.36)

(37)

http://fastmotoring.com

(33)

(Gallion,1969,p.361)

38

(41)

(42)

(38)

http://3bpblogspot.com

(43)

(39)

http://en.wikipedia.org/wiki/Street

(39) (38) (37) (36) (35)

(44)

(45)

http://en.wikipedia.org/wiki/Street
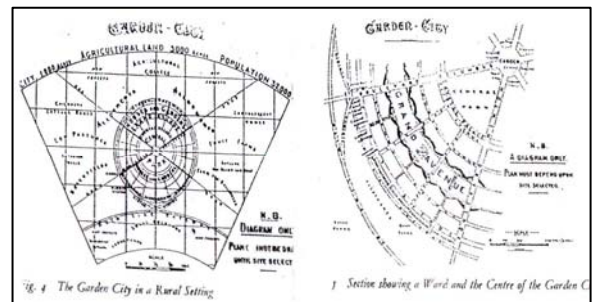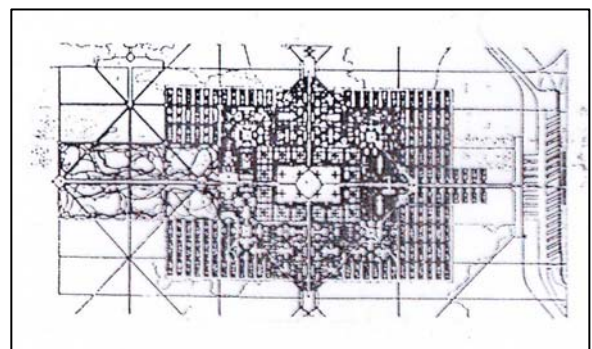
(40)

(44) (43) (42) (41) (40)

(Favro,1994,p.229-232)
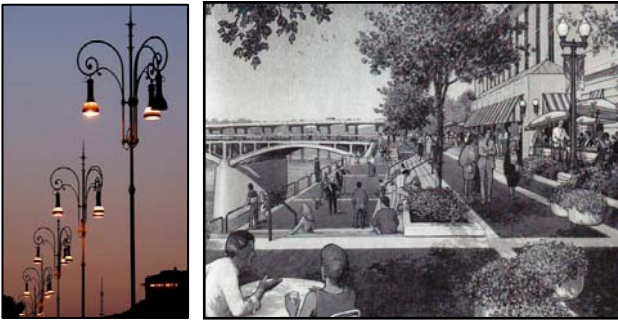
Times square (48)

Broad way (49)

(46)

(-47)

40

(53)

http://www.pps.org/graphics/ Copenhagen

Times square   (50)

http://gothamist.com/attachment/jsaxena/timessquare

(51)

http://www.pps.org/graphics/ Copenhagen

(52)

http://www.pps.org/graphics/ Copenhagen

: _____

-

.

: _____

-

.

"

-

"

.

-

.

-

.

-

.

-

.

-

.

-

.

-

.

: _____

- "

"

.1986

- "

"

_____

156

.1985

- "

"

_____

.1987

- "

"

.1988

- "

"

_____

7

643

.2012

: _____

- Abu H. Imamuddin, "A Unique Old City Settlement Dhaka", Architectural and Urban Conservation In The Islamic World, The Aga Khan Trust for Culture, 1991.
- Bacon, Edmund, "N .Design of Cities", Thames and Hudson, London, 1975.
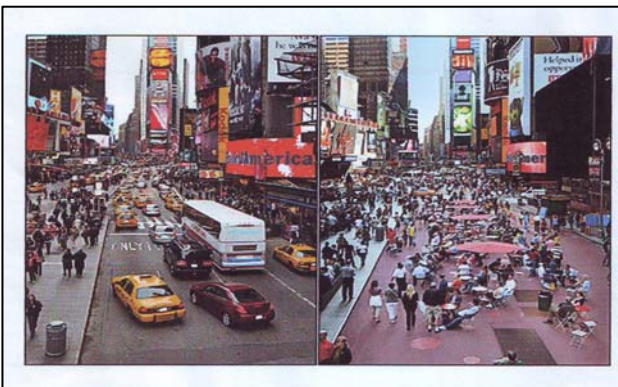
- Cliff Moughtin, "Urban Design, Street and Square", Third Edition, Architectural Oxford, 2003.
- Doxiadis C. A. , "Anthropoplis for Human Development", Center of Ekistics, Athens, 1974.
- Favro, Diane, Zeynep and Richard, "Streets" ,University of California Press,1994.
- Hegeman, Werner, Peets, and Elbert, "An Architect Handbook of Civic Art Bejamin Blom", New York, 1922.
- Gallion, Arthur B. ,"The Urban Pattern", Van Nostrand Reinhold Company, New York,1969.
- Gibed, Fredric, "Town Design", second Edition, Architectural Press , London, 1955.
- Jacobs, Jane; "The Death and Life of Greet American Cities", Random House, N.Y 1961.
- Kimberly Elam.," Geometry in Design"; Princton Architecture Press.
- Kenza, Baussora and Said Mazoua, "The Use of Golden Section in Kairouan Mosque". Nexus Journal Vol.6, 2004.
- Lidwell, Willim; etal; "Universal Principal of Design", Rockport Publishers, 2003.
- Lynch, Kevin, "The Image of City", M.I.T. Press Cambridge, Massachusettc, 1972 .
- Newman, Oscar, "Defensible Space" , Architectural Press, London, 1972.
- Parfect, Michael and Gordan Power, "Planning for Urban Quality", New York, 1997.

- Smithson, peter and Alison, "Urban Structure, Streets and Squares", Studio Vista; London, 1967.
- Spreiregen, Paul, "The Architecture of Towns and Cities", Mc Graw Hill, United States of America ,1965.
- http://www. History of Bath. localhistory.org./bath.htm
- http://wikipedia.org/wiki/List_of_countries_by_vehiches_per_capita
- http://en.wikipedia.ora/wiki/List_of_car_free_places
- http://en.wikipedi.org/wiki/world_columbian_exposition
- Hemenway, Priya; Divine Proportion
  http://book.google.com./books,
- http://en.wikipedia.org/wiki/Principals_of_Intellegent_Urbanisim
- http://en.wikipedia.org/wiki/Street
- http://www.flicker.com/photos
- http://gothamist.com/attachment/j saxena/timessquare
- http://www.pps.org/graphics/gpp/ Copenhagen
- http://blogs.villagevoice.com/runn inscared/tsquaremall4
- http://www.coursesite.uhcl.edu
- http://www.lib.utexas.edu/ mosul
- http://www.rodshot.com
- http://www.boklife.com
- http://www.lib.umd.edu
- http://www.sanftieben.com
- http://www.playbill.com
- http://en.wikipedia.org/ Street furniture
- http://www.ftscities.com
- http://whatsonsanya.com
- http://fastmotoring.com
  - http://3bpblogspot.com

Load Distribution Factors For Horizontally Curved Composite Concrete-Steel Girder Bridges

Lecturer Dr. Rafa'a Mahmood Abbas   **Zainab Saadi Qassem**
rafaamaa@yahoo.com

Department of Civil Engineering - University of Baghdad

ABSTRACT

This paper focuses on Load distribution factors for horizontally curved composite concrete-steel girder bridges. The finite-element analysis software"SAP2000" is used to examine the key parameters that can influence the distribution factors for horizontally curved composite steel girders. A parametric study is conducted to study the load distribution characteristics of such bridge system due to dead loading and AASHTO truck loading using finite elements method. The key parameters considered in this study are: span-to-radius of curvature ratio, span length, number of girders, girders spacing, number of lanes, and truck loading conditions.

The results have shown that the curvature is the most critical factor which plays an important role in the design of curved girders in horizontally curved composite bridges. Span length, number of girders and girder spacing generally affect the values of the moment distribution factors. Moreover, present study reveals that AASHTO Guide criterion to treat curved bridges with limited curvature as straight one is conservative. Based on the data generated from the parametric study, sets of empirical equations are developed for the moment distribution factors for straight and curved steel I-girder bridges when subjected to the AASHTO truck loading and due to dead loading.

KEYWORDS: Composite Bridges, AASHTO Loading, Load Distribution Factors, Horizontally Curved Bridges, Finite Element Analysis, Curved I-Girders, Warping Stresses.

م. د. رافع محمود عباس   **زينب سعدي قاسم**
rafaamaa@yahoo.com

قسم الهندسة المدنية ـ جامعة بغداد

الخلاصة:

يهدف هذا البحث لدراسة السلوك الإنشائي للجسور المركبة بسيطة الإسناد والمنحنية في المستوى الأفقي. حيثُ يهدف البحث لتحديد معاملات توزيع الأحمال الحية والأحمال الميتة على تلك الجسور المركبة. أن المواصفة الأمريكية للجسور المنحنية لا تعطي قيم أو صيغ رياضية لمعاملات توزيع الأحمال على الأعتاب الفولاذية لتلك الجسور وإنما تكتفي فقط بإعطاء صيغة مبسطة لتحليل تلك الجسور عندما تكون قيمة التقوس لها بسيطة وذلك بإهمال تاثير التقوس واحتساب معاملات توزيع الأحمال فيها كما في الجسور المستقيمة.

تم استعمال طريقة العناصر المحددة لتحليل نموذج ثلاثي الأبعاد لسطح الجسر والعتبات الفولاذية المقوسة. تم استعمال برنامج (SAP 2000) لعمل موديل ثلاثي الأبعاد للجسر المركب ودراسة تأثير عدد من العوامل المؤثرة على معاملات توزيع أحمال العجلات والأحمال الميتة لتلك الجسور. إن العوامل التي تمت دراستها في هذا البحث تشمل: درجة التقوس، طول الجسر، عدد الاعتاب الفولاذية، مسافة توزيع الأعتاب الفولاذية، عدد الممرات لسطح الجسر وعدد وطبيعة الممرات المحملة بالمركبات. بينت النتائج من هذه الدراسة إن درجة التقوس للمسقط الأفقي لسطح الجسر لها دور كبير في تحديد معاملات توزيع العزوم في الأعتاب المقوسة وانه كلما زادت درجة التقوس ازدادت تلك المعاملات. كما وان طول الجسر وعدد الأعتاب ومسافة توزيعها لها دور في تحديد تلك المعاملات. واعتماداً على النتائج النظرية التي تم التوصل إليها في هذه الدراسة تم تطوير عدد من المعادلات الرياضية المبسطة التي تساعد المصمم للجسور المركبة المنحنية على تحديد معاملات توزيع العزوم في الأعتاب الفولاذية وبطريقة مشابهة لمعاملات الجسور المستقيمة

كلمات المفتاح: تحليل العناصر المحددة، الجسور المركبة، الجسور المنحنية في المستوي الافقي، العتبات المقوسة، معاملات توزيع الاحمال، اجهادات الالتواء، احمال الجسور.

INTRODUCTION

During recent years, there is a trend toward the design and construction of horizontally curved highway bridges to accommodate higher volumes of traffic within geographical constrains. Due to its geometry, simple presence of curvature in curved bridges produces non uniform torsion and consequently, lateral bending moment (warping or bi-moment) in the girder flanges as shown in **Fig.1**. The simple presence of curvature in curved steel girders complicates, to a great extent, their behavior and design considerations over those of straight girders. **Fig. 2** shows typical cross-section of a four-girder bridge. It consists of a concrete deck slab supported over steel I-girders. Cross-bracings as well as top and bottom chords are used at equal intervals between bridge support lines to stabilize the girders during construction and enhance its structural integrity.

 In designing highway bridges, dead loading and live loading are imposed on bridges and used in the design of bridges**.** In the bridge design codes, the live load is the standard truck loading with concentrated wheel loads. Both longitudinal and lateral position of truck wheel loads is of great importance when calculating moment in the girders. Therefore, the truck load must be positioned longitudinally and transversely in a certain manner to produce maximum positive and negative bending moments, shear and deflection in the girders. Bridge design codes define lateral distribution factor that specify the fraction of each wheel load that must be applied to each girder and allows each girder to be designed as straight girder. For this reason, load distribution factor is of fundamental importance in bridge design.

BACKGROUND

The first treatment of the analysis of curved beams is presented in 1843 by Barré de Saint Venant as referred by Zureik (1998, 1999). McManus et al. (1969) present the first survey of the most published works related to horizontally curved bridges. His bibliography list contained 202 references.

Serious studies pertaining to the analysis and design of horizontally curved bridges begun only in 1969 when the Federal Highway Administration (FHWA) in the United States formed the Consortium of University Research Teams (CURT). This team consists of Carnegie Mellon University, University of Pennsylvania, University of Rhode Island, and Syracuse University, whose research efforts, along with those at University of Maryland, resulted in the initial development of working Stress Design (WSD) or Allowable Stress Design (ASD) criteria and tentative design specifications.

The American Society of Civil Engineers (ASCE) and the AASHTO Task Committee on flexural members (1977) compile the results of most of the research efforts prior to 1976 and presented a set of recommendations pertaining to the design of curved I-girder bridges. The CURT research activity is followed by the development of Load Factor Design (LFD) criteria adopted by AASHTO to go along with the ASD criteria. These provisions appeared in the first Guide (1980) as well as the Guide (1993). It is worthwhile to mention that the AASHTO guide specification for horizontally curved highway bridges (1993) is primarily based upon research work conducted prior to 1978.
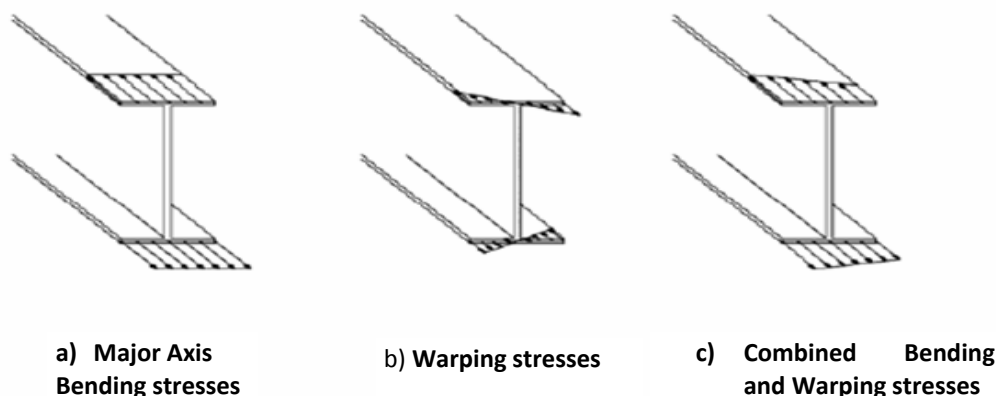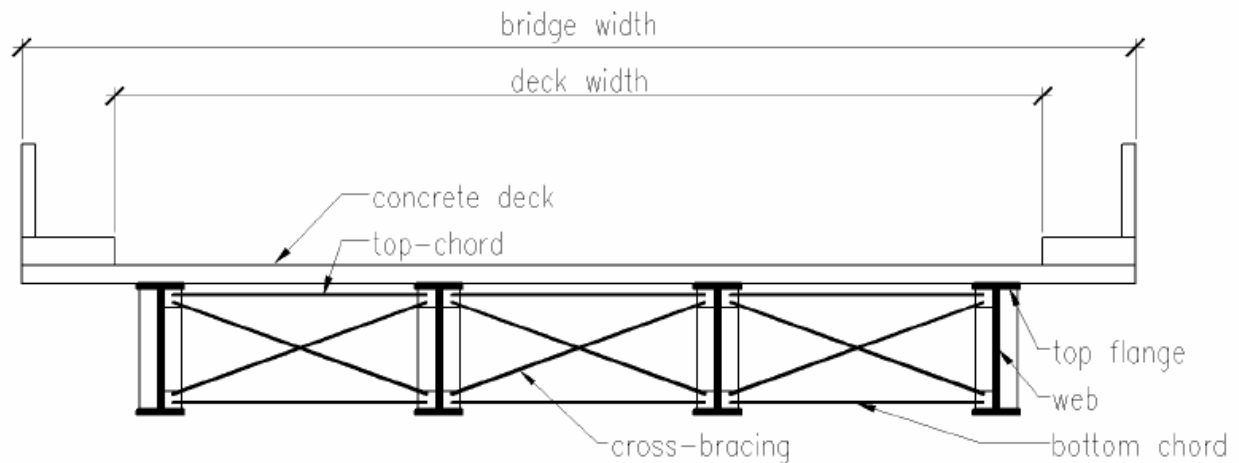

a) **Major Axis Bending stresses**   b) **Warping stresses**   c) **Combined Bending and Warping stresses**

Fig. 1: Normal Stresses Distribution in Curved I-Girder Flanges

Fig. 2: Typical Cross Section of Concrete Deck I-Girder Bridge

OBJECTIVES

The objectives of this study are:

1. Identifying the key parameters that influence the lateral distribution of loads in straight and horizontally curved composite concrete-steel bridges and calculating the load distribution factors,

2. Providing accurate database that can be used for developing simplified design method for horizontally curved composite concrete-steel bridges, and

3. Developing simplified formulas for moment distribution factors for straight and horizontally curved composite concrete-steel bridges when subjected to AASHTO truck loading as well as dead loading.

BRIDGE MODEL CONFIGURATIONS

102 simply supported straight and curved composite concrete-steel girder bridge prototypes are considered for finite-element analysis in this study. Several major parameters are considered as follows:

1. Span length **(L)**: 15, 25, and 35 m,

2. Girder spacing **(S)**: 2, 2.5, and 3 m,

3. Number of girders **(N)**: 3, 4, and 5, and

4. Span-to-radius of curvature ratio **(L/R)**: 0.0, 0.1, 0.2, & 0.3 for span L=15 m; 0.0, 0.1, 0.3,

Other bridge configurations are listed as below:

- The deck slab thickness is taken as 225 mm,

- The deck slab width (Wc) is taken equal to the total bridge width minus 1.0 m to consider the parapet thickness,

- The depth of the girder webs is taken (1/20) of the centre line span,

- The girder web thickness is considered equal to 16 mm,

- The over-hanging slab length is considered equal to half the girders spacing, and

- The bottom and top steel flanges width and thickness are maintained 300 mm, and 20 mm, respectively.

Table 1 shown below summarizes the straight bridge configurations considered in this study.

Table 1: Bridge Configurations Considered in the Parametric Study

Bridge Width (m)	Deck Width,Wc (m)	Number of Girders	Girder Spacing (m)	Number of Lanes
7.5	6.5	3	2.5	2-lanes
9	8	3	3	2-lanes
8	7	4	2	2-lanes
10	9	4	2.5	2-lanes
12	11	4	3	3-lanes
10	9	5	2	2-lanes
12.5	11.5	5	2.5	3-lanes
15	14	5	3	4-lanes

X-type cross-bracings with top and bottom chords are utilized in this study as shown in **Fig. 2**. These bracings are spaced at equal intervals between the support lines and are made of single steel angles having dimensions (150x150x25) mm. The equal intervals spacing between these cross-bracings are based on **equation A**, which is developed by Davidson et al. (1996) to reduce and limit the warping-to-bending stress ratio.

$$S_{max} = L\left[-Ln\left(\frac{Rb_f}{2000L^2}\right)\right]^{-1.52} \qquad (A)$$

Where: (L) is span length, (R) radius of curvature, (b_f) flange width.

 The study is based on the following assumptions:

1. The reinforced concrete slab deck has composite action with the top steel flange of the girders (shear interaction);

2. The bridges are simply-supported;

3. All materials are elastic and homogenous;

4. The effect of road super elevation, and curbs are ignored; and

5. Bridges have constant radii of curvature between support lines.

Regarding the first assumption, Wassef (2004) concludes that bridge composite action is accurately achieved when the shear connector studs are modeled in the finite element analysis using shell element rather than frame elements. Hence, the latter is ignored in this study and shell elements are adopted to represent the shear connectors in the finite element models.

The modulus of elasticity of concrete material is taken 28 GPa with Poisson's ratio of 0.20 while they are 200 GPa and 0.30, respectively, for structural steel material.

FINITE ELEMENTS MODELING

To analyze all the above mentioned composite bridge models and to determine their structural behavior, a three-dimensional finite-element model is used.

The composite bridge is divided into concrete deck slab, top steel flange, steel web, bottom steel flange, and the cross-bracings. In this study, four-node shell elements with six degrees of freedom at each node are used to model the concrete deck slab, the top and bottom girder flanges, and finally the girder web. Whereas, frame elements, pinned at both ends, are used to model the cross-bracings with the top and bottom chords.

Based on previous work on finite-element modeling, four vertical shell elements are used in each web, and another four are used horizontally for the deck slabs between the webs, whereas two shell elements are used for the over hanged deck slab, and for the upper and lower steel flanges. **Fig.3** shows a finite-element discretization of the four-girder cross section.

BOUNDARY CONDITIONS

In modeling the bridge supports in this study, the lower nodes of the web ends are restrained against translation in such way to simulate temperature-free bridge superstructure. The interior support at the right end of the bridge is restrained against movements in all direction. The middle supports and the exterior support at the same right end of the bridge are restrained against the vertical movement and against the movement in y-direction.
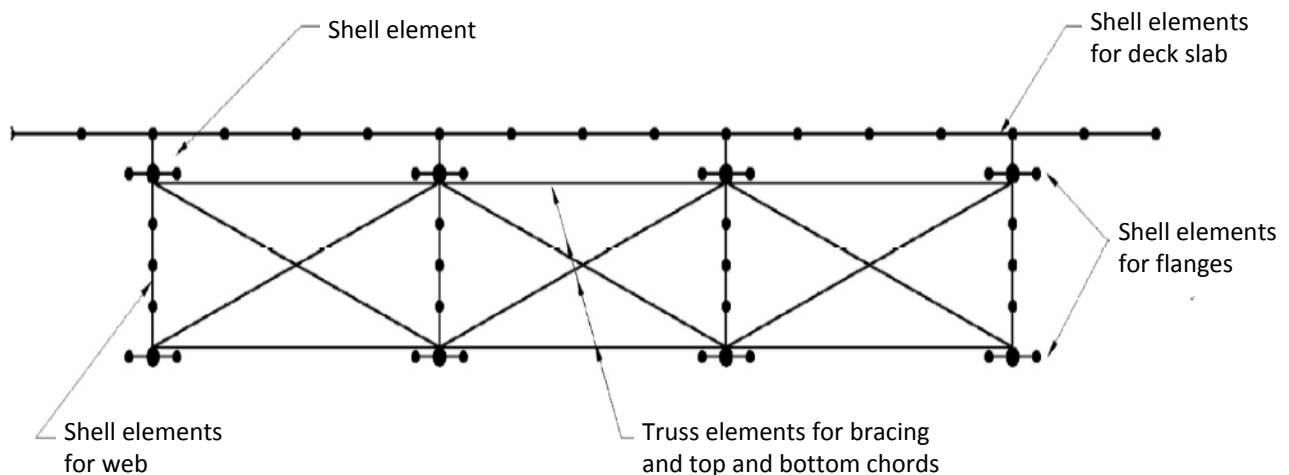
Fig. 3: Finite Element Discretization of the Bridge Cross-section

On the other end of the bridge (left end), all the supports are restrained only against vertical movement, except for the interior support which in addition to the vertical restraining, it is restrained in x-direction (towards the bridge transverse direction).
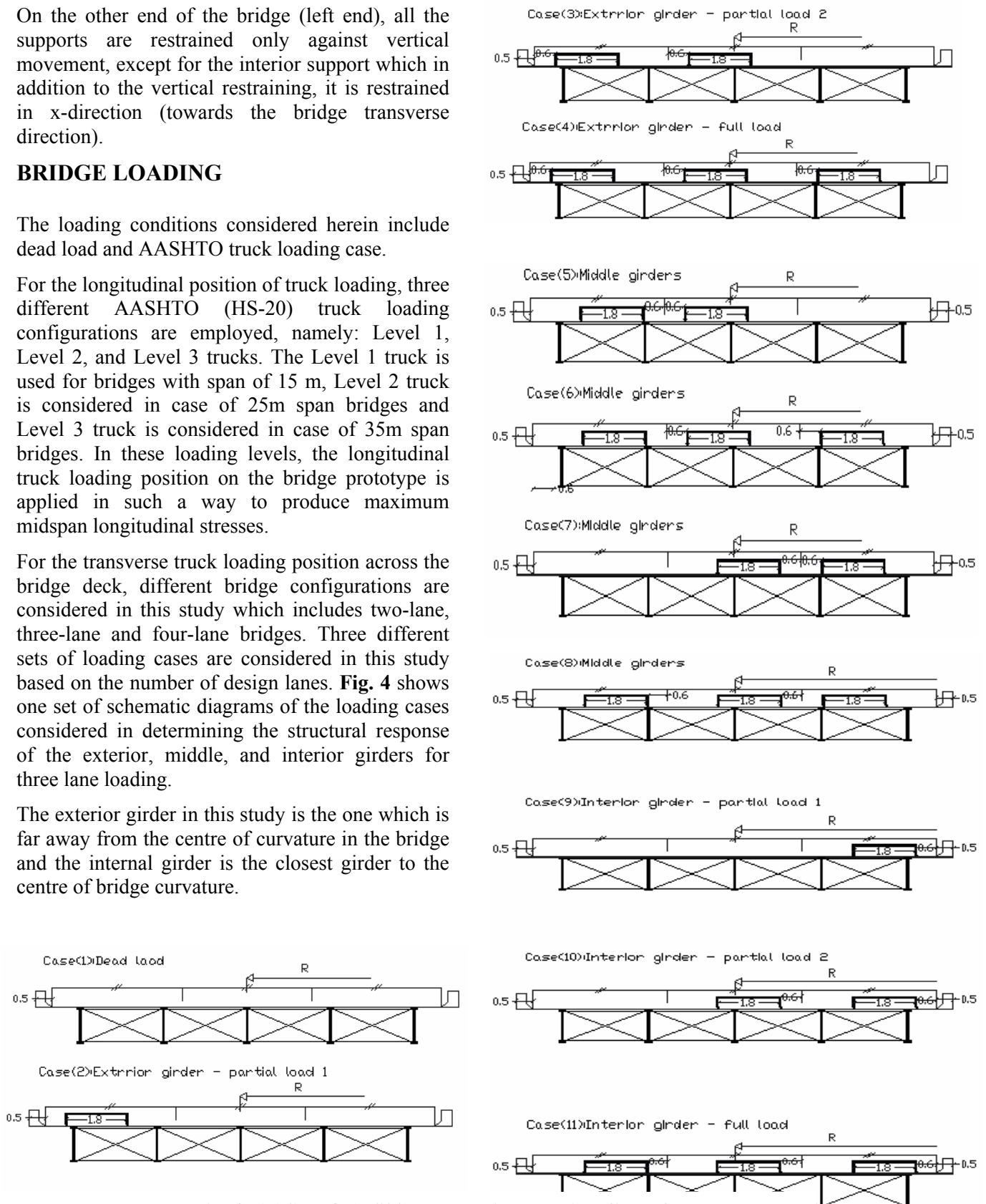
BRIDGE LOADING

The loading conditions considered herein include dead load and AASHTO truck loading case.

For the longitudinal position of truck loading, three different AASHTO (HS-20) truck loading configurations are employed, namely: Level 1, Level 2, and Level 3 trucks. The Level 1 truck is used for bridges with span of 15 m, Level 2 truck is considered in case of 25m span bridges and Level 3 truck is considered in case of 35m span bridges. In these loading levels, the longitudinal truck loading position on the bridge prototype is applied in such a way to produce maximum midspan longitudinal stresses.

For the transverse truck loading position across the bridge deck, different bridge configurations are considered in this study which includes two-lane, three-lane and four-lane bridges. Three different sets of loading cases are considered in this study based on the number of design lanes. **Fig. 4** shows one set of schematic diagrams of the loading cases considered in determining the structural response of the exterior, middle, and interior girders for three lane loading.

The exterior girder in this study is the one which is far away from the centre of curvature in the bridge and the internal girder is the closest girder to the centre of bridge curvature.

Fig. 4: AASHTO (HS20) Truck Live Loading Cases for Three-lanes Bridge

MOMENT DISTRIBUTION FACTORS

To determine the moment distribution factor (MDF) for curved girder, the maximum flexural stresses, $(\sigma_{straight})_{truck}$, $(\sigma_{straight})_{DL}$ are calculated for a straight simply supported beam subjected to AASHTO truck loading, and dead load, respectively.

The span of the straight simply supported girder is taken as the curved length of the bridge centerline. From the finite-element modeling, the maximum longitudinal moment stresses along the bottom flange for dead load, fully loaded lanes, and partially loaded lanes are calculated. Consequently, the moment distribution factors (MDF) were calculated as follows:

FOR EXTERIOR GIRDERS:

$$(MDF)_{DLext}=(\sigma_{FE.ext})_{DL}/(\sigma_{Straight})_{DL} \qquad (1)$$

$$(MDF)_{FL.ext}=(\sigma_{FE.ext})_{FL} \times N/((\sigma_{Straight})_{truck} \times n) \qquad (2)$$

$$(MDF)_{PL. ext} = (\sigma_{FE.ext})_{PL} \times N \times RL' / ((\sigma_{Straight})_{truck} \times \times RL) \qquad (3)$$

FOR MIDDLE GIRDERS:

$$(MDF)_{DL.mid}=(\sigma_{FE.mid})_{DL}/(\sigma_{Straight})_{DL} \qquad (4)$$

$$(MDF)_{FL.mid}=(\sigma_{FL.mid})_{FL} \times N/((\sigma_{Straight})_{truck} \times n) \qquad (5)$$

FOR INTERIOR GIRDERS:

$$(MDF)_{DL.int}=(\sigma_{FE.int})_{DL}/(\sigma_{Straight})_{DL} \qquad (6)$$

$$(MDF)_{FL.int}=(\sigma_{FE.int})_{FL} \times N/((\sigma_{Straight})_{Truck} \times n) \qquad (7)$$

$$(MDF)_{PL.int}= (\sigma_{FE.int})_{PL} \times N \times RL' / ((\sigma_{Straight})_{truck} \times n \times RL) \qquad (8)$$

Where $(MDF)_{DL}$, $(MDF)_{FL}$, and $(MDF)_{PL}$ are the moment distribution factors for dead load, fully loaded lanes, and partially loaded lanes, respectively. And the symbols ext, mid, and int. refer to the exterior, middle, and interior girders, respectively. $(\sigma_{FE. ext})_{DL}$, $(\sigma_{FE. ext})_{FL}$, and $(\sigma_{FE. ext})_{PL}$ are the maximum longitudinal stresses which are the greater at bottom flange, found from the finite-element analysis for the exterior girder due

to dead load, fully loaded lanes, and partially loaded lanes , respectively.

In the same criteria, $(\sigma_{FE.mid})_{DL}$, $(\sigma_{FE.mid})_{FL}$, $(\sigma_{FE.int})_{DL}$, $(\sigma_{FE.int})_{FL}$, and $(\sigma_{FE.int})_{PL}$ are the maximum stresses which are the greater of the flange stresses for the middle and interior girders under the same above types of loading. While RL, RL′, n, and N are defined as:

n: number of design lanes, as listed in **Table 2**,

RL: multi-lane factor based on the number of the design lanes; as shown in **Table 3**,

RL′: multi-lane factor based on the number of the loaded lanes; as shown in **Table 3**, and

N: number of girders.

Table 2: Number of Design Lanes

Deck Width, Wc	Number of Design Lanes, N
Over 6.0 m to 10.0 m incl.	2
Over 10.0 m to 13.5 m incl.	3
Over 13.5 m to 17.0 m incl.	4

Table 3: Modification Factors for Multilane Loading

Number of Loaded Design Lanes	Modification Factor
1 or 2	1
3	0.90
4 or more	0.75

PARAMETRIC STUDY

A parametric study is conducted to study the load distribution characteristics of the curved composite bridge system due to dead loading and AASHTO truck loading and to examine the key parameters that can influence the distribution factors for horizontally curved composite steel girders.

The key parameters considered in this study are:

- Span-to-radius of curvature ratio,
- Span length,
- Number of girders,
- Girders spacing,
- Number of lanes, and
- Truck loading conditions.

Results from the parametric study are presented herein below

EFFECT OF CURVATURE

Fig. 5 shows the variation in the moment distribution factors for the exterior, middle and interior girders of the three-lane, four-girder bridge with the increase in the span-to-radius of curvature (L/R) ratio due to dead load. Whereas, **Fig. 6** shows the moment distribution factors for the exterior, middle and interior girders for the same bridge with the increase in the span-to-radius of curvature (L/R) ratio due to fully-loaded lanes with AASHTO truck loading.

It can be observed that the moment distribution factors for the exterior and middle girder increases with the increase in span-to-radius of curvature ratio. It can also be noticed that the rate of increase of the moment distribution factor generally increases with the increase in span length. Whereas, the moment distribution factor for the interior girder increases with increase of curvature up to a certain value of L/R ratio, after which the moment distribution factor decreases with the increase in curvature.

These figures reveal that curvature of the bridge is one of the most significant parameters affecting the distribution of moments between the longitudinal girders.

It should be noted AASHTO Guide, 2003 states that curved bridges can be treated as straight ones if the span-to-radius of curvature ratio is less than 0.06 radians. While, the AASHTO-LRFD, 2004

specifications state that a curved bridge can be treated as a straight one in structural design if the central angle is less than 3° (≈ 0.05 radians) for bridge cross-section made of three or four girders and 4°(≈ 0.07 radians) if the number of girders is 5 or more.

It is evident from the results presented in **Figs. 5 and 6** that the limitation specified by AASHTO guide 2003 and AASHTO-LRFD, 2004 is in a good agreement with the results from this parametric study for simply supported composite concrete bridges with small L/R ratio. It is evident that AASHTO Guide criterion (Guide, 2003) to treat curved bridges as straight one is conservative.
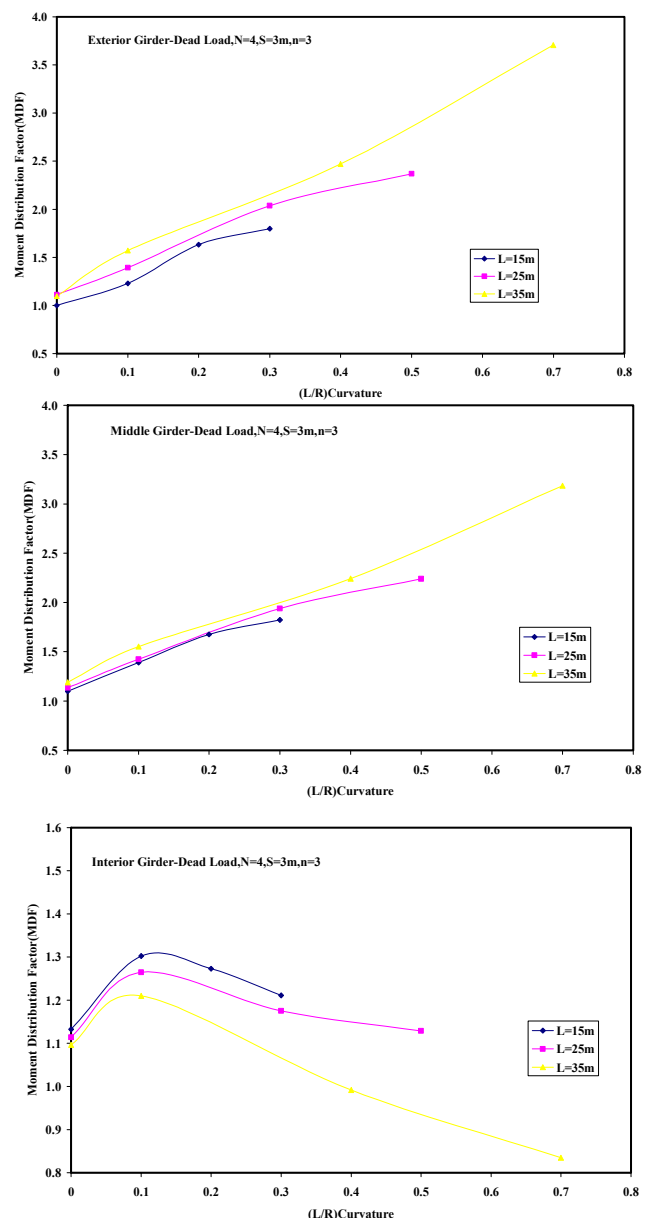
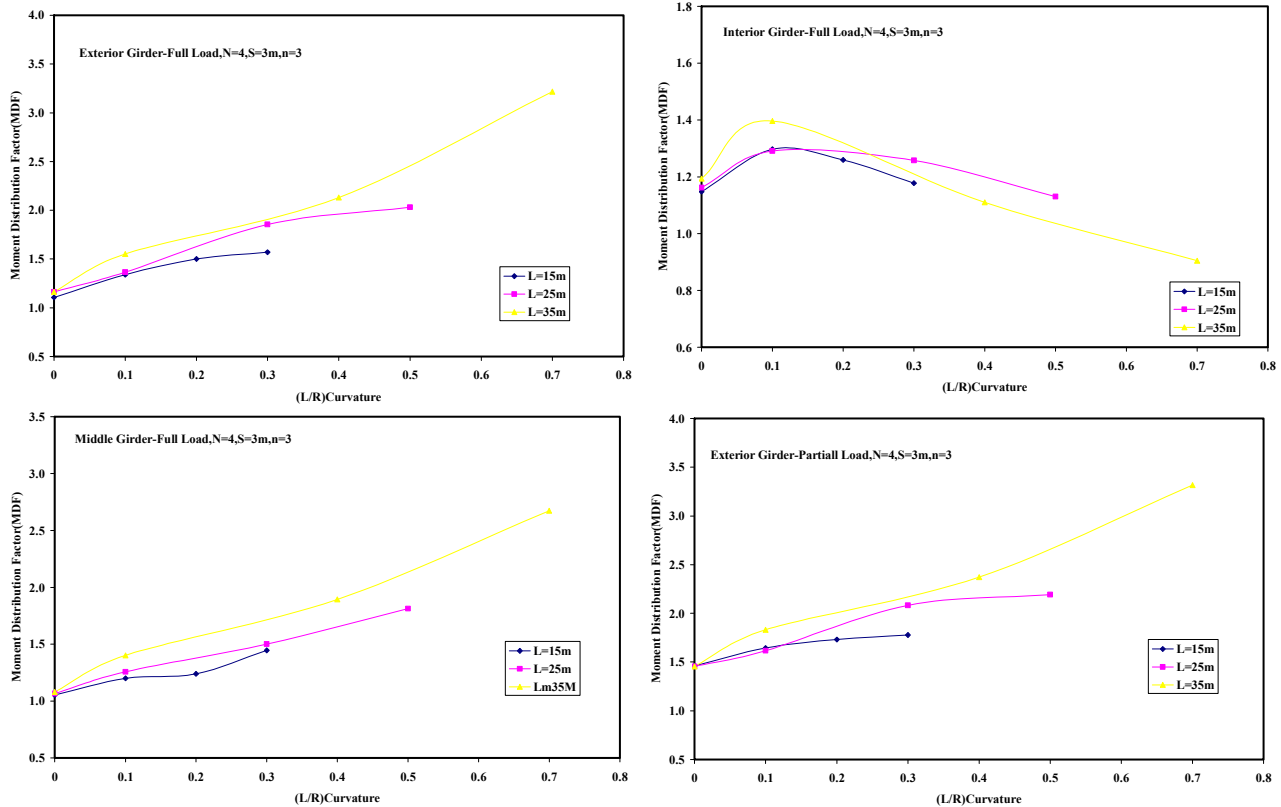**Fig.5: Effect of Bridge Curvature on moment distribution factors due to dead loading**

**Fig.6: Effect of Bridge Curvature on moment distribution factors
due to AASHTO Truck loading**

EFFECT OF SPAN LENGTH

Fig. 7 shows result for the effect of bridge span length on the moment distribution factors for the external girders of two-lane five-girder bridges due to dead load and fully-loaded lanes, respectively.

It can be observed that the effect of the span length on the moment distribution factors is insignificant for straight bridges with L/R=0. However, for curved bridges, the moment distribution factor of the exterior girder is observed to increase with the increase in the span length as shown in this figure.

EFFECT OF NUMBER OF LONGITUDINAL GIRDERS

To study the effect of number of girders on the moment distribution factors, a bridge with 2.5m girder spacing and 35m span length is considered. **Figs. 8 and 9** show the effect of number of longitudinal girders on the moment distribution factors due to dead load, fully-loaded lanes,

respectively, for the exterior, middle and interior girders

Generally, In case of dead load, there is insignificant change in the moment distribution factor for the exterior and interior girders with the increase in number of girders for any investigated curvature ratios. Whereas, moment distribution factor for the middle girder increases with the increase in the number of girders especially for larger curvature ratios.
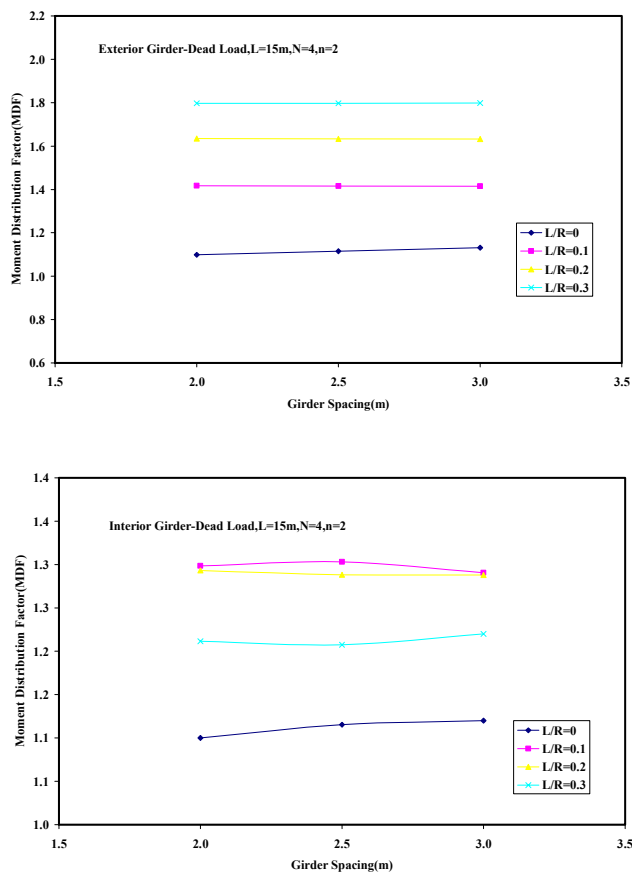
For the case of fully loaded lanes, it can be observed that the moment distribution factor for the exterior and interior girders increases with the increase of number of girders. It can also be noticed that the rate of increase of the moment distribution factor generally higher for the interior girder. Whereas, moment distribution factor for the middle girder generally increases with the increase in the number of girders especially for larger curvature ratios.
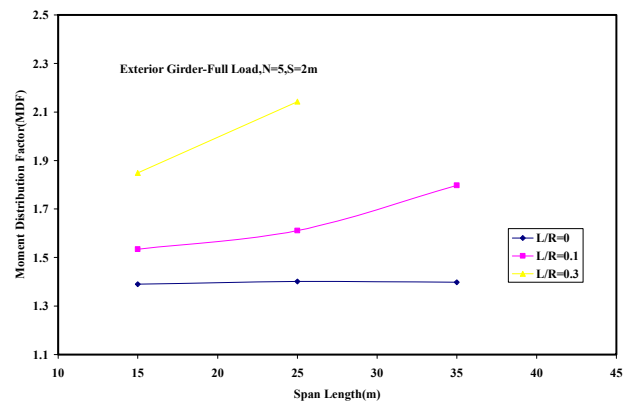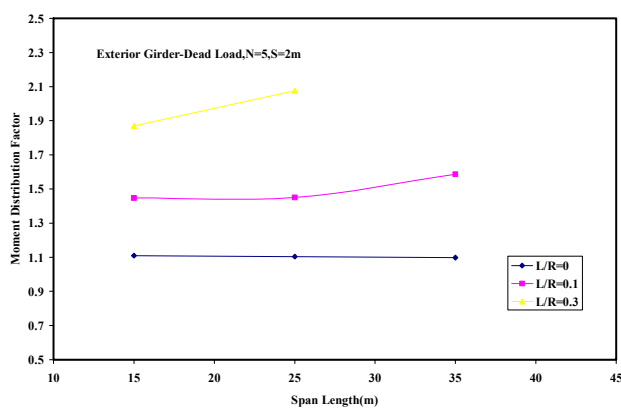
Fig.7: Effect of Bridge Span Length on moment distribution factors
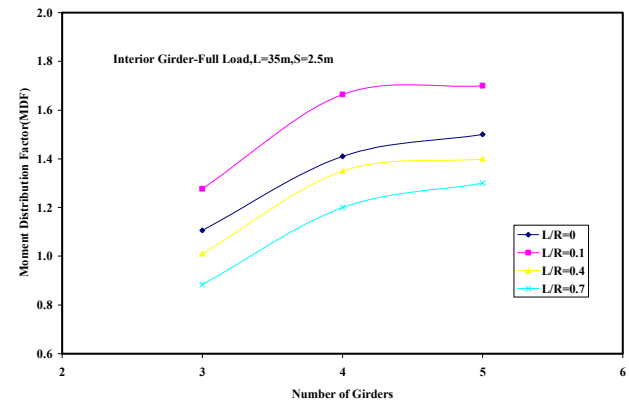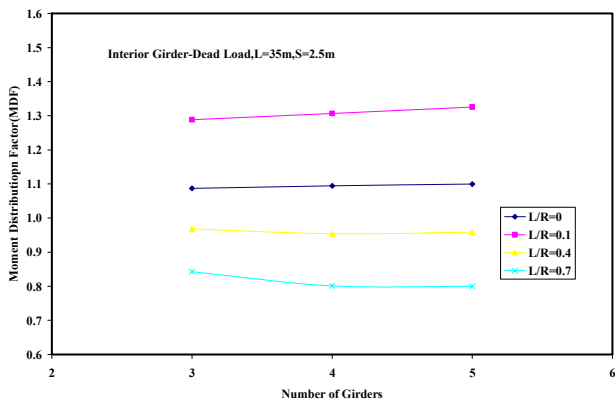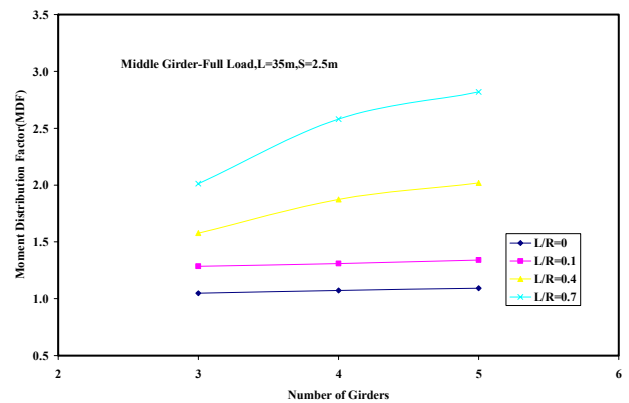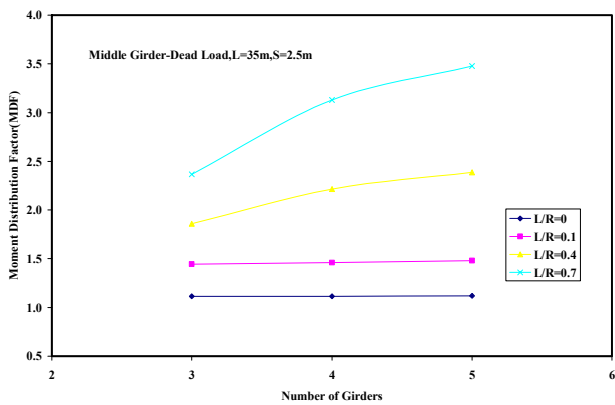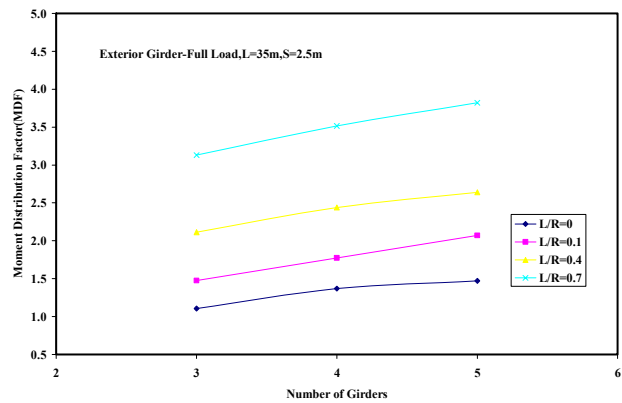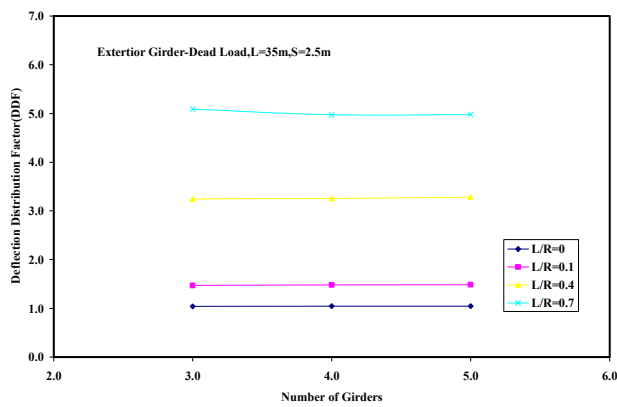
Fig.8: Effect of Number of Girders on moment distribution factors Due to Dead loading

175

Fig.9: Effect of Number of Girders on moment distribution factors Due to Live loading

EFFECT OF SPACING OF GIRDERS

Figs. 10 and 11 show the effect of the spacing of the longitudinal girders on moment distribution factors for the exterior, middle and interior girders of two-lane curved bridges of 15m span and having 4 girders due to dead load and fully-loaded lanes, respectively.

Generally, it can be observed that the moment distribution factors for all girders increases with the increase in girder spacing for AASHTO truck live loading (**Fig. 11)** especially for the exterior and interior girders. While, the moment distribution factors are almost unchanged with the increase in girder spacing in the case of dead load as shown in **Fig. 10**.

15m span length due to fully loaded lanes and partially loaded lanes, respectively.

It is observed that in the full loading case as the number of lanes increases, the moment distribution factors decreases. Hence, for the exterior girder shown in **Fig. 12,** as the number of lanes increases from 2 to 4 lanes the moment distribution factor decreases from 1.83 to 1.59 for L/R=0.3.

For partially loaded lanes no general trend is observed as shown in **Fig. 13**. But, generally the moment distribution factors increases for the exterior girder as the number of bridge lanes is increased.

Fig. 10: Effect of Girders Spacing on moment distribution factors Due to Dead loading

EFFECT OF NUMBER OF LANES

Figs. 12 and 13 show the relationship between the moment distribution factors and the number of lanes for the exterior and interior girders of a bridge with five girders, 2 m girder spacing and
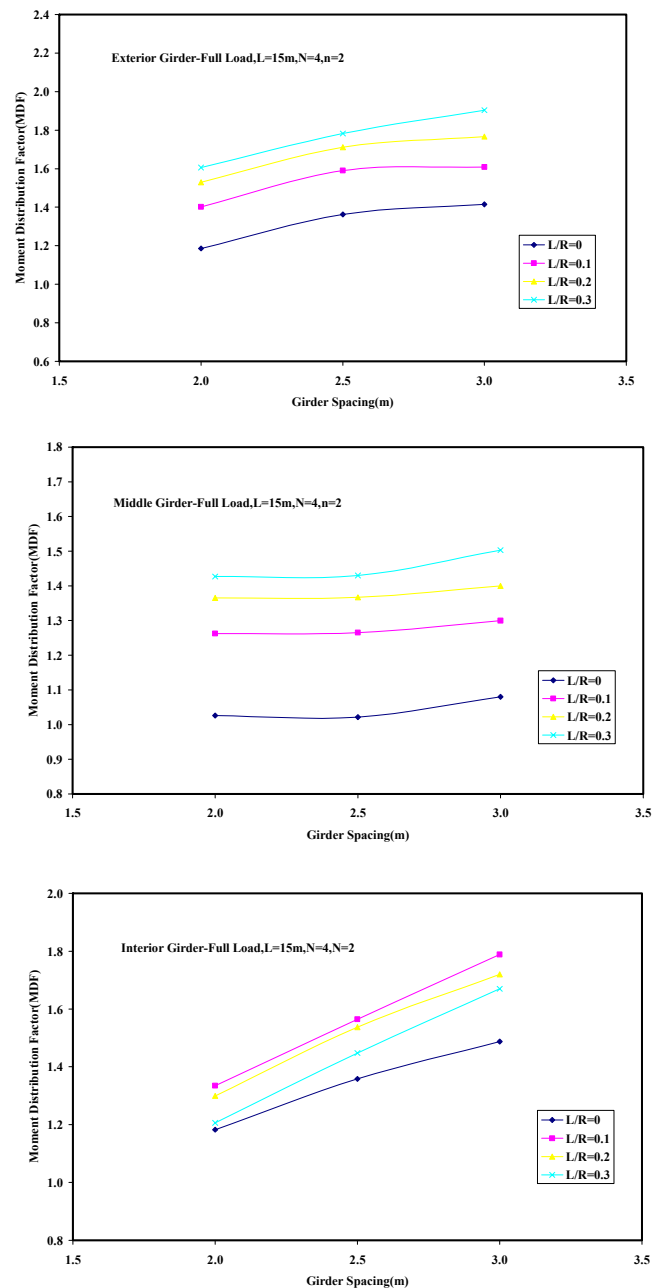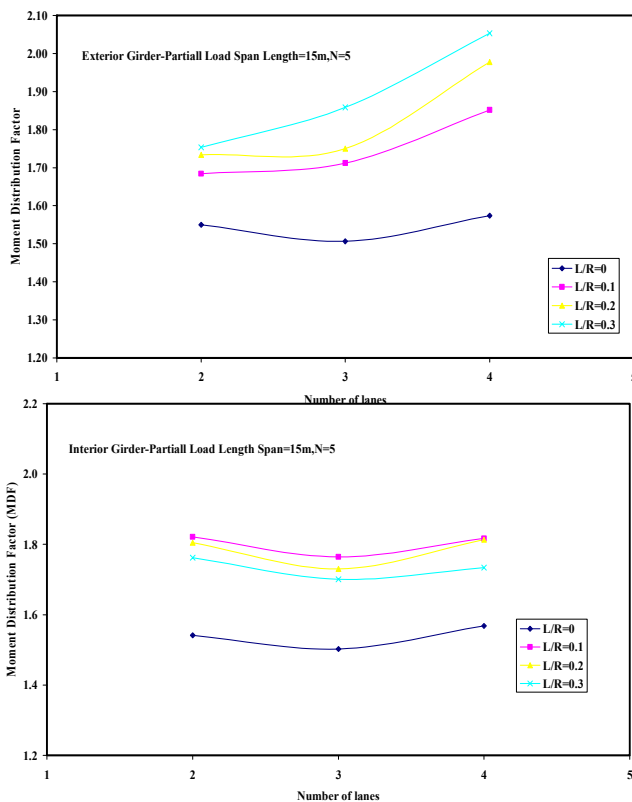

Fig. 11: Effect of Girders Spacing on moment distribution factors Due to Truck loading
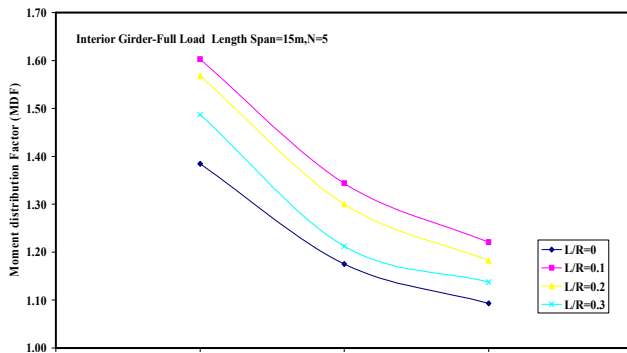
Fig. 12: Effect of Number of Lanes on moment distribution factors Due to Fully loaded Lanes

**Fig. 13: Effect of Number of Lanes on moment distribution factors Due to partially loaded**

EFFECT OF LOADING CONDITION

It is important to examine the effect of number of loaded lanes on the moment distribution factor to establish the critical cases that produce extreme values of moment distribution factors. Accordingly, two loading cases are considered; fully loaded lanes with truck loading and partially loaded lanes with truck loading.

Figs. 14 and 15 show the relationship between results obtained from the case of fully loaded lanes and the case that provides the maximum moment distribution factor of all the partially loaded cases for the exterior and interior girders, respectively. It is worthwhile to mention that these plotted values

are for all bridges of 35m and 15m spans regardless of number of lanes, or number of girders or girders spacing.

It can be observed from the above Figures that sometimes with partially loaded lanes are almost half of the live load of the fully loaded lanes, still they can provide extreme design values especially for the interior girder
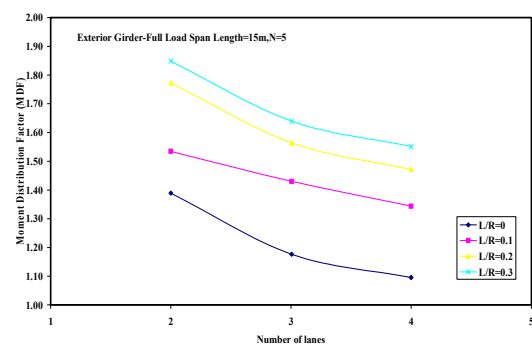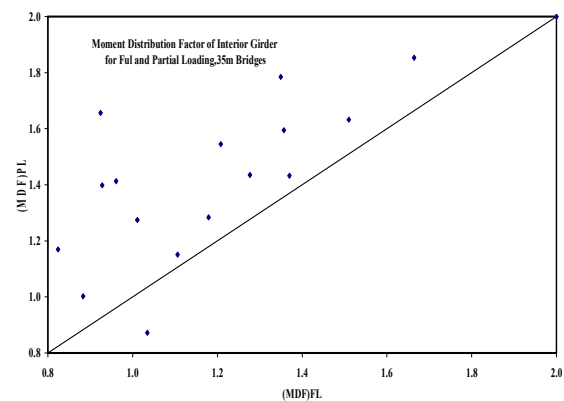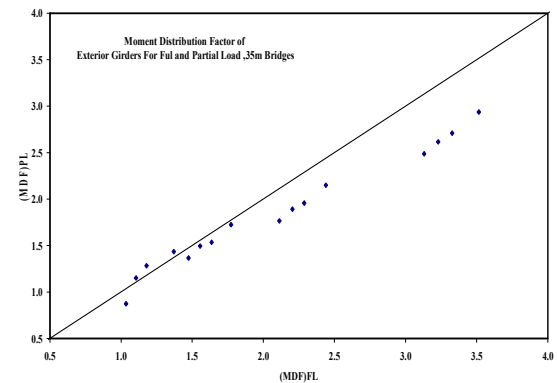
Fig. 14: Effect of loading condition on the moment distribution factor for the 35m span bridges

177
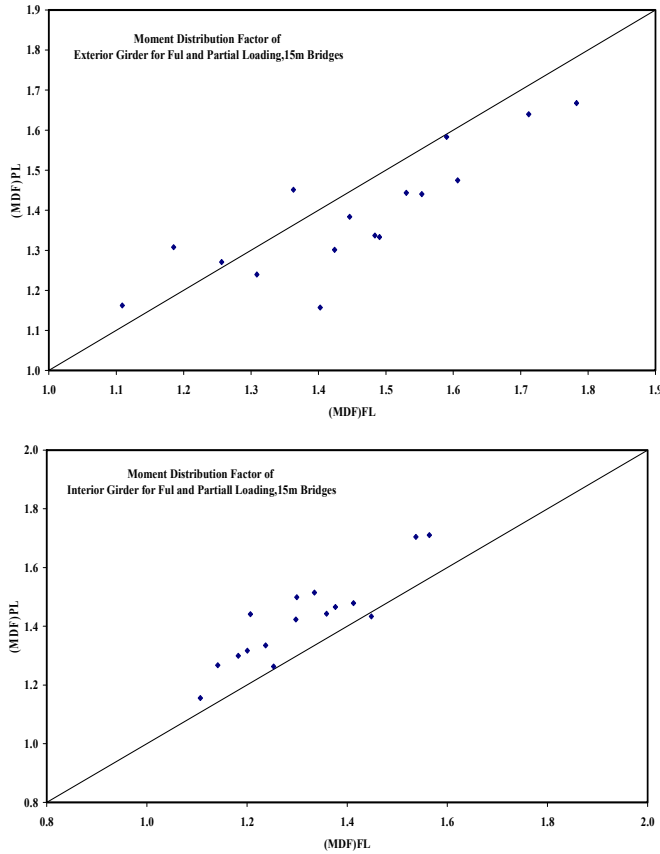
**Fig. 15: Effect of loading condition on the
moment distribution factor for the 15m span**

PROPOSED MOMENT DISTRIBUTION FACTOR EQUATIONS

The current parametric study provides a database for the moment distribution factors for straight and horizontally curved composite concrete-steel bridges. This database can be used to develop expressions for the moment distribution factors for such bridges.

The general equations for load distribution factor for exterior, middle and interior girders for straight and curved I-girder bridges due truck loading and dead loading are presented herein below.

Two equations are proposed for each girder. Equations A includes the three major parameters that affect load distribution factors, as indicated by the correlation matrices. Whereas, equations B includes the six parameters investigated in this study.

Equation B is intended to represent simple relation with the minimum number of variables that may yield sufficiently accurate load distribution factor results. Whereas, Equation B is intended to represent the most general relation that may yield the most accurate load distribution factor results to

be used for final analysis and design of curved bridge girders.

TRUCK LOADING

$$(MDF)_{EXT} = 1.11 + .025L + 3.862L/R - .116X \quad (9.A)$$

$$(MDF)_{EXT} = .124 + .025L + .243N + .297S + 3.925L/R$$
$$-.119X - .323n \quad (9.B)$$

$$(MDF)_{MID} = .969 + .019L + 3.071L/R - .088X \quad (10.A)$$

$$(MDF)_{MID} = .567 + .018L + .087N + .018S + 3.032L/R$$
$$-.088X - .003n \quad (10.B)$$

$$(MDF)_{INT} = .7 \times (MDF)_{EXT} \quad (11)$$

DEAD LOAD

$$(MDF)_{EXT} = .914 + .025L + 4.347L/R - .1X \quad (12.A)$$

$$(MDF)_{EXT} = .661 + .025L + .03N + .069S + 4.351L/R -$$
$$.1X - .017n \quad (12.B)$$

$$(MDF)_{MID} = 1.19 + .015L + 3.812L/R - .096n \quad (13.A)$$

$$(MDF)_{MID} = .595 + .014L + .114N + .053S + 3.764L/R$$
$$-.093X + .000n \quad (13.B)$$

$$(MDF)_{INT} = 0.75(MDF)_{EXT} \quad (14)$$

CONCLUTIONS

Based on the results from the parametric study, the following conclusions are drawn:

1- Curvature is the most critical factor which plays an important role in the design of curved girders in composite bridges. Moment distribution factors increase with the increase in bridge curvature,

2- Span length, number of girders and girders spacing generally affect the values of the moment distribution factors .In general, the increase in the number of girders, girders spacing, and span length results in an increase in the moment distribution factor,

3- The developed sets of empirical expressions for moment distribution factors can be used to obtain the MDF for such bridges.

4- Study reveals that fully loaded lane cases govern the extreme values of the moment distribution factors. Nevertheless, partially loaded lane cases sometimes provide the design value.

5- Results from this study have shown that AASHTO Guide and AASHTO-LRFD criterion to treat curved bridges with small specified amount of curvature as straight ones is safe and conservative.

REFERENCES

- American Association for State Highway and Transportation Officials, AASHTO. 2004. **AASHTO-LRFD Bridge Design Specifications**. Washington, D.C.

- American Association for State Highway and Transportation Officials, AASHTO. 2003. **Guide Specification for Horizontally Curved Highway Bridges**. Washington, D.C.

- American Association of State Highway and Transportation Officials, AASHTO. 1996. **Standard Specifications for Highway Bridges**. Washington, D.C.

- American Association for State Highway and Transportation Officials, AASHTO. 1993. **Guide Specification for Horizontally Curved Highway Bridges**. Washington, D.C.

- Davidson, J. S., Keller, M.A. and Yoo, C.H., "**Cross-frame Spacing and Parametric Effects in Horizontally Curved I-Girder Bridges**", ASCE Journal of Structural Engineering, 122(9): 1089-1096, 1996.

- Qassem, Z.S. , "**Load Distribution Factors for Horizontally Curved Composite Concrete-Steel Girder Bridges**", M.Sc. thesis, Civil Engineering Dept., University of Baghdad, 2004.

- McManus, P.F., Nasir, G.A. and Culver, C. G., "**Horizontally Curved Girders – State of the Art**", Journal of Structural Division. ASCE, 95(ST5): 853-870, 1969.

- Wassef J., "**Simplified Design Method of Curved Concrete slab-on-steel I-girder Bridges**", M.Sc. thesis, Civil Engineering Dept., Ryerson University, Toronto, Ont., Canada, 2004.

- Zuerick, A. and Naqib, R., "**Horizontally Curved Steel I-Girders State-of-the-Art Analysis Methods**", Journal of Bridge Engineering, 4 (1): 38-47, 1999.

- Zureick, A., Linzell, D., Leon, R. and Burrell J., "**Curved steel I-girder bridges: Experimental and analytical studies**". Engineering Structures, 22(2), Elsevier Science Ltd., 180-190, 1998.

NOTATION

L	centre line span of a simply supported bridge
n	number of design lanes
N	number of girders
R	radius of curvature of the centre span of the curved bridge
$R\,L$	multi-lane factor
W_c	width of design lane
$(\sigma_{simple})_{DL}$	mid-span stress in bottom flange fibres, for a straight simply supported girder subjected to dead load
$(\sigma_{simple})_{truck}$	mid-span stress in bottom flange fibres, for a straight simply supported girder subjected to AASHTO truck loading
$(MDF)_{DL\ ext}$	the moment distribution factor of exterior girder for dead load case
$(MDF)_{FL\ ext}$	the moment distribution factor of exterior girder for full load case
$(MDF)_{PL\ ext}$	the moment distribution factor of exterior girder for partial load case
$(MDF)_{DL\ mid}$	the moment distribution factor of middle girder for dead load case
$(MDF)_{FL\ mid}$	the moment distribution factor of middle girder for full load case
$(MDF)_{DL\ int}$	the moment distribution factor of interior girder for dead load case
$(MDF)_{FL\ int}$	the moment distribution factor of interior girder for full load case
$(MDF)_{PL\ int}$	the moment distribution factor of interior girder for partial load case